FORMATION AND GROWTH OF IRRADIATION-INDUCED DEFECT STRUCTURES IN CERIA

BY

BEI YE

DISSERTATION

Submitted in partial fulfillment of the requirements
for the degree of Doctor of Philosophy in Nuclear Engineering
in the Graduate College of the
University of Illinois at Urbana-Champaign, 2011

Urbana, Illinois

Doctoral Committee:

Professor James F. Stubbins, Chair
Associate Professor Brent J. Heuser
Professor Barclay G. Jones
Professor James N. Eckstein

Abstract

Radiation damage effects are of primary concern for materials used in nuclear energy production. In this study, emphasis was given to the processes of formation and growth of radiation-induced defect structures in oxide fuels. Due to the natural complexity of oxide fuels, which consist of both a metal sublattice and an oxygen sublattice, radiation effects are much more complex in oxides than in metals. As a result, there are many radiation effects that are still not well understood despite numerous research efforts engaged in the past. This study was aimed to help clarify some of these effects, such as the evolution process of dislocation structures during irradiation and how it is affected by various irradiation conditions.

In order to develop an understanding of the radiation damage process in the common fluorite-type ceramic oxide fuel, ceria (CeO_2) was selected as a surrogate material of UO_2 for this study. According to previous studies, ceramic materials with a fluorite crystal structure possess high radiation tolerance. Using CeO_2 single crystals allowed for the observation of the intrinsic behavior of defects while excludes the effects of grain boundaries.

To reveal the basic mechanisms responsible for the evolution of microstructure induced by irradiations, a group of coordinated experiments were designed by incorporating multiple techniques consisting of ion irradiation, *in situ* transmission electron microscopy (TEM) and *ex situ* TEM observation. Radiation damage in the materials was induced by irradiating them with krypton and xenon ions from an accelerator. Irradiation experiments were conducted at three temperature regimes: room temperature, 600°C and 800°C, in order to inspect the temperature dependence of atomic defect transportation. Ion energies were carefully chosen for low and high energy irradiations in order to produce a deposited ion peak within the specimen at low energy and a uniform distribution of defects at high energy. *In situ* TEM analysis was used in order to take advantage of real-time recording of defect nucleation and growth under gas ion irradiation, and *ex situ* TEM analysis was used to characterize the radiation-induced features at high image resolution along with

complementary elemental analysis techniques such as X-ray energy dispersive spectroscopy (EDS) and electron energy loss spectroscopy (EELS).

In addition to the experimental investigation, a rate theory model, as a part of the multi-scale simulation approach, was employed to study the growth behaviors of dislocation loops. The computational results were found to be consistent with the experimental observations.

Acknowledgements

First of all, I would like to express the most profound gratitude to my advisor Prof. James Stubbins. He ensured my academic, professional, financial and moral well being ever since my first day at the University of Illinois. Through my PhD, I am very much benifited from his guidance and knowledge. More important, he always has strong faith on students even long before they realize what they can really achieve. His vision on science always motivates me to explore more in the field. In every sense, none of this work would have been completed without him.

I am greatly indepted to my parents and family. During my PhD, although far away from them, they supported and encouraged me to do what I want to do, and provided a loving environment for me. It is not possible to accomplish this without them, so this thesis is dedicated to them.

I am deeply grateful to Dr. Mark A. Kirk and Dr. Jeffery Rest at Argonne National Laboratory for their insightful suggestions, encouragement and time. Dr. Mark A. Kirk answerd many of my questions about *in situ* irradiation, and taught me a lot of techniques used in transmission electron microscopy. All these are invaluable not only for this project but also for my future career. Dr. Jeffery Rest guided me through the rate theory modeling and always inspired me to think further. It is a huge pleasure for me to work with them. Their enthusiam toward the research and kindness to people are something I really long for.

I wish to express my sincere thanks to Prof. Jones, Dr. Heuser and Prof. Eckstein. They not only served in my committee but also gave me handful of constructive comments.

Many thanks go to my fellow colleagues: Aaron Oaks, Wei-ying Chen, Yinbin Miao, Brian Kleinfeldt and Carolyn Tomchik. I enjoyed every moments in your company. The technical and moral support you provided greatly relieved my stress in difficult times. Special thanks

are due to Wei-ying, who accompanied me in a lof of irradiation experiments and helped in many data analyses, and Aaron, who helped me correct my English without any complaints.

I would also like to address a sincere acknowledgement to the staffs at the experiment facilitys. They are Peter Baldo and Edward Ryan at the IVEM-Tandem facility at ANL, and Jianguo Wen, Changhui Lei, Wacek Swiech and Doug Jeffers at the Material Research Laboratory at the University of Illinois. They patiently trained me to use the instruments and kept the facilitys working properly.

I also would like to thank Idell Dollison, Gail Krueger and Becky Meline in the Nuclear Engineering department, who have always been very helpful and efficient in assistanting me in many ways.

Finally, this work is surported by DOE NERI DE-FC07-07ID14838 and DOE NERI DEFG-07-14891. The IVEM/Tandem facility at Argonne National Laboratory was supported by the ANL Center for Electron Microscopy under DE-AC02-06CH11357.

Table of Contents

I. Background and Objective

In order to meet the increasing energy demand and protect the environment for future generations, future energy production must base on abundant, clean, and economical energy sources. As a major clean energy source, nuclear energy provides about 20% of the total electricity in the United States, and it will continue to be a significant energy option for the future. To enable an expansion of nuclear power, it must overcome critical challenges in cost, waste disposal, and proliferation concerns while maintaining its currently excellent safety and reliability record, which requires an evolution of the nuclear fuel cycle. A resolution pattern with a closed fuel cycle based on plutonium startup of fast reactors has been proposed, which is in contrast with the "once through" or "open" fuel cycle currently used with light water reactors.

The pathway to a closed fuel cycle includes recovery of plutonium from light water reactor spent nuclear fuel and use of that plutonium to start fast reactors with high conversion ratios (figure I.1). Conversion ratios greater than one imply more fissile nuclear fuel is produced than consumed. In a closed fuel cycle, the ultra-long-lived radiotoxic constituents (Pu, Np, Am) of the spent fuel can be fission-destructed. A closed fuel cycle is thought to be beneficial because it allows the recovery of additional energy from the spent nuclear fuel (SNF) and greatly reduces the volume and radioactive lifetime of the high-level waste (HLW) package destined for geologic disposal.

A sodium-cooled fast reactor is considered the most practical reactor for the next-generation nuclear fuel cycle system. The fast or high energy neutrons in a fast reactor are able to fission long-lived transuranics and convert them into shorter-lived isotopes. During this process, significant amounts of energy are released while transuranics are destroyed. In the context of this application, the major constituents

of the nuclear fuel used in the envisioned fast reactors will be U, Pu and the minor actinides (Np, Am, Cm), which are retrieved from spent fuels taken out from light-water reactors.

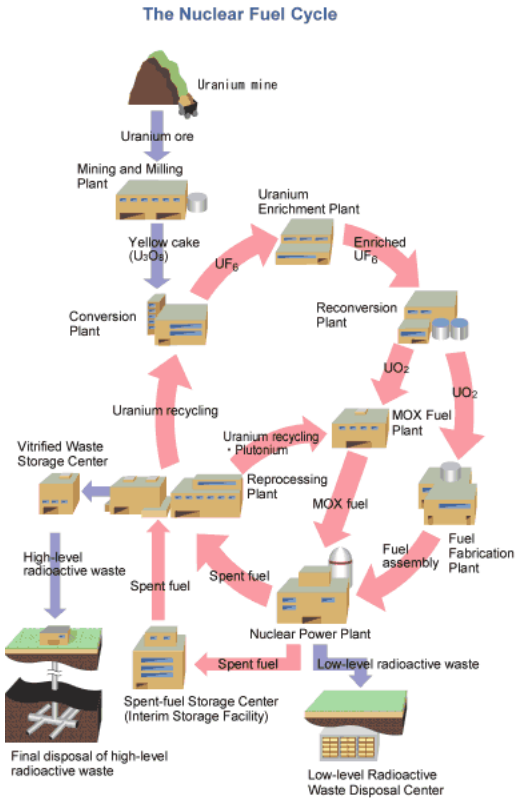

Figure I.1 A closed nuclear fuel cycle

In the design and development of fast breeder reactors (FBR), one of the key challenges is the development of innovative fuel forms. Oxides, metals, nitrides and carbides are the major viable fuel forms envisaged for sodium-cooled fast reactors. Among these candidates, the oxide fuel is selected due to its satisfactory dimensional and radiation stability and chemical compatibility with cladding metals. In addition, it has the advantage of demonstrated and commercially available manufacturing technology with the least technical uncertainty. The innovative part of mixed oxide (MOX) fuel used in FBRs is the incorporation of minor actinides in the $(U, Pu)O_2$ phase [1].

Moreover, the pressure of competing economically with electricity produced from coal and natural gas has driven current reactor operator to seek even higher burnup of their fuel, generally UO_2. The current fuel design has reached its limit at a burnup estimated to be ~80 MWd/kg U. Extending the operational life of nuclear fuel in the reactor improves the efficiency of the materials flow process and results in a reduction of the cost of the fuel cycle. However, the discovery of high burnup structure (figure I.2) in LWR spent fuels [2] raised some concern over the safety of extended fuel operation and highlighted the necessity of measuring and modeling the impact of the restructuring process on LWR fuel performance.

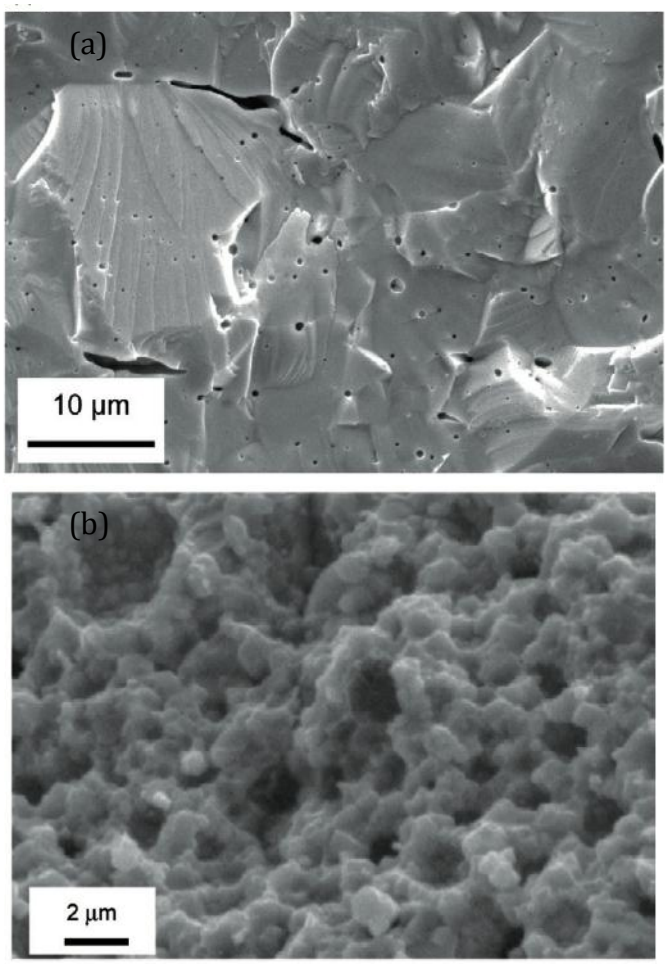

Figure I.2 High magnification SEM fracture surface micrograph of LWR UO_2 fuel (a) before irradiation [2], (b) with a local burn-up of around 160 GWd/tHM [3].

Understanding the oxide fuel behavior under high fast neutron dose and high operating temperature is critical in order to design advanced nuclear fuel and improve current fuel performance, which must fulfill the requirements of incorporation of minor actinides and high burnup achievement. Particularly, the basic microstructural aspects of fuel behavior are fundamental to understand fuel performance radiation effects and fission product transport processes in nuclear fuels. Therefore, the mechanisms of radiation damage production and annealing are of primary concern for nuclear fuel materials.

The objective of this study is to understand the growth of irradiation-induced defects and fission-product transportation in oxide nuclear fuel by combining experimental and modeling efforts. During the lifetime of nuclear fuel, many aspects of radiation damage occur in fuel materials, which determine the performance of the fuel and its behavior at long operation time. To achieve a thorough understanding of these physical and chemical processes, it is important to look into the basic kinetics of radiation-induced point defect accumulation in the matrix and the formation of point defect clusters, i.e. dislocation loops, voids and so on. In this study, cerium dioxide is used as a surrogate material of uranium dioxide. Ion implantation is chosen to create radiation-induced defects in the ceria single crystals. Inert gas ion Kr and Xe are chosen to examine transportation and trapping of simulated fission products.

II. Behavior of Oxide Fuels under Irradiation

This chapter deals with reactor operation conditions in LWRs and FBRs that influence the material properties of oxide fuels, uranium dioxide and mixed uranium-plutonium dioxide. Ever since the usage of UO_2 as the fuel for the Shippingport PWR in 1955, a vast amount of information on the behavior of this material under reactor conditions has been collected.

Oxide fuels have demonstrated very satisfactory dimensional and radiation stability and chemical compatibility with cladding metals and coolant in LWRs. However, under the much more severe conditions in a fast reactor, oxides begins to respond to their environment in a manner that is often detrimental to fuel performance.

The major disadvantages of oxide fuels are its low uranium density and low thermal conductivity. The low percentage of metal atoms in oxide fuels required a larger core to achieve a sufficient amount of fissile species, which raises the capital cost of the reactor. Poor thermal conductivity causes a substantial temperature difference between the center and the surface of the rod, which normally induces thermal stresses on the material and leads to deformation over an extended period of time.

II.1 MOX Fuel Performance in Fast Breeder Reactors (FBRs)

II.1.1 Operating Conditions of FBRs

The energy produced by the fast breeder reactors comes from the fission of fissile ^{239}Pu induced by fast neutrons. In order to maintain the fast spectrum of neutrons, there is no neutron moderator in this type of reactor. Associated with this nature, several important features of the design of FBRs are:

1. The fuel (generally MOX fuel) is highly enriched (15-18% ^{239}Pu compared with ~ 4% ^{235}U in a pressurized water reactor (PWR));
2. The neutron flux is high and has sufficient energy to cause displacement damage;
3. The rather high concentration of fissile material induces high specific power ratings and high heat flux to be removed from fuel elements (~200 W/cm^2);
4. A liquid metal coolant, with high thermal conductivity, is required to carry away this high flux;
5. The fuel temperature remains very high in the center of the fuel pins (~2000°C in steady-state conditions, liable to exceed 2500°C during operational transients);
6. The fuel cladding temperature reaches 650°C in steady state conditions, which severely restricts the choice of cladding materials (generally high-strength stainless steel).

II.1.2 Restructuring of the MOX Fuel

The MOX fuel, generally used in fast reactors, is normally prepared by sintering oxides of uranium, plutonium and minor actinides to achieve a homogeneous distribution of Pu and minor actinides in UO_2. This type of fuel is essentially a ceramic material and can sustain very high temperatures. It is enclosed in metallic

pins assembled together inside a hexagonal wrapper (figure II.1), and suffers high irradiation damage in a very hostile environment (high temperature, severe temperature gradients, corrosive atmosphere) for long periods of time.

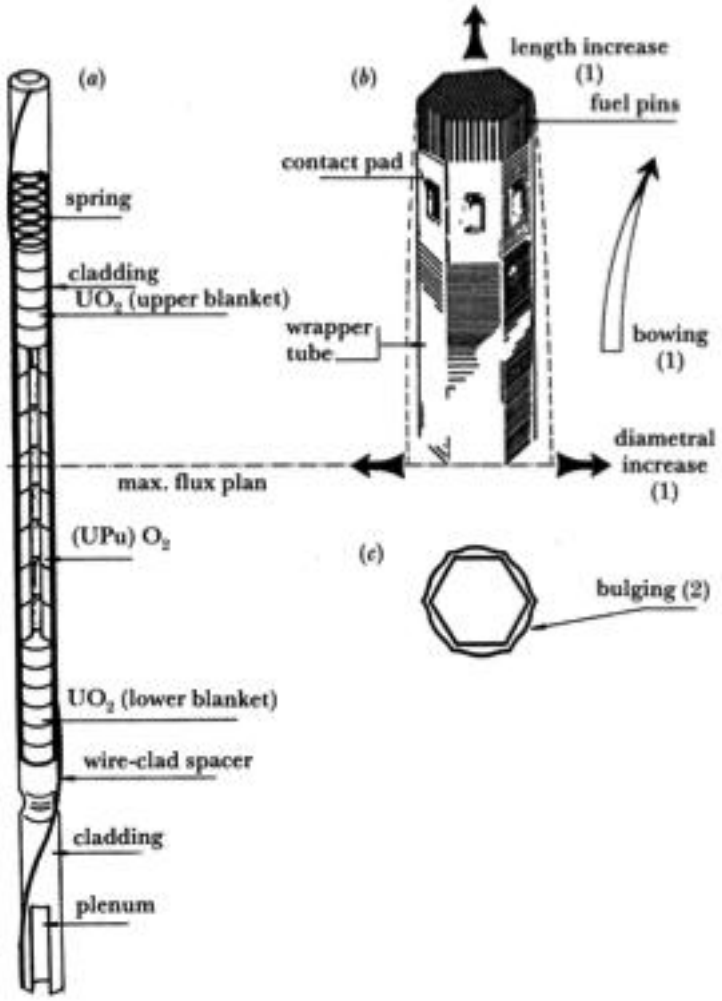

Figure II.1 (a) A fuel pin in Superphénix fast reactor; (b) and (c) fuel subassembly and in-pile deformations: (1) by swelling, (2) by irradiation creep. [4]

The fuel pellet temperature in normal operation ranges from about 800°C on the surface to over 2000°C at the center. The temperature and thermal gradient are so high that they induce significant oxide restructuring [4]. Micrographic examination of the cross section of an irradiated fuel element shows the major modifications in fuel structure (figure II.2) [4]:

1. The fuel is cracked radially, with the cracks annealed at the center;
2. The central pellet zone structure consists of highly elongated (columnar) grains;
3. The initial pellet-cladding gap has largely disappeared, and chimney has formed at the center of the pellet stack.

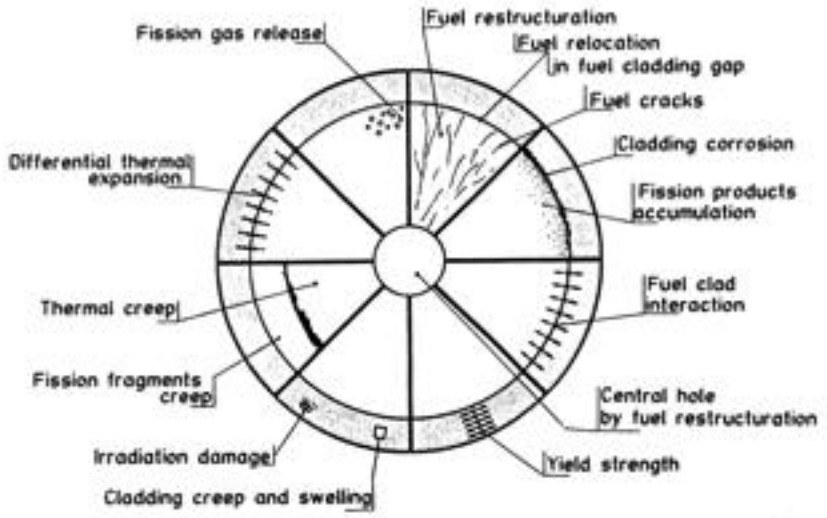

Figure II.2 Phenomena affecting the in-pile fuel behavior [4]

Under steady-state conditions, the MOX fuel swells at a rate estimated to be about 0.7% per atom percent fissioned. This mainly results from two aspects: (a) the difference between the volume of fissile plutonium and the volume of the solid fission products; and (b) the gas bubbles produced by the coalescence of gaseous fission products (krypton and xenon). The former is difficult to overcome, while the other one can be minimized by the careful choice of a proper fuel microstructure and depends also on temperature and time.

During fission process, two different atoms with almost equal atomic mass are generated from one fissile plutonium. Those atoms not only have a size different from the initial plutonium atom, but have also a different valence. The mean valence of the dissolved fission products is lower than that of fissioned plutonium, after taking into account their nature and solubility in the matrix. Consequently the

valence of the remaining plutonium increases to maintain the electrical neutrality of the crystal, which gives rise to a continuous increase of oxygen potential [4]. This is of utmost importance when considering the chemical interaction between fuel and cladding.

It should be noted that most of the previous studies on nuclear fuel were carried out on UO_2, which is a typical light water reactor (LWR) fuel. However, the usual fuel form for the liquid metal-cooled fast reactor is $(U, Pu)O_2$. LWR fuel (UO_2) is initially usually close to stoichiometry (oxygen/metal ratio ~ 2), whereas fast reactor fuel ($(U, Pu)O_2$) is normally initially substoichiometric (O/M ~ 1.98 ± 0.01) [5]. This is because of the ease of reduction of Pu^{4+} to Pu^{3+}. Due to the different operation conditions in LWRs and fast reactors, the fuels in these reactors sustain rather different thermal environment. The temperature profiles in the fuel pins are shown in figure II.3. The fuels in sodium-cooled fast reactor have much higher temperatures and steeper temperature profiles than the fuels in LWR. The steep temperature gradient serves as the driving force for material transport and pore mobility. As a result, a central void is likely to form in fast reactor fuels [6].

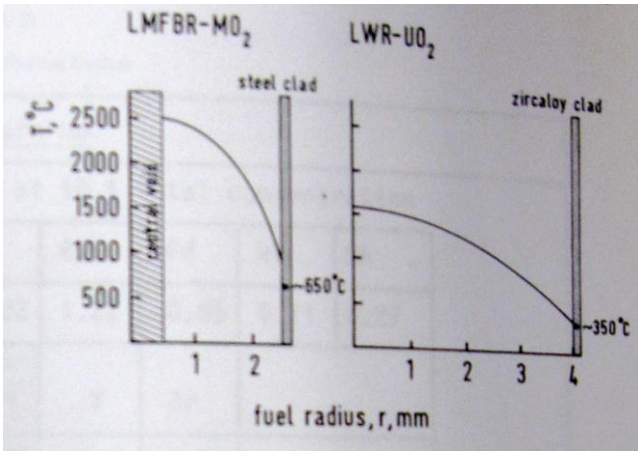

Figure II.3 Typical operating conditions for LMFBR $(U, Pu)O_2$ fuel and LWR U O_2 fuel [5]

II.2 Oxide Fuel Performance in Light Water Reactors (LWRs)

II.2.1 Operation Environment of LWRs

A LWR reactor core is comprised of fuel assemblies in an arrangement that satisfies the following requirements [7]:

1) Provide a rigid structure for holding the fuel elements;
2) Deliver the desired thermal power to the coolant;
3) Provide a critical assembly with a minimum of neutron leakage;
4) Provide adequate coolant flow to remove fission heat and sufficient coolant volume for thermalization of fission neutron by hydrogen;
5) Accommodate control rods that maintain criticality as the fuel is consumed.

A generic LWR fuel element (figure II.4) consists of a zirconium-tin alloy tube with a length of ~4 m and a diameter of ~1.2 cm for boiling-water reactor (BWR) fuel rods and a diameter of 0.8 cm for pressurized-water reactor (PWR) rods. This cladding tube is filled with a ~3 m stack of fuel pellets, either UO_2 with uranium enrichments up to 5% or a mixture of UO_2 and PuO_2. The remaining space above the fuel stack is an open volume called a plenum, which is designed to accommodate fission gas released from the fuel without overpressurizing the cladding. The typical structural evolution process in a LWR fuel pin is displayed in figure II.5.

In order to predict the fuel performance over long periods of time and in an intense radiation field, it is essential to understand the thermal effects on fuel elements. Fuel performance is influenced by two important characteristics of the temperature distribution: high temperature (approaching the melting temperature, ~2800°C) and steep temperature gradients (approaching 10^4 °C/cm). Most of solid-state reactions, which produce significant changes in material properties, occur at high operation temperatures during the lifetime of the fuel in the reactor. Phenomena primarily affected by high temperature include grain growth, densification (sintering), and fission-product diffusion. The steep temperature

gradient serves as the driving force for a set of deleterious events: thermal stresses resulting from the temperature gradient cause the fuel to either deform plastically in regions of high temperature or to crack in low-temperature zones; the distribution profiles of oxygen, plutonium and fission products deviate from their original uniform ones, and closed pores migrate from low-temperature regions toward the center of the fuel pin.

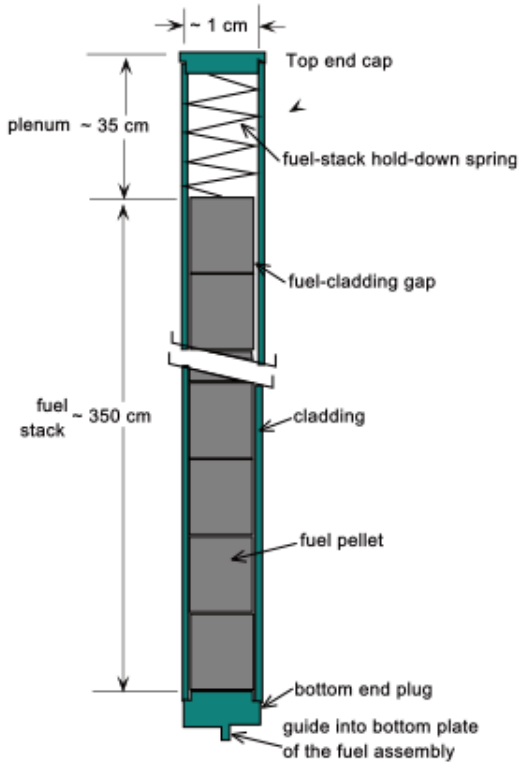

Figure II.4 A generic LWR fuel element

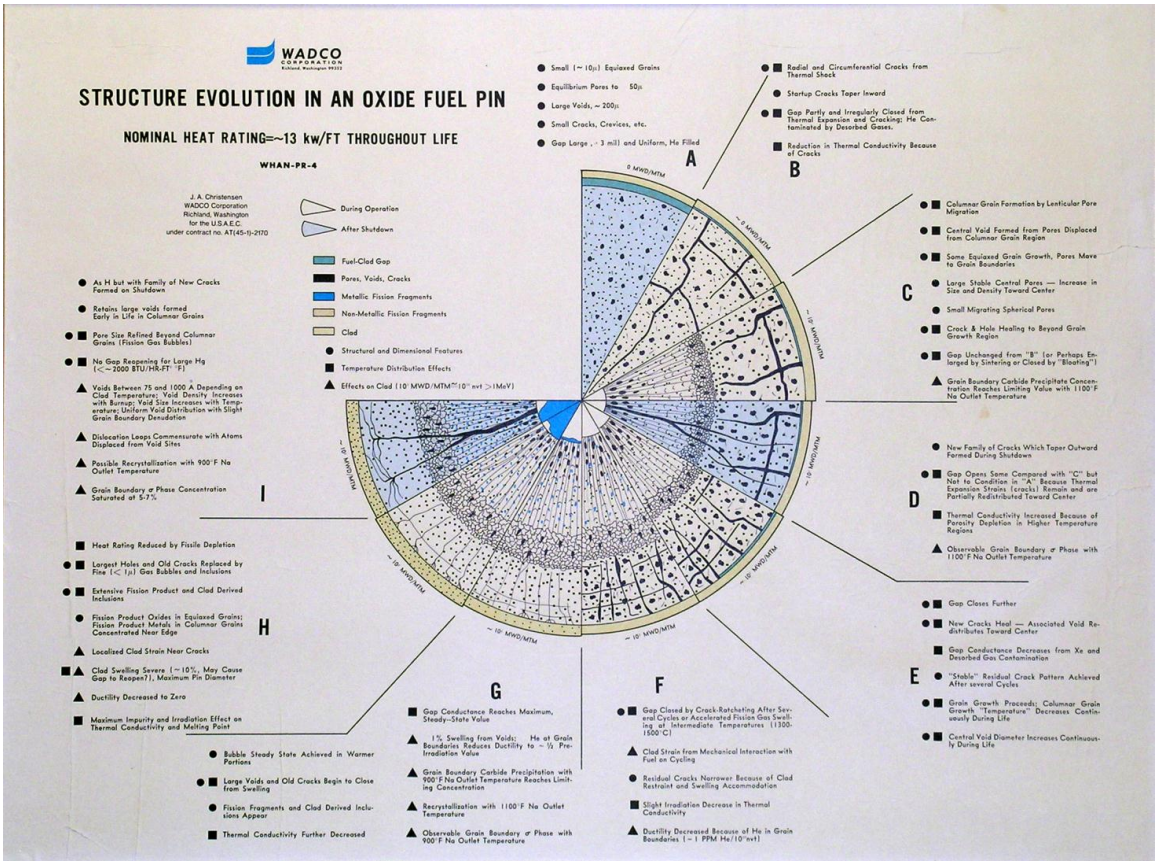

Figure II.5 Structure evolution in an oxide fuel pin

II.2.2 Life-limiting Phenomena

The life of LWR fuel elements can be limited by several phenomena, which are listed in table II. 1 [7]:

Table II. 1 Life-limiting phenomena of LWR fuel elements

Phenomena	Causes
Fretting failure of the cladding	Vertical thermal expansion of the rods due to temperature changes; or flow-induced vibration of the rods within the grid
Cladding corrosion	Combination of high temperature and chemical solutes in the coolant
Hydrogen embrittlement	Absorption of ~15% of the corrosion-product hydrogen in the substrate metal leading to precipitation of zirconium hydride
Pellet-cladding interaction (figure II.6)	Swelling of fuel pellets due to the fission reaction, and the thermal stress generated by the steep temperature gradient in the pellet
Fission gas release	Noble gases Kr and Xe, almost insoluble in UO_2, generated in fission reactions

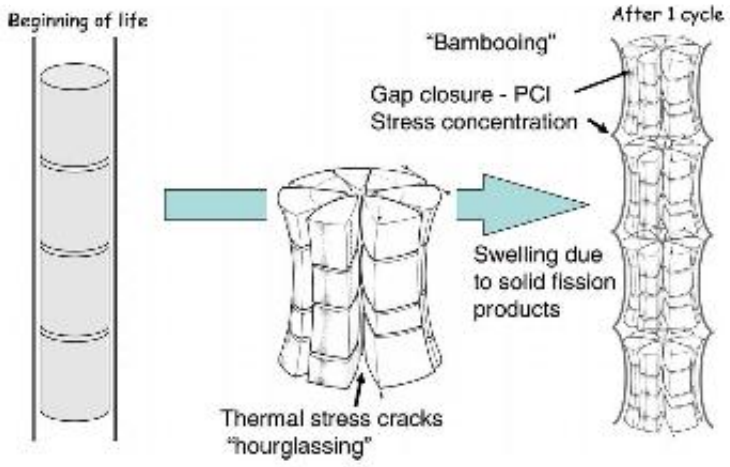

Figure II. 6 Effects of fuel swelling and thermal stresses: The "hourglass" shape of the pellet is due to the switch from plane-strain conditions near the pellet midplane to plane-stress at the upper and lower faces. [7]

The maximum burnup of current fuel design, ~60 MWd/kg U, is limited by the above phenomena. When the fuel is pushed to higher burnup, the probability of a cladding failure becomes significantly larger than the current value of $\sim 10^{-5}$ [7]. Rupture of the cladding of a single fuel element in the core is more of an economic concern than a safety issue. Release of fission products and fuel through the breach in the cladding spreads radioactivity throughout the primary coolant circuit, necessitating reactor shutdown, replacement of the fuel assembly containing the defective fuel rod and extensive decontamination of exposed components.

II.3 Comparison of Thermal and Fast Reactors

The differences in operation conditions between thermal and fast reactors result in various changes in the material properties of oxide fuels due to irradiation damage and thermal effects. Table II.2 summarized a few performance characteristics of typical thermal and fast reactors [8].

Table II.2 comparison of typical 1000-Mw(e) oxide reactors

	LWR	FBR
Fissile species enrichment	3% ^{235}U in ^{238}U	15% ^{239}Pu in ^{238}U
Microscopic fission cross-section σ_f (barns)	550	1.8
Core-averaged thermal neutron flux ($1/cm^2sec$)	$3x10^{13}$	$1x10^{11}$
Core-averaged fast neutron (>0.2 MeV) flux ($1/cm^2sec$)	$5x10^{13}$	$8x10^{15}$
Burnup (%)	3	10
Fast fluence ($1/cm^2$)	$3x10^{21}$	$3x10^{23}$
Irradiation time at full power (years)	2	1.5

From table II.2, it is evident that the flux in the fast reactor is a factor of 100 larger than that in the thermal reactor, and their fission cross sections differ by a factor of 300. However the fuel in the fast reactor produces more power per unit volume. On the other hand, the fast-neutron fluence in a fast reactor is ~100 times greater than in a thermal reactor. Since the fast fluence is primarily responsible for radiation damage to nonfuel components, it is apparent that the selection of the core structure materials becomes a much more severe problem in fast reactors.

Detailed characteristics of fuel elements in thermal and fast reactors are listed in table II.3 [8].

Table II.3 Fuel-element characteristics

	Thermal	Fast
Fuel material	UO_2	$(U,Pu)O_{1.96}$
Fuel-pellet density (% of theoretical)	92	90
Maximum $T_{center\text{-}line}$ (°C)	2450	2800
Cladding material	Zircaloy-4	316 stainless steel
Maximum $T_{cladding\ mid\text{-}wall}$ (°C)	380	660
$T_{coolant\text{-}in}$ - $T_{coolant\text{-}out}$ (°C)	H_2O: 280-320	Na: 470-650
Maximum rod linear power (w/cm)	620	550
Fuel assembly wrapper	Square, 30x30 cm	Hexagonal, 13 cm across flats
Number of fuel pins per assembly	200	220
Fuel-rod outside diameter (mm)	10.7	6.3
Cladding thickness (mm)	0.6	0.4
Fuel-cladding gap (mm)	0.08	0.07
Length of fueled portion (cm)	365	90

The maximum fuel center-line temperature in a fast reactor is set at the melting point of the fuel. In a water-moderated reactor, the power-limiting condition is determined by the change from nucleate to film boiling at the cladding surface. The fuel pins of a fast reactor are smaller in diameter than those of a thermal reactor. This design choice is primarily to provide adequate heat-transfer area per unit mass of fuel to accommodate the higher power density in the fast reactor.

III. Radiation Effects on Nuclear Fuel

During irradiation in a nuclear reactor, a large variety of fission products are generated in the nuclear fuel. Some of these are rare gases (krypton and xenon, etc.), which cause the fuel to swell due to their precipitation into bubbles [9]; others include volatile elements. The volatile elements, notably iodine, are of interest for their radiotoxicity and the possibility of causing fuel failure by stress-corrosion [10]. Other minor elements (Pd, Ru, Rh, Tc and Mo) can form solid precipitates in the fuel [11]. Besides the elements mentioned above, helium gas is another main concern in fuel technology, which is not directly from fission reactions but from α-particle emitters (^{238}Pu, ^{242}Cm, ^{244}Cm, ^{241}Am, etc.). A diagram of the sequential events, which occur during irradiation, is displayed in figure III.1.

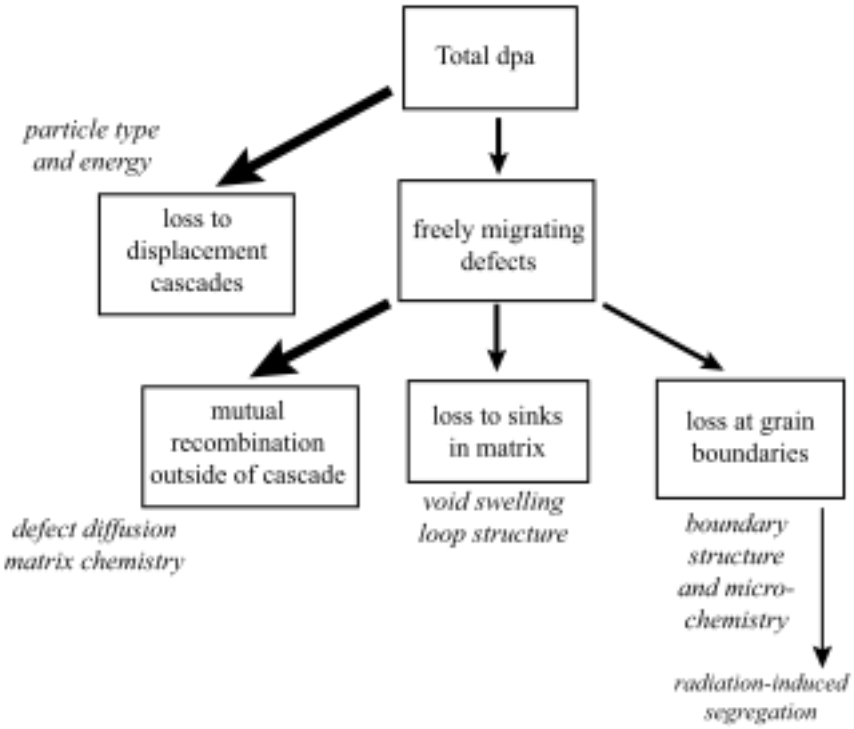

Figure III.1 History of point defects after creation in the displacement cascade [12]

III.1 Basic Effects of Irradiation Cascades

The primary, microscopic events that precede the appearance of gross changes in the solid are termed irradiation damage. When the energy transferred to a lattice atoms is larger than the energy binding the atom in its lattice site, the lattice atom is displaced from its original position. The displaced atom might carry high enough kinetic energy to create a series of lattice displacements before it finally comes to rest. The displaced atom ultimately appears in the lattice as an interstitial atom. The empty lattice sites left behind by the displaced atoms become vacancies. The ensemble of point defects created by a single primary knock-on atom is known as a displacement cascade.

During collision cascades, vacancies and interstitials can be produced so close to each other that clustering of the point defects occurs spontaneously within the short time required for completion of the primary event. Due to the proximity of the clustering point defects, many of the vacancies and interstitials produced by the high-energy collisions annihilate. Only as low as 1% of the initially produced point defects can survive and are capable of producing observable radiation effects [8].

The bombarding particle transfers energy of the order of tens to hundreds of kiloelectron volts to stationary lattice atoms. The total energy loss of a moving atom in the solid is separated into two parts: (1) discrete elastic atom-atom encounters which both reduce the energy of the incident atom and produce lattice displacements and (2) a continuous process of electronic excitation which contributes to energy loss but not to displacements. Interaction of moving atoms or ions with the electrons of the solid constitutes the major energy-loss process at high energies. Transfer of energy from the moving atom to electron does not lead to displacement, only to heat. Energy is transferred to the electrons in small increments so closely spaced that the process can be regarded as a continuous loss of energy. On the other hand, displacements are only caused during elastic atom-

atom collisions, in which a significant portion of the initial kinetic energy of the moving atom is transferred.

Recent molecular dynamics simulations [21-23] suggest that collision cascades have two main stages (figure III.2): an initial ballistic stage during which many atoms are dislodged from their lattice sites, and a subsequent thermal spike phase in which the cascade region attains thermal equilibrium with its surroundings. If the kinetic energy of the atoms in the region of dense collisions is recalculated into temperature (using the basic equation $E = 3/2 \bullet N \bullet k_B T$), the kinetic energy in units of temperature is initially of the order of 10,000 K. Because of this, the region can be considered to be very hot, and is therefore resulting in the formation of a highly disrupted, very hot, region ($R < 50$ Å) inside the solid. This phenomenon is called a "thermal spike". It can be viewed as the short term local melting of the irradiation affected region, and it is followed by a rapid quenching of the liquid phase to form a damaged, amorphous, solid structure. The thermal spikes normally cool down to the ambient temperature in 1-100 ps. Some experiments have shown that a thermal spike can induce a phase transition which is known to require a very high temperature [24].

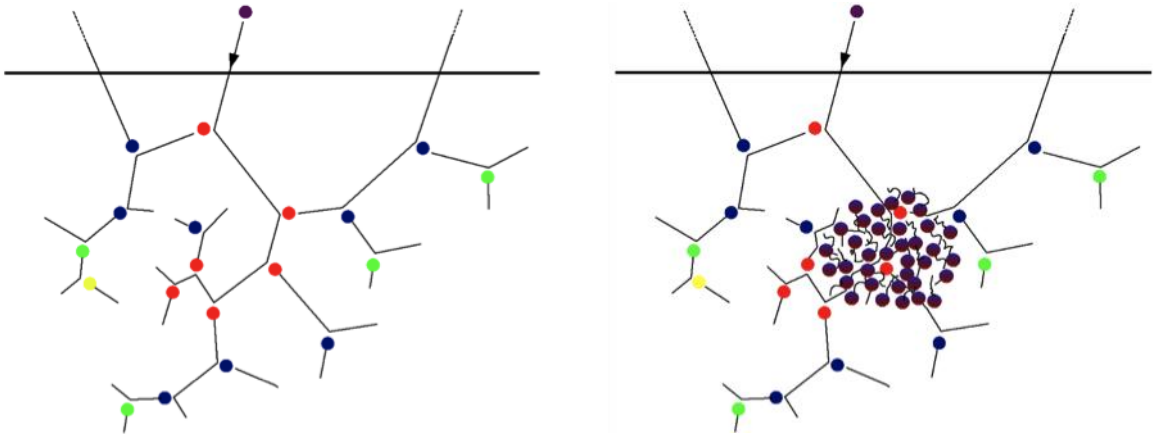

(a) (b)

Figure III.2 (a) schematic illustration of a linear collision cascade; (b) schematic illustration of a thermal spike (images are from wikipedia). The thick line illustrates the position of the surface, and the thinner lines represent the ballistic movement paths of the atoms from beginning until they stop in the material. The circles are incoming and recoiled ions.

The ballistic phase of the cascade, when the initial ion/recoil and its primary and lower-order recoils have energies well above the threshold displacement energy, typically lasts 0.1-0.5 ps. If a heat spike is formed, it can last for some 1-100 ps until the spike temperature has cooled down essentially to the ambient temperature [25]. The cooling down of the cascade occurs via lattice heat conductivity and by electronic heat conductivity. The last stage of a cascade is the relaxation phase, when the defects migrate and possibly recombine, can last from a few ps to infinite times, depending on the material, its defect migration and recombination properties, and the ambient temperature.

Foreman et al. gave an example of the evolution of irradiation damage cascade in copper simulated by molecular dynamics [26]. The cascade evolution has been characterized by the sudden emission of replacement collision sequences and with shape variations due to local channeling events. At the higher energies the core has

been shown to be liquid–like structure with cavitation. The annealing phase leaves loosely clustered vacancies at the cascade center. Figure III.3 shows the three stages in the evolution of a 1 keV cascade in Cu. The initial knock-on energy is divided between two atoms after 0.01 ps, and after 0.05 ps it has divided into a number of branches. After 0.25 ps, maximum cascade size and disorder is attained. After 0.75 ps, the disordered zone starts to recover. Considerable recombination occurs during this recovery and the number of defects is greatly reduced in the thermal spike regime. By approximately 2 ps recovery in the 1 keV cascade is virtually complete and after 10 ps only limited diffusion of the self interstitial atom (SIA) defects has occurred.

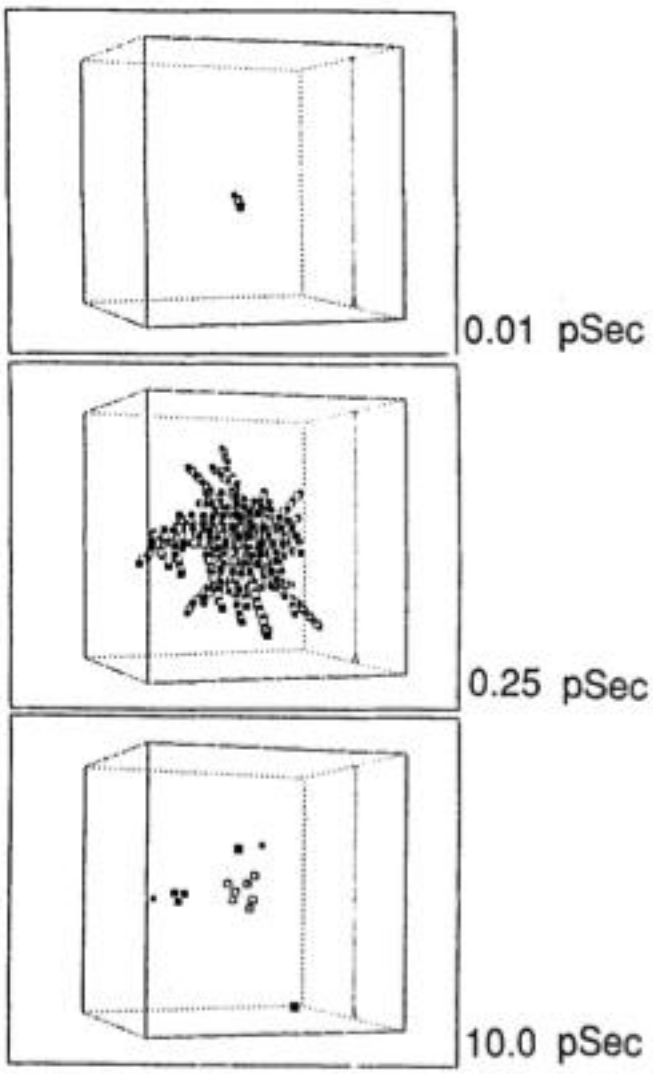

Figure III.3 Stages in the evolution of a 1 keV cascade at an initial block temperature of 100K. The open squares denote the vacancy and the closed square the interstitial atoms [26].

Since the kinetic energies in a cascade can be very high, it can drive the material locally far outside thermodynamic equilibrium. Typically this results in defect production. The defects can be Frenkel pairs, ordered or disordered dislocation loops, stacking faults, or amorphous zones. The defect production is harmful in nuclear fission and fusion reactors where the irradiation damage slowly degrades the mechanical properties of the materials, which is described in detail in the following section. However it can also be useful in modification of materials, for

example when ions are introduced into semiconductor quantum well structures to speed up the operation of a laser [27]. Collision cascades in the vicinity of a surface often lead to sputtering, both in the linear cascade and thermal spike regimes.

Swift heavy ions, which produce damage by very strong electronic stopping, can lead to strong lattice heating and transient disordered atom zone. Therefore swift heavy ions in insulators typically produce ion tracks forming long cylindrical damage zones of reduced density.

III.2 Radiation Effects in Nuclear Fuels

The slowing down of high-energy fission products, and hence damage production due to high-energy heavy ions in nuclear fuels, is the source of nuclear energy. Nuclear particles passing through reactor materials transfer part of their energy to the atoms of these materials and eject some of them from their normal positions in the materials. The cumulative result is manifested in significant modifications of the material properties of irradiated materials. These properties include physical dimensions, strength and hardness, conductivity of heat and electricity, magnetism, resistance to corrosion, and many others. An understanding of all these modifications is necessary to predict the service-life of any material considered for use in nuclear technology.

It is generally accepted that atomic displacements are the most important source of radiation effects in nuclear materials [28]. Atomic displacements are predominantly caused by the fission processes in nuclear fuels. Displacements often lead to the local changes in microstructure, composition and stoichiometry. Those effects result in the modification of physical properties. For example, the lattice parameter in UO_2 increases as a function of irradiation dose is due to the variation in the population of defects (interstitials and vacancies) and their clusters.

To understand damage effects, numerous study have been carried out on spent fuels taken out of reactors or by using controlled ion implantation with fission product ions to generate damage. The observed important phenomena on UO_2 and other fluorite crystals, related to their radiation performance, are summarized below.

III.2.1 Structural stability of actinide oxides (MO_2) against radiation

Extensive examination of spent nuclear fuel structure [2, 3, 11, 29-31] shows UO_2 fuel remains crystalline and does not become amorphous even under long-term reactor conditions. The absence of phase transformation in UO_2 fuel is owing to its fast recovery from lattice disorder.

Experiments focusing on radiation effects in the metal (U) sublattice in UO_2 show that metal atoms are much less mobile than the nonmetal atoms (O) [32]. Therefore metal defects are the rate-controlling species for many kinetic processes of technological interest, such as grain growth, sintering, creep, etc. Figure III.4 shows results on damage ingrowth during ion implantation of different elements into UO_2 single crystal of different orientations.

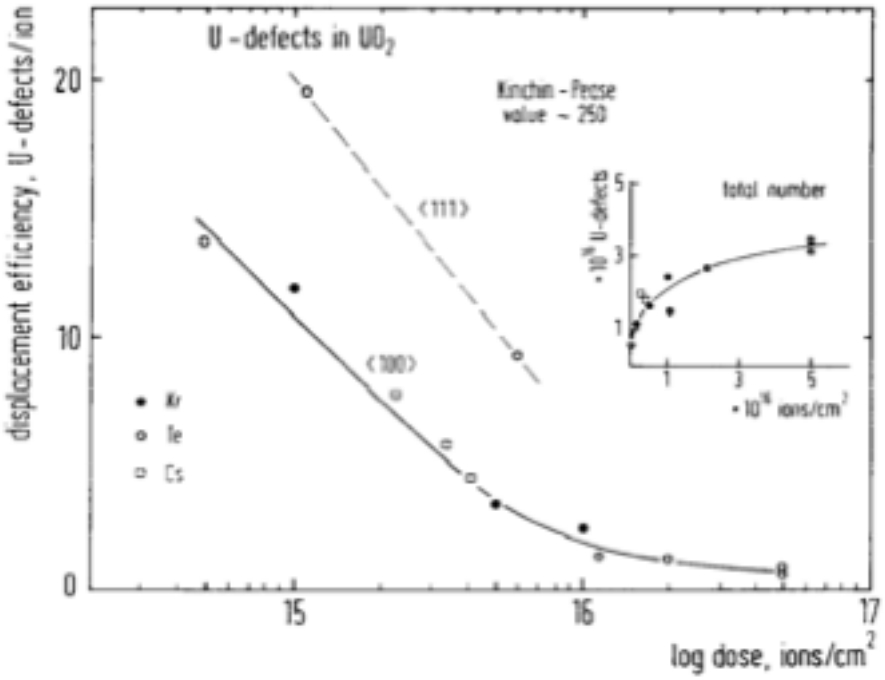

Figure III.4 Displacement efficiency (number of displaced U-atoms per incoming 40 keV implanted ion) implanted at room temperature as a function of the implantation dose and for two different orientations (<111> and <100>) of UO_2 single crystals [28].

As shown in the inset of figure III.4, the total number of surviving defects approaches a saturation value, so the surviving defects per bombarding ion decrease with the increase of dose. Based on the Kinchin-Pease theory, the primary defect production due to nuclear energy deposition is 250 U-defects per implanted ion. This value is largely overestimated and not even observed for the lowest doses [32]. This result indicates that the very effective defect recovery in the collision cascades, and defect recombination processes are dominant in the formation of the damage structure. During implantation of Kr, Te or Cs at room temperature, the number of surviving U-defects is less than one U-defect per bombarding ion, which means only ~0.25% of the defects formed survive. This low value explains the good stability of UO_2, and is in contrast to the ease of amorphization in other ceramics, such as Al_2O_3, TiO_2, and U_3O_8 [28]. Figure III.4 shows also that instantaneous defect recovery is orientation-dependent: defect recombination more easily occur in the <100> direction which has a larger atomic spacing than the close-packed <111> direction.

An experiment carried out by Matzke *et. al* [33] measured T_c, the temperature of thermal recrystallization of the amorphous substance of UO_2, is 675 ± 15°C. This crystallization temperature T_c fulfilled the criterion of structural stability against radiation ($T_c/T_m \leq 0.3$, T_m is the melting point) predicted by a thermal spike model [34]. This is based on the assumption that each ion impact leads to the formation of a small roughly spherical region in an amorphous form, and this disorder tends to anneal as soon as the local temperature falls below the melting point T_m. The model suggests that ion-impact-induced disorder can be instantaneously eliminated when $T_c/T_m \leq 0.3$, so the material shows good radiation stability. This explains the excellent structural stability of UO_2 fuel during high dose irradiation.

Besides UO_2 and (U, Pu)O_2, other fluorite crystals, such as ZrO_2 [35-38] and CeO_2 [39-42, 46], also exhibit exceptional irradiation tolerance, especially with regard to amorphization and volumetric swelling. As a candidate material for the inert matrix

used in nuclear waste transmutation, the material properties of ZrO_2 during irradiation were investigated. For example, during the irradiation with 340-400 keV Xe^{2+} ions or with I^+ ions at temperature up to 1170 K, no amorphization of zirconia was found by using the techniques of Rutherford backscattering spectrometry and ion channeling (RBS/C), X-ray diffraction and transmission electron microscopy (TEM) [35]. Another research group [38] also confirmed amorphization could not be proven in zirconia irradiated with Xe ions up to the fluence of $1.8x10^{16}$ Xe/cm^2 at temperatures between 300 and 1473 K.

CeO_2 as a surrogate material of UO_2 for studying its radiation performance is drawing more and more attention in recent days. In this work, it is also used to simulate oxide-type nuclear fuel to study its structure evolution during irradiation. The earliest neutron irradiation on CeO_2 was carried out in the High Flux Reactor (HFR) in the Netherlands [42]. A neutron fluence (E> 0.1 MeV) of $4.6x10^{25}$ m^{-2} was achieved on sintered CeO_2 pellet. The irradiated specimens remained crystalline in structure and isolated dislocation loops were observed. The alpha-irradiation-induced changes in the lattice parameter of CeO_2 studied by Weber [43] shows the minor increase of the lattice parameter in CeO_2 is comparable to that in UO_2 and PuO_2.

III.2.2 Defect Structure Formation in Oxide Fuels

In the primary recoil event, hundreds of vacancy and interstitial pairs are formed over a volume of ~ 10^3 nm^3. The fate of these point defects and how they affect material properties depends critically on the crystal structure and the irradiation temperature. In oxide fuels, two main defect structures, dislocation loops and bubbles/voids, might form from point defects clustering. Often it is believed that interstitials group together on a specific plane to form dislocation loops, and vacancies can agglomerate to form voids. Those voids can serve as potentials sinks and nucleation sites of gas bubbles.

During the lifetime of oxide fuel in a reactor (~ 3 years), 4% of the metal atoms are fissioned and the fuel reaches a damage level of 1000 displacement per atom (dpa) [11]. The UO_2 fluorite structure does not become amorphous, but a high burnup (> 40 MWd/kg metal average burnup) structure is observed on its peripheral region [2, 3, 11, 29-31], which is of great scientific interest. The peripheral region, also called the rim region, is up to a width of 200 μm. It exhibits the appearance of a "cauliflower structure", as shown in figure I.2, which is subjected to a grain subdivision process: each original grain of the sintered UO_2 with typical diameters of 5 to 15 μm divides into up to 10^5 very small grains. The formation of this unique structure is considered to be a result of the release of the increasing elastic stored energy during accumulation of fuel burnup. Some of dislocations will annihilate with each other in this process, and the others rearrange into walls of dislocations, forming small energy "sub-boundaries" and nearly perfect but slightly disoriented subgrains between those new boundaries [30].

In figure III.5 [47], a unique microstructure change is shown for a PWR fuel element with the highest burnup of 83 GWd/t. At the fuel rim where $r/r_0 = 1.0$, as-fabricated grains with an average diameter of 13 μm cannot be observed, instead, the grains appear to be divided into sub-grains of sub-micron size. Furthermore,

many faceted bubbles are observed. These features extend to about r/r_0 = 0.9. The as-fabricated grains still appear to remain at the positions of r/r_0 = 0.75 (figure III.5 (b)) and r/r_0 = 0.3 (figure III.5 (c)), the sub-divided grain structure is also clearly seen there. The loss of definable grains and the precipitation of many bubbles are typical features found in high burnup fuels.

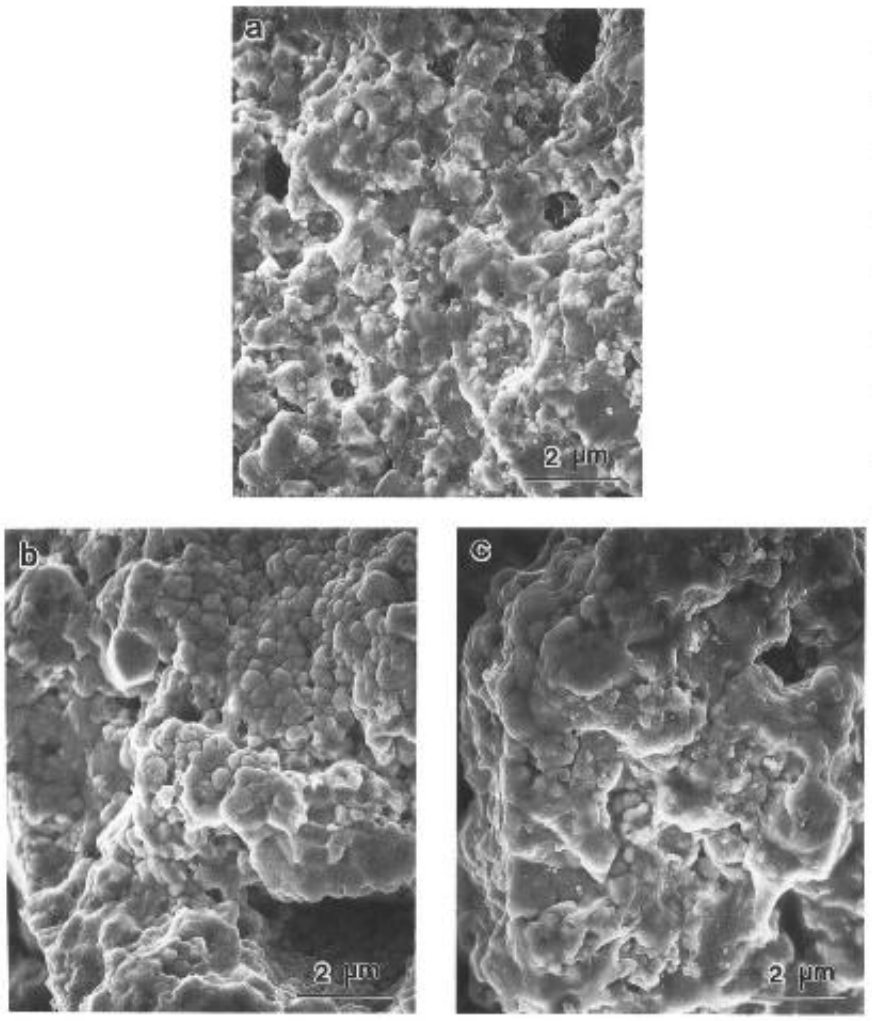

Figure III. 5 Scanning electron micrographs of fracture surface at (a) r/r_0 = 1.0; (b) r/r_0 = 0.75; (c) r/r_0 = 0.3 of as-irradiated PWR-type fuel (83 GWd/t).

TEM investigation on spent nuclear fuels was also carried out by Une et al. [47]. Both dark-field TEM images of the base-irradiated BWR (44 GWd/t) (figure III.6 (a)) and PWR (83 GWd/t) (figure III.6 (b)) fuels were taken from the cold fuel periphery

of r/r_0 = 1.0 – 0.8. On both types of fuels, a dislocation structure with very high density was seen, in which dislocations tend to aggregate as networks. Particularly in the region B on figure III.6 (b), an extremely high density of tangled dislocation is clearly seen, which themselves organize sub-grain boundaries. The selected area diffraction pattern of this region is shown in the inset of figure III.6 (b), in which streaky spots and Debye rings were recorded, and indicating a polygonization of the original grain.

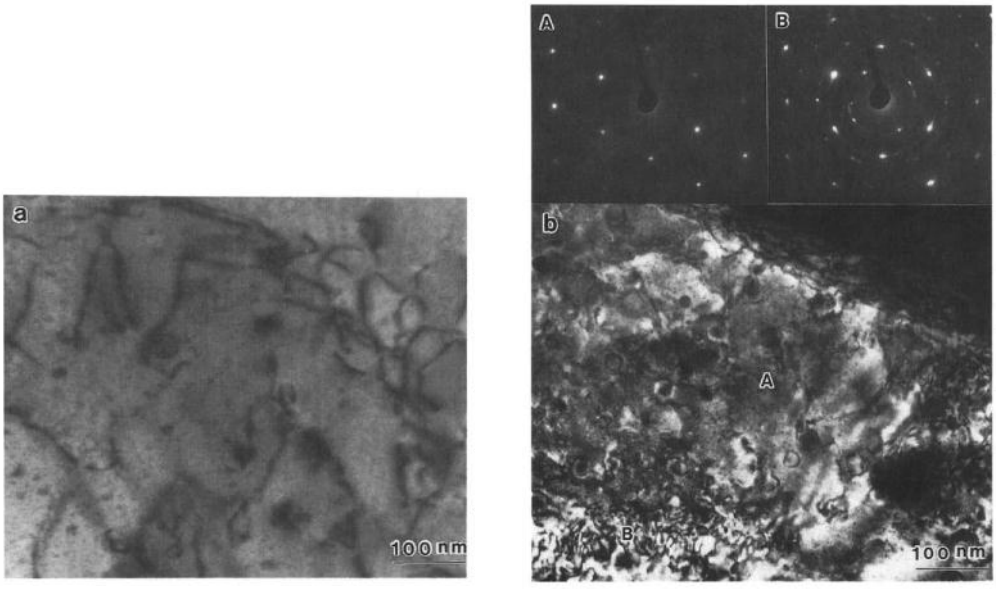

Figure III.6 Dark-field transmission electron micrographs at the fuel periphery of r/r_0 = 1.0-0.8 of as-irradiated (a) BWR (44 GWd/t), and (b) PWR-type (83 GWd/t) fuels [47].

IV. Fission Gas Behavior in Ceramic Fuels

Among the fission products contained in nuclear fuels, the behaviors of fission gases has drawn considerable interests in the past. Due to the insolubility of noble gases in nuclear fuel, their behavior can cause potential problems, such as fission gas bubble swelling and fission gas release from reactor fuel. Starting from the late 1950s, there has been a determined effort to understand the fundamental aspects of noble gas (Xe, Kr and He) behavior, such as gas atom diffusion, gas bubble nucleation, irradiation induced bubble resolution, gas bubble movement, accumulation at the grain boundaries and the final release along this pathway to the surface [13]. Hj. Matzke's paper [5] in 1980 reviewed the gas release mechanisms in UO_2 (LWR fuels) and (U, Pu)O_2 (LMFBR fuels). The transport of gas atoms to the grain boundaries can occur as single gas atom diffusion, or via the mobility of gas-filled bubbles or pores. At that time reliable knowledge about gas diffusion and release was scarce. In the 1990's and more recent years, there have been more experimental efforts engaged in verifying and understanding the mechanisms, see [9, 13-20]. However, there is still uncertainty regarding the gas behaviour in nuclear fuels. With the developing of technology, some knowledge gaps can be filled with advanced experimental techniques, such as high-resolution transmission electron microscopy (HRTEM), and positron annihilation spectroscopy (PAS) [48].

A coherent understanding of fission gas behavior in nuclear fuel requires comprehensive knowledge of transport properties of oxygen atoms and metal atoms in $MO_{2\pm x}$ (M is U or (U, Pu)). Metal and oxygen diffusion has been extensively studied with both experiments and modeling. The predominant defects are oxygen vacancies in MO_{2-x} and oxygen interstitials in MO_{2+x}. When $x = 0$, the system has the highest activation enthalpy compared to they in hypo- or hyper-stoichiometric systems ($x < \text{or} > 0$). Therefore, it is more difficult for atoms to diffuse in stoichiometric system. Vacancy clusters forms at large x values, which provide

trapping sites for gas atoms and thus retard gas diffusion. Metal vacancies and metal interstitials, in particular, are minority defects in $MO_{2\pm x}$. Their mobility is much smaller than that of oxygen. At 1400°C, the diffusion coefficient of O atoms is 5 orders of magnitude higher than that of U atoms in UO_2 [49]. However, because of the very low mobility of metal atoms, the diffusion of U or Pu dominates the rates of some processes at high-temperature, such as creep, grain growth, and densification.

IV.1 Important Physical Processes Associated with Fission Gas Release

Noble gases are very important products of the ^{235}U and ^{239}Pu fission events. The sum of the yields of the stable xenon and krypton isotopes is between 0.23 and 0.25 isotops per fission for both uranium and plutonium. Xenon constitutes the largest part of the fission gas. These gaseous fission products, krypton and xenon, have been the subjects of intensive study in the past, due to their unique properties: (1) they are almost insoluble in the fuel matrix and (2) they normally exist as gases rather than solids. As a result, the gas atoms are either released from the fuel or precipitates into bubbles within the matrix. Both consequences greatly impact the fuel performance as: the release of gas increases the pressure within the fuel pin and correspondingly increases the stresses on the cladding, which can lead to failure of the fuel pin, and the retention of fission gases can cause swelling of the fuel which promotes fuel-cladding contact and also results in cladding failure.

Swelling and release are complementary phenomena, and their rates are closely related with local temperatures. In the hot center region of the fuel pin, most of fission gases are released once they are generated, and the swelling is small. Near the cold periphery region, swelling is appreciable because the mobility of gas atoms is very low, and the released ratio is low. It also needs to be mentioned that the steep temperature gradient in a fuel rod provides a powerful driving force for the gas bubble migration and eventually changes the fuel structure.

There are a number of elementary processes that affect fission gas behavior in the fuel matrix, listed below in the order of occurrence [8]:

a. Generation of krypton and xenon by fission reactions.
b. Gas bubbles nucleation, either homogeneously by chance encounters of wandering gas atoms or heterogeneously on fission-fragment tracks or dislocation lines.

c. Growth of gas bubbles by atomic migration of fission-gas atoms to existing bubbles.
d. Re-solution of the gas atoms within the bubble caused by irradiation.
e. Migration of the bubbles either as random-walk in the absence of directed forces acting on the bubbles or as biased motion when such forces are present. The directed forces are induced by temperature or stress gradients, or retaining forces due to dislocations and grain boundaries.
f. Coalescence of bubbles moving either in a random or directional fashion.
g. Interaction of bubbles with dislocations and grain boundaries.
h. Release of fission gases, either to internal surfaces such as grain boundaries or to external surfaces such as the central void, cracks in the fuel, or the fuel-cladding gap.

In the presence of radiation damage, the gas atoms will interact with the damage and will be temporarily retarded or trapped. This damage can be in the form of small vacancy clusters, or dislocation loops formed by displacements produced during the slowing down of the fission products. Consequently the diffusion coefficient decreases with increasing irradiation dose due to the buildup of irradiation defects. In the radiation environment, radiation induced re-solution occurs and leads to a reentry of the gas or release of the gas from traps.

In real fuel, gas can precipitate and get temporarily immobilized in pre-existing pores. Gas reentry into the lattice is more difficult from pores than from gas trapped at damage. At high enough concentrations, gas-gas interactions occur and lead to the formation of gas-filled bubbles. These bubbles can move in the presence of a pronounced temperature gradient, which allows gas atoms to migrate within the fuel.

IV.2 Fission Gas Diffusion in Fuel Matrix

IV.2.1 Xenon in UO_2

Despite the large effort devoted to measuring the diffusion coefficient of fission gases in UO_2, there is no sound set of data presently available. Measurement results are greatly dependent on the nature of specimen materials (sintered or single-crystal) and the characterization techniques. Many measurements were made without considering the effect of trapping on the release curves. Stoichiometry also significantly influences xenon diffusivity. Miekeley and Felix's measurements show that Xe diffusivity can ranges over three orders of magnitude at a particular temperature [50], as shown in figure IV.1.

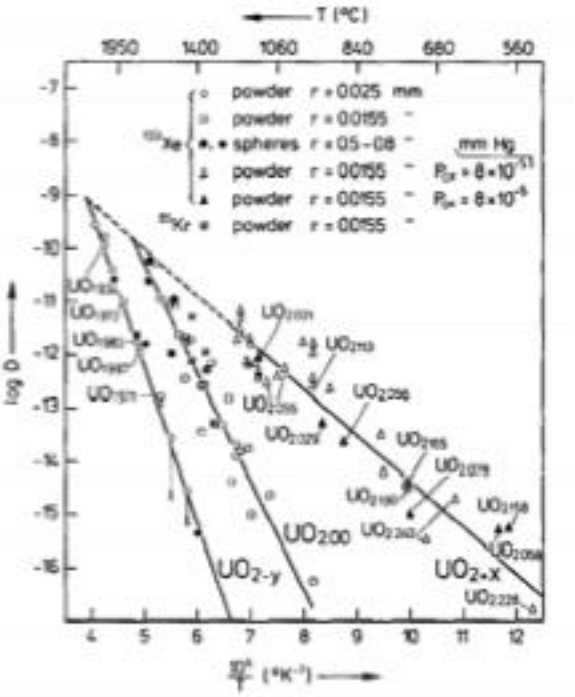

Figure IV.1 Temperature dependence of the diffusion coefficient of Xe in $UO_{2\pm x}$ [49].

A widely used diffusion coefficient of xenon in model calculations is suggested by Cornell [51]. He measured the diffusion coefficient by following the growth of individual gas bubbles in UO_2 with an electron microscope. By using this method, he could avoid the problems associated with trapping. His result is given by:

$$D_{Xe} = 2.1 \times 10^{-4} \exp\left[-\frac{380}{R(T/10^3)} \right] \qquad \text{(IV. 1)}$$

where D_{Xe} is the diffusion coefficient in cm^2/sec; R = 8.314 J/K/mol is the ideal gas constant, and T is the temperature in K.

In order to understand the diffusion behavior of fission gases, it is important to study their migration mechanisms. Migration of one species in a solid normally occurs by occasionally jumping to an interstitial or vacancy site. Therefore, it is reasonable to expect xenon atoms to move in UO_2 by an interstitial mechanism or a vacancy mechanism on either uranium or oxygen sublattice. However, this is not the case. Xenon atoms are too large to fit in any interstitial site in the lattice, hence it is too difficult for them to migrate by interstitial mechanism. On the other hand, experimental results [52] show that the diffusion of xenon in UO_2 is independent of the concentration of vacancies on either uranium or oxygen sublattice, which suggests xenon diffusion through single-vacancy site is inaccurate.

Based on the above facts, a complex model is proposed [8] to explain how xenon moves around in the UO_2 lattice, in which a xenon atom binds to a vacancy cluster composed of one or two uranium vacancies and two oxygen vacancies. A similar mechanism was applied to rare-gas diffusion in other ionic systems [53, 54], such as CsI. Large vacancy clusters were detected in some earlier studies [51]. They found stable vacancy clusters of about 10 Å in diameter in UO_2 irradiated to 10^{19} to 10^{20} fissions/cm^3.

Several simulation efforts have been conducted to understand Xe trapping sites and migration mechanisms in UO_2 [55, 56]. Defect energertics are calculated using computational programs based on inter-atomic potentials. These potentials use

formulas to describe the interaction between the neighboring atoms, which includes repulsive and attractive terms. The potentials are parameterized, with the free parameter values determined, by fitting to bulk crystal properties, such as lattice parameters and modulus. According to different fitting parameters, there are varied forms describing a specific crystal system.

A detailed description about computation on fission gas diffusion in UO_2 was given by Catlow [55]. Other than normal cation and anion vacancies, three vacancy aggregate configurations were proposed for Xe trapping sites. The vacancy aggregates are depicted in figure IV. 2. To understand the schematic drawing in figure IV.2, it is important to explain that UO_2 crystallized in the fluorite structure, which is a primitive cubic array of anions with half the cube centers occupied by cations.

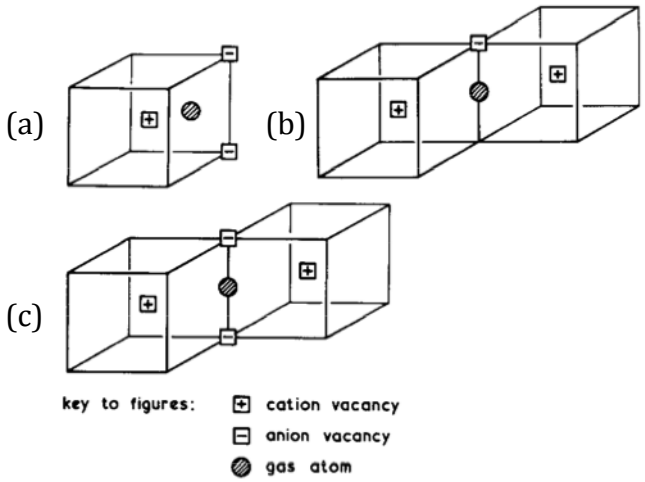

Figure IV.2 Possible trapping sites for a xenon atom in UO_2 unit cells: (a) the neutral trivacancy, comprising one cation and two anion vacancies; (b) the charged trivacancy, comprising one anion and two cation vacancies; (c) the tetravacancy, comprising two cation and two anion vacancies. [56]

Solution energies for Xe atoms in UO_2 are compared for five configurations of vacancy trapping sites in full thermodynamic equilibrium. The solution energy is defined as the energy required to introduce an isolated gas atom to a trap site. The

trap formation energy also needs to be added. The values of solution energies of Xe in different vacancy aggregates are listed in table IV.1.

Table IV.1 Solution energies for full thermodynamic equilibrium [56]

(a) Anion-deficient UO_2

Site	Energies (eV)			
	$T = 298$ K	1773 K	2273 K	2773 K
Anion vacancy	17.81	14.61	13.44	12.25
Cation vacancy	18.10	15.47	14.73	14.0
Neutral trivacancy	11.63	10.15	9.6	9.03
Charged trivacancy	23.61	20.06	18.86	18.34
Tetravacancy	18.20	15.89	15.09	13.07

(b) Stoichiometric UO_2

Site	Energies (eV)			
	$T = 298$ K	1773 K	2273 K	2773 K
Anion vacancy	20.47	16.95	15.71	14.45
Cation vacancy	12.78	10.79	10.19	9.60
Neutral trivacancy	11.63	10.15	9.60	9.03
Charged trivacancy	15.63	13.04	12.21	11.74
Tetravacancy	12.88	11.21	10.55	8.67

(c) Anion-excess UO_2

Site	Energies (eV)			
	$T = 298$ K	1773 K	2273 K	2773 K
Anion vacancy	23.13	19.29	17.98	16.65
Cation vacancy	7.46	6.11	5.65	5.20
Neutral trivacancy	11.63	10.15	9.60	9.03
Charged trivacancy	7.65	6.02	5.40	5.14
Tetravacancy	7.56	6.53	6.01	4.27

The results in table IV.1 clearly show that single Xe atoms are generally trapped at cation/anion vacancy aggregates, rather than at single vacancy sites. For anion-deficient and stoichiometric UO_2, the neutral trivacancy is clearly the preferred site. For the hyperstoichiometric materials, the calculations suggest several possible trap sites, with the charged trivacancy and the tetravacancy as well as the simple cation vacancy being preferred on energetic grounds. The prediction of neutral trivacancy traps for UO_2 and UO_{2-x} agrees with experimental results in [5]. The trivacancy's electrical charge neutrality is expected to be stable for Xe. The formation energy of a Schokky vacancy is too large to be created by the thermal activation. However it is the simplest and most dominant vacancy cluster among the irradiation-induced defects [57].

The migration of Xe atoms in UO_2 is via vacancy-assisted mechanisms [5, 52]. A recent investigation on the atomic diffusion mechanism of Xe in UO_2 employed the density functional theory (DFT) computation method [58]. It found that an oxygen vacancy lowers that migration energy of a uranium vacancy by about 1 eV, enhancing the effective movement of vacancy clusters consisting of both uranium vacancy and oxygen vacancies. Furthermore, the strain energy of Xe is large enough to contribute to the clustering of vacancies, making it the driving force for the vacancy-assisted diffusion of Xe in UO_2. Based on their calculation results of binding energies, incorporation energies of Xe for five configurations of vacancy clusters (same as in table IV.1), a possible diffusion pathway for Xe by the vacancy-assisted mechanism in UO_2 was given, as shown in figure IV.3.

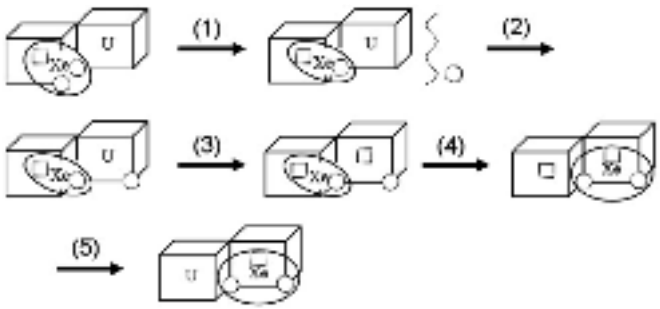

Figure IV.3 A possible diffusion pathway for Xe by the vacancy-assisted mechanism in UO_2: (1) a V_o is separated from an Xe_{UO2}, and Xe moves spontaneously to the center of the new configuration, (2) a new V_o is created at the nearest lattice site of Xe, (3) through the effective movement of a V_u with the help of the new V_o, a configuration of V_{UO2} is formed again, (4) Xe moves to the center of the V_{UO2} by the strain energy, (5) and a V_u moves out this configuration [58].

IV.2.2 Krypton in UO_2

Since the Kr atom has a smaller size than Xe, trapping into smaller sites is expected. Thus vacancy aggregates are no longer important trapping sites. Instead, trapping more likely happens into single vacancies. Kr tends to occupy cation vacancies in oxidized and stoichiometric crystals, and anion vacancies in the oxygen deficient oxides. The difference between the types of dominant traps for krypton and xenon should lead to major differences in the gas diffusion coefficients and their dependence on fuel composition. However, there is no extensive and reliable data for Kr diffusion [55]. It was speculated that the diffusion of Kr would be faster than Xe.

V. Experimental Approach

A series of experiments were carefully designed to study the microstructure evolution of nuclear fuel materials subjected to ion bombardment, especially the initial defect formation and accumulation processes. The approach started with implantation of gas ions (xenon an krypton) at different energies to introduce irradiation damage in the sample material. Careful examination of the damaged microstructure was carried out using transmission electron microscopy. The details of the experiments are described in this chapter.

Single crystal CeO_2, which shares the same fluorite structure as UO_2, was used to simulate oxide nuclear fuel. Defect structures were created in the material using ion implantation with controlled ion source, energy, flux and irradiation temperature. Both *ex situ* and *in situ* transmission electron microscopy (TEM) were employed to characterize microstructural changes in post-irradiation materials. Defects visible in transmission electron microscopy consist of black dots, dislocation loops and precipitates concentrated along the dislocation substructure. Microstructure examination was performed using combined lattice (high resolution), bright field and weak beam dark field imaging techniques. Some associated TEM analysis techniques, such as scanning TEM, electron energy loss spectroscopy (EELS) and energy dispersive spectroscopy (EDS), were used to help understand the atom transportation process. Positron annihilation spectroscopy is particularly sensitive to the size and density of vacancy type defects. This technique is extremely useful in detecting defects in the size ranges from several vacancies up to small voids containing ~50-100 vacancies [59], which are normally difficult to observe with TEM.

V.1 Specimen Materials

CeO_2 is used as a surrogate of UO_2 in this study. Both CeO_2 and UO_2 crystallize in the same cubic fluorite structure (shown in Figure V.1). Their lattice parameters are a_{UO2} = 5.4708 Å and a_{CeO2} = 5.4110 Å [60]. They also show similar physical properties, such as high melting points and irradiation tolerance. Therefore, ceria is of great interest for studying urania properties as nuclear fuel [39-42, 65]. Table V.1 summarizes the comparison of their physics parameters. (U, Ce)O_2 has also been widely used to simulate (U, Pu)O_2 MOX nuclear fuel in numerous studies, e.g. [60, 61]. A number of molecular dynamics studies have also tried to reveal the interal structure stability of CeO_2 [61-64]. At the same time, CeO_2 is considered as a candidate for the inert matrix to contain Am for transmutation [68, 71].

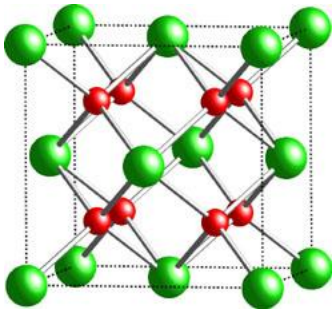

Figure V.1 Unit cell of cerium dioxide. Cerium atoms are assemblied in a face-centered cubic structure, and oxygen atoms are in a simple cubic structure.

Table V.1 Comparisons of Material Properties of UO_2 and CeO_2

	UO_2	CeO_2
Lattice parameter (Å)	5.4708	5.4110
Space group	Fm3m, No. 225	Fm3m, No. 225
Density (g/cm^3)	10.97	7.215
Melting point (ºC)	2865	2600
Thermal diffusivity (m^{2}s^{-1})		
at 600 K	1.82 x 10^{-6} [69]	1.96 x 10^{-6} [70]
At 1000 K	1.09 x 10^{-6}	1.15 x 10^{-6}

Cerium, with a $4f^2 5d^0 6s^2$ electron configuration, can exhibit both the +3 and +4 oxidation states, and intermediate oxides with compositions between Ce_2O_3-CeO_2 can be formed. Thermodynamic data indicates that cerium metal is unstable in the presence of oxygen and that Ce_2O_3 and CeO_2 are easily formed. The final stoichiometry is strongly dependent on temperature and oxygen pressure [72].

The fluorite structure, which CeO_2 is crystallized in, has a face-centerd cubic unit cell (f.c.c). In this structure, each cerium cation is octahedrally coordinated by eight equivalent nearest-neighbor oxygen anions at the corner of a cube, while each oxygen anion is tetrahedrally coordinated by four cerium cations, as shown in figure V.1.

CeO_2 is reduced at elevated temperatures and low oxygen pressures to form a seeming continuum of oxygen-deficient non-stoichiometric oxides, which upon cooling organize into highly ordered fluorite-related superstructures, often with complex stoichiometries. Reduced ceria results from the removal of O^{2-} ions from the CeO_2 lattice, which generate an anion vacant site according to the following scheme:

$$4Ce^{4+}+O^{2-} \rightarrow 4Ce^{4+}+2e^-/\square+0.5O_2 \rightarrow 2Ce^{4+}+2Ce^{3+}+\square+0.5O_2 \qquad (V.1)$$

where $\square$ represents an empty position (anion-vacant site) originating from the removal of O^{2-} from the lattice, here represented as an oxygen tetrahedral site (Ce_4O). Electrostatic balance is maintained by the reduction of two cerium cations from +4 to +3. The lattice parameter of the cubic phase CeO_x increases as x decreases.

The materials used in the experiments were single crystal CeO_2 thin films, which were grown with molecular beam epitaxy (MBE) at the University of Illinois. A schematic drawing of a MBE system is shown in figure V.2. MBE is one of several methods of depositing single crystals. MBE takes place in a high vacuum (10^{-8} Pa)

environment. The most important aspect of MBE is the slow deposition rate, which allows the film to grow epitaxially. During operation, reflection high-energy electron diffraction (RHEED) is often used for monitoring the growth of the crystal layers. A computer controls shutters in front of each furnace, allowing precise control of the thickness of each layer, down to a single layer of atoms. Such layers are now a critical part of many modern semiconductor devices. In this study, the atomic layer-by-layer MBE was used to precisely control the composition of the crystal and mix in impurities, such as lanthanum, to study their diffusion mechanisms. CeO_2 thin films were deposited from a Ce ion source and excessively supplied oxygen. The $SrTiO_3$ or r-cut sapphire substrates were mounted on a tantalum plate with silver paste and heated during deposition. After growth, the specimens were annealed in a furnace circulated with oxygen at the temperature of 1250°C for 12 hours to help release the internal stresses created during deposition. The CeO_2 thin films were characterized by the means of atomic force microscopy (AFM) and X ray diffraction (XRD). The measurements confirmed that the films grown on both of these substrates had good crystalline quality and surface morphology.

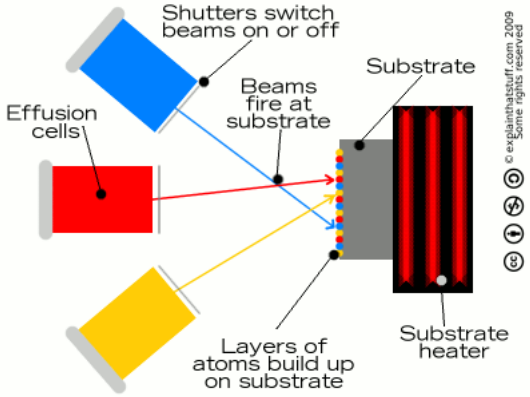

Figure V.2 A molecular beam epitaxy system

Epitaxial CeO_2 thin films used in the irradiation experiments were grown on $SrTiO_3$ substrate, which has (001) planes parallel to the surface. One side of the substrate had been pre-polished. The selection of substrate was based on the matching of lattice parameters. $SrTiO_3$ is in a cubic structure with a lattice parameter of 3.905 Å, so the length of diagonal line in each face is 5.522 Å. This is

close to the lattice parameter of CeO_2 = 5.411 Å. So CeO_2 lattice matches $SrTiO_3$ lattice with 45° in-plane rotation. Figure V.3 shows the interface of CeO_2 thin film with $SrTiO_3$ substrate taken with high resolution TEM.

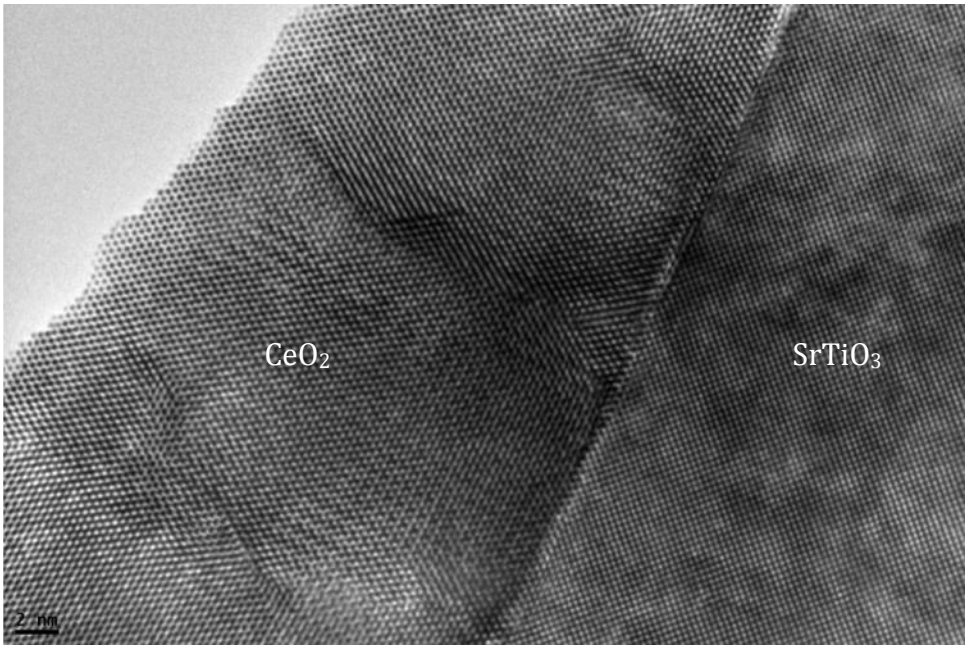

Figure V.3 High resolution TEM micrograph of CeO_2 thin film on $SrTiO_3$ substrate grown with MBE technique. The image was taken on JEOL LaB6 at the University of Illinois.

Using single crystal CeO_2 samples can help eliminate the grain-boundary effects in the investigation of the intrinsic behavior of Kr and Xe. Real nuclear fuels are normally fabricated by sintering powder into pellets, so they are in polycrystalline form with grain size ranging from 4 to 15 μm in diameter. Since the grain boundaries can increase the complexity of atom transportation processes in the material, which might obscure the basic defect nucleation and formation process, the simpler single crystal system was adopted in this study.

V.2 Ion Implantation Technique

In this study, krypton and xenon atoms were incorporated into the CeO_2 crystals by ion implantation. This technique, combined with implantation computer simulation, provides good monitoring of the depth distribution and concentration of implanted species. It also allows for the fundamental diffusion processes to be studied individually by reduction unnecessary complications as much as possible.

Heavy ion irradiation was developed for the purpose of simulating neutron damage in support of the fast breeder reactor program [73, 74] in the 1960s and 1970s. Energetic ions are implanted into the samples to induce defects, which cause the evolution of local microstructure and microchemistry. The application of ion irradiation to the study of neutron irradiation damage is of interest to the light water reactor community to address issues such as stress corrosion cracking of core materials that are affected by irradiation [12]. Ion irradiation is also used to understand the irradiated microstructure of reactor materials.

Using ion irradiation instead of a test reactor environment to study irradiation damage is beneficial for studying basic damage processes, in addition to providing significant savings in time and money. Test reactor irradiation experiments can provide realistic irradiation environments for the study of material properties, but they are not amenable to studies involving a wide range of conditions, which is required for understanding the basic damage processes. In contrast, ion irradiation allows for variation of the irradiation parameters, such as dose, dose rate and temperature over a wide range of values. By carefully controlling those parameters, it is possible to precisely control the depth distribution and concentration of implanted species. A single cycle of reactor irradiation through microanalysis can take 3~5 years. Such a long cycle length reduces flexibility in altering irradiation programs. In addition, the long cycle length together with the special requirements of facilities and sample handling can result in very high costs for reactor irradiation

experiments. Ion irradiation normally only requires on the order of tens of hours to reach desired damage levels, and produces little or no residual radioactivity, allowing handling of samples without the need for special precautions. All of these features make it a very attractive technique in studying radiation effects in nuclear materials.

There were two ion implantation facilities used in this study. The high voltage engineering Van de Graaff is an accelerator located in Materials Research Laboratory at the University of Illinois (shown in figure V.4). This accelerator was employed to irradiate samples that were to be analyzed using *ex situ* irradiation. The Van de Graaff operates at energies up to 2.3 MeV for H, He, Ar, Kr, Xe and Ne with 3-4-5 mm beam-size apertures in shapes of circular or square. The sample stages allow the irradiation temperature to be controlled in the range of room temperature to 800°C.

Figure V.4 High voltage engineering Van de Graaff accelerator at the University of Illinois

The other irradiation facility used in this study was IVEM-Tandem facility at Argonne National Laboratory, as shown in figure V.5. All of the *in situ* irradiation experiments were carried out on this instrument. It is a transmission electron microscope interfaced with an ion accelerator for *in situ* ion beam studies involving ion implementation and/or ion damage.

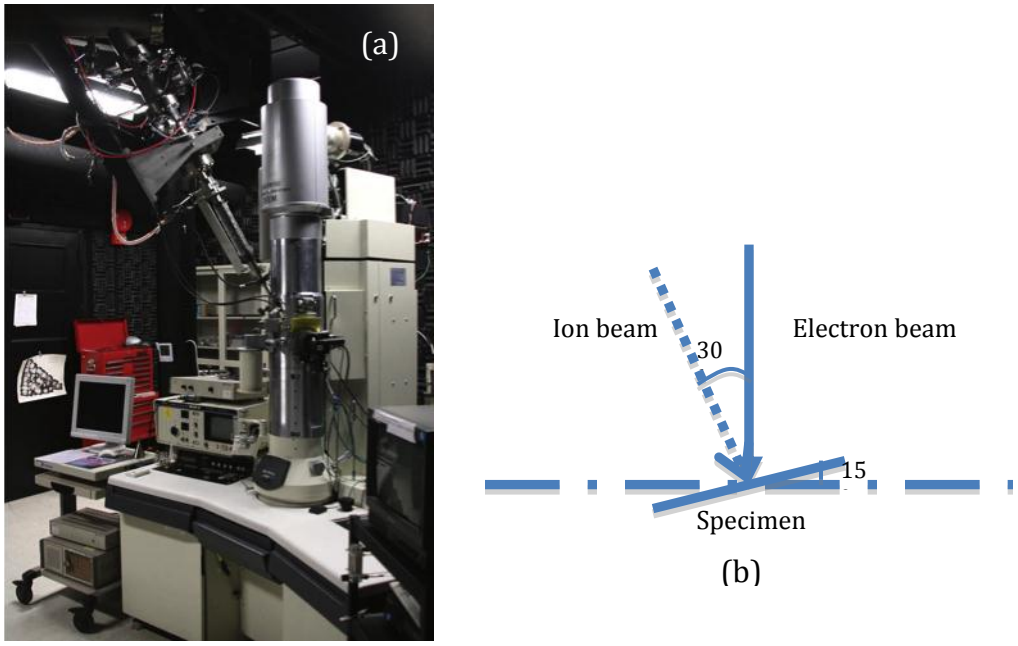

Figure V.5 (a) IVEM-TANDEM facility at Argonne National Laboratory, USA [75]; (b) Schematic diagram of ion beam and electron beam in IVEM-Tandem. The specimen is normally tilted 15º in the *y* direction during irradiation.

The IVEM is a 300 kV Hitachi H-9000NAR with the ion beam entering at 30° to the electron beam. The objective pole gap was widened to allow the incorporation of the ion beam but with a much smaller detrimental effect on resolution. The ion flux is monitored constantly during irradiation. In addition to a variety of specimen holders allows in situ cooling and heating experiments (with or without ion irradiation) from 15-1200K. Data recording is provided by choices of film, a Gatan 622 video rate camera, and a Gatan Orius SC 1000 CCD camera with Digital Micrograph software.

The available ion sources include noble gases, H, S, Fe, Ni, Cu and Au, and the typical flux at the specimen is $1x10^{12}$ $1/cm^2s$. The ion-beam is raster scanned across an aperture in the ion beam line just before it enters the TEM column which is giving rise to a uniform irradiated area on the sample of a 2 mm diameter circle in the center of a standard 3 mm TEM specimen [76]. The 30° incline angle permits

continuous observation and data recording during irradiation. As shown in figure V.5 (b), the specimen is tilted ~15° facing the ion beam to assure enough exposure area on the specimen to the ion beam.

The goal of this study is to understand the formation processes of defect structures. Therefore the irradiation experiments were designed to achieve the desired damage level and gas atom concentration. There are several variable parameters in the selection of irradiation conditions: ion source and energy, irradiation temperature, and dose. Irradiation damage levels were estimated with SRIM 2008 [94]. In these calculations, E_d = 51 eV was used for Ce displacement energy instead of E_d = 25 eV which is the default value in SRIM. This value is measured by Yasunaga et al. [41]. In their experiments of electron irradiation, Ce displacement energies of 44 to 58 eV were measured. Parameters of all ion irradiation conditions are listed in table V.1, and ion distributions calculated with SRIM are displayed in figure V.6.

Table V.2 (a) Parameters of Xe ion irradiation of CeO_2

	In situ		*Ex situ*		
Ion source	Xenon		Xenon		
Temperature (°C)	20, 600, 800		20, 600		
CeO_2 film thickness (nm)	130		160		
Energy (keV)	150	500	700		
Peak depth (nm)	97		133.9		
Cumulated dose (ions/cm^2)	5x10^{15}		2x10^{16}	5x10^{16}	1x10^{17}
Peak dpa	24.1	18.4	72.8	182.1	364.1
Peak concentration (at.%)	1.58	0.68	3.14	7.85	15.7

Table V.2 (cont.) (b) Parameters of Kr ion irradiation of CeO_2

	In situ			*Ex situ*	
Ion source	Kryton			Kryton	
Temperature (°C)	20, 600, 800			20, 600	
CeO_2 film thickness (nm)	130			160	
Energy (keV)	150	1000		1000	
Peak depth (nm)	44	> 130		133.9	
Cumulated dose (ions/cm^2)	$5x10^{15}$		$2x10^{16}$	$5x10^{16}$	$1x10^{17}$
Peak dpa	23.8	8.5	38.8	97.0	193.9
Peak concentration (at.%)	1.12	0.05	0.19	0.49	0.97

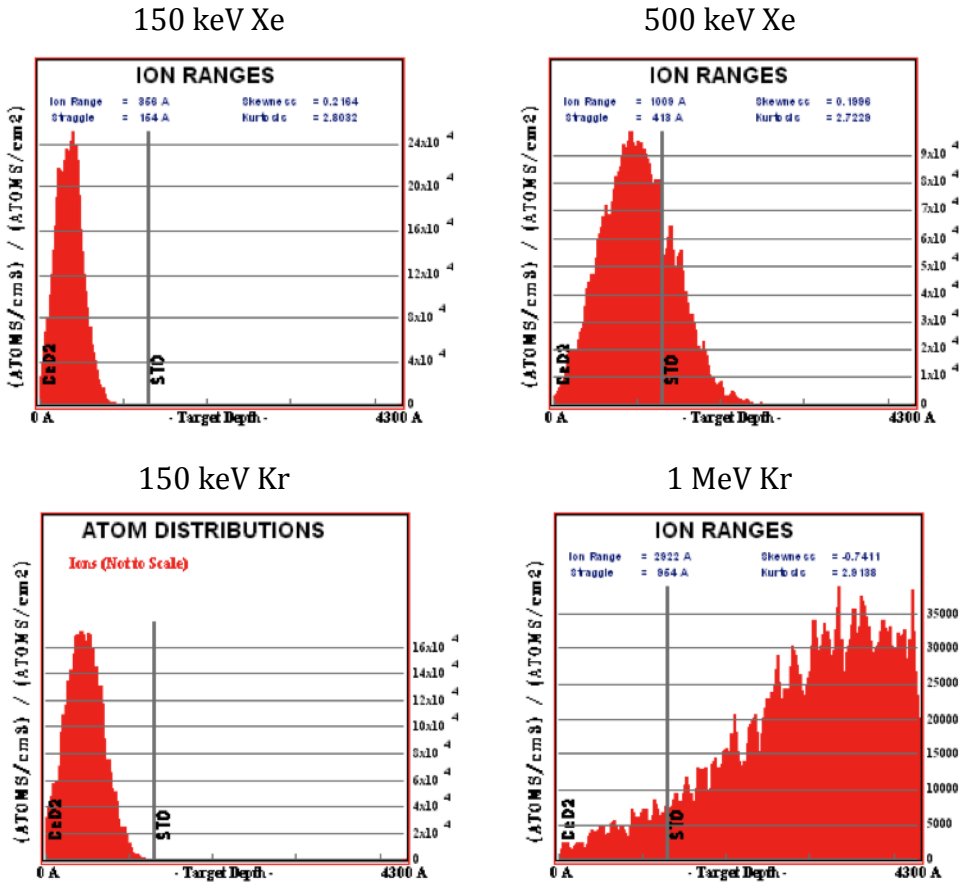

Figure V.6 Ion distributions in CeO_2 thin films for different ion species and energies.

V.3 Transmission Electron Microscopy (TEM)

Both *in situ* and *ex situ* TEM were applied to characterize the irradiated structures. TEM is a microscopy technique widely applied in both physical and biological sciences. Owing to the small de Broglie wavelength of electrons, TEMs are capable of imaging at a significantly higher resolution than light microscopes. This allows for the examination of very fine details in materials, down to a single column of atoms. The basic transmission electron microscope consists of an electron source and an assembly of magnetic lenses arranged in a vertical column, which is evacuated to a pressure of about 10^{-5} torr or less. A coherent parallel beam of electrons, generated by the electron source, passes through an ultra-thin specimen, interacting with the specimen as it transmits. An image is formed from the interaction of the electrons transmitted through the specimen and focused onto an imaging device, such as a fluorescent screen, or a sensor such as a CCD camera. With a typical modern microscope the final magnification of displayed images can be varied between 100 to several 10^6 times. A schematic diagram of the basic optical components in a TEM is displayed in figure V.7.

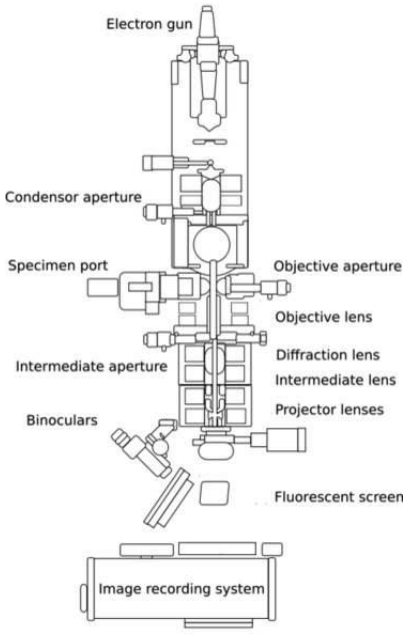

Figure V.7 Schematic diagram of basic optical components in a TEM

Ex situ TEM analyses were carried out at the University of Illinois with three instruments: JEOL 2010 LaB6 TEM, JEOL 2010 F (S) TEM and JEOL 2200 FS (S) TEM. In order to take advantage of the configuration of each instrument, some are especially used for crystal defect study, and others can be used for atomic imaging and elemental analysis.

The 2010 LaB6 is a conventional TEM. It is optimized for bright-field (BF)/dark-field (DF) imaging, diffraction and high sample tilts. A double tilt holder is available which allows +/- 45° of tilt in both X and Y-axes. Heating (up to 800°C) and cooling (using liquid nitrogen) stages are also available. This TEM is the most frequently used in crystal defect observation due to its convenient configuration which favors high angle tilting needed to achieve desired weak-beam diffraction conditions.

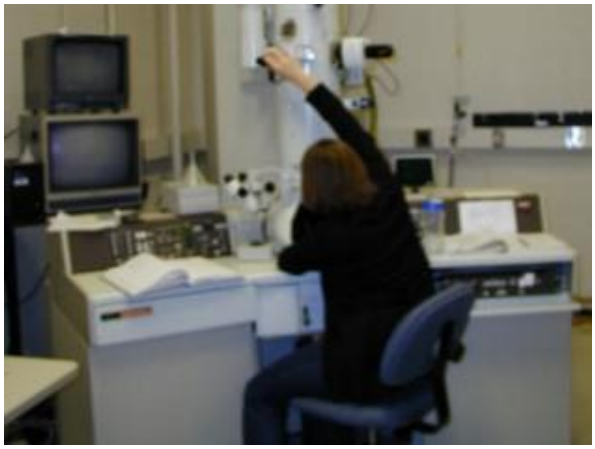

Figure V.8 JEOL 2010 LaB6 TEM in the Materials Research Laboratory at the University of Illinois

The 2010F is an energy filtering, field-emission analytic TEM/S(canning)TEM. It is ideal for small probe work including: HAADF STEM, nanodiffraction, spatially resolved electron energy-loss spectroscopy (EELS) and X-ray energy dispersive spectroscopy (EDS). The 2010F is equipped with an energy filter to filter both images and diffraction patterns as well as act as an energy-loss spectrometer. This makes it a powerful tool for chemical and composition analysis. The system is

controlled by the JEOL FasTEM system allowing total computer control of all operations. Both intensified video rate and slow-scan CCD cameras are available.

Figure V.9 JEOL 2010F (S)TEM in the Materials Research Laboratory at the University of Illinois

The aberration-corrected JEOL 2200FS (S)TEM is a state-of-the-art analytical electron microscope. It is equipped with a 200 kV field emission gun (FEG), a CEOS probe Cs-corrector, and an in-column energy filter (Omega Filter) that allows elemental analysis and chemical analysis of specimens. With an available small probe size of ~0.1 nm, atomic level high-resolution high-angle annular dark-field (Z-contrast) images, and high resolution EELS and EDS spectrum imaging can be obtained.

Figure V.10 JEOL 2200FS (S)TEM in the Materials Research Laboratory at the University of Illinois

TEM with *in situ* ion irradiation is unique among experimental techniques in that it allows the direct observation of the internal microstructure of materials on the nanoscale while they are being subjected to bombardment with energetic particles. Invaluable insights into the underlying atomistic processes at work can be gained through direct observation of radiation induced and radiation enhanced effects such as: phase changes and segregation; mechanical and structural changes; atomic/layer mixing and chemical disorder; compositional changes; grain growth and shrinkage; precipitation and dissolution; defect/bubble formation, growth, motion, coalescence, removal and destruction; ionization; diffusion; and collision cascades. The experimental results obtained can be used to validate the predictions of computational models which in turn can elucidate the mechanisms behind the phenomena seen in the microscope [75]. This technique was extremely useful in this study in following the formation and growth process of dislocation structure and gas bubbles with the increasing dose.

Imaging methods in TEM utilize the information contained in the electron waves exiting from the sample to form an image. Different imaging methods attempt to modify the electron waves exiting the sample to obtain information which is of interest for the investigator. Several imaging techniques are implemented here,

which include high-resolution TEM imaging (HRTEM), TEM diffraction contrast and Z-contrast scanning TEM (STEM) imaging.

HRTEM is an imaging mode that allows the imaging of the crystallographic structure of a sample at an atomic scale. The best resolution can be achieved on JEOL LaB6 is at ~0.3 nm. At such small scales, individual atoms and crystalline defects can be imaged. As opposed to conventional microscopy, HRTEM does not use electron wave absorption by the sample for image formation. Instead, contrast arises from the interference in the image plane of the electron wave with itself. When the electron beam penetrates the sample, the sample no longer changes the amplitude of the incoming electron wave function but does modify its phase, resulting in a phase-contrast imaging. In practice, this technique requires very high quality samples with ultra thin areas. It is important to note that the recorded image with this technique is not a direct representation of the sample's crystallographic structure. For instance, high intensity may or may not indicate the presence of an atom column in a precise location. The relationship between the exit wave and the image wave is a highly nonlinear one and closely related to the aberrations of the microscope.

The most commonly used imaging technique in the application of transmission electron microscopy to study crystal defects is diffraction contrast. This is realized by inserting an aperture into the back focal plane of the objective lens. This aperture allows only one beam to pass through, which is the only beam that contributes to the final image. If the transmitted beam is the one selected then a bright-field image is obtained, whereas if a diffracted beam is selected then a dark-field image is formed (figure V.11). The electron image obtained in this way is a highly magnified image of the variation in the intensity of the selected beam across the bottom surface of the crystal. One obvious structural feature which would give rise to such variation in intensity is the local distortion of the crystal which is normally associated with, for example, crystal defects, precipitates, etc [77]. It is expected that the image contrast obtained with this technique is dependent on the diffraction

conditions. Therefore an electron micrograph can provide useful information only when the relevant diffraction information is available.

Any scattered electrons can be used to form a dark-field image showing mass-thickness contrast. However, to get good strong diffraction contrast in both bright-field and dark-field images, the specimen needs to be tilted to the two-beam condition, in which only one diffracted beam is strong [78]. The electrons in the strongly excited *hkl* beam are diffracted by a specific set of *hkl* planes and so the area that appears bright in the dark-field image is the area where the *hkl* planes are at the Bragg condition. Therefore, in this case the dark-field image contains specific orientation information, not just general scattering information as mass-thickness contrast. Dark-field images can form from each strongly diffracted beam after tilting the specimen, and they are all different. Hence precise tilting of the specimen is extremely important to set up two-beam conditions, and this is manipulated through a double-tilt eucentric sample holder.

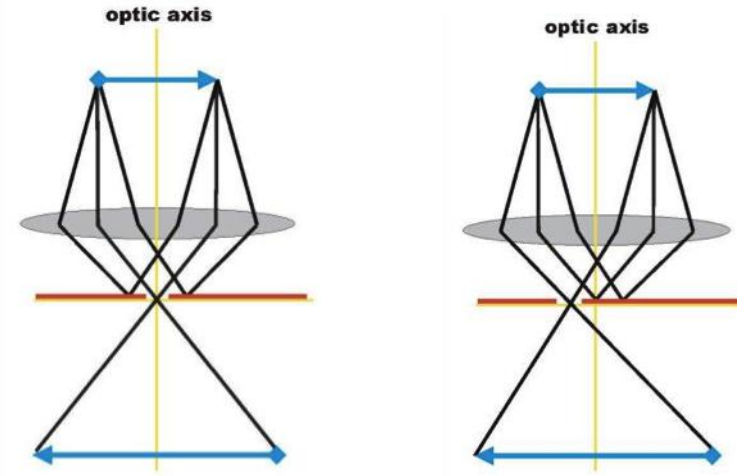

Figure V.11 Schematic ray diagrams for producing a bright-field image and a dark-field image

A particularly important imaging technique using diffraction contrast is weak-beam microscopy, which is able to reveal much finer details than normal two-beam

microscopy. This technique enables images of closely spaced partial dislocations to be resolved. Although HRTEM can give details down to below 0.2 nm, it requires the defect to be absolutely straight, parallel to the beam, and located in a very thin region of the specimen. The segment of dislocation studied by HRTEM will thus be no longer than 20 nm and less than 10 nm for the highest resolution. In a weak-beam image, the defect can be micrometers long and, in a relatively thick foil, it can even change direction [78].

The Z-contrast imaging technique discussed here is associated with STEM. Z is referred to atomic number. The basic difference between TEM and STEM lies in the fact that in TEM the whole area of interest is examined at one time whereas in STEM a far smaller electron probe is scanned across the area of interest to produce the electron micrograph. With a high-angle annular (HAADF) detector installed, detection of small clusters or even single atoms of a heavy metal in a matrix of light elements (Z-contrast) and direct visualization of structures and defects become possible. The detector is arranged to collect a large fraction of the total elastically scattered flux and therefore provides the most efficient imaging mode for beam-sensitive materials, coupled with strong atomic number or Z-contrast characteristic of the total elastic scattering cross-section [79].

V.4 TEM Specimen Preparation

All of the TEM specimens in this study were prepared in MRL at the University of Illinois. TEM sample preparation is a rather complex procedure. TEM specimens are required to be at most hundreds of nanometers thick to allow the electron beam to transmit. The thickness must be comparable to the mean free path of the electrons that travel through the samples, which may be only a few ten of nanometers. Extra care is required during the entire process of making and handling TEM specimens due to safety concerns and their fragility. Preparation of TEM specimens is specific to the material to be analyzed and the desired information to be obtained from the specimen. The specimen preparation processes in this study includes three main steps:

i. Cut the bulk sample into proper size, normally in stripes with a dimension of 2 mm x 4 mm.

ii. Mechanical thinning to make a slice of material between 30-50 μm thick with boron carbide powder and diamond lapping film.

iii. Final thinning and polishing to achieve desired thickness (< 100 nm) in thin area by ion milling.

The bulk material initially provided is in a square shape with a size of 14 mm x 14 mm. The specimen material is ceramic, so it is reasonably hard and mechanical damage is not crucial. A diamond saw (figure V.12) is used to cut the stripes from the as-grown material. In order to section the sample precisely, the sample is adhered to a stage with crystalbond, and the size of sectioned piece can be read from an advanced digital micrometer. After slicing, the sectioned stripes need to be cleaned with acetone in an ultrasonic cleaner to remove residue crystalbond and lubricant oil.

Figure V.12 Low speed diamond saw located in Materials Research Laboratory at the University of Illinois

Two types of TEM specimens are prepared: cross-section specimens and plan view specimens. Cross-section specimens are prepared from the *ex situ* irradiated materials to better review ion distribution depth profile, and plan view specimens are prepared for *in situ* irradiation for providing better stability.

Cross-section specimen is a special type of specimen. Rather than trying to thin one interface only, the sample need to be cut (figure V.13(a)), and glued together with M-bond with two films facing each other to form sandwich like structure (figure V.13(b)). After curing with a hot plate at 120°C untill M-bon solidifies, it can be mounted on a tripod for mechanical thinning (figure V.13(c)). In this process, the gluing of the sections to form the sandwich is a critical step. It can protect the thin film areas in the following thinning processes.

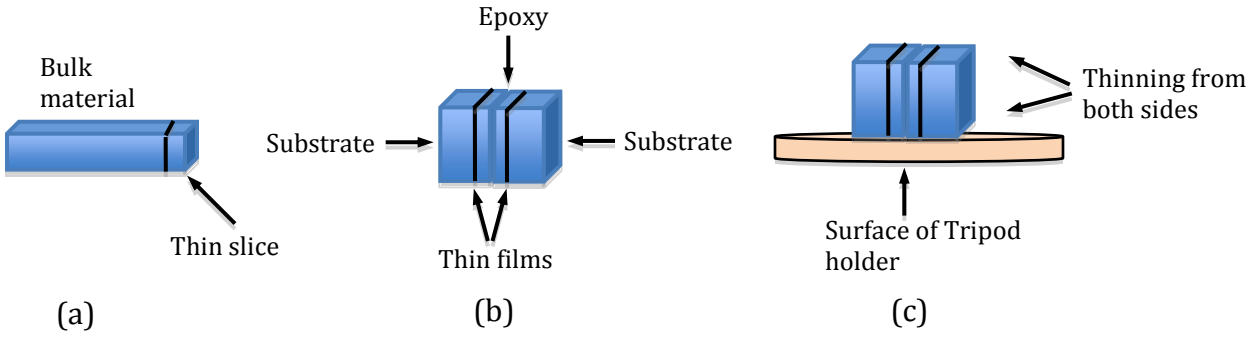

Figure V.13 Sequence of steps for preparing cross sectional TEM specimens.

Mechanical thinning needs to be done to a high quality to ensure constant sample thickness across the region of interest. This is achieved by tripod thinning on boron carbide power to a thickness of 50-60 μm. Subsequently, it has to be followed with further thinning and final polishing on diamond lapping films. The final thickness is ~ 30-40 μm, and the fine polishing can remove scratches which are produced during grinding and may cause contrast fluctuations in TEM observation. Tripod polishing can be used to prepare sections in all orientations (planar longitudinal and cross section orientations). This technique is best suited to hard, brittle and multiphased materials. It consists in two main tools: a specimen holder (figure V.14) and a polishing machine (figure V.15). The specimen holder is adjusted by means of three micrometer screws ("tripod"). The diamond lapping films are placed on the low speed rotary polisher, and polishing is carried out using water as a lubricant. In this step, the stacked sandwich-like slices for cross sectional samples are thinned and polished from both sides, and the pieces for plan view samples are thinned only from the substrate side.

Figure V.14 The top, side and bottom view of a tripod specimen holder

Figure V.15 The polisher located in the Materials Research Laboratory at the University of Illinois

For the ion milling process, a GATAN 691 Precision Ion Polishing System (PIPS) (figure V.16) is used. In this machine, two focused Ar ion beams mill the pre-thinned sample in such a way that a hole results at the desired position. In general, the parameters for the ion milling process are specific for each material and have to be optimized. The ion milling rate increases with higher etching angle and higher etching voltage; however, the sample is also more severely damaged. Therefore, the angle, as well as the voltage, should be kept rather low to minimize the damage induce by ion beams. Generally, a higher voltage combined with lower angle is less harmful to the sample than lower voltage combined with higher angle. In this thinning process, an accelerating voltage of 5 keV and an incline angle of 6-7° were

chosen to achieve perforation. The accelerating voltage was then reduced to 3 keV for final polishing to remove deposited material on the sample surface. The sample is rotated during etching to promote even polishing of the sample surface.

Figure V.16 GATAN 681 PIPS ion miller located in the Materials Research Laboratory at the University of Illinois

For a cross sectional TEM sample, its position on PIPS specimen holder is shown in figure V.17. During ion milling, one of the ion beams etches from the top (incline angle = +7°), while the other etches from the bottom (incline angle = -7°). This is done to eliminate the re-deposition layers on both sides of the specimen. Two ion beams are aligned to focus on the center of the specimen. In this case, the modulator is switched to "double" mode, which ensures each ion beam works only half of the cycle in each stage rotation. For a plan view TEM sample, the specimen is mounted on a sample stage (figure V.17 (b)) with Crystalbond with the substrate side facing up. Two ion beams etch from the top at the same time and are focused on the center. The modulator is turned off, so the sample will be etched continuously. It is necessary to coat the film (down) side with a thin layer of protector (here is Crystalbond) for a plan view specimen, and then dissolve this coating after thinning to remove sputtered material. The ion milling time varies with the thickness of the

pre-thinned sample. Typically, it takes ~3 hours to perforation and another 15 minutes for fine polishing.

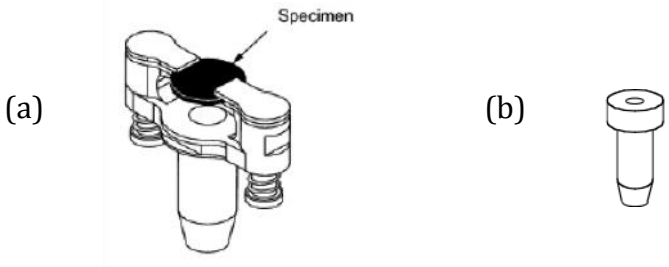

Figure V.17 (a) TEM specimens on a clamp-type sample holder for ion milling of cross-section TEM specimens, (b) a post-type sample holder for ion milling of plan view TEM specimens

Figure V.18 Schematic drawings of thin areas in (a) cross-section and (b) plan-view TEM specimens after ion milling.

VI. Experimental Results and Discussion

In this chapter, experimental results are presented to show the defect structure evolution processes in different irradiation conditions: ion source, irradiation dose and irradiation temperature. Comparison of the results obtained at various conditions is also made to help reveal the mechanisms behind the phenomena.

The results are organized into the following sections in this chapter, and more TEM micrographs can be found in appendix A:

1. Detailed analysis on as-prepared cross-section and plan-view CeO_2 TEM specimens. There are pre-existed defects in the specimens, which are induced during film growth and sample preparation.

2. Dislocation loop/dislocation structures develop with the dose increase during *in situ* irradiation. In this section, series of images obtained during several *in situ* irradiation experiments are displayed: ion irradiation of 500 keV Xe ions at 800°C, ion irradiation of 150 keV Xe ions at 800°C and 600°C, and ion irradiation of 1 MeV Kr ions at 800°C, 600°C and room temperature.

3. Temperature effects in the evolution of dislocation structure, which are demonstrated by comparing the *in situ* irradiation results from 1 MeV Kr ions at three temperatures (800°C, 600°C and room temperature).

4. Gas bubble formation process, which is demonstrated by the *in situ* irradiation result of 150 keV Kr ions at 600°C and room temperature.

5. Defect structure formed in high-dose *ex situ* irradiation experiments. Both temperature effect and dopant (lanthanum) effect are discussed in the case of 700 keV Xe ion irradiation.

VI.1 TEM Analysis on Unirradiated CeO_2

As shown in bright-field and dark-field images in figure VI.1, the thickness of CeO_2 thin film was measured to be ~160 nm. Pre-existed defects/defect clusters can be easily found, which stem from thin film growth.

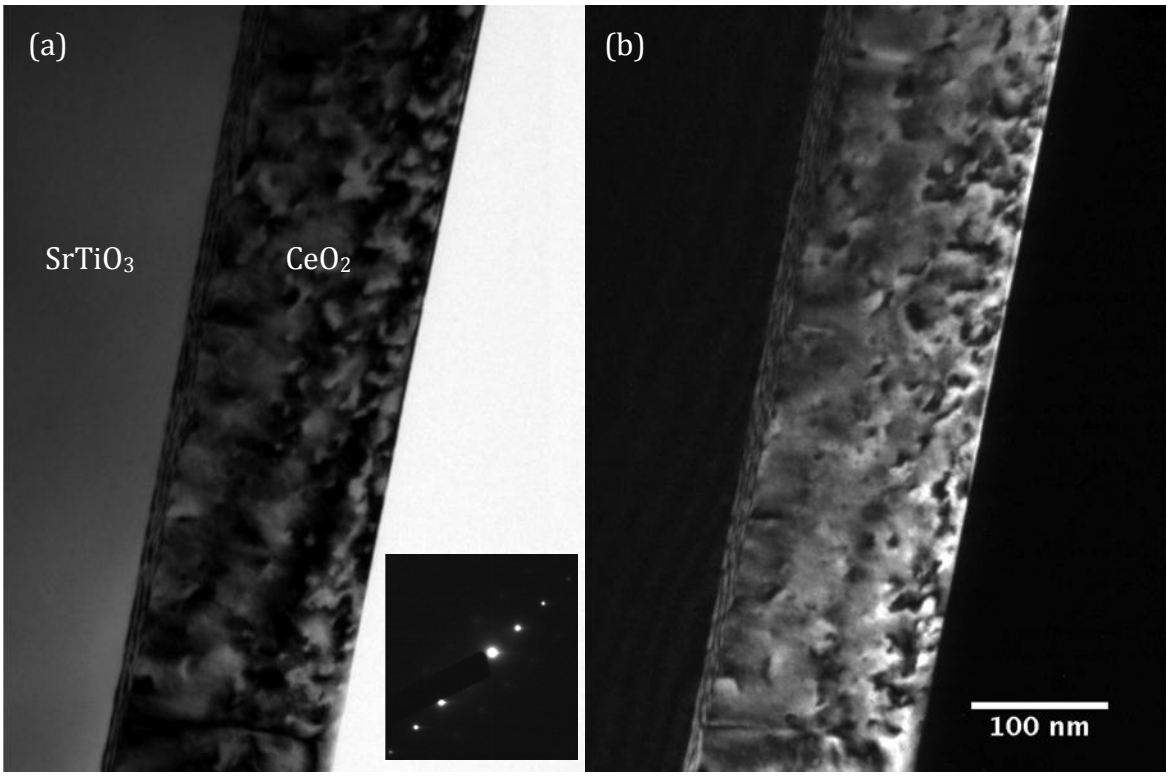

Figure VI.1 Cross-section TEM micrographs (a) bright-field and (b) dark-field of CeO_2 thin film on $SrTiO_3$ substrate before irradiation. Images were taken along the electron beam direction of [011], and the diffraction vector g = 1-11.

Detailed crystal structure of the CeO_2 thin film can be found in figure VI.2, which is a HRTEM image taken along [011] orientation. The diffraction pattern shown in the inset confirmed that the thin film, grown with MBE technique, was indeed single crystal. However, there were some inherent defects caused by slight mismatch of lattices of CeO_2 and $SrTiO_3$. The two dislocations, indicated by pairs of white arrows in this area, were identified as the dislocations formed during growth, since there

was no such kind of defects found in the substrate area, which eliminated the possibility of damage during sample preparation.

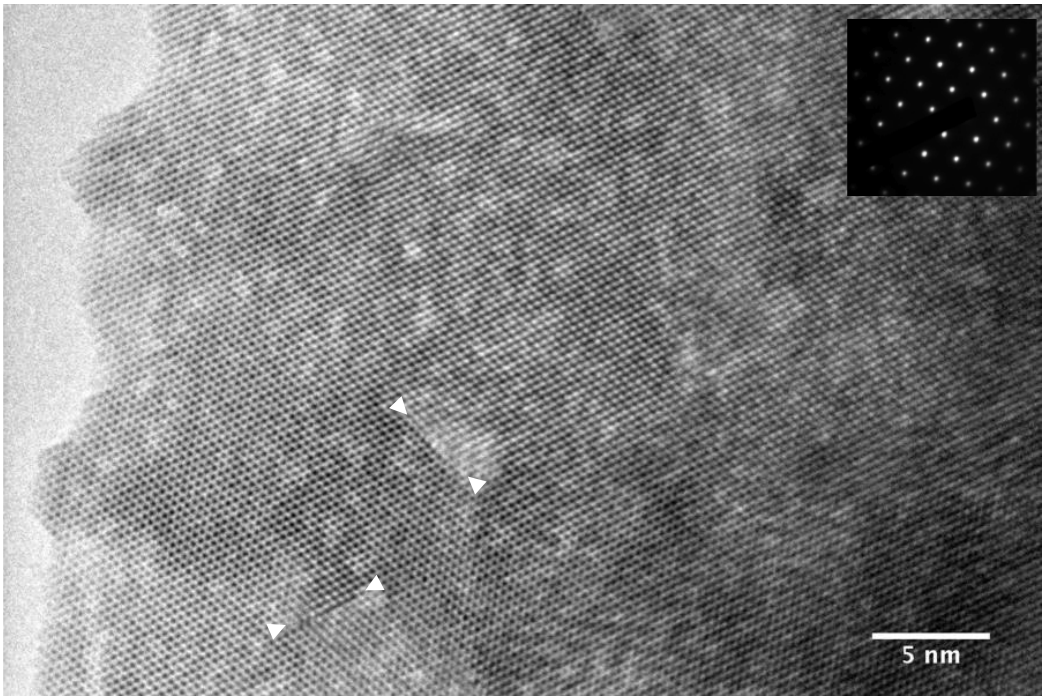

Figure VI.2 Cross-section high-resolution TEM (HRTEM) image of CeO_2 before irradiation. Images were taken along the electron beam direction of [011].

In order to further investigate the defect structures in as-prepared TEM specimens, more microscopy was performed on plan-view samples, which were used for *in situ* irradiation. An annealing experiment was performed by using the heating stage in the IVEM facility, and the results are shown in figure VI.3. Dark-field images are presented here to show more clearly the details of defect structures. Figure VI.3 (a) and (b) are images taken before and after annealing at 600°C, and figure VI.3 (c) is a micrograph taken after annealing but in higher magnification.

The dislocation loops shown in figure VI.3, in white contrast, were likely to be caused by argon ion bombardment during the ion-milling process. This is owing to the fact that the density of dislocation loops changes dramatically from the left side in figure VI.3 (a) and (b) to the right side (near the edge). Referring to the

configuration of plan-view sample (figure V.17 (b)), the area near edge is pure CeO_2, and the area further toward the thicker part is covered with $SrTiO_3$ substrate. Moriè fringes (figure VI. 3(b)), which form from the overlapping of CeO_2 and $SrTiO_3$ lattices, can help distinguish these two areas (pure CeO_2 and CeO_2 covered by substrate). If the defects were all generated from film growth, a uniform distribution of defect structures across the area should be observed.

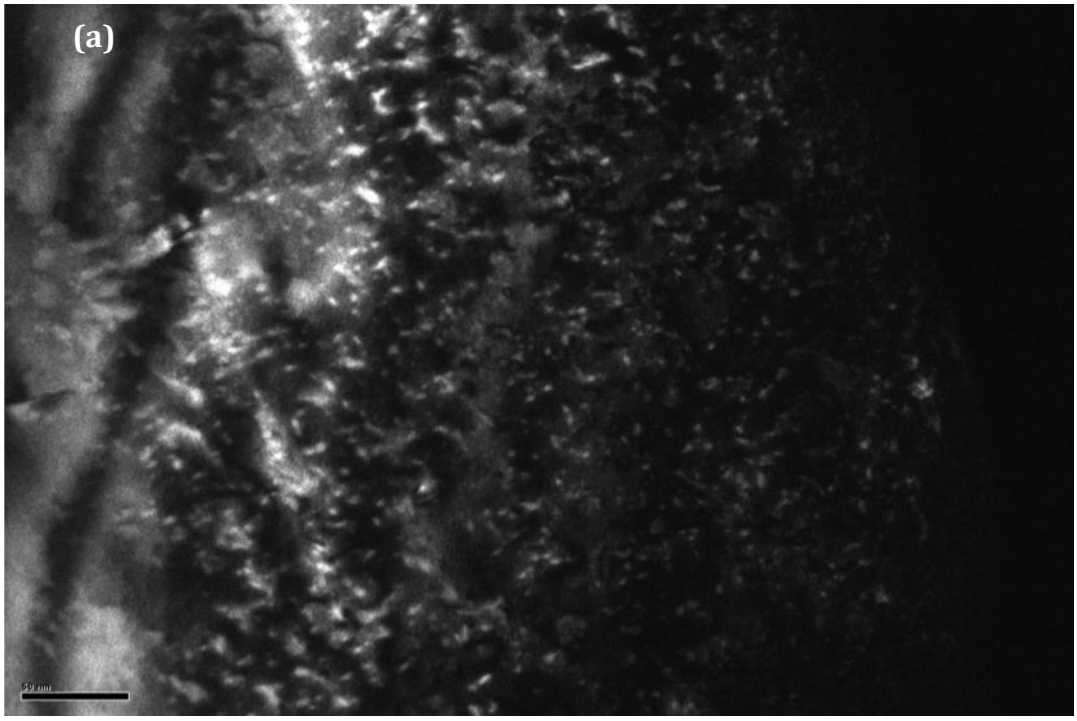

Figure VI.3 Weak-beam dark-field micrographs of as-prepared plan-view specimen (a) before annealing

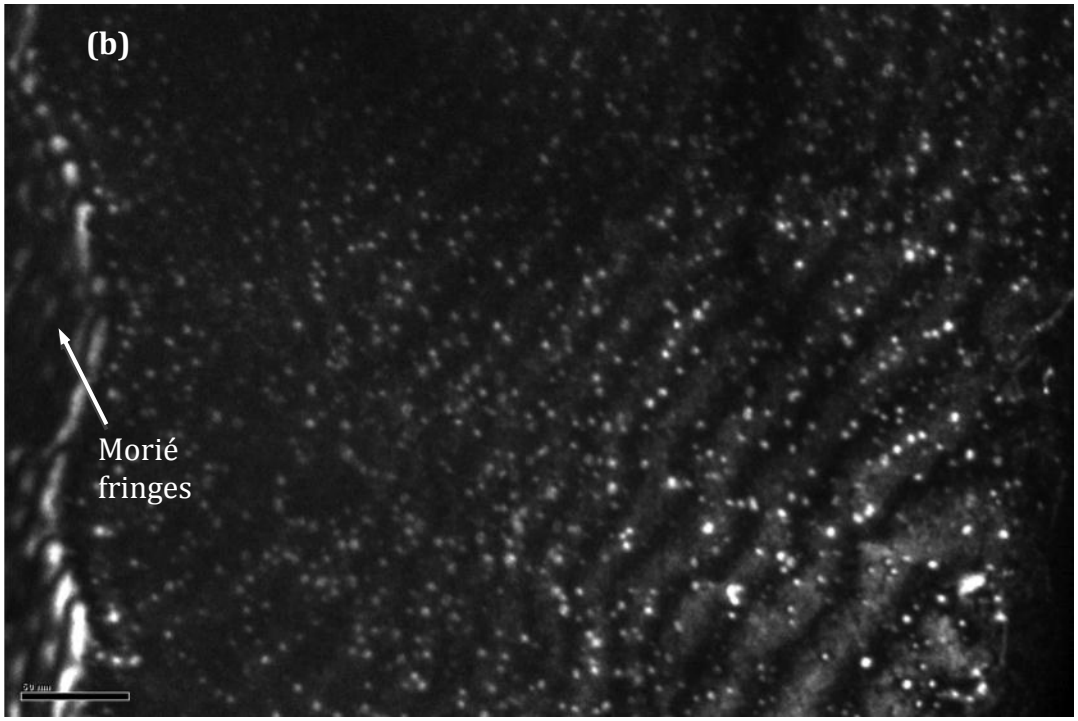

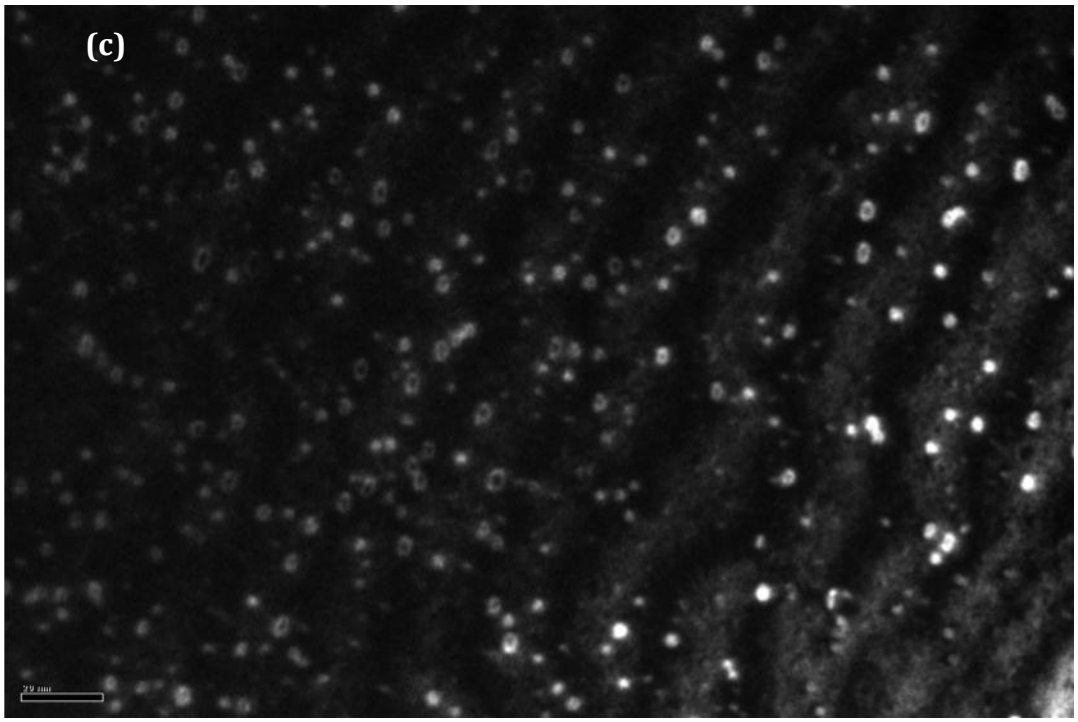

Figure VI.3 (cont.) Weak-beam dark-field micrographs of as-prepared plan-view specimen (b) annealed at 600°C for 3 hours and (c) after annealing at 600°C for 3 hours in higher magnification. All images were taken alone the direction of [001] with g = -2-20.

The defect structures observed in the specimens without ion irradiation provide pre-existing nucleation sites/sinks for point defects generated during later ion implantation. Such effects might obscure the observation of the nucleation process of defect structures. Further improvement of TEM sample preparation techniques is needed to reduce the pre-irradiation damage in specimens, which is extremely important for observation the nucleation process at the beginning stage of ion irradiation.

VI.2 Dislocation Loop/Dislocation Structures Development During *In Situ* Irradiation

Figure VI.4 shows the sequential change of defect cluster damage in CeO_2 with 500 keV Xe ions at 800°C. This dose sequence was taken during irradiation in the ANL IVEM/Tandem facility where the dose levels could be tracked in the same sample area. The choice of 800°C irradiation temperature is sufficiently high that O defects should be mobile as should vacancies on the O sublattice.

The evolution of a fine defect structure was evident in the microstructure. In figure VI.4, image (a) and (b) show the microstructure of the specimen before irradiation as prepared and annealed respectively. There were defect clusters to begin with (black contrasts), which were induced by the ion milling process. The defect clusters changed from irregular shapes to almost circular ones after annealing. This shows defects become mobile when temperature rises. The exact characteristic of these defect clusters is not yet clear.

To understand the nature of the defect clusters, $g \bullet b$ analysis and trace analysis will be applied in the future. From previous studies [8], it is believed that interstitials generated during irradiation displacement are inclined to form dislocation loops. Furthermore, the relatively excessive vacancies left in the matrix group into voids, which provide perfect traps for gas atoms.

The size of defect structures, which were characterized as dislocation loops, grew with increasing dose (0 – $3x10^{14}$ ions/cm^2), as displayed in figure VI.4 (c-e). Meanwhile, the density of defect clusters remained nearly unchanged. This suggests that nucleation of defect clusters is completed in a very early stage of irradiation (during ion milling in this case). A similar result was observed in CeO_2 irradiated with electrons [41].

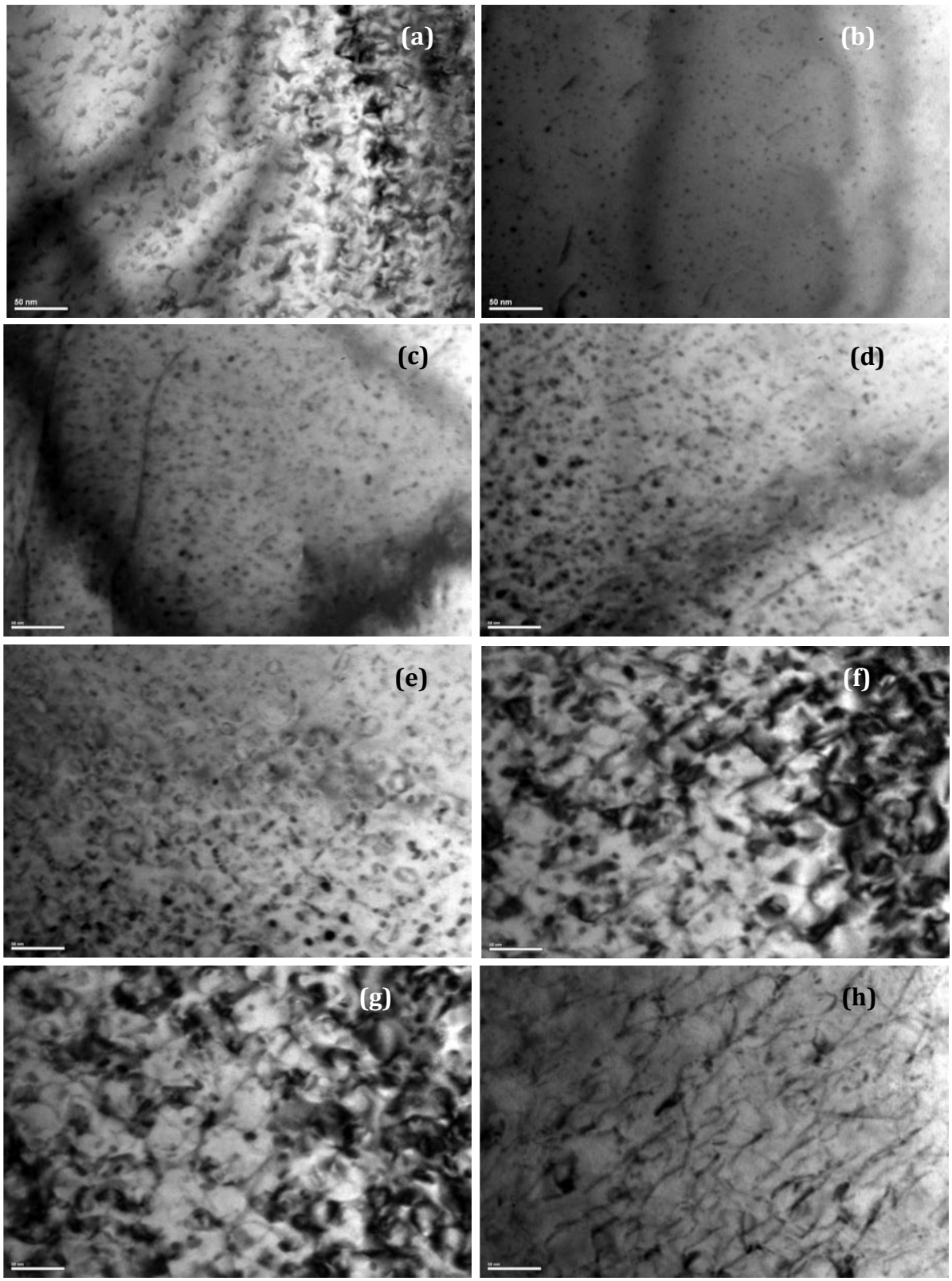

Figure VI.4 Bright-field TEM micrographs recorded during the *in situ* irradiation of single crystal CeO_2 with 500 keV Xe ions at 800°C. The applied flux is $1.25x10^9$

ions/cm^{2}s before 3x10^{14} ions/cm^2 and 6.25x10^9 ions/cm^{2}s after that. The corresponding dose are (a) 0 (as prepared) (b) 0 (annealed) (c) 5x10^{13} (d) 1x10^{14} (e) 3x10^{14} (f) 8x10^{14} (g) 1x10^{15} (h) 1.8x10^{15}

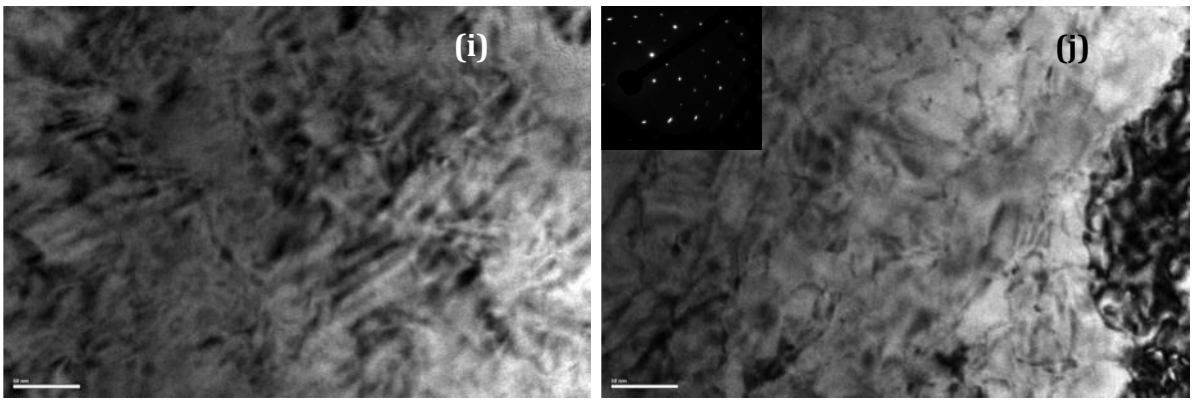

Figure VI.4 (cont.) Bright-field TEM micrographs recorded during the *in situ* irradiation of single crystal CeO_2 with 500 keV Xe ions at 800°C. The applied flux is 1.25x10^9 ions/cm^{2}s before 3x10^{14} ions/cm^2 and 6.25x10^9 ions/cm^{2}s after that. The corresponding dose are (i) 3x10^{15} (j) 5x10^{15} in unit of ions/cm^2. The scale length is 50 nm.

When the dose reached 8x10^{14} ions/cm^2 (figure VI.4 (f)), dislocation loops became much less distinguishable. Some of them merged with each other and developed into micro-cells walled with extended dislocation loops. This process continued through a dose of 1x10^{15} ions/cm^2 (figure VI.4 (g)). Finally tangled dislocation networks clearly appeared when the dose reached 1.8x10^{15} ions/cm^2 (figure VI.4 (h)). The same processes occurred during *in situ* irradiation of 390 keV Xe and 300 keV Cs in UO_2 [83].

When incremental implantation went beyond 1.8x10^{15} ions/cm^2, it became difficult to maintain the same diffraction condition during TEM observation due to sample bending. The detailed defect structure, shown in figure VI.4 (i, j), was difficult to clearly resolve. Nevertheless by comparing figure VI.4 (i) and (j), it can be seen that the defect structure approached a stable configuration by this stage of

irradiation. The inset in figure VI.4 (j) is a diffraction pattern taken after the irradiated specimen was cooled to room temperature. The round diffraction spots demonstrated the specimen remains crystalline.

Cavities (bubbles/voids) generated during irradiation with Xe are displayed in figure VI.5. They are characterized as white dots in underfocus (figure VI.5 (a)) and black dots in overfocus conditions (figure VI.5 (b)). These features are 1 to 2nm in diameter, and the area density is ~1.5×10^{17} nm^{-2}. Comparable results were obtained on UO_2 irradiated with 260 keV Xe at a dose of 8×10^{15} ions/cm^2 [20] and with 390 keV Xe at a dose of 1×10^{16} ions/cm^2 [83].

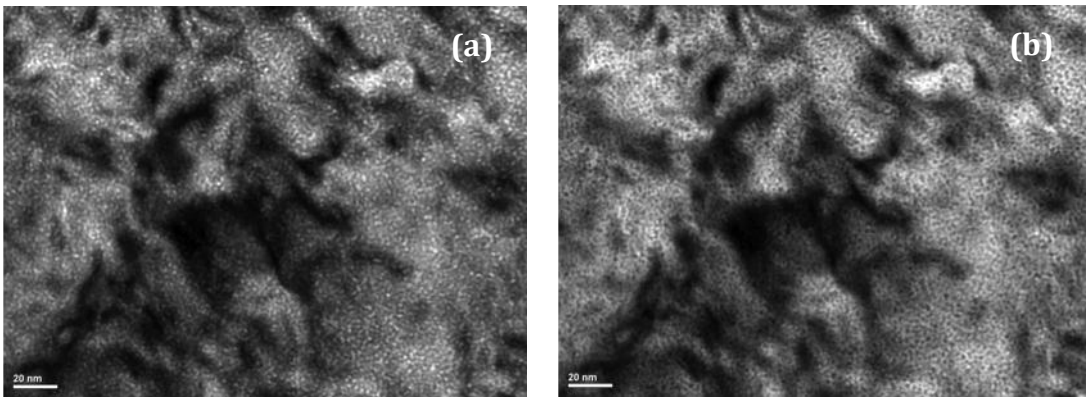

Figure VI.5 Bright field TEM micrographs of CeO_2 thin foil irradiated with 500 keV Xe at 800°C to a dose of 5×10^{15} ions/cm^2, registered with (a) underfocusing and (b) overfocusing the objective lens. The scale length is 20nm.

Temperature plays an important role in Xe precipitation. Previous experiments [13, 20] have shown there is a threshold temperature (> 400°C) at a dose of 1×10^{16} ions/cm^2 for fission gas (Xe or Kr) bubble formation. This phenomenon is closely related with mobility of oxygen defects [13].

Fission gas bubble size and density were examined in spent nuclear fuel over a wide range of burnups [84-87] (6 - 83 GWd/t). In low burnup fuels (1-23 GWd/t),

the mean size of gas bubbles was found to be 1-3 nm [86], and increased to 4.7 nm in base-irradiated fuel at 83 GWd/t [86], with the density decreasing from $9.0x10^{23}$ m^{-3} to $4.4x10^{23}$ m^{-3}. In experiments by Cornell [87], UO_2 fuel pellets were irradiated to doses between $3.2x10^{16}$ to $4.6x10^{17}$ fissions/mm^3 at temperature between 700 to 1600°C. Gas bubble diameters were measured from TEM micrographs at 1.7 to 3.1 nm. The results obtained here are similar to the data shown by Cornell [87], and are in a good agreement with the values on the fuel with 23 GWd/t [86] and irradiation temperature of 1070 K. This shows that the current irradiation experiments have conditions for bubble formation that are similar to the low burnup neutron irradiation results. The mechanisms of bubble growth, coalescence or ripening, together with fission gas diffusion paths will be explored in future experiments.

The evolution and growth behavior of irradiation-induced defect structures was studied as a function of dose during incremental irradiation of CeO_2 with 500 keV Xe at 800°C using *in situ* TEM techniques.

The evolution process of the dislocation structure developed through several stages:

1. Nucleation of dislocation loops was completed at the very early stage of irradiation. For this case, it was finished during ion milling process.
2. With the increasing dose, dislocation loops expanded radically and began to interact with each other. Some of them coalesced, which accelerated loop growth.
3. By the time the dose reached $1.8x10^{15}$ ions/cm^2, a tangled dislocation network had evolved in the specimen.
4. Following the evolution of the dislocation network structure, the microstructure remained stable to higher doses.

Sequential images recorded during *in situ* irradiation of 150 keV Xe ions at 800°C are displayed in figure VI.6. The evolution of loop structure experienced similar stages as the *in situ* irradiation of 500 keV Xe ions at 800°C shown in figure VI. 3. In this experiment, the rapid growth stage of individual loops was from the beginning of the irradiation to the dose of $3x10^{14}$ ions/cm^2. On the image taken at $5.2x10^{14}$ ions/cm^2, line segments started to appear, and the population of individual loops decreased. This phenomenon suggested some of the loops joined together to form line segments, and the strain field around the loops, induced by irradiation, might be the driving force behind this.

At the dose of $2x10^{15}$ ions/cm^2, tangled dislocations formed along with individual loops. At the final dose of $5x10^{15}$ ions/cm^2, although the damage structures developed further, individual loops could still be easily resolved. This is different from the features shown in figure VI.3 (j), in which there were almost no individual loops appearing. There are two possible causes for this. One is that the observed area in figure VI.6 is thicker than in figure VI.3. In the ultra thin TEM foils (< 100 nm), defects tend to escape from surfaces of the specimen, so the thicker area helps to retain the defects, which can explain why the small individual loops could still survive in this situation. The other possibility might be due to nucleation of new dislocation loops. This process is not obvious during irradiation of 500 keV Xe ions at 800°C, but the damage scale measured by dpa value is almost twice as high at the depth of 40 nm, which is the typical thickness of area of interest, in the irradiation of 150 keV Xe ions than 500 keV Xe ions. Continuous nucleation of dislocation loops might occur in this situation.

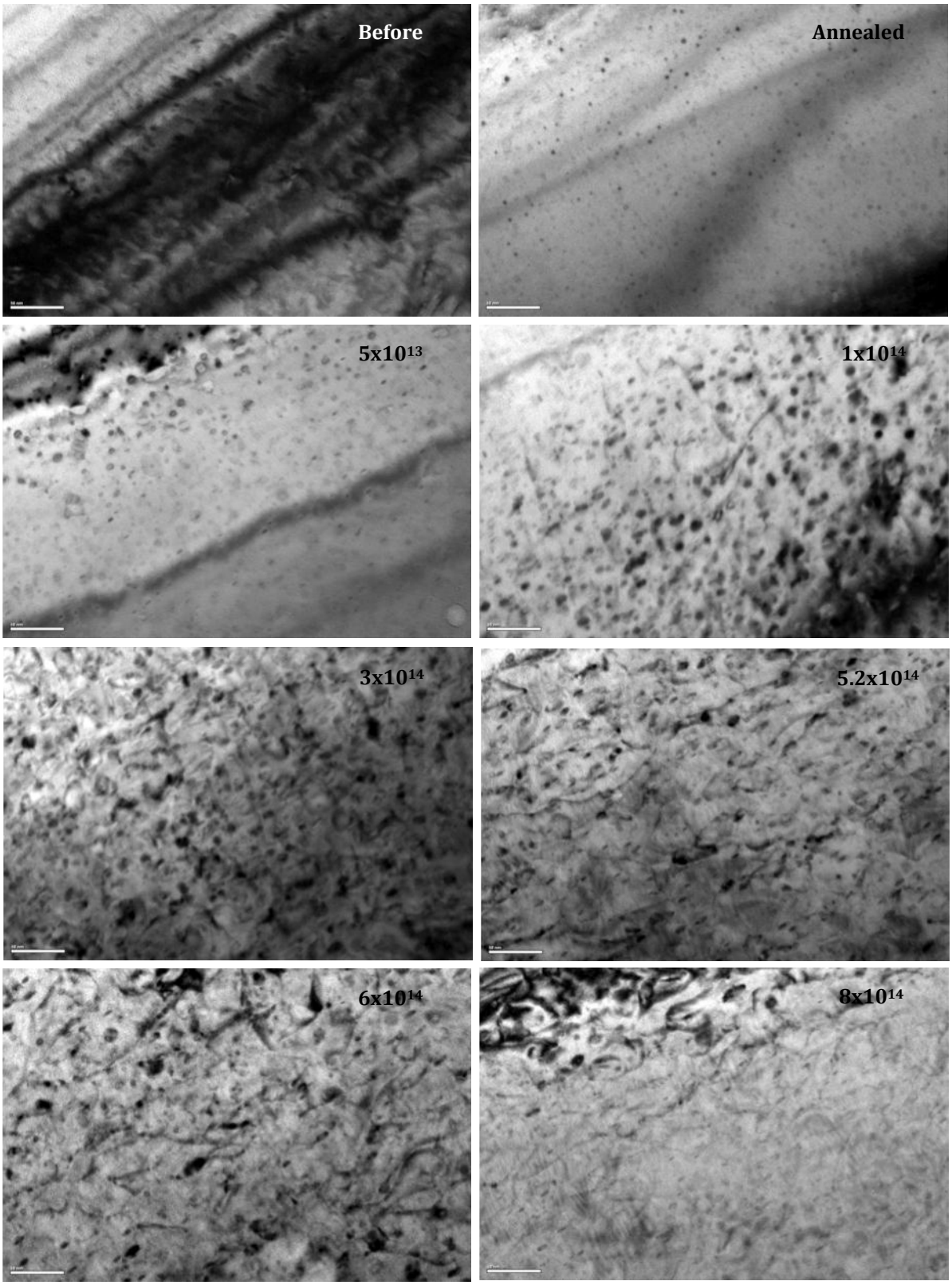

Figure VI.6 Bright-field TEM micrographs recorded during the *in situ* irradiation of single crystal CeO_2 with 150 keV Xe ions at 800°C. All the scale bars are in 50 nm.

The dose level is indicated on the up-right corner of each image, and the unit is ions/cm^2. During this observation, the diffraction condition was kept at g = 220 near [001] zone.

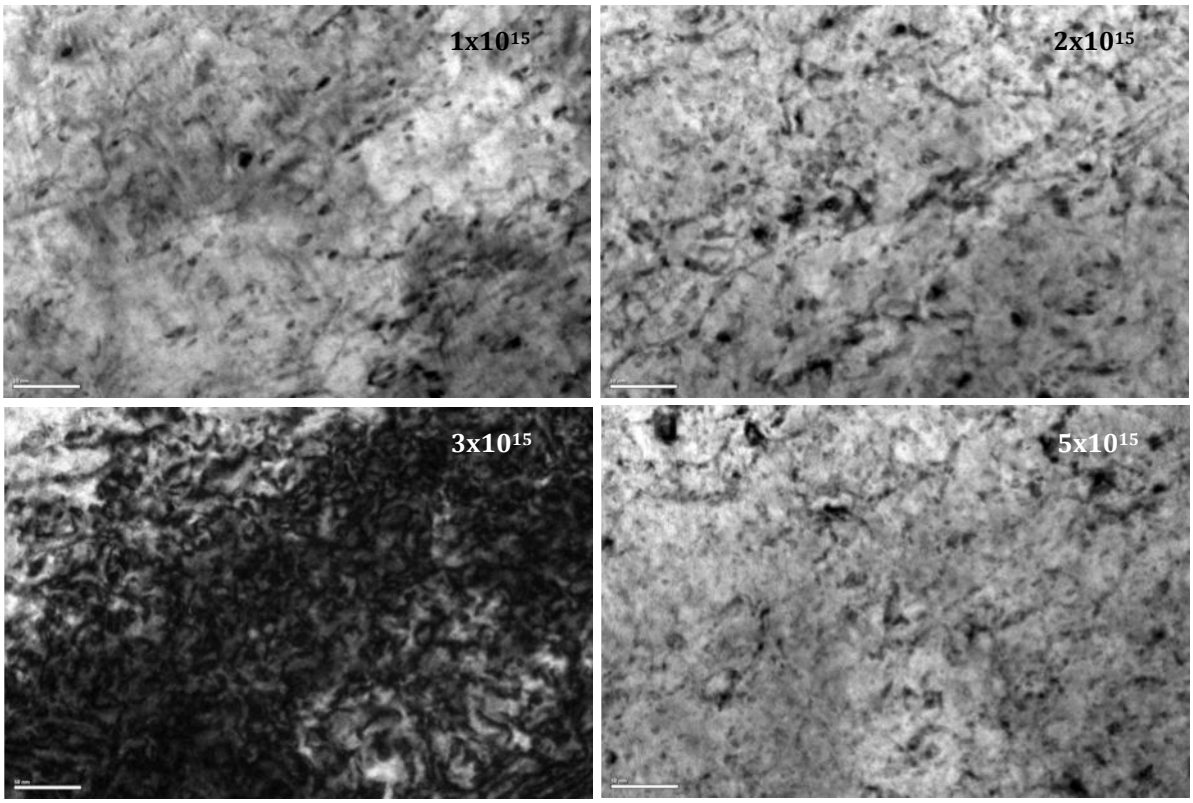

Figure VI.6 (cont.) Bright-field TEM micrographs recorded during the *in situ* irradiation of single crystal CeO_2 with 150 keV Xe ions at 800°C. All the scale bars are in 50 nm. The dose level is indicated on the up-right corner of each image, and the unit is ions/cm^2. During this observation, the diffraction condition was kept at g = 220 near [001] zone.

Similar evolution processes were found in the irradiation of 150 keV Xe ions at 600°C, shown in figure VI.7. Comparing with the same irradiation at 800°C, the temperature difference caused the evolution processes to be less obvious. At the dose of 1x10^{15} ions/cm^2, tangled dislocation network formed. However, the growth of loops was slower at this temperature. Detailed analyses of the temperature effect

in defect structure evolution are elaborated in section VI.3, in which the comparison of *in situ* irradiation of 1 MeV Kr ions at 600°C and 800°C is studied.

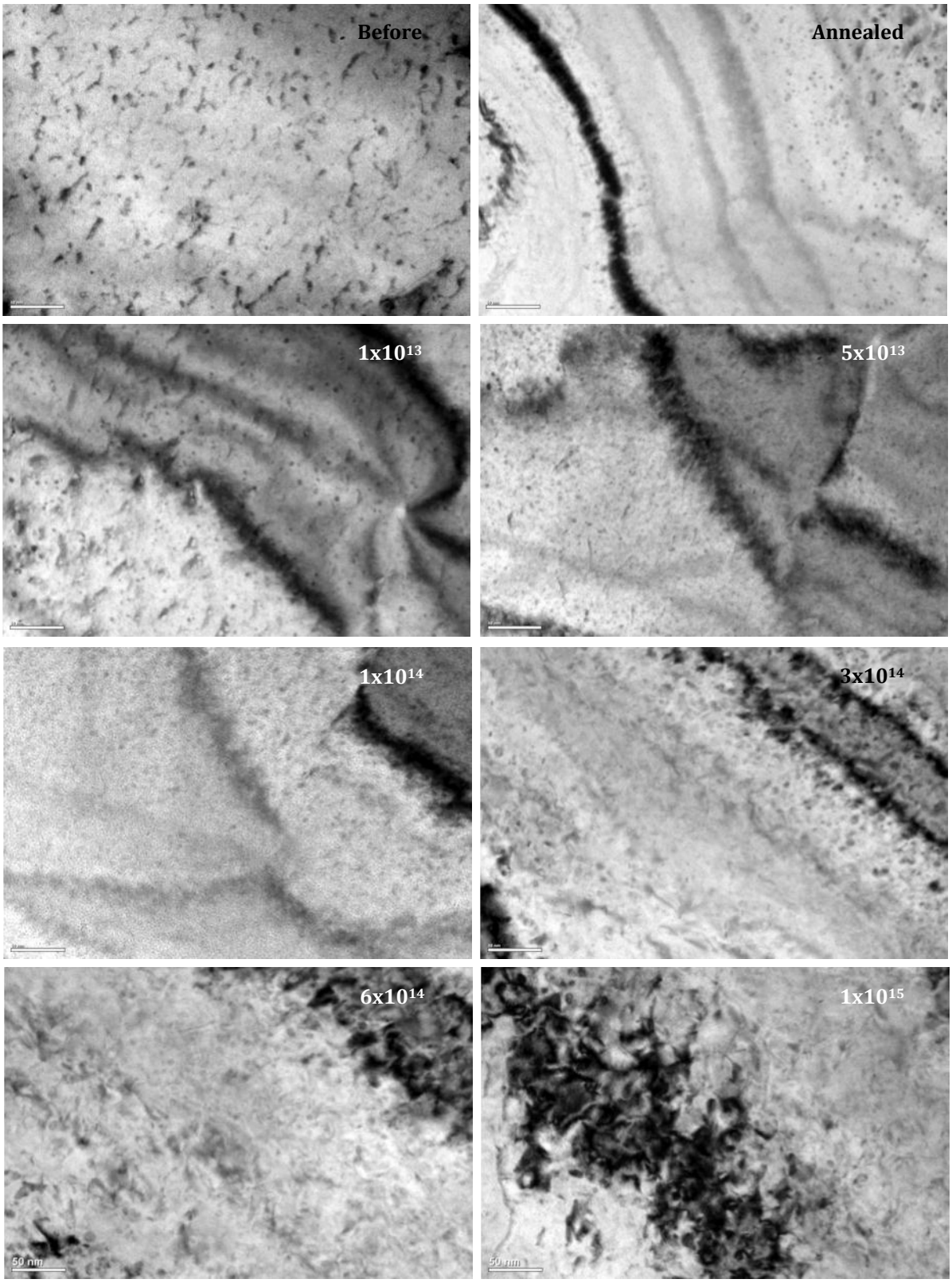

Figure VI.7 Bright-field TEM micrographs recorded during the *in situ* irradiation of single crystal CeO_2 with 150 keV Xe ions at 600°C. All the scale bars are in 50 nm.

The dose level is indicated on the up-right corner of each image, and the unit is ions/cm^2. During this observation, the diffraction condition was kept at g = 220 near the [001] zone.

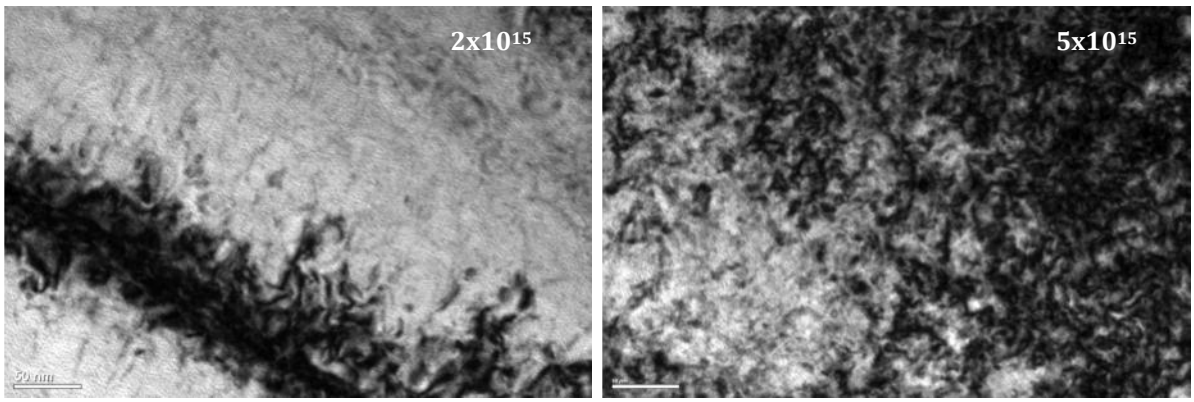

Figure VI.7 (cont.) Bright-field TEM micrographs recorded during the *in situ* irradiation of single crystal CeO_2 with 150 keV Xe ions at 600°C. All the scale bars are in 50 nm. The dose level is indicated on the up-right corner of each image, and the unit is ions/cm^2. During this observation, the diffraction condition was kept at g = 220 near the [001] zone.

Sequential TEM micrographs taken during in-situ irradiation of 1 MeV Kr ions at 800°C, 600°C and room temperature are displayed in figure VI.8, figure VI.9 and figure VI.10 respectively. Quantitative analysis of loop structure growth from the results obtained at 600°C and 800°C is presented in section VI.3, in terms of the variation of loop size and density as functions of dose.

In these experiments, observation area and diffraction condition were carefully kept unchanged throughout the whole process. It is therefore possible to compare one image to another to reveal the structure change within each dose step. At 800°C, the enhanced defect mobility resulted in accelerated precipitation of interstitials, and the loop growth behavior is clearly observed during in-situ irradiation. Dislocation loops appear as round shape consisting of two black lobes at small size (< 15 nm) in bright-field images; when they grow bigger (> 20 nm), they show the

contrast of thin lines in elliptical shape. The loop coalescence process was recorded in real-time with digital video equipment during irradiation. The process could be clearly seen by comparing the images taken at the doses of $1x10^{15}$ and $1.5x10^{15}$ ions/cm^2. The loops highlighted in circles grew, interacted with each other, and finally merged into one loop.

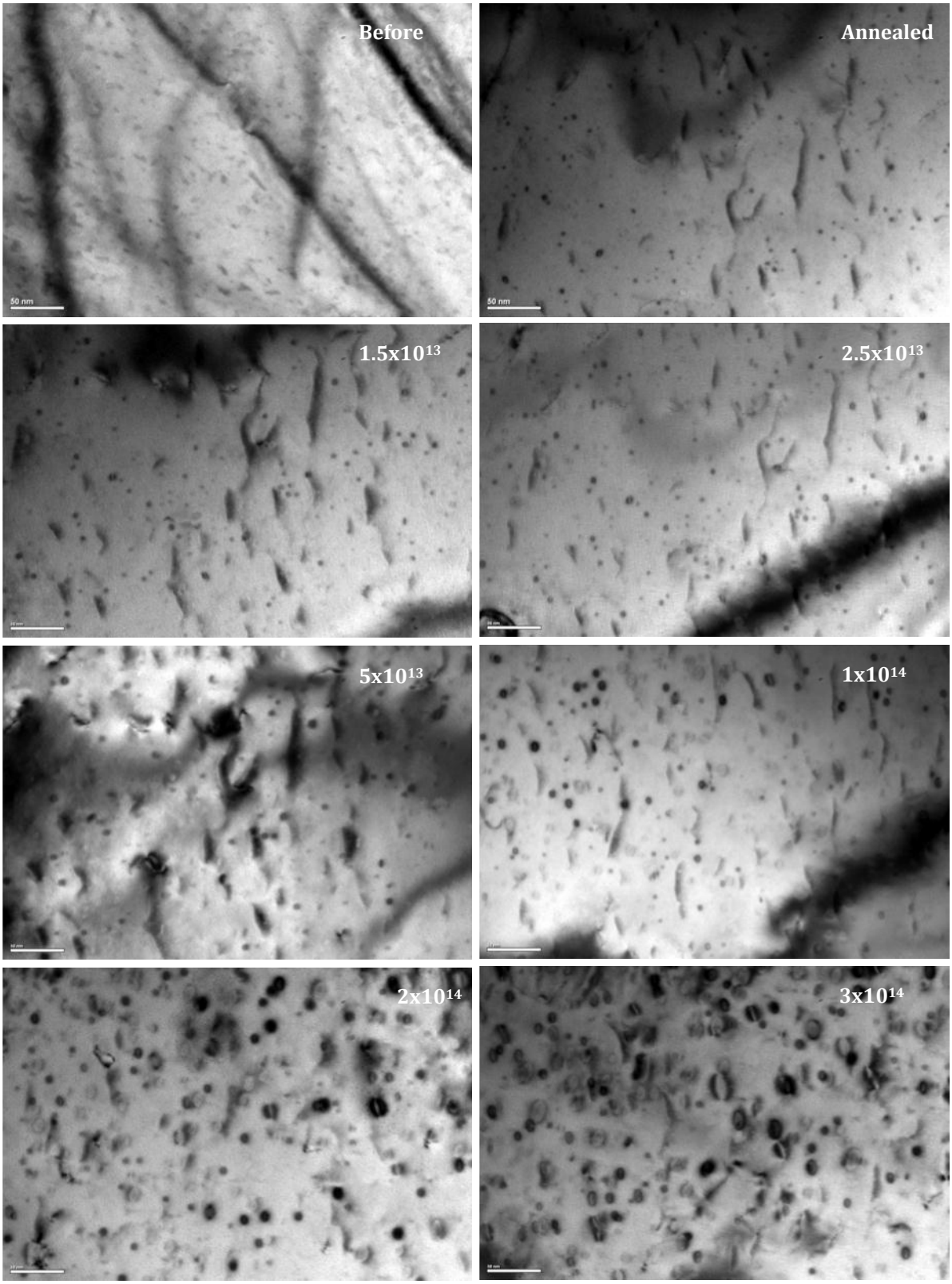

Figure VI.8 Bright-field TEM micrographs recorded during the *in situ* irradiation of single crystal CeO_2 with 1 MeV Kr ions at 800°C. All the scale bars are in 50 nm. The

dose level is indicated on the up-right corner of each image, and the unit is ions/cm^2. During this observation, the diffraction condition was kept at g = 220 near the [001] zone.

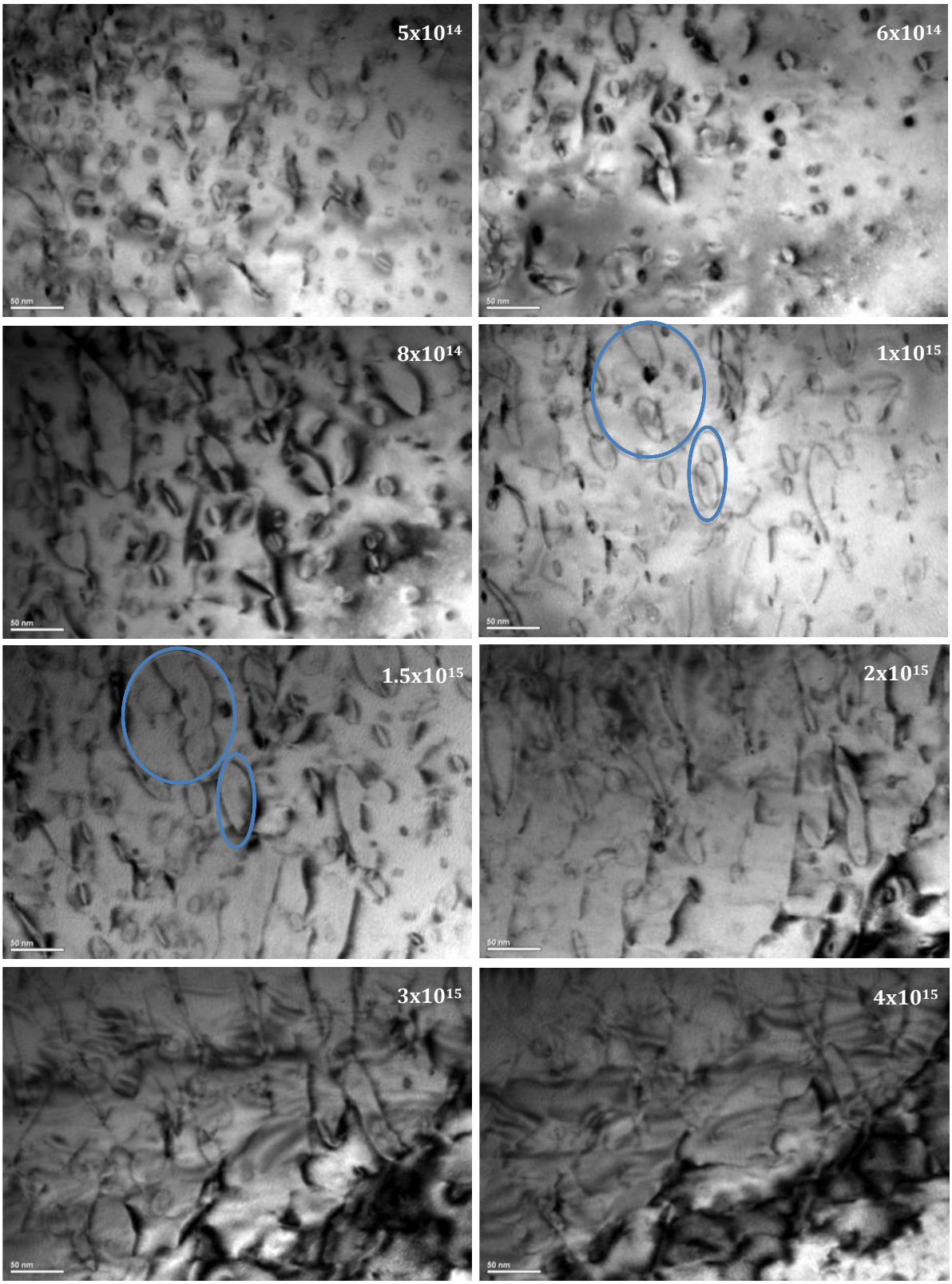

Figure VI.8 (cont.) Bright-field TEM micrographs recorded during the *in situ* irradiation of single crystal CeO_2 with 1 MeV Kr ions at 800°C. All the scale bars are

in 50 nm. The dose level is indicated on the up-right corner of each image, and the unit is ions/cm^2. During this observation, the diffraction condition was kept at g = 220 near the [001] zone.

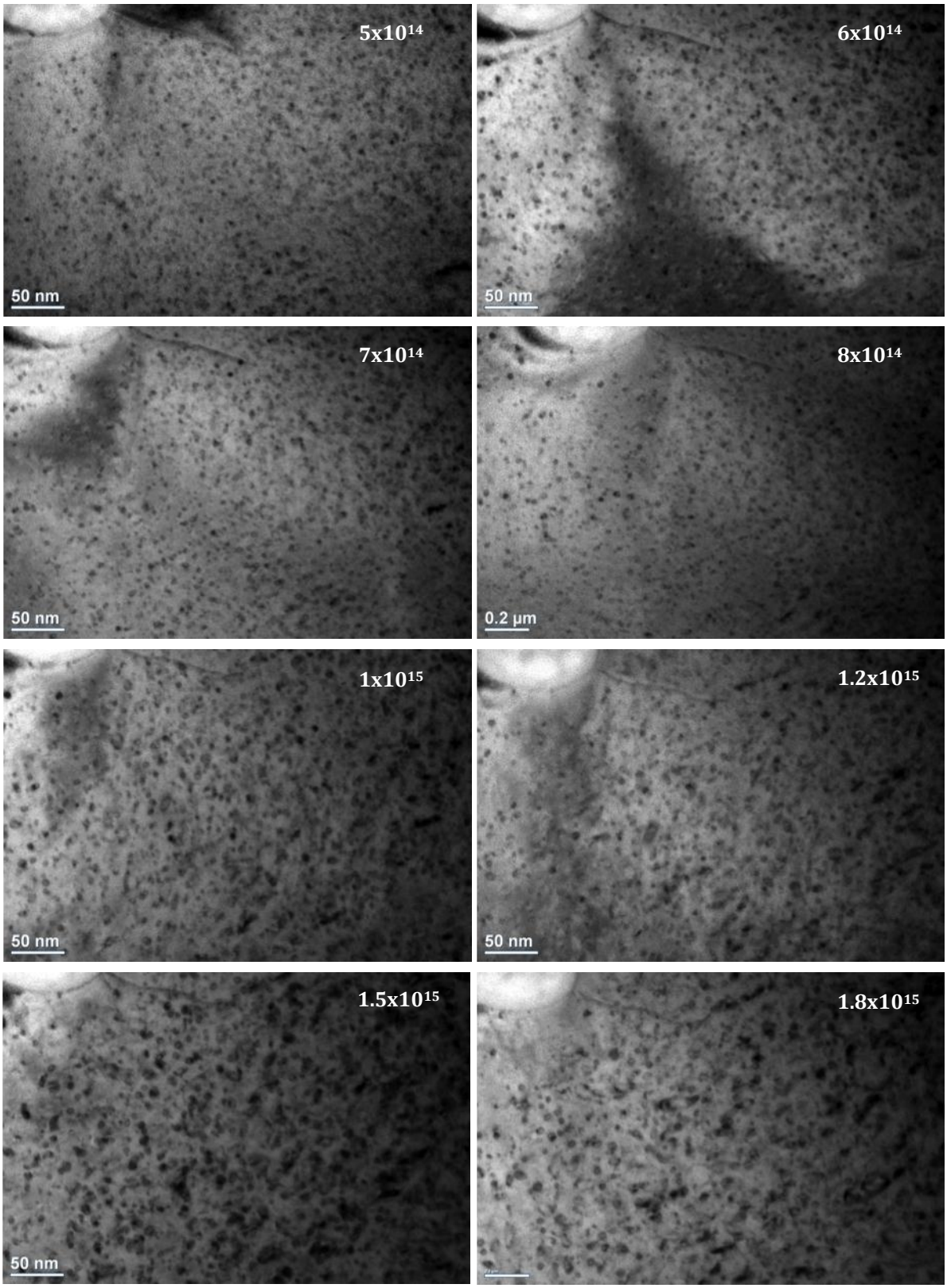

Figure VI.9 Bright-field TEM micrographs recorded during the *in-situ* irradiation of single crystal CeO_2 with 1 MeV Kr ions at 600°C. All the scale bars are in 50 nm. The

dose level is indicated on the up-right corner of each image, and the unit is ions/cm^2. During this observation, the diffraction condition was kept at g = 220 near the [001] zone.

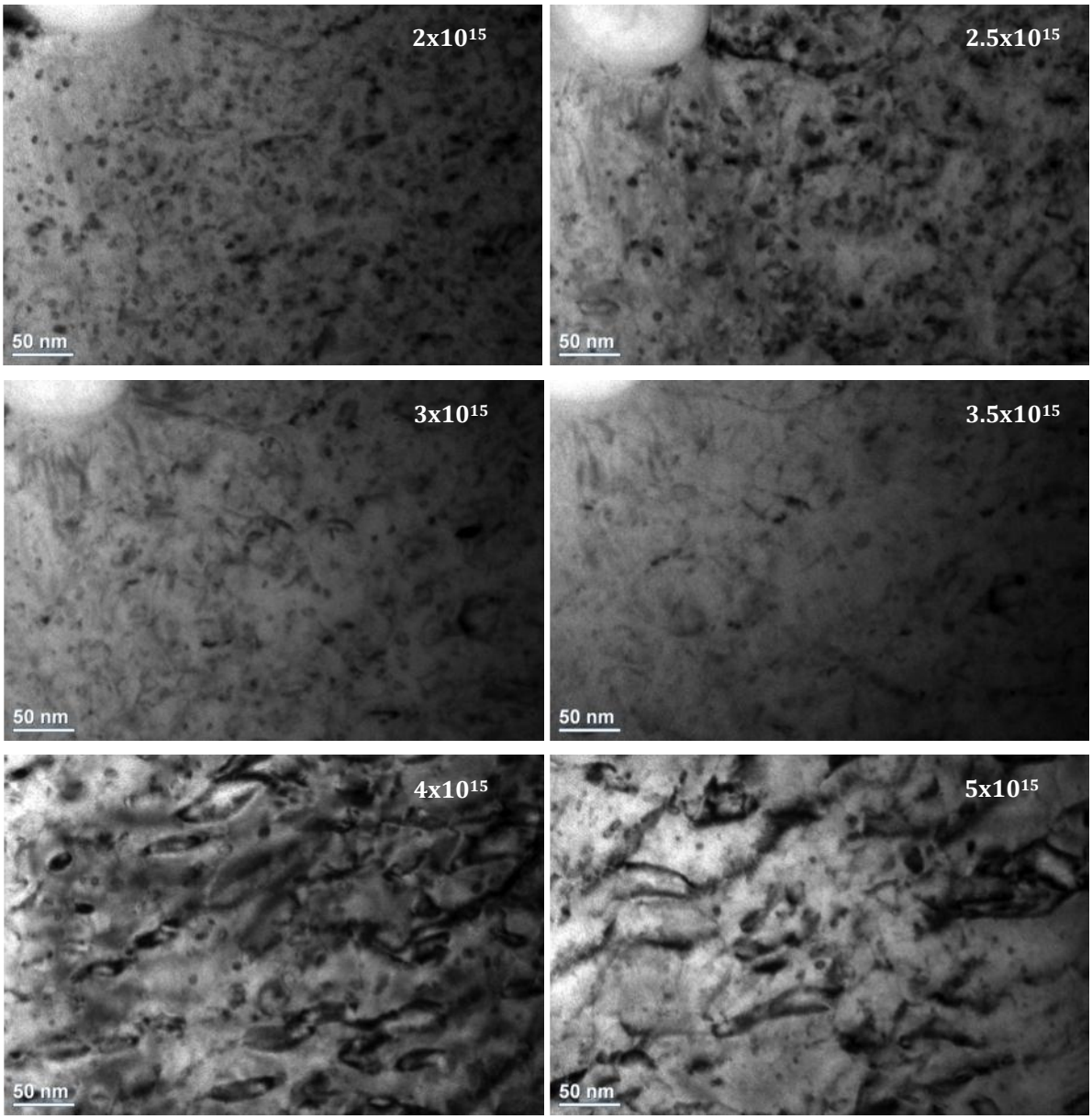

Figure VI.9 (cont.) Bright-field TEM micrographs recorded during the *in-situ* irradiation of single crystal CeO_2 with 1 MeV Kr ions at 600°C. All the scale bars are in 50 nm. The dose level is indicated on the up-right corner of each image, and the unit is ions/cm^2. During this observation, the diffraction condition was kept at g = 220 near the [001] zone.

Before the irradiation experiment at room temperature, the specimen was annealed at 800°C for 30 minutes to allow the defects to migrate fully untill they got trapped in the pre-existed defect structures (loops, pores). This was done to assure the same pre-radiation condition in experiments with different temperatures. The image taken after annealing (figure VI.10 annealed at 800°C) shows similar features as shown in figure VI.8 annealed. Both bright-field and dark-field images are displayed for each dose. Features show opposite contrast at these two imaging conditions. In dark-field images, defect clusters/loops appear as white dots. At room temperature, loops developed much slower than at 600°C and 800°C. Nevertheless, a tangled dislocation network formed at $1x10^{15}$ ions/cm^2, which is much earlier than at 600°C ($3x10^{15}$ ions/cm^2) and 800°C (> $3x10^{15}$ ions/cm^2). Strain field surrounding the loop structures is considered the main driving force of dislocation network formation. Hence, it is deduced that elevated temperature helps to release some of the stress and delay the dislocation network formation. In addition, point defects can barely move at room temperature. Once they are generated from ion bombardment, it is difficult for them to recombine. Consequently, recovery of the lattice from radiation damage is much slower at room temperature.

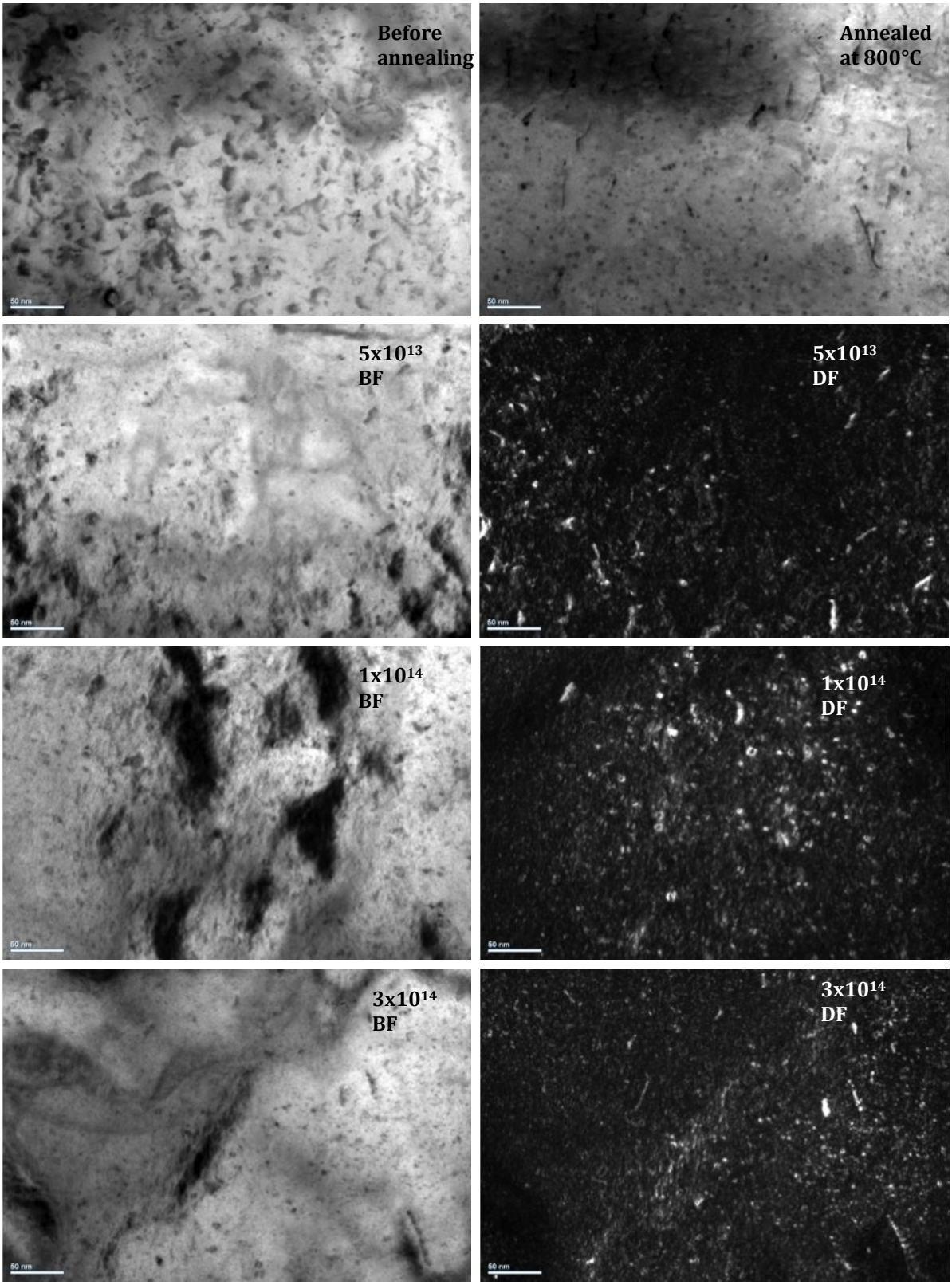

Figure VI.10 Bright-field ad dark-field TEM micrographs recorded during the *in-situ* irradiation of single crystal CeO_2 with 1 MeV Kr ions at room temperature. All

the scale bars are in 50 nm. The dose level is indicated on the up-right corner of each image, and the unit is ions/cm^2. During this observation, the diffraction condition was kept at g = 220 near the [001] zone.

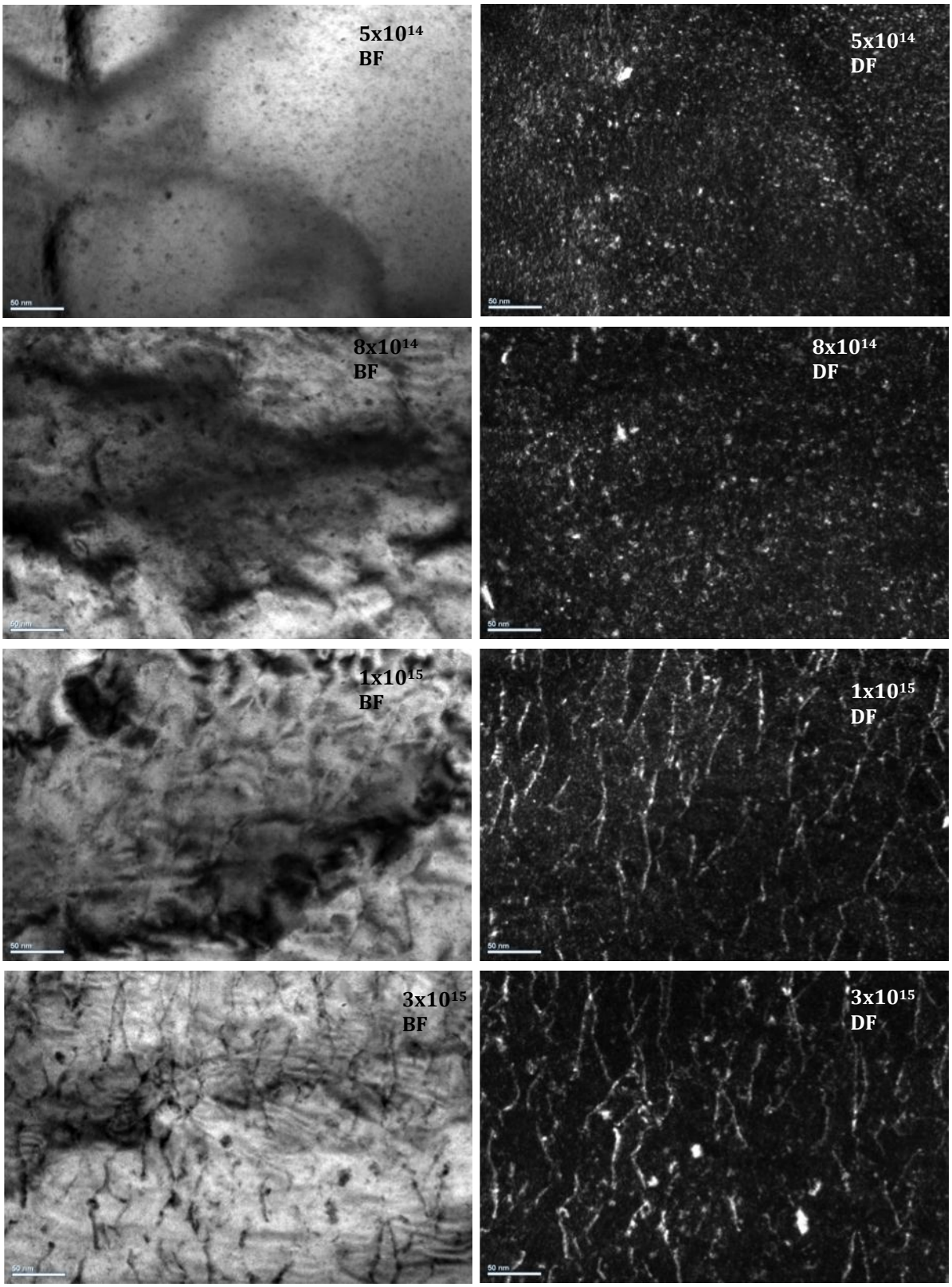

Figure VI.10 (cont.) Bright-field ad dark-field TEM micrographs recorded during the *in-situ* irradiation of single crystal CeO_2 with 1 MeV Kr ions at room

temperature. All the scale bars are in 50 nm. The dose level is indicated on the up-right corner of each image, and the unit is ions/cm^2. During this observation, the diffraction condition was kept at g = 220 near the [001] zone.

Two more series of TEM micrographs obtained from irradiation of 500 keV Xe ions and 150 keV Xe ions at room temperature are presented in figure VI.11 and figure VI.13 respectively. The irradiation was performed with the IVEM-Tandem facility at ANL, while the post-irradiation TEM investigation was carried out in the MRL at the University of Illinois with the JEOL 2010 LaB_6 microscope. In each irradiation condition, a number of virgin specimens, prepared with the same procedure, were irradiated to the desired dose levels, so each image was taken from different specimen. Since they were prepared with the same material and technique, the difference from one specimen to another should be within the allowable range. Therefore, it is still possible to study the evolution process of defect structures from comparison of the images.

The left column images in figure VI.11 are bright-field images taken on specimens irradiated with 500 keV Xe ions to the doses of $1x10^{13}$, $1x10^{14}$, $1x10^{15}$ and $5x10^{15}$ ions/cm^2, and the images on right are the corresponding dark-field images. The growth behavior of defect structures is similar to what was observed in the 1 MeV Kr ion irradiation at room temperature (figure VI.10). It was found that at $1x10^{14}$ ions/cm^2, defect structures with sizes of 10 – 15 nm appeared in the specimen bombarded with 500 keV Xe ions, in addition to the much smaller nm defect clusters. Such features were not found in the irradiation of 1 MeV Kr ions at the same dose. It is possible that higher damage (dpa value) gave rise to the formation of such features. At $1x10^{15}$ ions/cm^2, dislocation network appeared in both of cases.

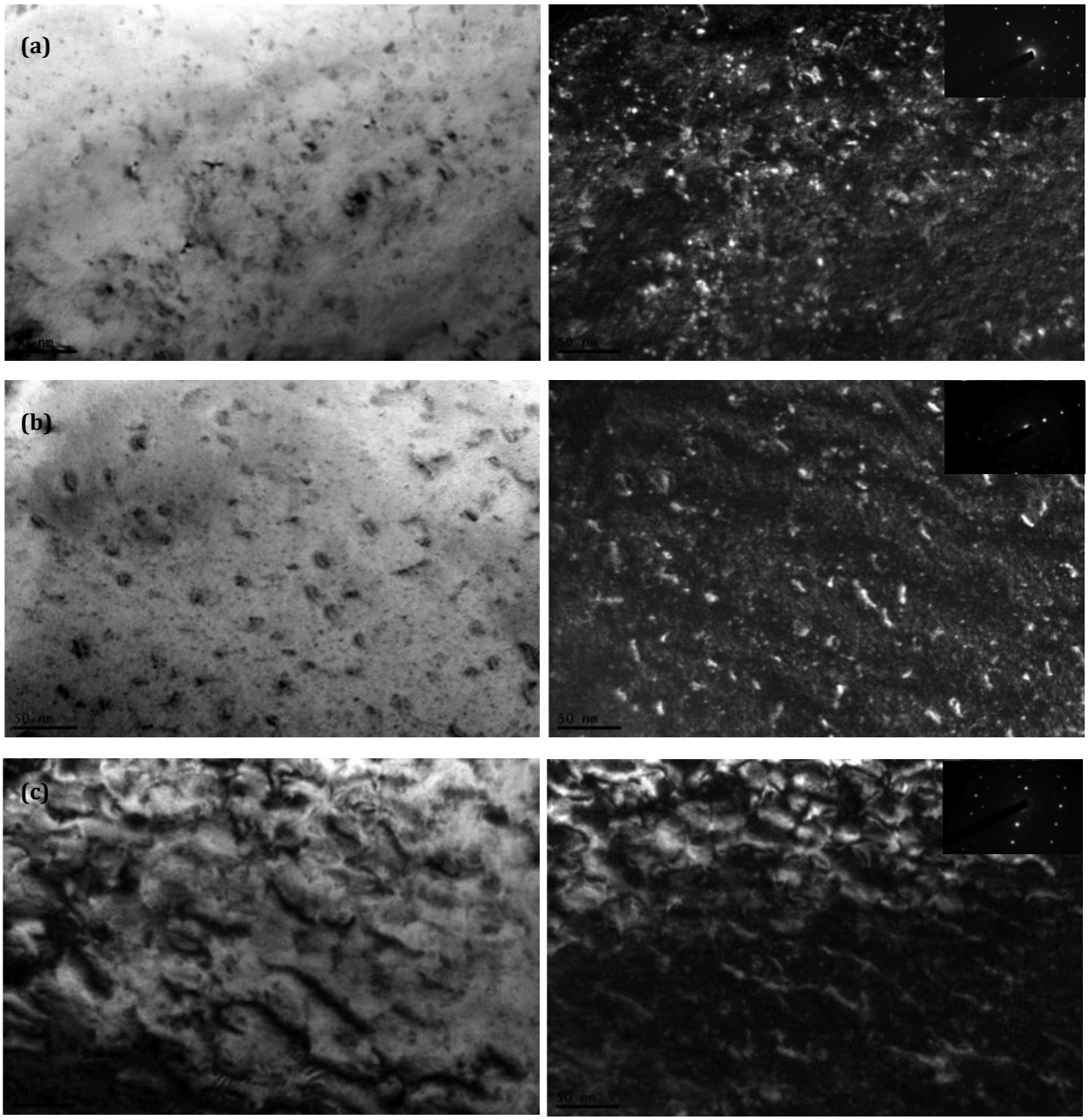

Figure VI.11 TEM micrographs of CeO_2 irradiated with 500 keV Xe at room temperature to different doses: (a) $1x10^{13}$ ions/cm^2; (b) $1x10^{14}$ ions/cm^2; (c) $1x10^{15}$ ions/cm^2; (d) $5x10^{15}$ ions/cm^2. The left column shows bright-field images, and the right column shows dark-field images. The inset in each DF image shows the diffraction condition when the image was taken. All images are taken near [001] zone axis along g=<220>.

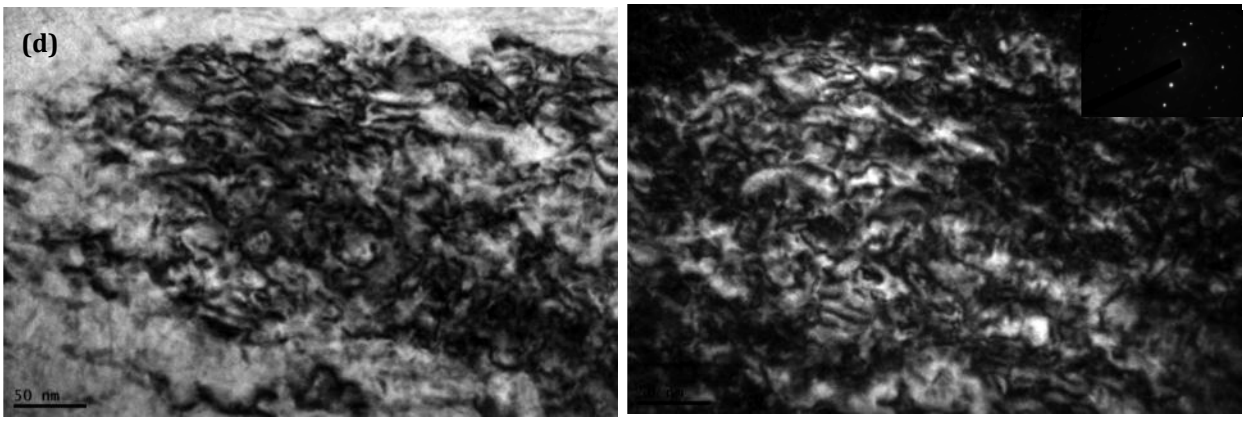

Figure VI.11 (cont.) TEM micrographs of CeO_2 irradiated with 500 keV Xe at room temperature to different doses: (a) $1x10^{13}$ ions/cm^2; (b) $1x10^{14}$ ions/cm^2; (c) $1x10^{15}$ ions/cm^2; (d) $5x10^{15}$ ions/cm^2. The left column shows bright-field images, and the right column shows dark-field images. The inset in each DF image shows the diffraction condition when the image was taken. All images are taken near [001] zone axis along g=<220>.

Atomic-scale STEM images taken on the specimens irradiated with 1 MeV Kr ions to the doses of $1x10^{13}$ ions/cm^2, $1x10^{15}$ ions/cm^2 and $5x10^{15}$ ions/cm^2 are displayed in figure VI.12 (a), (b) and (c) respectively. All of the images were taken from the [001] zone axis. The white dots arranged in square lattice are cerium atoms. In these dark-field Z-contrast images, heavier atoms show brighter contrast. Therefore, oxygen atoms are not visible here.

In figure VI.12 (a), the lattice shows almost even contrast across the whole area, comparing to the fluctuating contrast in figure VI.12 (c). The < 2 nm diameter areas that show darker contrast in figure VI.12 (b) and (c) are considered as damaged areas, since the darker contrast indicates missing layers of atoms in the areas or substitution with lighter elements in the specific location. During bombardment of high-energy ions, some lattice atoms were knocked out from their original sites, and they might have been replaced by implanted gas ions. Both of these processes could result in the darker contrast. These detailed structures might not be seen with

conventional TEMs, as their size might fall below the resolution limit of the instruments.

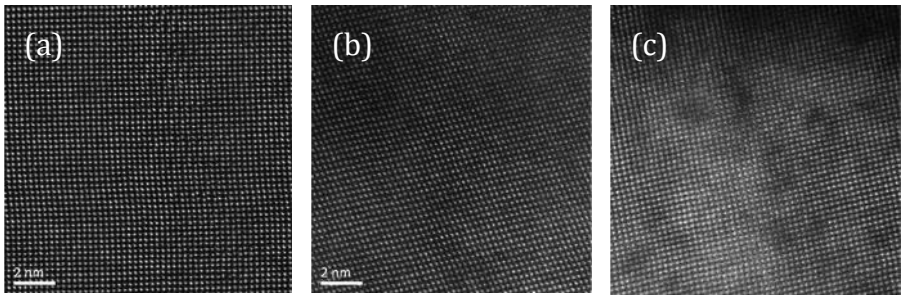

Figure VI.12 STEM images of single crystal CeO_2 irradiated with 500 keV Xe ions at room temperature to different doses: (a) $1x10^{13}$ ions/cm^2; (b) $1x10^{15}$ ions/cm^2; (c) $5x10^{15}$ ions/cm^2. All images are in the same magnification and taken with JEOL 2200FS.

Similar TEM investigation was carried out on the specimens irradiated with 150 keV Xe ions at room temperature. Three dose levels were selected: $5x10^{13}$ ions/cm^2 (figure VI.13 (a)), $5x10^{14}$ ions/cm^2 (figure VI.13 (b)) and $2x10^{15}$ ions/cm^2 (figure VI.13 (c)). Atomic-scale STEM images of radiated specimens are shown in figure VI.14.

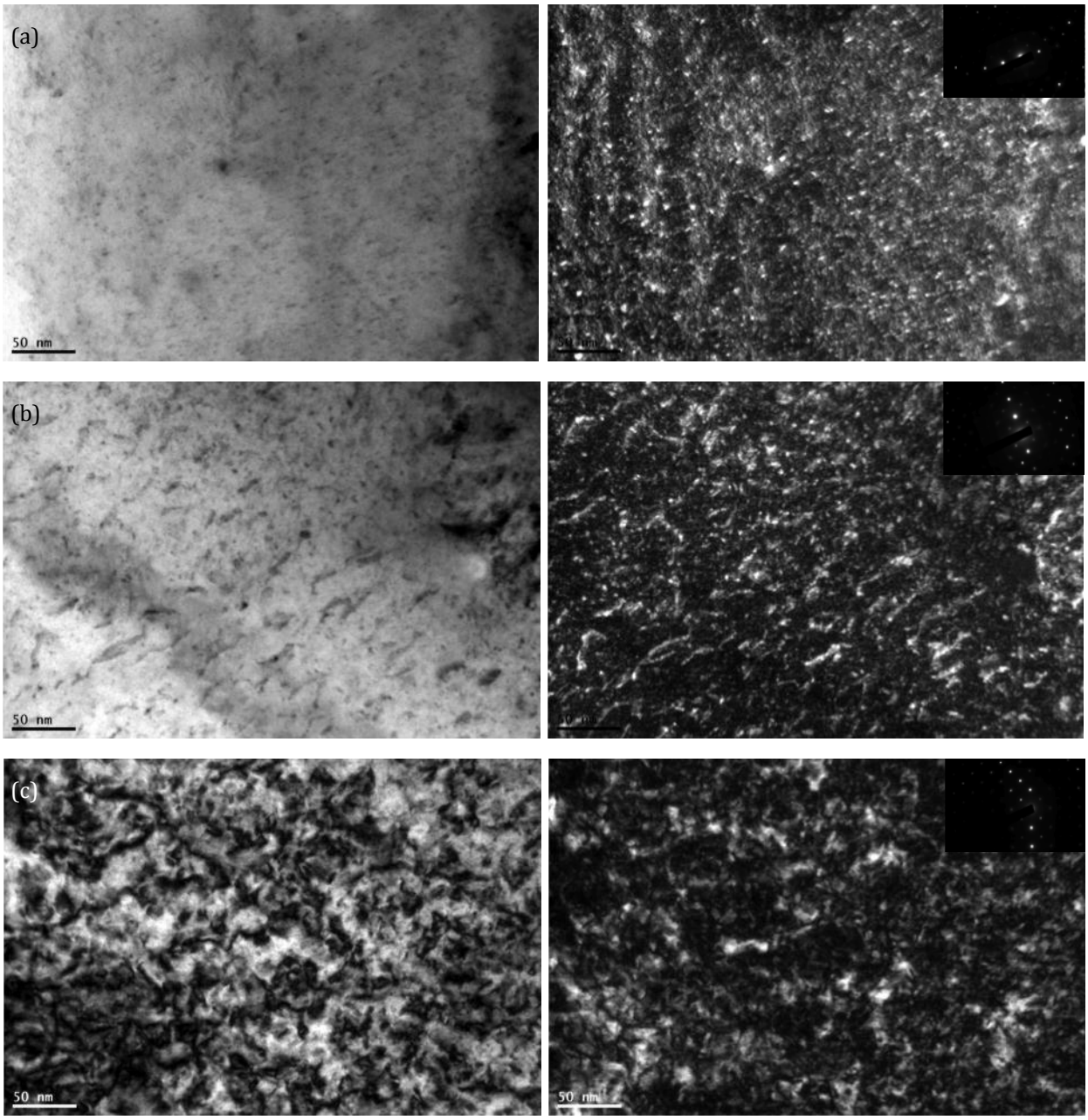

Figure VI.13 TEM micrographs of CeO_2 irradiated with 150 keV Xe at room temperature to different doses: (a) $5x10^{13}$ ions/cm^2; (b) $5x10^{14}$ ions/cm^2; (c) $2x10^{15}$ ions/cm^2. The left column shows bright-field images, and the right column shows dark-field images. All images are taken near [001] zone axis along g=<220>.

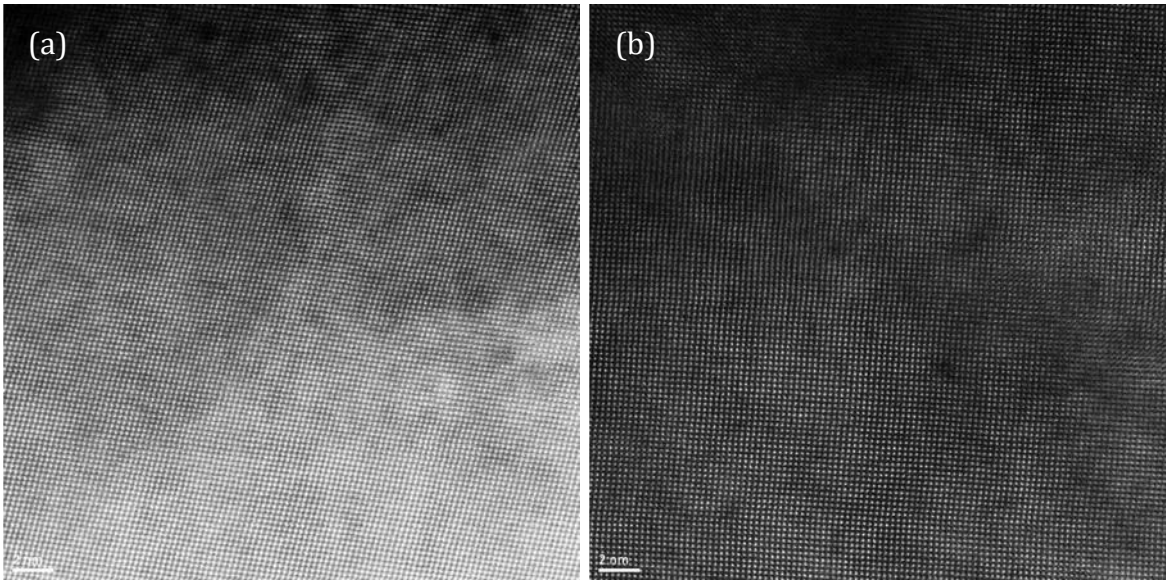

Figure VI. 14 STEM images of single crystal CeO_2 irradiated with 150 keV Xe ion at room temperature to different doses: (a) $5x10^{13}$ ions/cm^2; (b) $2x10^{15}$ ions/cm^2. All images are in the same magnification and taken with JEOL 2200FS.

VI.3 Comparison of in-situ irradiation of 1 MeV Kr ions at 600°C and 800°C

(This part of results has been published [80])

Two series of bright-field TEM micrographs taken on single crystal CeO_2 during *in-situ* irradiations of 1 MeV Kr at 600°C and 800°C are presented in figure VI.15 (a1) – (a7) and (b1) – (b7) respectively. Figure VI.15 shows the sequential change of microstructure of the same areas as a function of dose: from the condition before irradiation to an accumulated dose of $5x10^{15}$ ions/cm^2. The microstructures acquired at different irradiation temperatures with the same ion irradiation dose are displayed side by side.

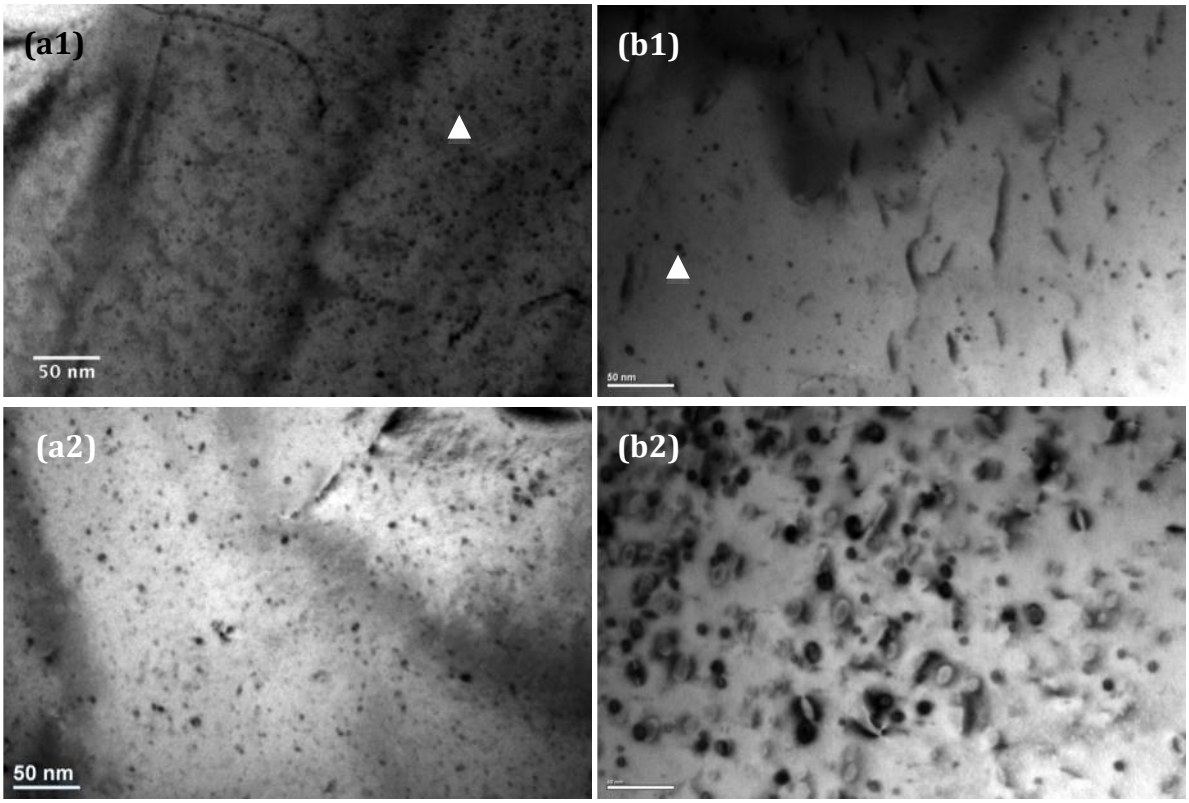

Figure VI.15. Sequential change in the nucleation and growth of defect clusters in singe crystal CeO_2 irradiated with 1 MeV Kr at 600°C (left column) and 800°C (right column) at various dose levels: (a1) and (b1) before irradiation, (a2) and (b2)

$3x10^{14}$ ions/cm^2. The observations were carried out from the [001] direction with g = 220 reflection.

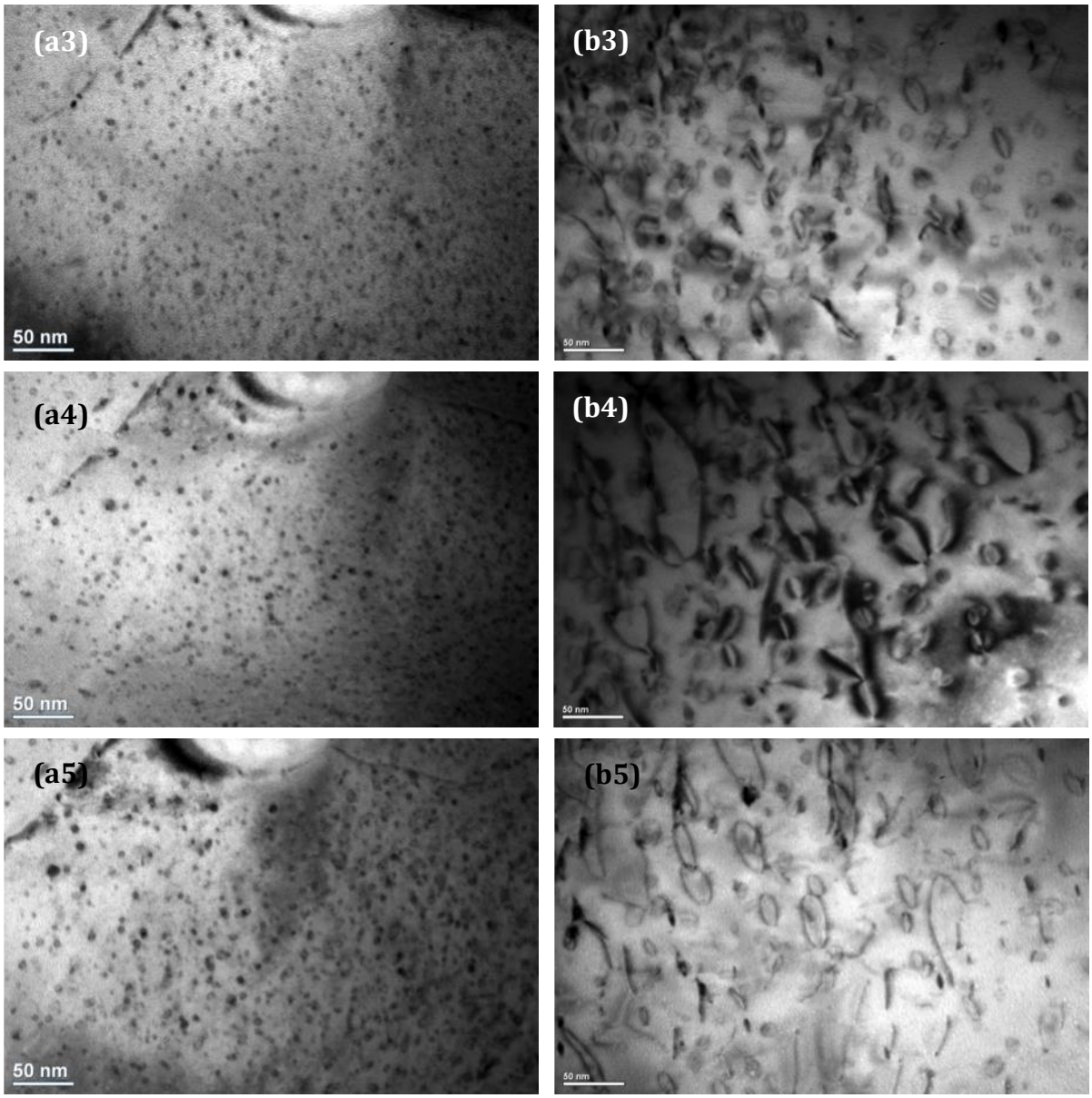

Figure VI.15 (cont.) Sequential change in the nucleation and growth of defect clusters in singe crystal CeO_2 irradiated with 1 MeV Kr at 600°C (left column) and 800°C (right column) at various dose levels: (a3) and (b3) $5x10^{14}$ ions/cm^2, (a4) and (b4) $8x10^{14}$ ions/cm^2, (a5) and (b5) $1x10^{15}$ ions/cm^2. The observations were carried out from the [001] direction with g = 220 reflection.

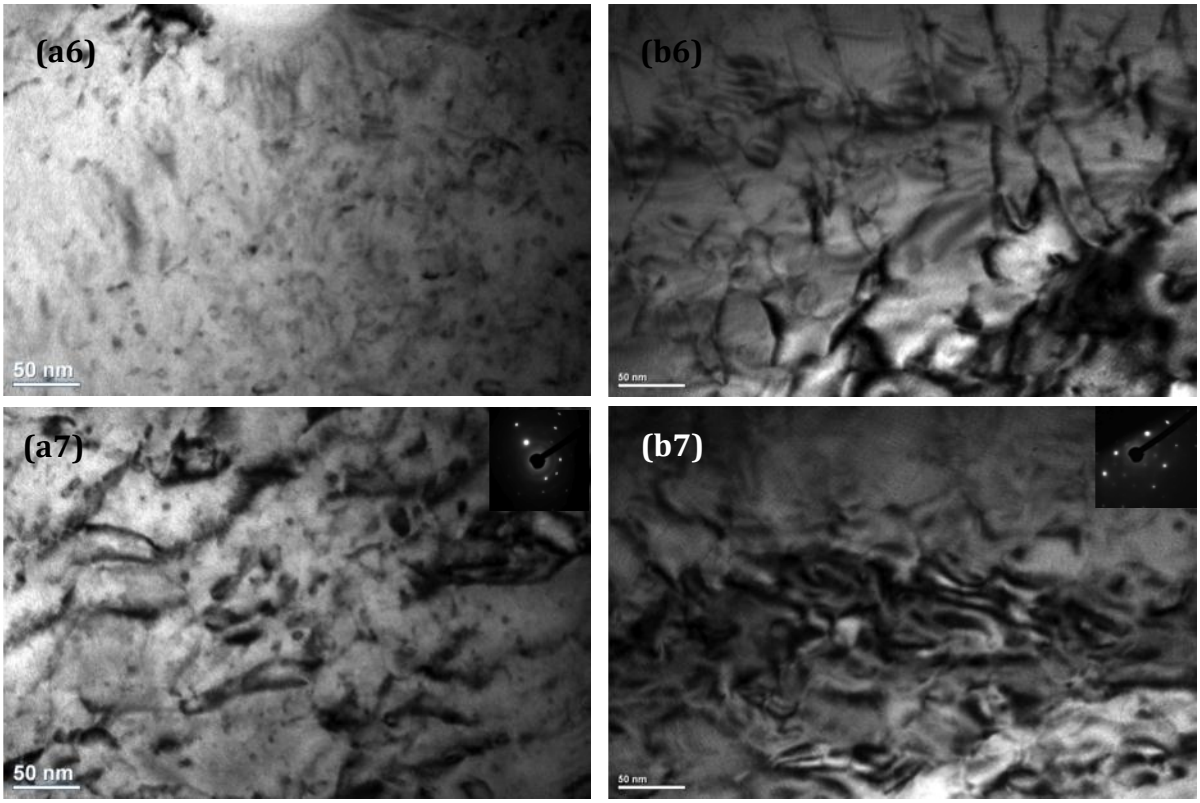

Figure VI.15 (cont.) Sequential change in the nucleation and growth of defect clusters in singe crystal CeO_2 irradiated with 1 MeV Kr at 600°C (left column) and 800°C (right column) at various dose levels: (a6) and (b6) $3x10^{15}$ ions/cm^2, and (a7) and (b7) $5x10^{15}$ ions/cm^2. The observations were carried out from the [001] direction with g = 220 reflection.

Figure VI.15 (a1) and (b1) show the as-annealed specimens at 600°C and 800°C respectively. A high density of black dots, indicated by arrows, is exhibited on both micrographs. These features were identified as dislocation loops induced during the Ar ion-milling process, and had the same appearance as the loops produced by Kr ion irradiation. Such polishing damage might be removed by annealing at a high temperature (~ 1400°C) [17, 83]. This step will be included in the future specimen preparation procedure. The density of black dots in figure VI.15 (a1) appears higher than in (b1), which is due to the different thicknesses of the observed areas.

As displayed in figure VI.15 (a2) – (a5) and (b2) – (b5), when the ion dose increases from $3x10^{14}$ ions/cm^2 to $1x10^{15}$ ions/cm^2, the average size of dislocation loops grows continuously: from 4.4 nm to 6.4 nm in diameter at 600°C, and from 10 nm to 25.6 nm in diameter at 800°C.

Figure VI.16 (a) depicts the comparison of average loop diameter during this irradiation process at 600°C and 800°C. It is clearly seen that the loop size grows slightly at 600°C, which is in contrast to the fast growth behavior at 800°C. In addition, the average loop diameter at 600°C at the same dose level is much smaller than the one at 800°C. For example, the loop size difference is ~ 5 times at $1x10^{15}$ ions/cm^2.

Unlike the constantly increasing behavior of the loop size, the density of dislocation loops was found to increase at the beginning up to $8x10^{14}$ ions/cm^2 at 600°C, as shown in figure VI.16 (b), and then decrease at higher ion doses. The peak dose can be considered to correspond to the irradiation damage limit to sustain the maximum amount of individual loops. Before this dose, most of the radiation damage events contribute to the nucleation process of dislocation and dislocation loops. The formation and growth of dislocation loops at this stage is attributed to the accumulation of point defects. Beyond the peak dose, dislocation loops grow rapidly through coalescence/coarsening mechanisms. As displayed in figure VI.16 (b), the process of nucleation completed in an earlier stage at 800°C, since the peak of density profile could have appeared before $3x10^{14}$ ions/cm^2.

In order to understand the nature of the dislocation loops, Burgers vector determination was applied. However, the obtained information was not enough to specify the Burgers vectors: <001>, <110>, or <111>. This is due to the limited tilting range (±40° in both of axes) around the single crystal orientation of [001]. In spite of the ambiguity, the analysis results helped to exclude the possibility of b = <110>. Helpful information was obtained from the past studies. Analogous dislocation loops were observed with TEM on ion-irradiated UO_2 [19, 83, 88], and

their nature was characterized as interstitial type. Moreover, during 1000 keV electron irradiation in CeO_2 [41], defect clusters appeared as circular contrasts on bright-field TEM images. The $g \bullet b$ and trace analyses suggested the defect clusters were interstitial-type dislocation loops lying on {111} planes with Burgers vector of <111> direction.

The expanding of loop size leads to interaction of dislocation loops at higher doses, which started from the dose of $3x10^{15}$ ions/cm^2 (figure VI.15 (a6)) at 600°C and $8x10^{14}$ ions/cm^2 (figure VI.15 (b4)) at 800°C. The dislocation loops then developed into line structure as shown in figure VI.15 (b6), and slowly aggregated to form dislocation networks by climb motion [85] (figure VI.15 (b7)).

At 600°C, the transition from individual loops to dislocation networks occurred in a much later stage. At the final dose of $5x10^{15}$ ions/cm^2 (figure VI.15 (a7)), in addition to the similar dislocation line structure, small individual dislocation loops could still be distinguished.

There were no remarkable changes of defect microstructure observed in the investigated dose range once the tangled dislocation networks formed. Moreover, such inhomogeneous accumulations of dislocations are believed to serve as nuclei for recrystallization in high burnup nuclear fuel [89-91].

The diffraction patterns taken after irradiation at both 600°C and 800°C indicate the specimens remain perfectly crystalline (shown in the inset of figure VI.15 (a7) and (b7)). Hence, at the highest dose investigated, no amorphization or recrystallization of CeO_2 occurred.

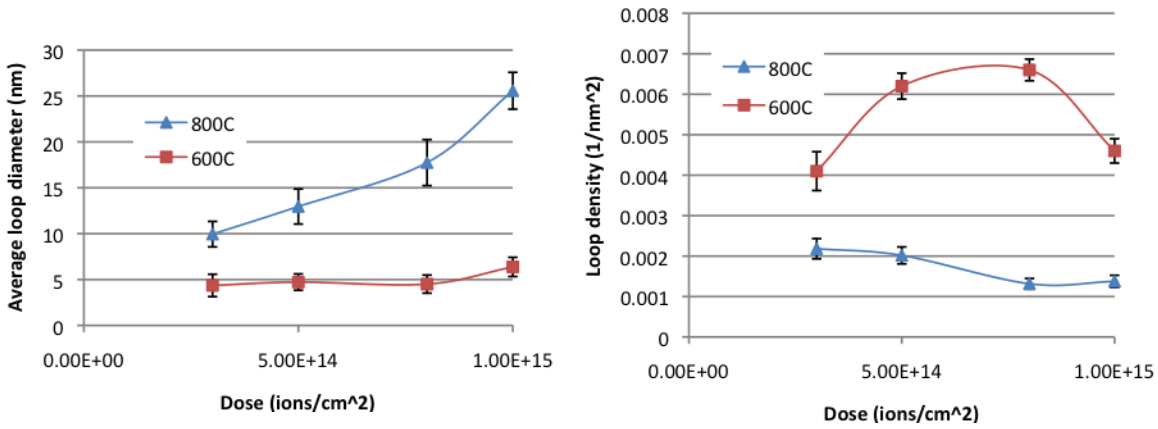

(a) (b)

Figure VI.16. Variation of (a) the average diameter and (b) the density of dislocation loops as a function of ion dose during the irradiation of 1 MeV Kr ions at 600°C and 800°C.

The substantial differences in damage ingrowth at irradiation temperatures of 600°C and 800°C were observed during irradiation of 1 MeV Kr ions, as presented in figure VI.15 and VI.16: much faster growth rate of defect structure at the higher temperature, and slight different defect morphology at the high doses. These facts may result from a combined effect of different temperature dependence of the accumulation rate of radiation damage and the mobility of defects (vacancies, interstitials and fission gas atoms) [47].

The temperature dependence of the kinetics of defect transformation in UO_2 has been investigated through thermal recovery of defects in irradiated UO_2 [17, 92]. U-vacancy mobility was accounted for the recovery stage centred around 870 K, and the migration of U-self-interstitials occurred in the temperature range 77 - 293 K in the UO_2 irradiated with $1x10^{15}$ Xe ions/cm^2 at 5 K at 100 keV energy.

Given the similarity in crystal properties, it is reasonable to deduce that the accelerated evolution process of defect structures at 800°C might be closely related to thermally activated Ce-vacancy mobility. At lower temperatures, Ce-interstitial

mobility enables short-range migration of atoms [17] and is the governing factor in dislocation growth.

A chemical rate theory developed by Maehara [93] also correlated the growth behavior of interstitial-type dislocation loops with the mobility of vacancies [41]. At low temperatures where the vacancies are immobile, most of the interstitials recombine with the vacancies. At elevated temperatures, dislocation loops can grow quickly since migration efficiencies of interstitials and vacancies balance with each other at this condition.

Comprehensive TEM observations were performed to characterize the evolution of defect structures in single crystal CeO_2 induced by Kr ion irradiation. The results are summarized as follows:

1. Evolution of microstructure in CeO_2 was observed during *in-situ* irradiation of 1 MeV Kr ions at 600°C and 800°C. Sequential TEM micrographs (figure VI.15) clearly illustrate the evolution process: the defects start to form clusters and loops at low dose, develop into extended dislocation lines and finally segregate together to form extremely tangled dislocation networks.

2. The comparison of growth behavior of defect structures at 600°C and 800°C reveals the thermal activated Ce-vacancy mobility plays an important role in dislocation loop development.

VI.4 Gas Bubble Formation During 150 keV Kr Irradiation

(This part of results has been published [80, 81])

In order to investigate the precipitation of gas atoms in CeO_2 crystal, 150 keV Kr ions were implanted into single crystal CeO_2 TEM thin foils. At this low energy, most of gas atoms were stopped inside the specimens according to the SRIM [94] calculation, shown in table V.1.

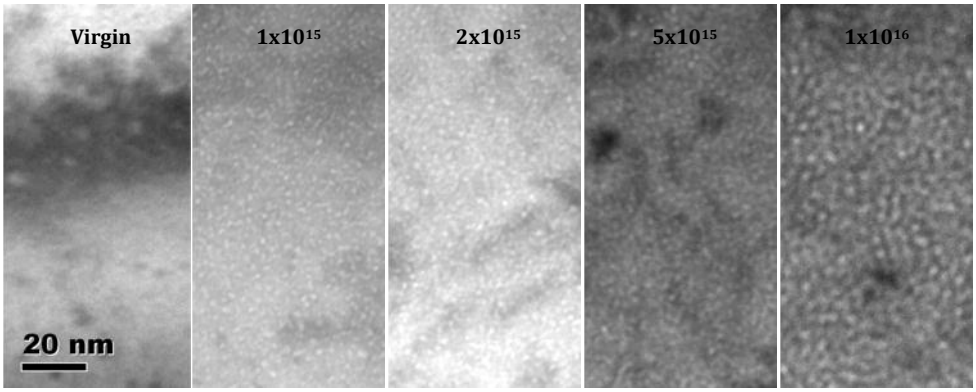

Figure VI.17. Bright-field images show sequential change of Kr bubbles with the increase of dose (ions/cm^2) at 600°C. These micrographs are taken by underfocusing the objective lens.

Figure VI.17 shows the sequential change of Kr bubbles during implantation of 150 keV Kr ions at 600°C. In these micrographs, Kr bubbles show as white dots with black edges (taken by underfocusing the objective lens). The size and density of Kr bubbles grow with the increase of dose. For the specimen irradiated to a dose of $1x10^{16}$ ions/cm^2, the bubble density reaches 0.15 nm^{-2}, and the average bubble diameter is 1.2 nm. Similar features are observed on UO_2 irradiated with 200 keV Kr at 600°C [13].

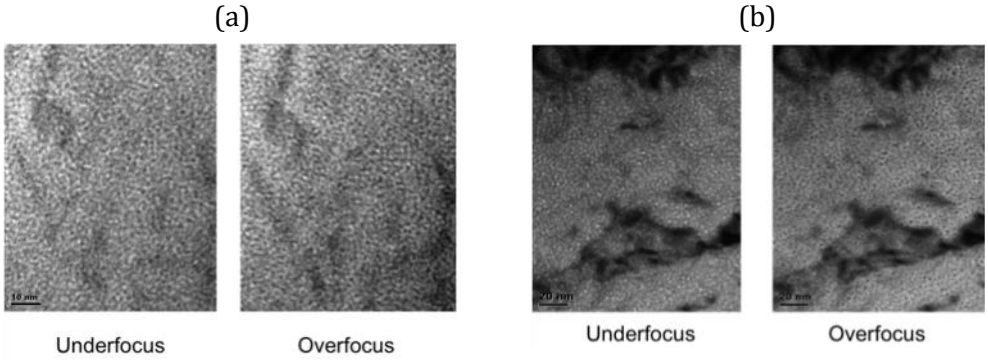

Figure VI.18 Bright-field TEM micrographs of single crystal CeO_2 implanted with 150 keV Kr ions at a dose of $1x10^{16}$ ions/cm^2 at (a) room temperature and (b) 600°C.

Figure VI.18 shows the bright-field TEM micrographs of *in-situ* irradiated CeO_2 with Kr at 150 keV ion energy to a dose of $1x10^{16}$ ions/cm^2. The peak Kr concentration is estimated to be 4.9% at this dose. Irradiation results at room temperature (figure VI.18 (a)) and 600°C (figure VI.18 (b)) are compared here. Typically, gas bubble features display opposite contrast at underfocus and overfocus conditions, as seen in figure VI.18 (b). However, such features were not found in figure VI.18 (a). In other words, gas bubbles did not form at room temperature. This fact might lead to the conclusion that a threshold temperature exist between room temperature and 600°C for Kr precipitation in CeO_2 which is correlated with metal-vacancy mobility [13]. Another explanation of this phenomenon can be tied to the gas solubility limit dependent on temperature. The gas in solution needs to reach a critical value before a multi-atom nucleation process can occur. At higher temperatures, this dynamic solubility limit is reduced so that the nucleation occurs at a lower dose [102].

This result is confirmed by previous studies of gas atom precipitation conditions. Evans [13] reported that no visible bubbles were found below 400°C in irradiation of 200 keV Kr in UO_2 for the dose of $5x10^{15}$ ions/cm^2. More recently, Sabathier [83] found Xe bubbles in UO_2 at $1x10^{16}$ ions/cm^2 after annealing to 670 K.

For the quantitative characterization, gas bubbles in figure VI.18 (b) were measured as ~1.2 nm in average diameter and 1.5×10^{17} m^{-2} for area density. These values are in good agreement with previously reported values [13, 83, 86]. Kashibe [86] observed the bubble size and density in low burnup spent fuel (23 MWd/kg) were 2 nm and 10^{24} m^{-3}, which are comparable with present ion irradiation results. In addition, Xe bubbles which were 1.8±0.3 nm in size with a density of $(4\pm2) \times 10^{23}$ m^{-3} were found by Sabathier [83].

VI.5 Defect Structure Evolution During 700 keV Xe Irradiation at 600°C

(this part of results has been published [82])

700 keV Xe ion beams were obtained at the University of Illinois with a Van de Graaff accelerator. Ion beams hit the CeO_2 crystals along [45] orientation. Irradiations were performed at room temperature and 600°C. Three dose levels were achieved: $2x10^{16}$, $5x10^{16}$ and $1x10^{17}$ ions/cm^2, which result in peak dpa values of 106.3, 265.7 and 531.4 respectively, calculated with SRIM 2008 [94]. Following irradiation, TEM specimens were prepared by mechanically polishing followed by 3 – 5 kV Ar ion milling. TEM observation of irradiation damage was preformed with JEOL 2010LaB_6 and JEOL 2200FS electron microscopes. The *in-situ* annealing experiment was conducted in the IVEM-Tandem facility at Argonne National Laboratory.

In the first series of experiments, the microstructures of irradiated CeO_2 single crystals as a function of various dose levels are compared. As shown in figure VI.19, pure CeO_2 was irradiated with 700 keV Xe at 600°C to varied dose levels. The thicknesses of thin films reduced during irradiation due to the sputtering effect. At the highest dose level, $1x10^{17}$ ions/cm^2, the film thickness decreased ~15 nm. The inset diffraction patterns demonstrate that the specimens remain crystalline at 600°C even at a dose as high as $1x10^{17}$ ions/cm^2, which confirms the high irradiation tolerance in fluorite-structure materials. Under similar irradiation conditions, Matzke [11] reported a fully developed polygonization process in UO_2 bombarded with 300 keV Xe at 500°C in the range of 5 – $7x10^{16}$ ions/cm^2 with the Rutherford backstattering (RBS) technique. In contrast to the results presented by Matzke [11], possible polygonization processes were not found in current TEM observations.

Solid precipitates, which appear as black/black lobes, are visible in all three micrographs. Their average diameter grows from ~ 1.9 nm in figure VI.19 (a) to ~ 4.2 nm in figure VI.19 (c). These features were initially thought to be gas bubbles with a very high pressure or containing solid Xe precipitates. In a previous study, Nogita and Une [84] found solid Xe aggregated in spent fuel pellet with 45-83 Gwd/t. They observed Moiré fringes within the bubble area and extra spots in diffraction patterns, which indicates the existence of other solid particles in addition to the matrix UO_2.

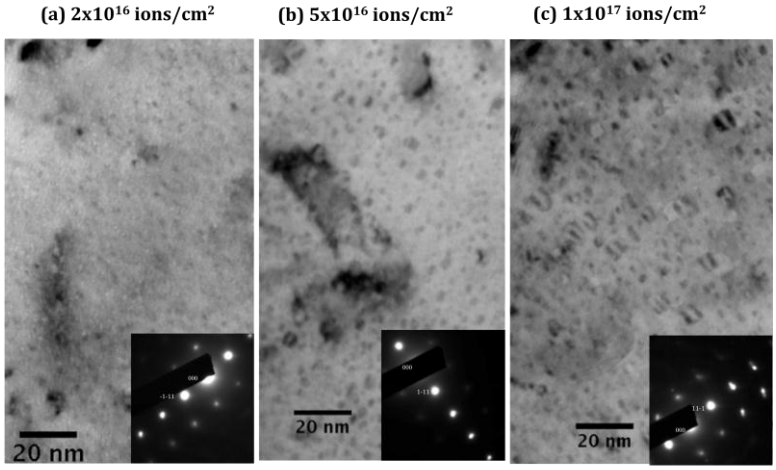

Figure VI.19 Cross-section bright-field TEM micrographs of pure CeO_2 single crystals irradiated with 700 keV Xe at 600°C. (a), (b) and (c) show the specimen irradiated to a dose of $2x10^{16}$, $5x10^{16}$ and $1x10^{17}$ ions/cm^2 respectively. All images are taken with g = <1-11>. The electron beam is along the <011> orientation.

However, there was no solid evidence obtained in this study that would lead to the same conclusion. Careful scanning TEM (STEM) analysis with JEOL 2200FS was performed. A dark-field Z-contrast STEM image of a precipitate area and its vicinity is displayed in figure VI.20 (a), along with its corresponding nano-beam diffraction pattern in figure VI.20 (b). In the faceted damaged area shown in figure VI.20 (a), the atomic lattices are slightly distorted, and the darker contrast suggests the absence of atomic layers or aggregation of a lower Z element. If the precipitates were highly condensed gas atoms, this area should be enriched with Xe.

Nevertheless, there are no extra spots shown in figure VI.20 (b) and no Xe peaks detected with nano-area energy dispersive X-ray spectroscopy (EDX). These phenomena suggest another explanation for the nature of the precipitates as metallic Ce. The formation of Ce precipitates might be due to the active redox process in CeO_2 at elevated temperatures and low oxygen pressures [72]. This is also supported by a subsequent annealing experiment. In this experiment, the specimen irradiated to $1x10^{17}$ ions/cm^2 was placed in a TEM and heated with a heating stage so that the changes in microstructure could be monitored during annealing. The fringes in precipitated area disappeared at 600°C, close to the melting point (795°C) of metallic Ce, and reappeared after cooling back to room temperature. Although the irradiation was done at 600°C, the microstructure of the specimen might change after taking it out from the accelerator and cooling down to the room temperature. The *in situ* annealing results shown in figure VI.21 demonstrate this possible change: the precipitates were in solid state at room temperature while became partial solid at 600°C. Further investigation into the nature of the precipitates will be carried out with X-ray techniques.

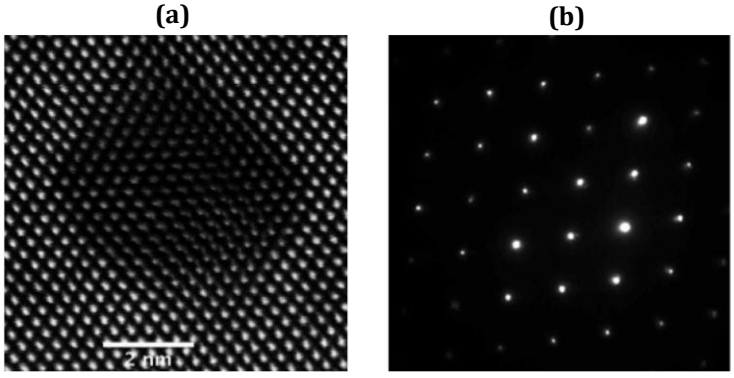

Figure VI.20 (a) Dark-field STEM micrograph of pure CeO_2 irradiated at 600°C to a dose of $1x10^{17}$ ions/cm^2. (b) Nano-beam diffraction pattern from the corresponding area.

The presence of the lanthanum dopant induces oxygen vacancy defects due to its alternate bonding nature. Given the chemistry of ceria doped with tri-valent dopants, the vacancies induced by La doping can help study the non-stoichiometric

effects in ceria to the hypo-stoichiometric end, which resembles (U, Pu)O_2 fuel. In addition, as one of the possible fission fragments, La can also help reveal the effect of fission fragments inside nuclear fuel material systems [103].

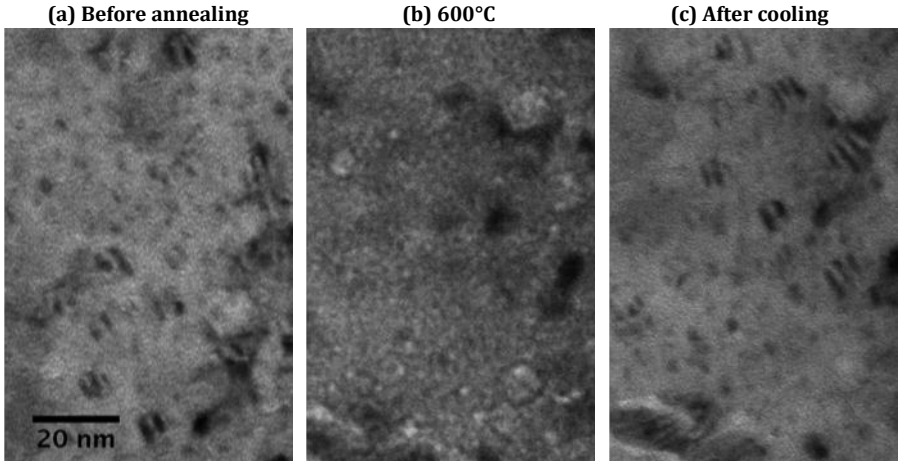

Figure VI.21 Sequential bright-field TEM micrographs during in-situ annealing of pure CeO_2 irradiated at 600°C to a dose of $1x10^{17}$ ions/cm^2. (a) microstructure of the specimen before annealing; (b) microstructure of the specimen heated at 600°C; (c) microstructure of the specimen after cooling back to room temperature.

Figure VI.22 displays the through focus bright-field TEM micrographs taken on CeO_2 doped with 5% La at 600°C to a dose of $1x10^{17}$ ions/cm^2. Fresnel fringes on the edges of gas bubbles change from white to black with the objective lens adjusted from underfocus to overfocus conditions. On the infocus image, solid precipitates appear as round shaped features with fringes, which have a similar size and density as the ones shown in Figure VI.19 (c). However, such features were absent up to doses of $4x10^{16}$ ions/cm^2, and were completely developed in the range of 4 - $10x10^{16}$ ions/cm^2 for 600°C irradiation experiments. This delayed formation of precipitates compared to pure CeO_2 might be attributed to lower xenon mobility and higher oxygen vacancy mobility in the doped materials [104]. Parallel experiments will be performed on CeO_2 doped with 25% La, which should provide more information to help understand the La dopant effect.

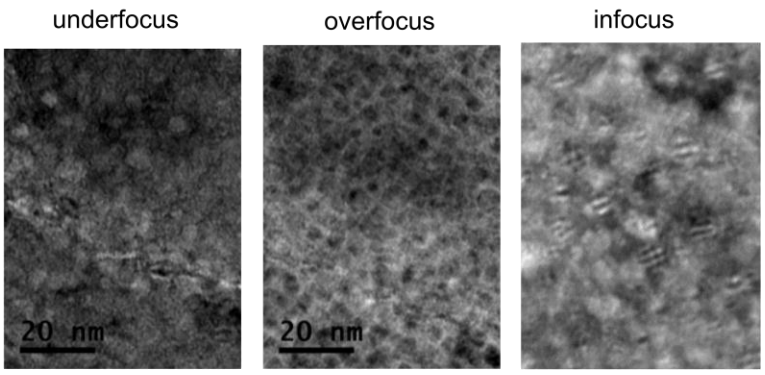

Figure VI.22 Plan view bright-field TEM micrographs on CeO_2 doped with 5% La at 600°C to a dose of $1x10^{17}$ ions/cm^2. Electron beam is along <001> orientation. All of the images were taken with the same magnification.

In irradiation experiments to very high doses, e.g. $1x10^{17}$ ions/cm^2 at room temperature, there are no precipitates found in any of the materials studied. Thus, the formation of such precipitates must be a thermally activated process. There should be a threshold temperature for precipitate formation, existing between room temperature and 600°C, which is due to the thermal activation of the oxygen vacancy mobility.

Xenon ion implantation in CeO_2 and Ce/LaO_2 using 700 keV Xe ions were employed in this study to simulate irradiation processes in oxide fuel. A parametric study investigating the effects of ion fluence, irradiation temperature and La dopant concentration provide useful information for understanding the formation and growth processes of defect structures. Post-irradiation analyses were performed using *ex-situ* and *in-situ* TEM. Several important observations were made:

1) The materials remain crystalline after achieving very high doses ($1x10^{17}$ ions/cm^2), which is due to the high irradiation tolerance of the fluorite crystal structure.
2) There was no evidence of grain subdivision or polygonization found. A possible explanation is that the thin film structure (~ 160 nm along ion beam direction),

surface sputtering, and radiation-enhanced gas diffusion help relieve internal stresses accumulated during irradiation.

3) Solid precipitates appear in pure CeO_2 at and above $2x10^{16}$ ions/cm^2, but are absent in CeO_2 doped with 5% La until the fluence exceeds $4x10^{16}$ ions/cm^2.
4) The nature of those precipitates is still being investigated using X-ray techniques. So far, the most probable interpretation is that Xe forms in the solid state in gas bubbles under very high internal pressure.
5) The formation of solid precipitates is a temperature dependent process. There is a threshold temperature existing between room temperature and 600°C.

VI.6 Atomic-scale STEM Defect Structure Visualization

In this section, STEM images taken on single crystal CeO_2 before and after irradiation are presented: as-prepared CeO_2 plan-view TEM specimen (figure VI.23) as a reference, the specimens irradiated with 150 keV Kr ions at room temperature to a dose of $1x10^{16}$ ions/cm^2 (figure VI.24), 150 keV Xe ions at room temperature to a dose of $2x10^{16}$ ions/cm^2 (figure VI.25), 150 keV Kr ions at 600°C to a dose of $1x10^{16}$ ions/cm^2 (figure VI.26) and 500 keV Xe at 600°C to a dose of $2x10^{16}$ ions/cm^2 (figure VI.27). Each specimen is displayed in two images with different magnification, in order to show the overall and detailed structures.

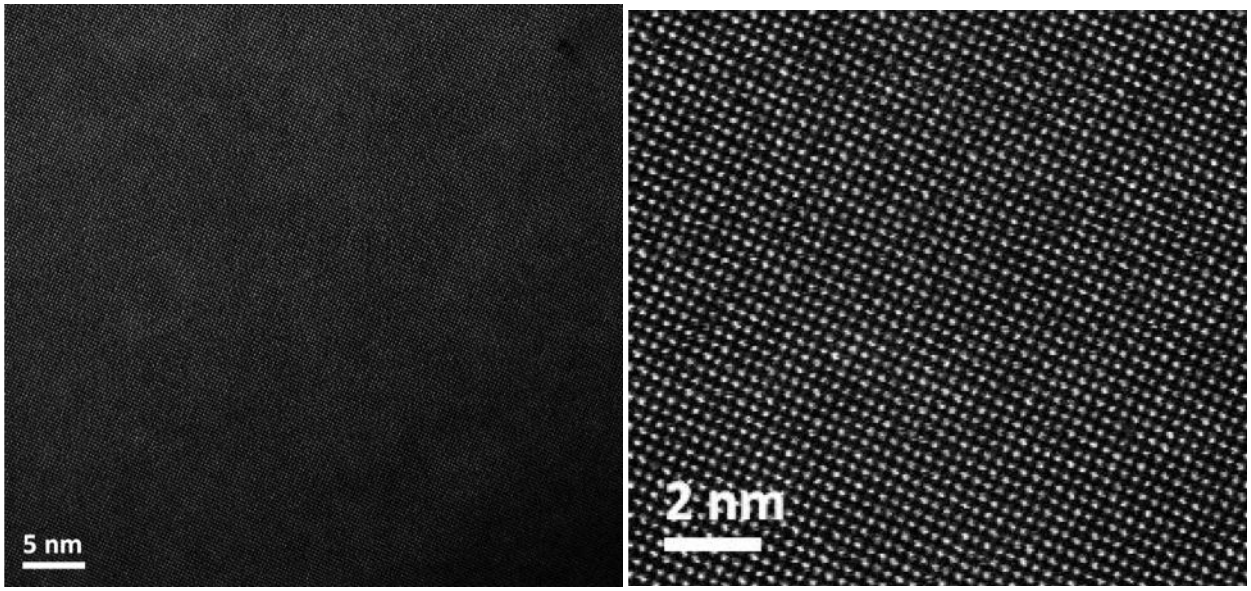

Figure VI.23 STEM images of CeO_2 before irradiation

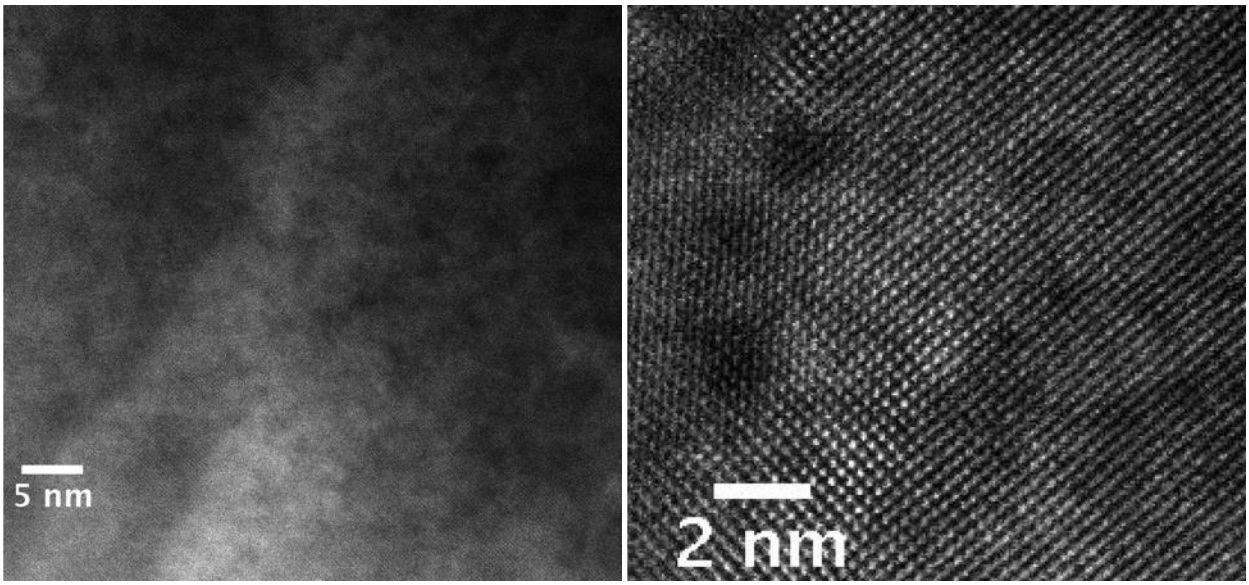

Figure VI.24 STEM images of CeO_2 irradiated with 150 keV Kr at room temperature to a dose of $1x10^{16}$ ions/cm^2.

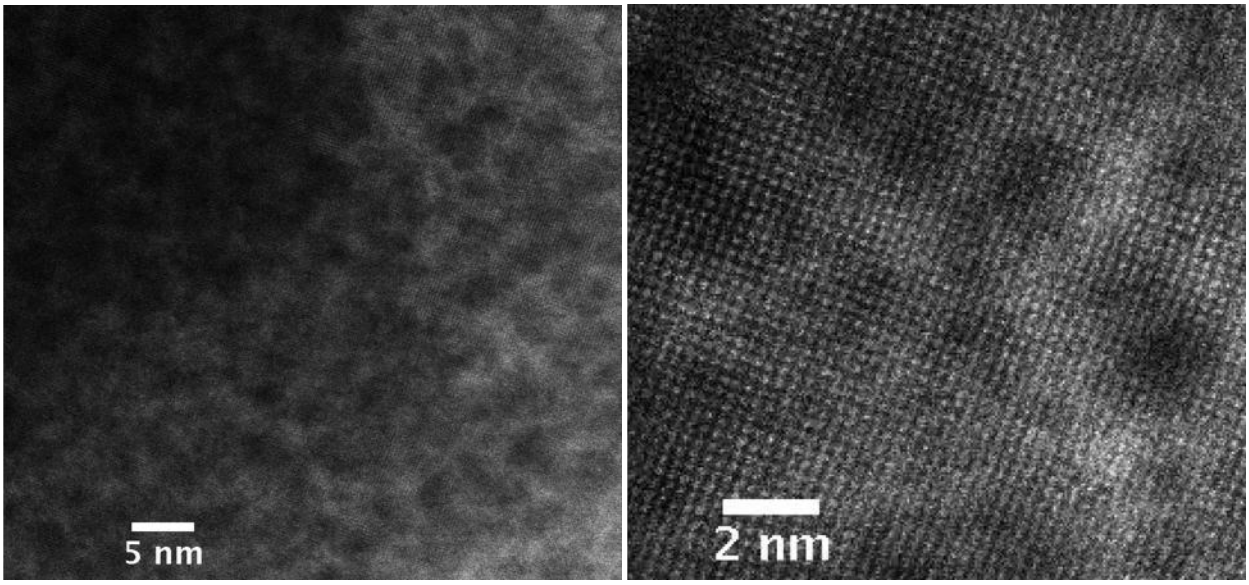

Figure VI.25 STEM images of CeO_2 irradiated with 150 keV Xe at room temperature to a dose of $2x10^{16}$ ions/cm^2.

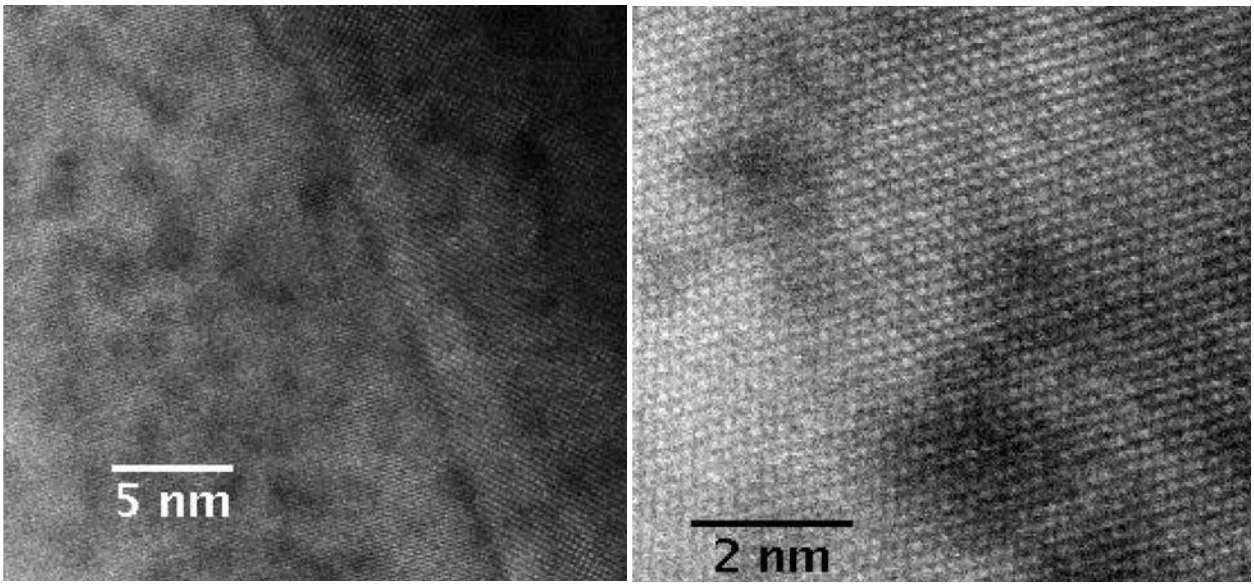

Figure VI.26 STEM images of CeO_2 irradiated with 150 keV Kr at 600°C to a dose of $1x10^{16}$ ions/cm^2.

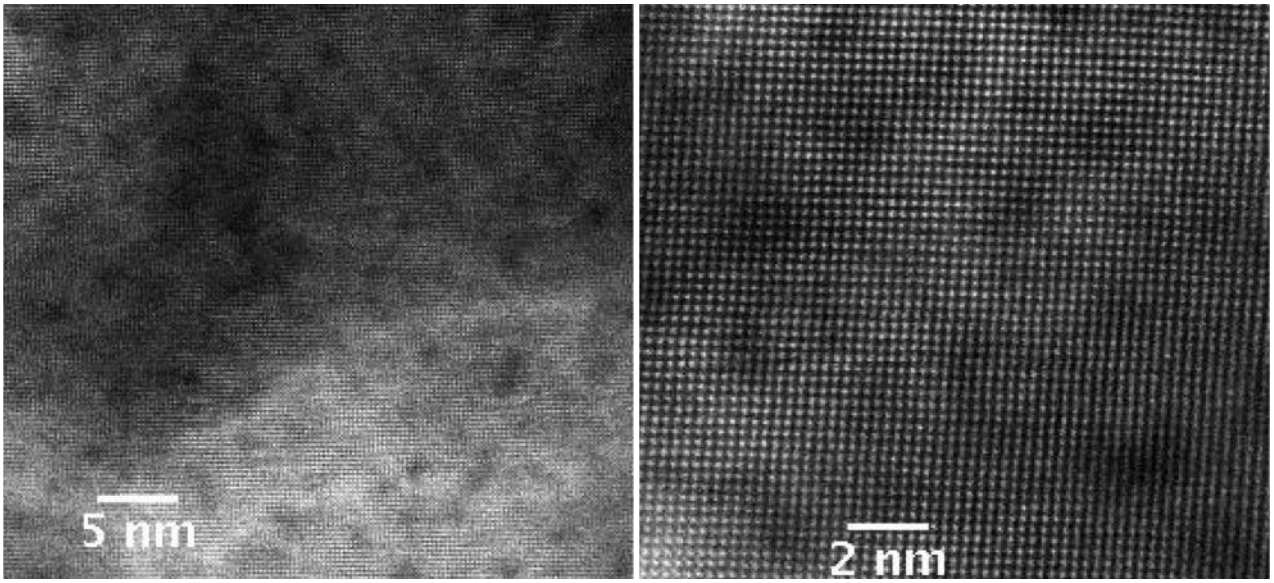

Figure VI.27 STEM images of CeO_2 irradiated with 500 keV Xe at 600°C to a dose of $2x10^{16}$ ions/cm^2.

All the TEM specimens are plan-view specimens, so all images were taken from [001] orientation. Ion irradiation was performed in the IVEM-Tandem facility at

ANL. JEOL 2200FS at the University of Illinois was used to take the micrographs shown in figure VI.23-27.

In all the images shown in figure VI.23-27, even in the specimen irradiated with 150 Xe ions to the dose of $2x10^{16}$ ions/cm^2 (figure VI.25), in which the peak dpa value is 96.54, cerium atoms are organized in a perfect square lattice. This confirms that the material remains crystalline even after high dose ion bombardment, which proves that CeO_2 has very high radiation resistance.

VII. Modeling Approach

Both computational modeling and experimental tests are essential in studying the irradiation effects and damage. Given the frequent difficulties in obtaining and interpreting experimental results, theoretical studies are indispensable complements for experimental work. At the same time, computer simulation provides an effective way to understand many phenomena in the evolution of the nuclear fuel at the atomic scale.

Although the main focus of this work is on the experimental investigation of irradiation-induced defects and fission gas behavior, using simulation methods to model the processes of defect migration and growth is also employed. Due to the inherent difficulties in interpreting the data sets measured in experiments, modeling is used to help reveal insights of the mechanisms of evolution processes of material structures.

Modeling of fuel behavior under irradiation has drawn considerable attention in recent years due to the above reasons. A number of calculations have been attempted on defect parameters of UO_2, see [95-100]. The calculated defect energies are mainly dependent on the interatomic potentials applied [105, 106]. The agreement between experimental results and calculated values on defect energies and their trends is satisfactory. The situation of quantification of defect energies is better for oxygen defects than that for metal defects. Gas mobility is also investigated by calculation [55, 107-109], which is helpful for understanding experimental data.

There are still many open questions about the mechanisms of dislocation structure formation and their configurations. For example, in an early study [110], large interstitial clusters and dislocation loops were observed in UO_2 irradiated with

1.8 MeV electrons at room temperature. Those features were attributed to the migration and dissociation of small uranium interstitial clusters and the release of interstitials from shallow traps. However, this explanation is contary to the argument raised by Yasunaga et al. [40, 41], who tied the formation of dislocation loops at similar irradiation condition to the oxygen interstitials. Therefore, looking into the detailed microstructure of dislocations in oxide fuels, which exceeds the limits of most of current experimental techniques, will rely on the application of modeling methods.

VII.1 Multiscale Modeling Methodology

The modeling approach taken in this area is combined multi-scale simulation. Radiation damage is an inherently multiscale phenomenon involving processes spanning a wide range of length and time-scales. Multi-scale simulation has been demonstrated to be an efficient approach to study evolution of microstructure in materials caused by radiation damage processes [111-114]. The modeling methodology integrates ab initio electronic structure calculations, molecular dynamics (MD) simulations, kinetic Monte Carlo (KMC), phase-field equations or rate theory simulations with thermodynamics and kinetics by passing information about the controlling physical mechanisms between modeling techniques over the relevant length and time scales [111, 112], as shown in figure VII.1. Such an approach is able to track the fate of point defects produced during irradiation and thereby predict microstructural evolution. Material property parameters, such as defect diffusion coefficients, lattice constants and tensile modulus can be predicted by MD or KMC. At a higher scale, rate theory simulations can benefit from the more accurately estimated parameters from MD or KMC calculations, such as defect migration energies. Finally, the integration of multi-scale simulation with experiments (ion-implantation/in-reactor irradiation) offers the possibility to fully predict and improve nuclear fuel performance in the complicated reactor environment.

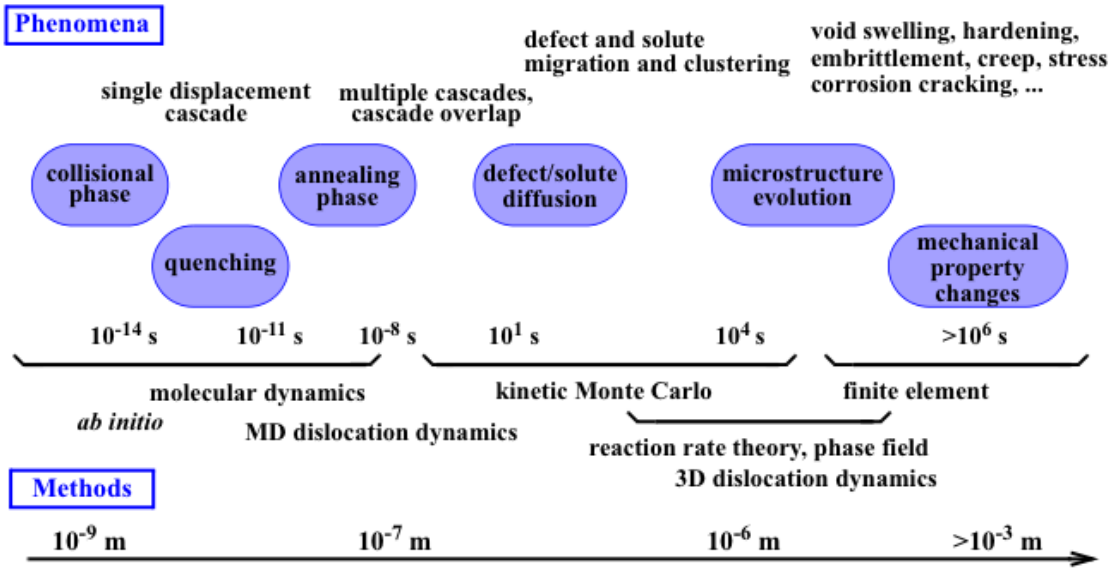

Figure VII.1 Schematic diagram: relevant phenomena and computational methods [115]

Ab initio calculation is a method of calculating atomic and molecular structure directly from the first principles of quantum mechanics, without using quantities derived from experiments as parameters. Basic defect properties (formation, binding and migration energies of point defects and small point defect clusters including the interaction with solutes) can be obtained from ab initio methods. The electronic structure calculations of interatomic forces, interactions and energetics provide key parameters for MD and KMC models. Particularly, ab inito methods are essential in the development and fitting of semiempirical, embedded atom method (EAM) interatomic potentials, which are the basis of MD calculations. Ab-initio calculations are computationally intensive, and the amount of computing time required increases rapidly as the size of the atom or molecule increases.

Molecular statics (MS)/molecular dynamics (MD) simulations provide information on the kinetics and energetics of point defects and small defect clusters. In the case of MS, the relaxed configuration of atoms is found using conjugate gradient or some

similar (constrained) minimization of the total energy. This provides information about crystal lattice structure in different phases and under different conditions. In the case of MD, the actual motion of the atoms is simulated by evolving the atomic configuration in time according to Newton's equation. This allows the direct study of the dynamical and thermodynamical evolution of the system.

The KMC simulations use the MS/MD results as input and provide a description of defect diffusion and interaction over longer time scale and length scale. Molecular dynamics can also give thermodynamic and kinetic properties, but is computational costly and only simulated over very small time scales. The advantages of the kinetic Monte Carlo calculations are that the atomic level vibrations of the atoms are ignored; the system only evolve on relatively "important" events that are organized in the event list. By doing this, kinetic Monte Carlo algorithm extends the limitations of time scale and length scale by orders of magnitude compared to the molecular dynamics algorithms which normally deals with a rather small system ($\sim$ 500 atoms) and short time scale (on the order of pico-seconds) [116, 117]. However, the simplification made by ignoring all atomic vibration states and other "unimportant" events might induce significant deviation from the original system, therefore extra caution must be taken in selecting which events to include in the simulation. Including smaller time scale events will make the simulation more realistic, but will reduce the time scale of evolution of the system.

Rate theory modeling is one of the mesoscale modeling methods used to simulate radiation effects. Mesoscale models are normally relevant to many phenomena in materials science and radiation effects, such as grain growth, void swelling, dislocation evolution caused by thermo-mechanical or radiation-induced processes. The length scale used in these models permits direct comparison with experiments such as TEM and mechanical property measurements. Their primary application is the investigation of point defect, and solute kinetics and microstructural evolution [115].

The starting point of rate theory modeling is a set of continuity equations describing point defect populations (vacancy, C_v and interstitial, C_i), for example:

$$\begin{aligned}\nabla \bullet (D_v \nabla C_v + \frac{D_v C_v}{kT} \nabla U_v) + G_v - \alpha C_i C_v - D_v C_v S_v^T = \frac{\partial C_v}{\partial t} \\ \nabla \bullet (D_i \nabla C_i + \frac{D_i C_i}{kT} \nabla U_i) + G_i - \alpha C_i C_v - D_i C_i S_i^T = \frac{\partial C_i}{\partial t}\end{aligned} \quad \text{(VII.1)}$$

where the ∇ denote spatial derivatives. The first terms on the left-hand-side of the equations describe point defect drift to discrete sinks; the U_v and U_i are interaction energies between the point defects and discrete sinks. The G_v and G_i are the total point defect generation rate, and the S_v and S_i are the total sink strengths for continuum sinks (e.g. cavities, dislocations, grain boundaries, etc.).

Some of the typical assumptions and simplifications applied in rate theory modeling are listed [115]:

- The material is treated as a spatially-homogeneous effective medium with embedded effectives sinks and sources for point defects.
- Spatially-averaged point defect generation rates are also generally employed.
- These assumptions have been relaxed in particular cases, e.g. to investigate cascade-induced fluctuations in point defect concentrations.
- The models are formulated as a series of differential equations describing the production and fate of point defects and fate of point defects and the corresponding evolution of microstructure.

From the above description, it is clear to see that rate theory modeling is a parameter-rich model which may limit the confident in model extrapolation. Hence, it is important to use ab initio and MS/MD methods to provide improved material parameters, such as diffusion and formation energies of point defects, as well as primary radiation damage parameters. In addition to the high parameter-dependence, there are other inherent limitations of this modeling method need to be kept in mind: real materials are not spatially homogeneous; observed diffusion behavior of defect structures are much more complex than simple 3D pattern (small

clusters are mobile too), which means reaction kinetics may be modified when diffusion mechanisms alternate.

Rate theory modeling has been used in radiation effects for long time. However kinetic Monte Carlo also find its increasing use in this area with the rapid development computational power. Both kinetic Monte Carlo and rate theory modeling can be used to simulate microstructure evolution, but some of the details are handled quite differently in the two approaches. Direct comparison between these two kinetic models is displayed in table VII.1.

Table VII.1 Inherent differences between rate theory and object kinetic Monte Carlo modeling [115]

Parameter or mechanism	Rate theory	Object kinetic Monte Carlo
solution method	deterministic	stochastic
time	explicit variable	inferred from processes and reaction rates
space	smeared, effective medium, possible multi-region RT	full spatial dependence
defect production	time and space-averaged, but c.f. Mansur's cascade diffusion model	discrete in time and space
sink strength, e.g. dislocations	explicit mathematical expression	inferred from fate of point defects
defect or sink density	essentially unlimited	limited (computationally) by simultion cell size, i.e. $N = 1/(x \cdot y \cdot z)$

VII.2 A Rate Theory Model of Nucleation and Growth of Interstitial Dislocation Loops

In this thesis, modeling effort focuses on using rate theory method to model the nucleation and growth of interstitial dislocation loops. Combining with other simulation methods, implemented by other members in this research group, a systematic multiscale simulation approach was formed, which covers a wide range of time and length scales. By integrating the theoretical modeling with experimental efforts, it becomes a powerful approach to obtain basic understanding of the nucleation and growth mechanism of defect structures in CeO_2. Figure VII.2 describes this combined approach in a form of a flow chart. The parts framed in golden lines are the main objects covered in this thesis.

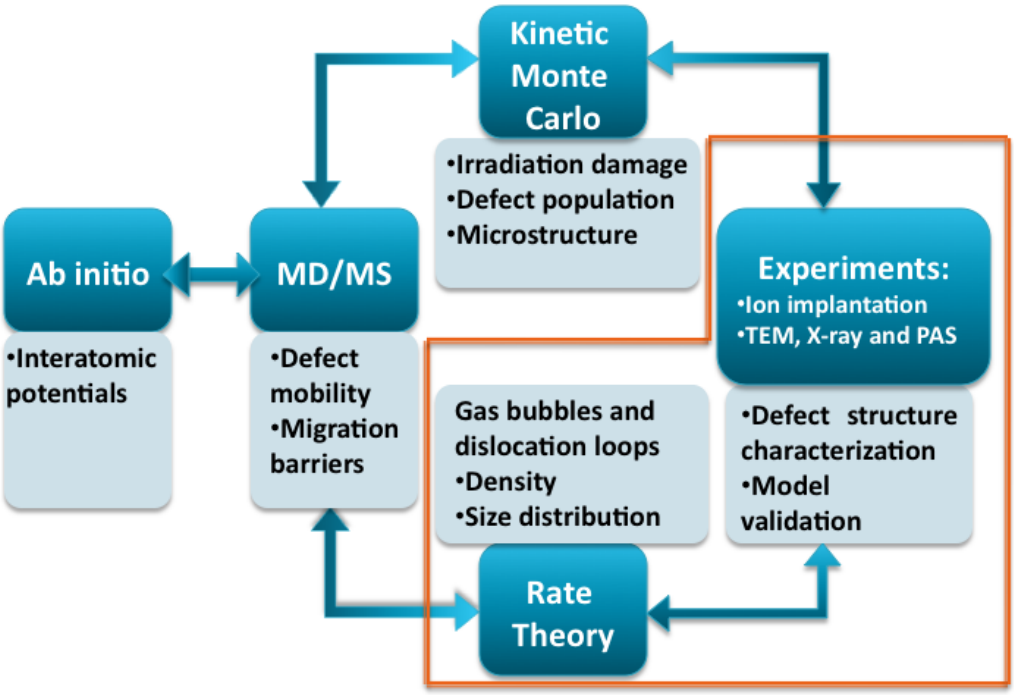

Figure VII.2 An integrated system of combining multiscale simulation and experimental approach to investigate evolution of defect structures in nuclear fuel material

This part of the study aims to gain insights into defect evolution process in CeO_2 during ion irradiation, especially the nucleation and growth of interstitial dislocation loops. Interstitial dislocation loops play an important role in the swelling of irradiated materials [118]. They are known to nucleate very rapidly giving rise to an essentially constant concentration which then acts as a preferential sink for interstitials [119]. Some recent irradiation studies on CeO_2 also suggest the dislocation structure observed with TEM is interstitial-type loops [40]. These facts make it critical to understand the basic growth mechanisms of interstitial dislocation loops.

A theoretical model proposed by Hayns [119] was chosen to describe the nucleation and growth of interstitial dislocation loops during in-situ irradiation in CeO_2. This model allows a detailed investigation of the nucleation and early growth stages of the development of the loop. In most rate theory models, dislocation loops are assumed to have a constant loop concentration, with the size distribution approximately represented by a single, average radius. Unlike this commonly used assumption, this model considers loop growth with a size distribution resulted from the homogeneous nucleation of precipitates, making it advantageous in investigating the loop nucleation process. Some important effects which have not been taken into account are surface effects, impurity trapping, and high-temperature thermal emission of vacancies. Surfaces especially can serve as sinks during in-situ irradiation on TEM thin foils. At high temperatures, this effect becomes more vigorous, which can contribute to the discrepancy between theoretical calculation and experimental observation.

A set of linear first-order differential equations which is integrated numerically is used to describe the model [120]. It is important to note that only the diffusion of cerium interstitials and vacancies is considered here, since they are the rate-controlling species in loop growth due to their low-mobility.

$$\frac{dc_v(t)}{dt} = K - \alpha_r c_v(t) c_i(t) - \sum_{n=2}^{n_{eq}} L_n c_{ni}(t) c_v(t) - Dv\rho_d c_v(t) \quad \text{(VII.2)}$$

$$\frac{dc_i(t)}{dt} = K - \alpha_r c_v(t) c_i(t) - \sum_{n=2}^{n_{eq}} R_n c_{ni}(t) c_i(t) + L_2 c_{2i}(t) c_v(t) \quad \text{(VII.3)}$$

$$\frac{dc_{2i}(t)}{dt} = \frac{1}{2} K_2 c_i(t) c_i(t) + L_3 c_{3i}(t) c_v(t) - L_2 c_{2i}(t) c_v(t) - R_2 c_{2i}(t) c_i(t) \quad \text{(VII.4)}$$

$$\frac{dc_{3i}(t)}{dt} = R_2 c_{2i}(t) c_i(t) + L_4 c_{4i}(t) c_v(t) - R_3 c_{3i}(t) c_i(t) - L_3 c_{3i}(t) c_v(t) \quad \text{(VII.5)}$$

...

$$\frac{dc_{ni}(t)}{dt} = R_{n-1} c_{(n-1)i}(t) c_i(t) + L_{n+1} c_{(n+1)i}(t) c_v(t) - R_n c_{ni}(t) c_i(t) - L_n c_{ni}(t) c_v(t) \quad \text{(VII.6)}$$

...

$$\frac{dc_{neqi}(t)}{dt} = R_{neq-1} c_{(neq-1)i}(t) c_i(t) - L_{neq} c_{neqi}(t) c_v(t) \quad \text{(VII.7)}$$

The parameters in equations (VII.2-7) are defined as follows: C_v = concentration of vacancies, C_i = concentration of interstitials, C_{ni} = concentration of dislocation loops containing n atoms, K = production rate of vacancies and interstitials (assumed equal), K_2 = production rate of di-interstitials (interstitial loop nucleus), α_r = rate constant for the recombination of vacancies and interstitials, R_n = rate constant for the production of loops containing (n+1) atoms by interstitial absorption from loops containing n atoms, L_n = rate constant for the production of loops containing (n-1) atoms by vacancy absorption from loops containing n atoms, D_i = interstitial diffusion coefficient, D_v = vacancy diffusion coefficient, ρ_d = concentration of a background dislocation network, *neq* = the number of equations of the system, which corresponds to the maximum number of interstitials involved in a loop.

The rate theory computation code used in this study was originally developed by Jonnet [120-122] based on Hayns' model. In his study, the object was loop growth in α-doped UO_2. Given the similarity of material properties in both UO_2 and CeO_2 systems, it is logical to study the irradiation effects in CeO_2 with the same approach. In this model, K is a constant which corresponds to the dose rate in ion irradiation, and R_n and L_n are defined as:

$$R_n = z_i D_i (\frac{2\pi}{\Omega}) \sqrt{\frac{nc_{cell}^2}{\pi}} \qquad \text{(VII. 8)}$$

$$L_n = z_v D_v (\frac{2\pi}{\Omega}) \sqrt{\frac{nc_{cell}^2}{\pi}} \qquad \text{(VII. 9)}$$

Where Ω = 3.96x10^{-23} cm^3 is the atomic volume; z_i is the bias for interstitials, which is taken as unity in this study; c_{cell}^2 is the area per atom in a loop. Here the loop is considered as consisted by CeO_2 Schottky trios, in order to maintain the electrical neutrality of the material, c_{cell}^2 = 2.115x10^{-15} cm^2 is approximately calculated from:

$$c_{cell}^2 = (2d_{O-O})d_{Ce-Ce} \qquad \text{(VII.10)}$$

where $d_{O\text{-}O}$ and $d_{Ce\text{-}Ce}$ are the oxygen-oxygen and cerium-cerium distances respectively [120].

The temperature dependence of loop growth is only correlated with interstitial and vacancy diffusivities. Detailed expression of these diffusivities [120] is shown in equation VII.11:

$$D_v = x_i^2 a^2 \nu_v \exp(-\varepsilon_{vm} / kT)$$
$$D_i = \frac{2}{3} x_i^2 a^2 \nu_i \exp(-\varepsilon_{im} / kT) \qquad \text{(VII.11)}$$

Where a = 5.411 Å, which is the lattice constant of CeO_2 crystal; k is the Boltzmann constant; ε_{vm} and ε_{im} are the vacancy and interstitial migration enthalpies respectively; ν_v and ν_i are the vacancy and interstitial jumping frequencies respectively; x_i^2 is a factor related to stoichiometry of the material, and its value varies in the range of 0.01–1 which is adopted directly from UO_2 system [125].

The values of most parameters are taken from UO_2 system, due to the similarity of UO_2 and CeO_2 crystals and deficiency in CeO_2 experimental data. The values of some parameters are listed in table VII. 2.

Table VII.2 Values of some parameters used in the calculation of loop growth during ion irradiation in CeO_2 [120]

Parameter	Value
ν_v	$5x10^{13}$ s^{-1}
ν_i	$5x10^{12}$ s^{-1}
ε_{vm}	2.4 eV
z_v	1.0
z_i	1.0005

Calculation results are very sensitive to the values of ε_{im} and x_i^2. Furthermore, there is a range of data available for these parameters instead of a certain value. For the ε_{im} in UO_2, numerous experimental measurements and theoretical computations were attempted in the past, but there is no real agreement on its value. A number of 2 eV was measured by Matzke [49], which is the only data available from experiments so far [120]; Morelon et al. [126] suggested a value of 5 eV from molecular dynamics calculation. Other researchers in the community selected different values to employ in their simulations, for example, Rest and Hofman [127, 90] used 0.6 eV. A sensitivity study was performed for these parameters to investigate how much they can impact the result in Jérôme's thesis [120].

The re-solution process of interstitials back into the matrix due to the collision with the recoil atom is not considered here, since it was not observed during the experiments. However, an apparent migration and coalescense (M&C) process of interstitial loops was noticed (figure VI.8), which suggests a sensible coarsening mechanism is essential to accurately simulate the loop growth behavior. This part of simulation is still under investigation and will be continued in the future.

The approach proposed by Jonnet [120] to simulate the M&C process was to add additional terms into equations VII.7 as follows:

$$\frac{dc_{ni}(t)}{dt} = R_{n-1}c_{(n-1)i}c_i(t) + L_{n+1}c_{(n+1)i}(t)c_v(t) - R_n c_{ni}(t)c_i(t) - L_n c_{ni}(t)c_v(t) + \sum_{j=2}^{n} W_{j,n-j}(t) - \sum_{j=2}^{neq-1} W_{n,j}(t) \quad \text{(VII.12)}$$

where $$W_{n,j}(t) = \frac{8(r_n + r_j)(D_n + D_j)}{\Omega}\left[1 + \frac{r_n + r_j}{\sqrt{\pi(D_n + D_j)t}}\right]c_{ni}(t)c_{ji}(t) \quad \text{(VII.13)}$$

is the rate of collisions between loops with radii r_n and r_j. The first summation in equation VII.12 represents the creation of a loop containing (n)-intersitials from a (n-j)-interstitial loop colliding with a (j)-interstitial loop. The second summation represents the loss of (n)-interstitial loops which have collided with any other loop. In this approach, it is assumed that the interstitial loops are able to move in the absence of temperature or stress gradients, along the normal of their cylindrical plane. This method can take into account the coalescense phenomena in the basic simulation of loop growth, but is not able to study the exact shape of loops and their various interactions, which is possibly done with molecular dynamics simulation [123]. This part of simulation was incorporated into the rate theory computation code, but might still need some modifications to perform accurate simulations.

VIII. Preliminary Numerical Results and Discussion

In this chapter, some preliminary numerical results are presented, which were calculated with the rate theory model described in chapter VII. These results include loop growth behavior and loop size distributions as a function of dose and temperature. The computation code is still under development, and further improvement is necessary to enable the code to simulate the experiment conditions. At the current stage, the goal is not to reproduce the experiment results exactly, but to achieve consistent trends with experimental measurements.

The numerical solution of equations VII.2 – VII.7 is achieved by a classical forward integration method, the Euler method [120]:

$$y_{n+1} = y_n + hf(t_n; y_n) \qquad \text{(VIII.1)}$$

equation VIII.1 is used to linearly approximate

$$y'(t) = f(t, y(t)) \qquad \text{(VIII.2)}$$

in one time step, from t_n to $t_{n+1} = t_n + h$. This method is an explicit method for numerical integration of ordinary differential equations (ODE). It is a basic first-order numerical procedure for solving ODEs, and is economical in terms of computing time. Nevertheless, it still requires a lot of computation power to solve large number of equations. When the loop size increases, the number of required interstitials, which is equal to the required equation numbers, almost increases as a function of square, for example, ~ 2000 equations are needed for a loop with a radius of ~12 nm. Consequently, it takes long time to complete a calculation involving the growth of big loops. The computation time for a run at 250°C (6000 equations) is normally ~ 2 days, and the estimated computation time for the simulation of ion irradiation at 400°C is more than a week. This is why the irradiation temperatures (room temperature, 150°C and 250°C) chosen for this numerical calculation are well below the temperatures (up to 800°C) in experiments.

The computation code to implement the rate theory model is a Fortran code, and was initially developed by Jérôme Jonnet [120] in his PhD dissertation. The code was transposed into this work with some modifications to better suit the simulation of ion irradiation in CeO_2. The details of the code are presented in appendix B. In Dr. Jonnet's thesis, careful parameter analysis was performed to determine the ralative importance of various parameters. He found that ε_{im} and x_i^2 had the most important effects on the loop mean radius, skewness and normalized kurtosis of loop size distributions. Decrease ε_{im} has both positive and negative effects on loop growth. On one hand, a smaller value of ε_{im} improves the mobility of metal interstitials, on the other hand, this increases the Frenkel pair recombination coefficient, which retards

the nucleation and growth of interstitial loops. On the contrary, the variation of x_i^2 only impacts the diffusion of metal-interstitials. The smaller x_i^2 is, the higher mobility metal-interstitials have.

The uranium-interstitial diffusivity D_i is very sensitive to the value of ε_{im}. For example, D_i can increase 5 orders of magnititude when ε_{im} decreases from 0.6 eV to 0.3 eV. A value of 0.7 eV was used for cerium-interstitial migration energy in this study, which was taken from uranium-interstitial migration energy. The impact of ε_{im} on Frenkel pair recombination coefficient α_r is also significant. A deviation of 0.15 eV in ε_{im} can result in 350 times of difference in α_r [120].

As mentioned in chapter VII, re-solution process was not considered in this study, and the attempt to incorporate a coarensing process was made and still under process. Therefore, the preliminary results presented here are based on the basic equations VII.2-7. The calculated loop mean diameters, densities and size distributions at various temperatures were compared to the experimental results. Such comparison is critical to verify the theoretical model.

Figure VIII.1 (a) shows the calculated variations of average loop diameter as a function of dose at room temperature, 150°C and 250°C. As expected, the growth rate of dislocation loops was fast at higher temperature when the diffusion coefficient is the only parameter related to the temperature. Similar tendency can be seen in figure VIII.1 (b), which shows the measured variations of average loop diameter as a function of dose at 600°C and 800°C.

(a)

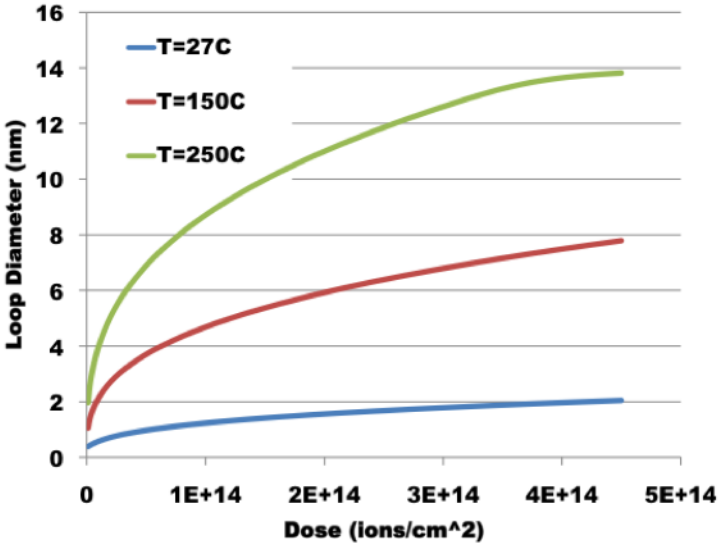

(b)

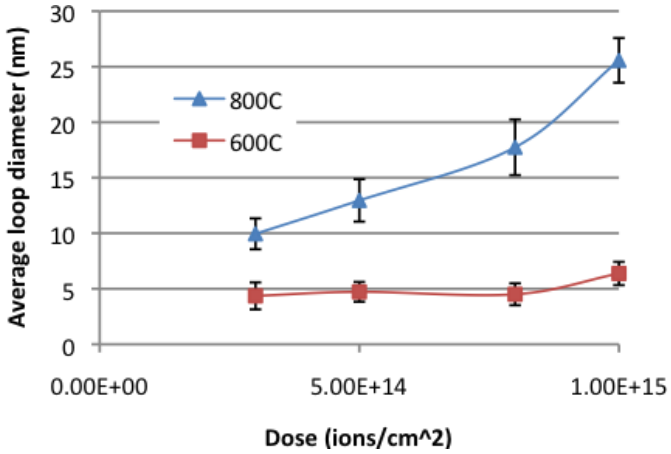

Figure VIII.1 Loop diameter variation as a function of dose during irradiation of 1 MeV Kr at three temperatures: room temperature, 150°C and 250°C. The damage rate K = 0.00033 dpa/s is equivalent to the dose rate of 1.25×10^{11} ions/cm^2 during experiments; (b) Measured loop size variations as a function of dose during the irradiation of 1 MeV Kr ions at 600°C and 800°C.

In contrast to the continuously increasing loop size, loop density increased at the beginning of irradiation and reached saturation in a very short period (figure VIII.2 (a)). This evolution behavior indicates that the nucleation stage of dislocation loops completes in a short time from the start of ion irradiation process, which is analogous to the experimental obsevations (figure VIII.2 (b)). Figure VIII.2 (b) is the measured loop density variation as a function of dose.

It was also noticed that the density of loops was higher at lower temperature in both figures VIII.2 (a) and (b). At the same dose, almost equal numbers of point defects were produced by irradiation at different temperatures. If most of interstitials are assumed to be accommodated in dislocations, then there will be fewer loops in the system when the interstitials aggregate in bigger loops.

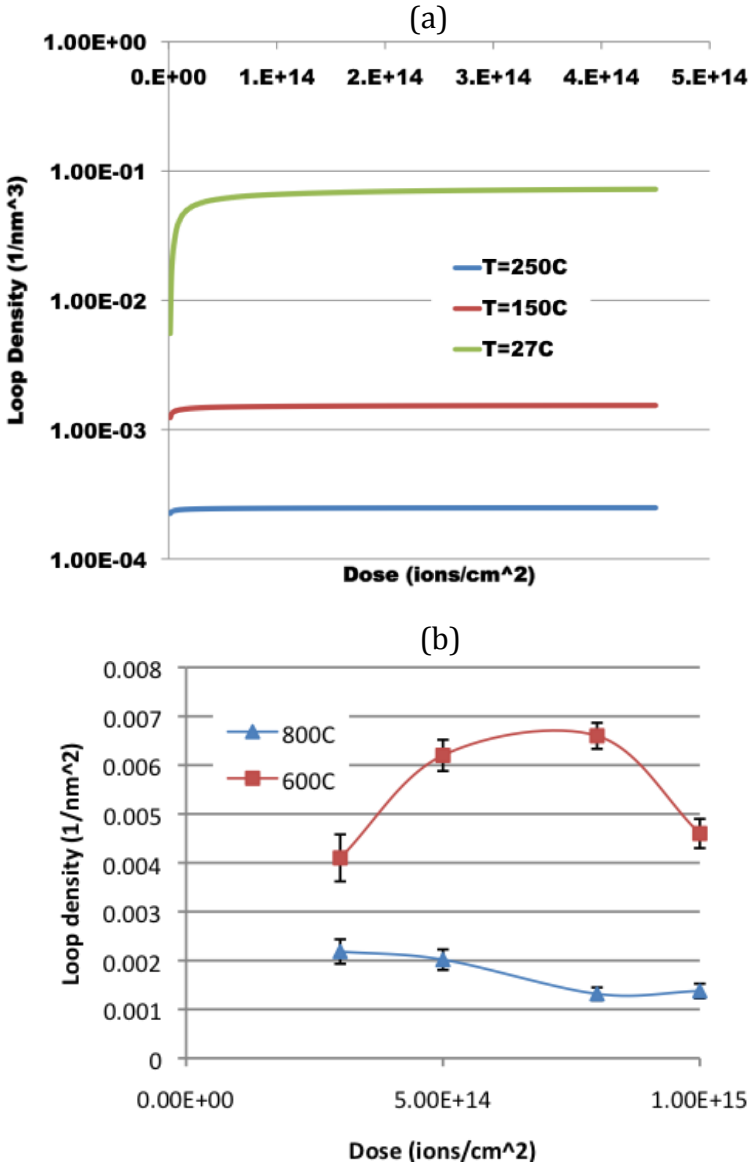

Figure VIII.2 (a) Simulated loop density variation as a function of dose during irradiation of 1 MeV Kr at three temperatures: room temperature, 150°C and 250°C. The damage rate K = 0.00033 dpa/s is equivalent to the dose rate of 1.25×10^{11} ions/cm^2 during experiments. (b) Measured loop density variations as a function of dose during the irradiation of 1 MeV Kr ions at 600°C and 800°C.

Loop size distributions were also calculated. Figure VIII.3 shows the comparison of calculated loop size distributions at three temperatures at the same dose, and figure VIII.4 (a) shows the calculated loop size distributions at two different doses during the same irradiation. As depicted in figure VIII.3, the majority of the loops had a smaller size at lower temperature, which resulted in the smaller average loop size as shown in figure VIII.1 (a). During the same irradiation, loops grew by absorbing interstitials and developed from small features to big ones. The development of calculated loop size distributions shown in figure VIII.4 (a) is consistent with this description, and has the same tendency as the behavior observed in experiments (figure VIII.4 (b)).

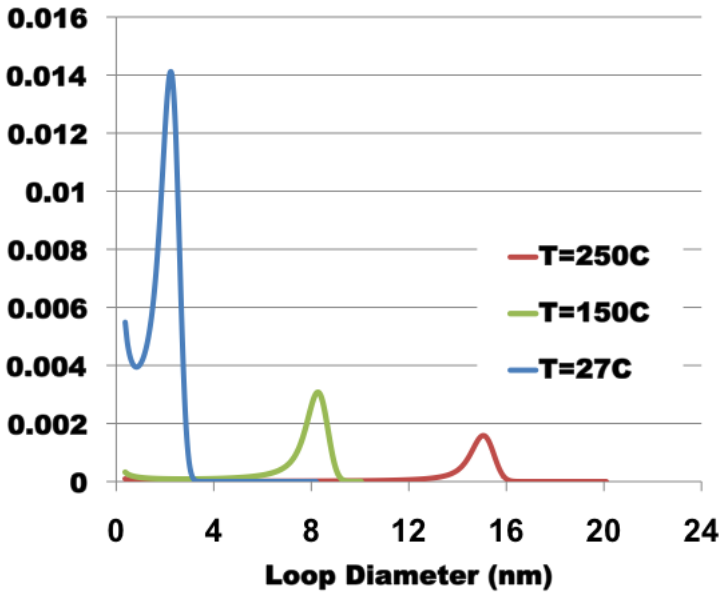

Figure VIII.3 Loop size distributions at the dose of 4.5×10^{14} ions/cm^2 for the irradiation of 1 MeV Kr ions at three temperatures: room temperature, 150°C and 250°C. The damage rate K = 0.00033 dpa/s is equivalent to the dose rate of 1.25×10^{11} ions/cm^2 during experiments.

(a)

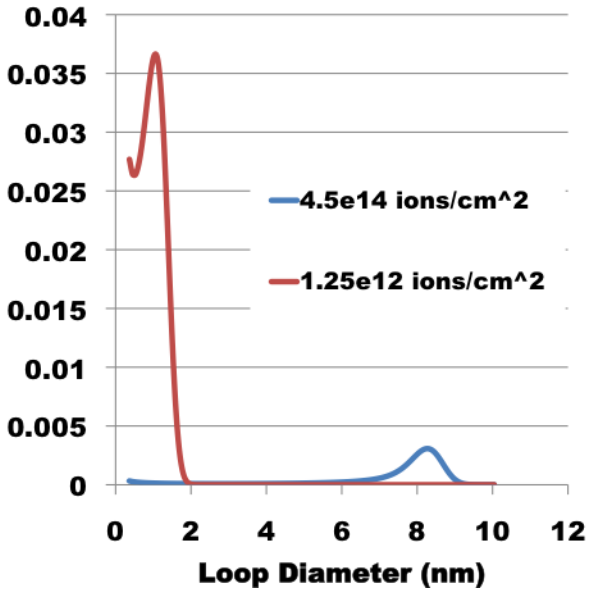

(b)

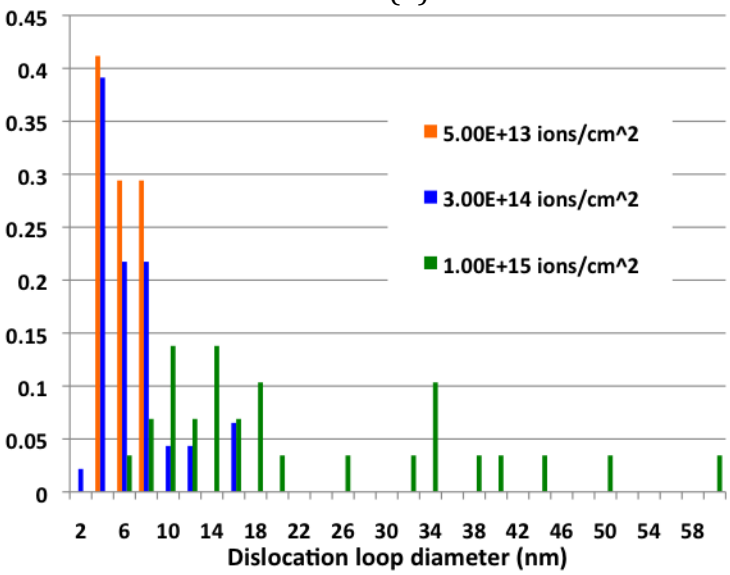

Figure VIII.4 (a) Simulated loop size distributions for the irradiation of 1 MeV Kr ions at two doses: 4.5×10^{14} and 1.25×10^{12} ions/cm^2 at 150°C. The damage rate K = 0.00033 dpa/s is equivalent to the dose rate of 1.25×10^{11} ions/cm^2 during experiments; (b) Measured loop size distributions during the irradiation of 1 MeV Kr ions at 800°C.

The final goal of this modeling effort is to be able to reproduce experimental results, and to eventually use the computation model to predict the defect structure evolution in fuel materials. In order to fulfill this goal, it is necessary to integrate of the coalescence and re-solution processes, which requires much higher calculation efficiency. In fact, the costly computation (in time) limited the usage of the current code in the simulation of lower temperatures in this work. Therefore, improving the calculation efficiency will be the first step to work on in the future. It will also help the coarensing mechanism to be explored further.

IX. Conclusions and Future Work

This PhD thesis has been focused on studying the nucleation and evolution processes of defect structures in nuclear fuel materials during irradiation. The growth mechanisms of the defect structures and their possible relationship with grain sub-division phenomenon in high burn-up fuel have also been investigated. For this purpose, a literature review was given on the irradiation conditions of nuclear fuel in a reactor, characterization of features on spent fuels, and models of formation of defect structures in fuel materials. From the bibliographical review, it is found that basic processes of defect structure formation still remain unclear despite extensive efforts. There are still a lot of open questions on the nature and configration of dislocation loops formed during irradiation, the exact mechanism of dislocation formation and its role on fuel structural evolution and nucleation and resolution of fission gas bubbles, which are all critical in affecting fuel performance during reactor operation. The basis of understanding these phenomena is the transportation and aggregation process of point defects. For this reason, a series of ion implantation experiments were performed, and a rate theory modeling of dislocation loop growth was carried out.

The experiments were designed to apply the ion implantation technique to induce damage in the materials, and transmission electron microscopy to characterize post-irradiation structures. CeO_2 single crystal was used as a surrogate material of UO_2. Since both of the materials are fluorite-type oxides and have similar material properties, they are expected to display comparable modifications in crystal structure subjected to ion irradiation.

The evolution processes of both dislocation loop/dislocation structure and gas bubbles were observed during *in-situ* irradiation experiments. Some of the results are summarized as below:

- Evolution of microstructure in CeO_2 was observed during *in-situ* irradiation of Kr or Xe ions at room temperature, 600°C and 800°C. Sequential TEM micrographs clearly illustrated the evolution process: the defects start to form clusters and loops at low dose, develop into extended dislocation lines and finally segregate together to form extremely tangled dislocation networks. Nucleation of dislocation loops was completed at the very early stage of irradiation. It might have even finished during ion milling process in most of irradiation experiments.

- The comparison of growth behavior of defect structures at 600°C and 800°C reveals that the thermally activated Ce-vacancy mobility plays an important role in dislocation loop development.

- Gas atom precipitation in CeO_2 was investigated through implantation of 150 keV Kr ions at $1x10^{16}$ ions/cm^2. Gas bubble formation was found at 600°C but not at room temperature. This might be either due to the threshold temperature for gas bubble formation between room temperature and 600°C, or the gas solubility limit as a function of temperature.

The *ex situ* irradiation experiments were aimed to study the defect structures in fluorite oxides at high irradiation doses. 700 keV Xe ions were implanted into single crystal thin films of CeO_2 and CeO_2 doped with 5% La at room temperature and 600°C to various doses ($2x10^{16}$ – $1x10^{17}$ ions/cm^2). TEM micrographs show that there are solid precipitate-like features formed in the materials after irradiation. In order to reveal the nature of those precipitate-like features, an *in situ* annealing experiment was also conducted. Here are some important observations found in the experiments:

- The materials remain crystalline after achieving very high doses ($1x10^{17}$ ions/cm^2), which is due to the high irradiation tolerance of the fluorite crystal structure [70, 125]. There was no evidence of grain subdivision or

polygonization found. A possible explanation is that the thin film structure (~ 160 nm along ion beam direction), surface sputtering, and radiation-enhanced gas diffusion help relieve internal stresses accumulated during irradiation.

- Solid precipitates appear in pure CeO_2 at and above $2x10^{16}$ ions/cm^2, but are absent in CeO_2 doped with 5% La until the fluence exceeds $4x10^{16}$ ions/cm^2. Besides the composition dependence, the formation of solid precipitates is also a temperature dependent process. There is a threshold temperature existing between room temperature and 600°C.

- The nature of those precipitates still needs to be investigated using X-ray techniques. So far, the most probable interpretation is that Xe forms in the solid state in gas bubbles under very high internal pressure.

In addition to the experimental investigation in the development of defect structures in CeO_2 during ion irridation, a theoretical analysis with a rate theory model was also attempted. The model, which considers loop growth from absorbing interstitials, was initially proposed by Hayns [119] and later developed by Jonnet [120]. Further extension of the model is needed to include a coarsening mechanism, which plays an important role in loop growth. Such extension will also require improvement of computational efficiency of the code. Along with the incorporation of a coarsening mechanism, another necessary continuation of the current model is taking into account the surface effect, which makes the model more solid in simulating the experimental conditions.

In the time frame of this PhD thesis, the highest irradiation temperature achieved in the simulation is 250°C. Therefore, the simulation results cannot be directly compared with experiment observation (600°C and 800°C). Other than that, the preliminary results from the calculation showed reasonably consistant trends with experimental measurements. The comparison was made for average dislocation size and density as a function of dose and loop size distributions at various temperatures

and doses. With further modification of the code, it can be applied in oxide fuel analysis.

Apart from the above ongoing meso-scale simulations of loop structure, simulation methods in different time and length scales, such as ab inito, molecular dynamics and kinetic Monte Carlo, are indispensable in obtaining insights into defect structure formation [111-114]. Those methods can help verify some of the assumptions and provide more accurate parameters to be used in rate theory modeling, which might be very difficult to measure in experiments (e.g. uranium/cerium interstitial migration enthalpy). This integrated multi-scale simulation approach will help interpret the phenomena observed by experiments, and eventually predict material structure development at different irradiation conditions.

Reference

[1] J.P. Raison, T. Mizuno, F. Delage, J. Carmack, Chan Bock Lee, "Sodium Fast Reactor Fuel Evaluation: Oxide Fuels", Transactions of the American Nuclear Society, vol. 98, pp. 1052-1055, 2008

[2] V.V. Rodinella and T. Wiss, "*The High Burn-up Structure in Nuclear Fuel*", Materials today, vol. 13, pp. 24-32, 2010

[3] Hj. Matzke, "*On the Rim Effect in High Burnup UO_2 LWR fuels*", Journal of Nuclear Materials, vol. 189, pp. 141-148, 1992

[4] R. Lallement, A. Tuzov, K. Q. Bagley, "*Fast Breeder Reactor Fuel Performances*", Philosophical Transactions of the Royal Society of London. Series A, Mathematical and Physical Sciences, vol. 331, pp. 343-354, 1990

[5] Hj. Matzke, "*Gas Release Mechanisms in UO2 – A Critical Review*", Radiation Effects, vol. 53, pp. 219-242, 1980

[6] F.A. Nichols, "*On the Thermal Gradient Migration of Lenticular Voids*", Journal of Nuclear Materials, vol. 84, pp. 319-326, 1979

[7] D. Olander, "*Nuclear Fuels – Present and Future*", Journal of Nuclear Materials, vol. 389, pp. 1-22, 2009

[8] D.R. Olander, "*Fundamental Aspects of Nuclear Reactor Fuel Elements*", Energy Research and Development Administration, 1976

[9] Hj. Matzke, A. Turos, "*Ion Implantation Studies of UO2 and UN*", Journal of Nuclear Materials, vol. 188, pp. 285-292, 1992

[10] W.H. Hocking, R.A. Verrall, I.J. Muir, "*Migration Behaviour of Iodine in Nuclear Fuel*", Journal of Nuclear Materials, vol. 294, pp. 45-52, 2001

[11] Hj. Matzke, A. Turos, G. Linker, "*Polygonization of Single Crystals of the Fluorite-type Oxide UO2 due to Dose Ion Implantation*", Nuclear Instruments and Methods in Physics Research B, vol. 91, pp. 294-300, 1994

[12] G.S. Was, "Fundamentals of Radiation Materials Science Metals and Alloys", Springer, 2007

[13] J.H. Evans, A. van Veen, K.T. Westerduin, "*A TEM and TDS Study of Gas Release from Bubbles in Krypton-implanted Uranium Dioxide*", Journal of Nuclear Materials, vol. 195, pp. 250-259, 1992

[14] H.E. Evans, J.H. Evans, P. Rice-Evans, D.L. Smith, C. Smith, "*A Slow Positron Study into the Recovery Behavior of As-polished and Krypton-implanted Uranium Dioxide*", Journal of Nuclear Materials, vol. 199, pp. 79-83, 1992

[15] A. Turos, Hj. Matzke, M. Wielunski, L. Nowicki, "*Radiation Defects in the Oxygen Sublattice of UO2 Single Crystals*", Nuclear Instruments and Methods in Physics Research B, vol. 80/81, pp. 1259-1263, 1993

[16] J. H. Evans, A. van Veen, K. T. Westerduin, "*An Investigation into the Influence of Implanted Oxygen on Krypton Behaviour in Dioxide during Annealing*", Journal of Nuclear Materials, vol. 208, pp. 211-218, 1994

[17] F. Garrido, L. Nowicki, G. Sattonnay, T. Sauvage, L. Thome, "Lattice Location of Helium in Uranium Dioxide Single Crystals", Nuclear Instruments and Methods in Physics Research B, vol. 219-220, pp. 196-199, 2004

[18] L. Desgranges, B. Pasquet, "*Measurement of Xenon in Uranium Dioxide (UO2) with SIMS*", Nuclear Instruments and Methods in Physics Research B, vol. 215, pp. 545-551, 2004

[19] G. Sattonnay, F. Garrido, L.Thome, "*Behaviour of Helium in UO2 Single Crystals: a Transmission Electron Microscopy Investigation*", Philosophical Magazine Letters, vol. 84, pp. 109-115, 2004

[20] G. Sattonnay, L. Vincent, F. Garrido, L. Thome, "*Xenon versus Helium Behaviour in UO2 Single Crystals: a TEM Investigation*", Journal of Nuclear Materials, vol. 355, pp. 131-135, 2006

[21] T. Diaz de la Rubia, R.S. Averback, Horngming Hsieh, R. Benedek, "*Molecular Dynamics Simulation of Displacement Cascades in Cu and Ni: Thermal Spike Behavior*", Journal of Materials Research, vol. 4, pp. 579-586, 1989

[22] H.L. Heinish, B.N. Singh, "*On the Structure of Irradiation Induced Collision Cascades in Metals as a Function of Recoil Energy and Crystal Structure*", Philosophy Magazine, vol. 67, pp. 407-424, 1993

[23] D.J. Bacon, T. Diaz de la Rubia, "*Molecular Dynamics Computer Simulations of Displacement Cascades in Metals*", Journal of Nuclear Materials, vol. 216, pp. 275-290, 1994

[24] A. Meldrum, S.J. Zinkle, L.A. Boatner, R.C. Ewing, "*A Transient Liquid-like Phase in the Displacement Cascades of Zircon, Hafnon and Thorite*", Nature, vol. 395, pp. 56-58, 1998

[25] A. Struchbery, E. Bezakova, "*Thermal-spike Lifetime from Picosecond-Duration Preequilibrium Effects in Hyperfine Magnetic Fields Following Ion Implantation*", Physical Review Letters, vol. 82, pp. 3637-3640, 1999

[26] A.J.E. Foreman, W.J. Phythian, C.A. English, "*Molecular Dynamics Simulation of Irradiation Damage Cascades in Copper Using a Many-body Potential*", Radiation Effects and Defects in Solids, vol. 129, pp. 25-30, 1994

[27] V.D.S. Dhaka, N.V. Tkachenko, H. Lemmetyinen, E-M. Pavelescu, S. Suomalainen, M. Pessa, K. Arstila, K. Nordlund, J. Keinonen, "*Ultrafast Dynamics of Ni^{+}-irradiated and Annealed GaInAs/InP Multiple Quantum Wells*", Journal of Physics D: Applied Physics, vol. 39, pp. 2659-2663, 2006

[28] Hj. Matzke, "Radiation Damage in Nuclear Materials", Nuclear Instruments and Methods in Physics Research B, vol. 65, pp. 30-39, 1992

[29] Hj. Matzke, P.G. Lucuta, T. Wiss, "*Swift Heavy Ion and Fission Damage Effects in UO_2*", Nuclear Instruments and Methods in Physics Research B, vol. 166-167, pp. 920-926, 2000

[30] Hj. Matzke, M. Kinoshita, "*Polygonization and High Burnup Structure in Nuclear Fuels*", Journal of Nuclear Materials, vol. 247, pp. 108-115, 1997

[31] L.E. Thomas, C.E. Beyer, L.A. Charlot, "*Microstructural Analysis of LWR Spent Fuels at High Burnup*", Journal of Nuclear Materials, vol. 188, pp. 80-89, 1992

[32] Hj. Matzke, A. Turos, "*A Channeling Study of Ion Implantation Damage in UO_2 and UN*", Nuclear Instruments and Methods in Physics Research B, vol. 46, pp. 117-121, 1990

[33] Hj. Matzke, V. Nitzki, C. Ronchi, "*The Crystallization of Amorphous UO_2*", Thin Solid Films, vol. 22, pp. 75-82, 1974

[34] R. Kelly, H.M. Naguib, Proceeding of International Conference on Atomic Collision Phenomena in Solids, pp. 172, 1970

[35] K.E. Sickafus, Hj. Matzke, Th. Hartmann, K. Yasuda, J.A. Valdez, P. Chodak III, M. Nastasi, R.A. Verrall, "*Radiation Damage Effects in Zirconia*", Journal of Nuclear Materials, vol. 274, pp. 66-77, 1999

[36] K. Yasuda, C. Kinoshita, S. Matsumura, A.I. Ryazanov, "*Radiation-induced Defect Cluster in Fully Stabilized Zirconia Irradiated with Ions and/or Electrons*", Journal of Nuclear Materials, vol. 319, pp. 74-80, 2003

[37] L.M. Wang, S.X. Wang, S. Zhu, R.C. Ewing, "*Effects of Fission Product Incorporation on the Microstructure of Cubic Zirconia*", Journal of Nuclear Materials, vol. 289, pp. 122-127, 2001

[38] N. Sasajima, T. Matui, K. Hojou, S. Furuno, H. Otsu, K. IZui, K. Murumura, "*Radiation Damage in Yttria-stabilized Zirconia under Xe Ion Irradiation*", Nuclear Instruments and Methods in Physics Research B, vol. 141, pp. 487-493, 1998

[39] T. Sonoda, M, Kinoshita, N. Ishikawa, M. Sataka, Y. Chimi, N. Okubo, A. Iwase, K. Yasunaga, "*Clarification of the Properties and Accumulation Effects of Ion Tracks in CeO_2 "*, Nuclear Instruments and Methods in Physics Research B, vol. 266, pp. 2882-2886, 2008

[40] K. Yasunaga, K. Yasuda, S. Matsumura, T. Sonoda, "*Electron Energy-dependent Formation of Dislocation Loops in CeO_2 "*, Nuclear Instruments and Methods in Physics Research B, vol. 266, pp. 2877-2881, 2008

[41] K. Yasunaga, K. Yasuda, S. Matsumura, T. Sonoda, "*Nucleating and Growth of Defect Clusters in CeO_2 Irradiated with Electrons*", Nuclear Instruments and Methods in Physics Research B, vol. 250, pp. 114-118, 2006

[42] T. Sonoda, M. Kinoshita, Y. Chimi, N. Ishikawa, M. Sataka and A. Iwase, "*Electronic Excitation Effects in CeO_2 under Irradiations with High-energy Ions of Typical Fission Products*", Nuclear Instruments and Methods in Physics Research B, vol. 250, pp. 254-258, 2006

[43] R.J.M. Konings, K. Bakker, J.G. Boshoven, R. Conrad, H. Hein, "*The Influence of Neutron Irradiation on the Microstructure of Al_2O_3, $MgAl_2O_4$, $Y_3Al_5O_{12}$ and CeO_2*", Journal of Nuclear Materials, vol. 254, pp. 135-142, 1998

[44] W.J. Weber, Radiat. Eff., vol. 83, pp. 145, 1984

[45] A. Iwase, H. Ohno, N. Ishikawa, Y. Baba, N. Hirao, T. Sonoda, M. Kinoshita, "*Studay on the Behavior of Oxygen Atoms in Swift Heavy Ion Irradiated CeO_2 by Means of Synchrotron Radiation X-ray Photoelectron Spectroscopy*", Nuclear Instruments and Methods in Physics Research B, vol. 267, pp. 969-972, 2009

[46] M. Song, Wang Weiguo, F. Chu, X. Yang, K. Mitsuishi, K. Furuya, H. Yasuda, "*Structure and Chemical Changes of CeO_2 Irradiated with Hydrogen Ions*", Nuclear Instruments and Methods in Physics Research B, vol. 191, pp. 586-590, 2002

[47] K. Une, K. Nogita, S. Kashibe, M. Imamura, "*Microstructural Change and Its Influence on Fission Gas Release in High Burnup UO_2 Fuel*", Journal of Nuclear Materials, vol. 188, pp. 65-72, 1992

[48] J. Kocík, E. Keilová, J. Cízek and I. Procházka, "*TEM and PAS study of neutron irradiated VVER-type RPV steels*", Journal of Nuclear Materials, vol. 303, pp. 52-64, 2002

[49] Hj. Matzke, "*Atomic Transport Properties in UO2 and Mixed Oxides (U, Pu)O2*", Journal of Chemistry Society, Faraday Transaction 2, vol. 83, pp. 1121-1142, 1987

[50] W. Miekeley and F.W. Felix, "Effect of Stoichiometry on Diffusion of Xenon in UO_2", Journal of Nuclear Materials, vol. 42, pp. 297-306, 1972

[51] R.M. Cornell, "", Philosophy Magazine, vol. 19, pp. 539, 1969

[52] Hj. Matzke, "*Xenon Migration and Trapping in Doped ThO_2*", Journal of Nuclear Materials, vol. 21, pp. 190-198, 1967

[53] Hj. Matzke, "*Inert Gas Diffusion and Radiation Damage in Ionic Crystals and Sinters Following Ion Bombardment*", Canadian Journal of Physics, vol. 46, pp. 621-634, 1968

[54] T.S. Elleman, C.H. Fox, Jr., L.D. Mears, "*Influence of Defects on Rare-gas Diffusion in Solids*", Journal of Nuclear Materials, vol. 30, pp. 89-106, 1969

[55] C.R.A. Catlow, "*Fission Gas Diffusion in Uranium Dioxide*", Proceedings of Royal Society of London. Series A. vol. 364, pp. 473-497, 1978

[56] R.A. Jackson, C.R.A. Catlow, "*Trapping and Solution of Fission Xe in UO_2*", Journal of Nuclear Materials, vol. 127, pp. 161-166, 1985

[57] Hj. Matzke, R.R. Agarwala (Eds.), Diffusion Processes in Nuclear Materials, North Holland, 1992

[58] Y. Yun, H. Kim, H. Kim, K. Park, "*Atomic Diffusion Mechanism of Xe in UO_2*", Journal of Nuclear Materials, vol. 378, pp. 40-44, 2008

[59] M. Li, M. Eldrup, T.S. Byun, N. Hashimoto, L.L. Snead and S.J. Zinkle, "*Low Temperature Neutron Irradiation Effects on Microstructure and Tensile Properties of Molybdenum*", Journal of Nuclear Materials, vol. 376, pp. 11-28, 2008

[60] W. DÖrr, S. Hellmann and G. Mages, "*Study of the Formation of UO_2-PuO_2 Solid Solution by Means of UO_2-CeO_2 Simulate*", Journal of Nuclear Materials, vol. 140, pp. 7-10, 1986

[61] H.S. Kim, C.Y. Joung, B.H. Lee, J.Y. Oh, Y.H. Koo, P. Heimgartner, "*Applicability of CeO_2 as a Surrogate for PuO_2 in a MOX Fuel Development*", Journal of Nuclear Materials, vol. 378, pp. 98-104, 2008

[62] A. Gotte, D. Spangberg, K, Hermansson and M. Baudin, "*Molecular Dynamics Study of Oxygen Self-diffusion in Reduced CeO_2*", Solid State Ionics, vol. 178, pp. 1421-1427, 2007

[63] L. Minervini, M.O. Zacate and R.W. Grimes, "*Defect Cluster Formation in M_2O_3–doped CeO_2*", Solid State Ionics, vol. 116, pp. 339-349, 1999

[64] S. Vyas, R.W. Grimes, D.H. Gay and A.L. Rohl, "*Structure, Stability and Morphology of Stoichiometric Ceria Crystallites*", Journal of the Chemical Society. Faraday Transactions, vol. 94, pp. 427-434, 1998

[65] K. Ohhara, N. Ishikawa, S. Sakai, Y. Matsumoto, O. Michikami, Y. Ohta, "*Oxygen Defects Created in CeO_2 Irradiated with 200 MeV Au Ions*", Nuclear Instruments and Methods in Physics Research B, vol. 267, pp. 973-975, 2009

[66] K. Yamada, S. Yamanaka and M. Katsura, "*Mechanical Properites of (U, Ce)O_2*", Journal of Alloys and Compounds, vol. 271-273, pp. 697-701, 1998

[67] P. Martin, M. Ripert, T. Petit, T. Reich, C. Hennig, F. D'Acapito, J.L. Hazemann and O. Proux, "*A XAS Study of the Local Environments of Cations in (U, Ce)O_2*", Journal of Nuclear Materials, vol. 312, pp. 103-110, 2003

[68] Hj. Matzke, V.V. Rondinella, T. Wiss, "*Materials Research on Inert Matrices: a Screening Study*", Journal of Nuclear Materials, vol. 274, pp. 47-53, 1999

[69] J.K. Fink, "*Thermophysical Properties of Uranium Dioxide*", Journal of Nuclear Materials, vol. 279, pp. 1-18, 2000

[70] M. Burghartz, Hj, Matzke, C. Léger, G. Vambenepe and M. Rome, "*Inert Matrics for the Transmutation of Actinides: Fabrication, Thermal Properties and Radiation Stability of Ceramic Materials*", Journal of Alloys and Compounds, vol. 271-273, pp. 544-548, 1998

[71] E.A.C. Neeft, K. Bakker, R.P.C. Schram, R. Conrad and R.J.M. Konings, "*The EFTTRA-T3 Irradiation Experiment on Inert Matrix Fuels*", Journal of Nuclear Materials, vol. 320, pp. 106-116, 2003

[72] A. Trovarelli, "*Structural Properties and Nonstoichiometric Behavior of CeO_2*", Eds. A. Trovarelli, Imperial College Press, 2002

[73] C. Abromeit, "*Aspects of Simulation of Neutron Damage by Ion Irradiation"*, Journal of Nuclear Materials, vol. 216, pp. 78-96, 1994

[74] D.J. Mazey, "*Fundamental Aspects of High-energy Ion-beam Simulation Techniques and Their Relevance to Fusion Materials Studies*", Journal of Nuclear Materials, vol. 174, pp. 196-209, 1990

[75] J.A. Hinks, "*A Review of Transmission Electron Microscopes with In Situ Ion Irradiation*", Nuclear Instruments and Methods in Physics Research B, vol. 267, pp. 3652-3662, 2009

[76] M.A. Kirk, P.M. Baldo, A.C.Y. Liu, E.A. Ryan, R.C. Birtcher, Z. Yao, S. Xu, M.L. Jenkins, M. Herhandex-mayoral, D. Kaoumi and A.T. Motta, "*In Situ Transmission Electron Microscopy and Ion Irradiation of Ferritic Materials*", Microscopy Research and Technique, vol. 72, pp. 182-186, 2009

[77] M.H. Loretto, R.E. Smallman, "*Defect Analysis in Electron Microscopy*", Chapman and Hall, London, 1975

[78] D.B. Williams, C.B. Carter, "*Transmission Electron Microscopy – A Textbook for Materials Science*", Plenum Press, New York and London, 1996

[79] S.J. Pennycook, "*Z-contrast STEM for Materials Science*", Ultramicroscopy, vol. 30, pp. 58-69, 1989

[80] B. Ye, M.A. Kirk, W. Chen, A. Oaks, J. Rest, A. Yacout, J.F. Stubbins, "*TEM Investigation of Irradiation Damage in Single Crystal CeO_2*", Journal of Nuclear Materials, in press, 2011

[81] B. Ye, J.F. Stubbins, M.A. Kirk, "*In situ TEM Study of Gas Bubble Formation in Krypton-implanted CeO_2*", Transactions of the American Nuclear Society, vol. 102, pp. 848-849, 2010

[82] B. Ye, D. Yun, A.J. Oaks, W. Chen, M.A. Kirk, J. Rest, A.M. Yacout, J.F. Stubbins, "*The Effects of Xenon Implantation in Ceria with and without Lanthanum*", Nuclear Instruments and Methods in Physics Research B, in press, 2011

[83] C. Sabathier, L. Vincent, P. Garcia, F. Garrido, G. Carlot, L. Thome, P. Martin, C. Valot, "*In Situ TEM Study of Temperature-induced Fission Product Precipitation in UO_2*", Nuclear Instruments and Methods in Physics Research B, vol. 266, pp. 3027-3032, 2008

[84] K. Nogita, K. Une, "*High Resolution TEM Observation and Density Estimation of Xe Bubbles in High Burnup UO_2 Fuels*", Nuclear Instruments and Methods in Physics Research B, vol. 141, pp. 481-486, 1998

[85] K. Nogita, K. Une, "*Thermal Recovery of Radiation Defects and Microstructural Change in Irradiated UO_2 Fuels*", Journal of Nuclear Science and Technology, vol. 30, pp. 900-910, 1993

[86] S. Kashibe, K. Une, K. Nogita, "*Formation and Growth of Intragranular Fission Gas Bubbles in UO_2 Fuels with Burnup of 6-83 GWd/t*", Journal of Nuclear Materials, vol. 206, pp. 22-34, 1993

[87] R.M. Cornell, "*An Electron Microscope Examination of Matrix Fission-gas Bubbles in Irradiated Uranium Dioxide*", Journal of Nuclear Materials, vol. 38, pp. 319-328, 1971

[88] A.D. Whapham, B.E. Sheldon, Philosophy Magazine, vol. 12, pp. 1179, 1965

[89] K. Nogita, K. Une, "*Irradiation-induced Recrystallization in High Burnup UO_2 Fuel*", Journal of Nuclear Materials, vol. 226, pp. 302-310, 1995

[90] J. Rest and G.L. Hofman, "*Dynamics of Irradiation-induced Grain Subdivision and Swelling in U_3Si_2 and UO_2 Fuels*", Journal of Nuclear Materials, vol. 210, pp. 187-202, 1994

[91] J. Rest, G.L. Hofman, "*Fundamental Aspects of Inert Gases in Solids*", eds. S.E. Donnelly, J.H. Evans, Plenum, New York, 1991

[92] N. Nakae, Y. Iwata, T. Kirihara, "*Thermal Recovery of Defects in Neutron Irradiated UO_2*", Journal of Nuclear Materials, vol. 80, pp. 314-322, 1979

[93] M. Kiritani, N. Yoshida, H. Tanaka, Y. Maehara, "", Journal of Physics Society Japan, vol. 38, pp. 1677, 1975

[94] J.F. Ziegler, J.P. Biersack, et al. "*The Stopping and Range of Ions of Solid*", Pergamon Press, New York, 1985

[95] R.A. Jackson, C.R.A. Catlow, A.D. Murray, "*Point-defect Calculations in UO2*", Journal of Chemistry Society, Faraday Transaction 2, vol. 83, pp. 1171-1176, 1987

[96] J.H. Harding, "*Defects and Clusters in UO2 and (U, Pu)O2*", Journal of Chemistry Society, Faraday Transaction 2, vol. 83, pp. 1177-1187, 1987

[97] C.R.A. Catlow, "*Recent Problems and Progress in the Study of UO2 and mixed UO2-PuO2*", Journal of Chemistry Society, Faraday Transaction 2, vol. 83, pp. 1065-1072, 1987

[98] C.R.A. Catlow, V.L. Bulatov and R.W. Grimes, "*Computational Studies of the Structures, Energetics and Dynamics of Clusters*", Nuclear Instruments and Methods in Physics Research B, vol.122, pp. 301-310, 1997

[99] C. Meis and A. Chartier, "*Calculation of the Threshold Displacement Energies in UO_2 Using Ionic Potentials*", Journal of Nuclear Materials, vol. 341, pp. 25-30, 2005

[100] R.A. Jackson, A.D. Murray, J.H. Harding and C.R.A. Catlow, "*The Calculation of Defect Parameters in UO_2*", Philosophical Magazine A, vol. 53, pp. 27-50, 1986

[101] C.R.A. Catlow, "*Point Defect and Electronic Properties of Uranium Dioxide*", Proceedings of Royal Society of London. Series A. vol. 353, pp. 533-561, 1977

[102] J. Rest, "*An Analytical Study of Gas-bubble Nucleation Mechanisms in Uranium-alloy Nuclear Fuel at High Temperature*", Journal of Nuclear Materials, vol. 402, pp. 179-185, 2010

[103] D. Yun, Ph. D Dissertation, University of Illinois at Urbana-Champaign, United States, 2010

[104] R. Pornprasertsuk, P. Ramanarayanan, C.B. Musgrave, F.B. Prinz, "*Predicting Ionic Conductivity of Solid Oxide Fuel Cell Electrolyte from First Principles*", Journal of Applied Physics, vol. 98, pp. 103513-103521, 2005

[105] K. Govers, S. Lemehov, M. Hou, M. Verwerft, "*Comparison of Interatomic Potentials for UO2 Part I: Static Calculations*", Journal of Nuclear Materials, vol. 366, pp. 161-177, 2007

[106] K. Govers, S. Lemehov, M. Hou, M. Verwerft, "*Comparison of Interatomic Potentials for UO2 Part II: Molecular Dynamics Simulations*", Journal of Nuclear Materials, vol. 367, pp. 66-77, 2008

[107] R.G.J. Ball, R.W. Grimes, "*Diffusion of Xe in UO2*", Journal of Chemistry Society, Faraday Transaction, vol. 86, pp. 1257-1261, 1990

[108] E. Ya. Mikhlin, V.F. Chkuaseli, "*Gas Release and Swelling in Oxide Fuel; Modeling of the Kinetics of Gas Porosity Development*", Journal of Nuclear Materials, vol. 105, pp. 223-230, 1982

[109] I.R. Brearley, D.A. MacInnes, "*Modelling of Fission-gas Release from Fuel Undergoing Isothermal Heating*", Journal of Nuclear Materials, vol. 118, pp. 68-72, 1983

[110] J. Soullard, "*High Voltage Electron Microscope Observations of UO_2*", Journal of Nuclear Materials, vol. 135, pp. 190-196, 1985

[111] B.D. Wirth, G.R. Odette, J. Marian, L. Ventelon, J.A. Young-Vandersall, L.A. Zepeda-Ruiz, "*Multiscale Modeling of Radiation Damage in Fe-based Alloys in the Fusion Environment*", Journal of Nuclear Materials, vol. 329-333, pp. 103-111, 2004

[112] B.D. Wirth, M.J. Caturla, T. Diaz de la Rubia, T. Khraishi, H. Zbib, "*Mechanical Property Degradation in Irradiated Materials: A Multiscale Modeling Approach*", Nuclear Instruments and Methods in Physics Research B, vol. 180, pp. 23-31, 2001

[113] D.J. Bacon, Yu.N. Osetsky, "*Multicale Modeling of Radiation Damage in Metals: from Defect Generation to Material Properties*", Materials Science and Engineering A. vol. 365, pp. 46-56, 2004

[114] L. Malerba, A. Caro, J. Wallenius, "*Multicale Modeling of Radiation Damage and Phase Transformations: the Challenge of FeCr Alloys*", Journal of Nuclear Materials, vol. 382, pp. 112-125, 2008

[115] R.E. Stoller, "*Atomic-scale Simulation of Radiation Damage in Structure Materials*", NESLS summer seminar series, 2007

[116] M. Jaraiz, E. Rubio, P. Castrillo, L. Pelaz, L. Bailon, J. Barbolla, G.H. Gilmer and C.S. Rafferty, "*Kinetic Monte Carlo Simulations: an Accurate Bridge Between Ab Initio Calculations and Standard Process Experimental Data*", Materials Science in Semiconductor Processing, vol. 3, pp. 59-63, 2000

[117] K. Morishita, R. Sugano and B.D. Wirth, "*MD and KMC Modeling of the Growth and Shrinkage Mechanisms of Helium-vacancy Clusters in Fe*", Journal of Nuclear Materials, vol. 323, pp. 243-250, 2003

[118] A.D. Brailsford, R. Bullough, "*The Rate Theory of Swelling due to Void Growth in Irradiated Metals*", Journal of Nuclear Materials, vol. 44, pp. 121-135, 1972

[119] M.R. Hayns, "*The Nucleation and Early Growth of Interstitial Dislocation Loops in Irradiated Materials*", Journal of Nuclear Materials, vol. 56, pp. 267-274, 1975

[120] J. Jonnet, "*A Contribution to the Understanding of the High Burn-up Structure Formation in Nuclear Fuels*", Ph. D thesis, Institut National Polytechnique de Lorraine, 2007

[121] J. Jonnet, P. Van Uffelen, T. Wiss, D. Staicu, B. Rémy, J. Rest, "*Growth Mechanisms of Interstitial Loops in α-doped UO_2 Samples*", Nuclear Instruments and Methods in Physics Research B, vol. 266, pp. 3008-3012, 2008

[122] J. Jonnet, J. Rest, P. Van Uffelen, D. Staicu, T. Wiss, C. Ronchi, "*Radiation Damage and Strain Energy in Self-irradiated UO_2*", Proceeding of IAEA Technical Meeting on Fuel Behaviour under Normal, Transient and Accident Conditions, and High Burn-ups, Sep. 5-8, 2005

[123] D.C. Parfitt, C.L. Bishop, M.R. Wenman, R.W. Grimes, "*Strain Fields and Line Energies of Dislocations in Uranium Dioxide*", Journal of Physics: Condensed Matter, vol. 22, pp. 175004-175012, 2010

[124][3] K.E. Sickafus, L. Minervini, R.W. Grimes, J.A. Valdez, M. Ishimaru, F. Li, K.J. McClellan, T. Hartmann, "*Radiation Tolerance of Complex Oxides*", Science, Vol. 289, pp. 748-751, 2000

[125][132] A.B. Lidiard, "*Self-diffusion of Uranium in UO_2*", Journal of Nuclear Materials, vol. 19, pp. 106-108, 1966

[126][133] N.D. Morelon, D. Ghaleb, J.M. Delaye, L. Van Brutzel, "*A New Empirical Potential for Simulating the Formation of Defects and Their Mobility in Uranium Dioxide*", Philosophical Magazine, vol. 83, pp. 1533-1550, 2003

[127][134] J. Rest, "*Derivation of Analytical Expressions for the Network Dislocation Density, Change in Lattice Parameter and for the Recrystallized Grain Size in Nuclear Fuels*", Journal of Nuclear Materials, vol. 349, pp. 150-159, 2006

Appendix A. Results from *ex situ* Irradiation Experiments

A.1 SRIM calculation results for *ex situ* irradiation experiments

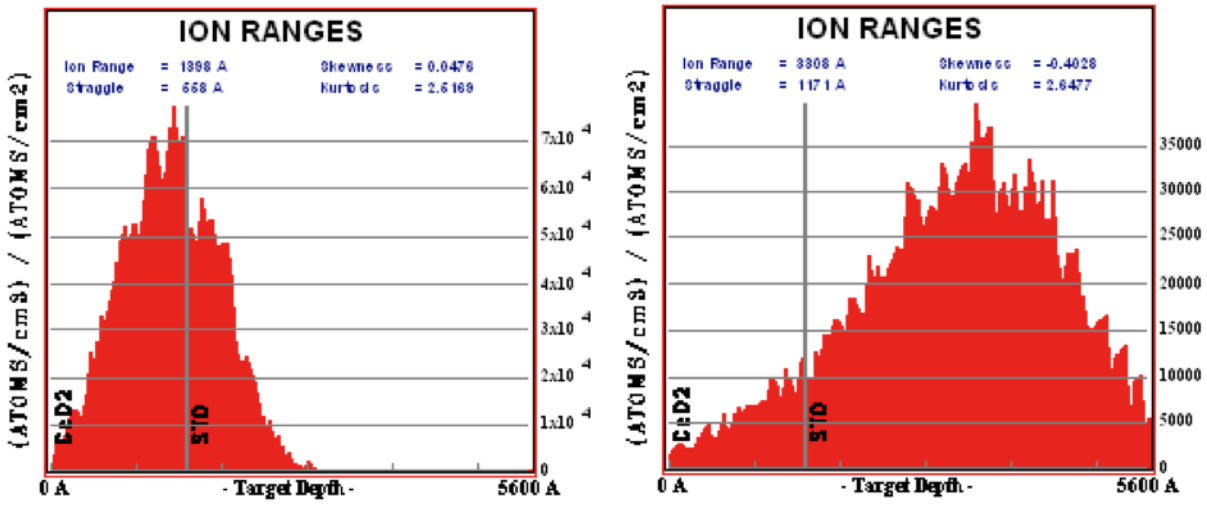

(a) (b)

Figure A.1 (a) The depth distribution of irradiated 700 keV Xe and (b) the depth distribution of irradiated 1MeV Kr into 160 nm CeO_2 thin film on $SrTiO_3$ substrate. (calculated with SRIM 2008)

Table A.1 Estimated peak dpa values in CeO_2 thin film

Dose (ions/cm^2)	700 keV Xe^+	1 MeV Kr^+
$2x10^{16}$	132.85	65.94
$5x10^{16}$	265.70	131.89
$1x10^{17}$	531.39	263.77

A.2 Microstructure of unirradiated CeO_2

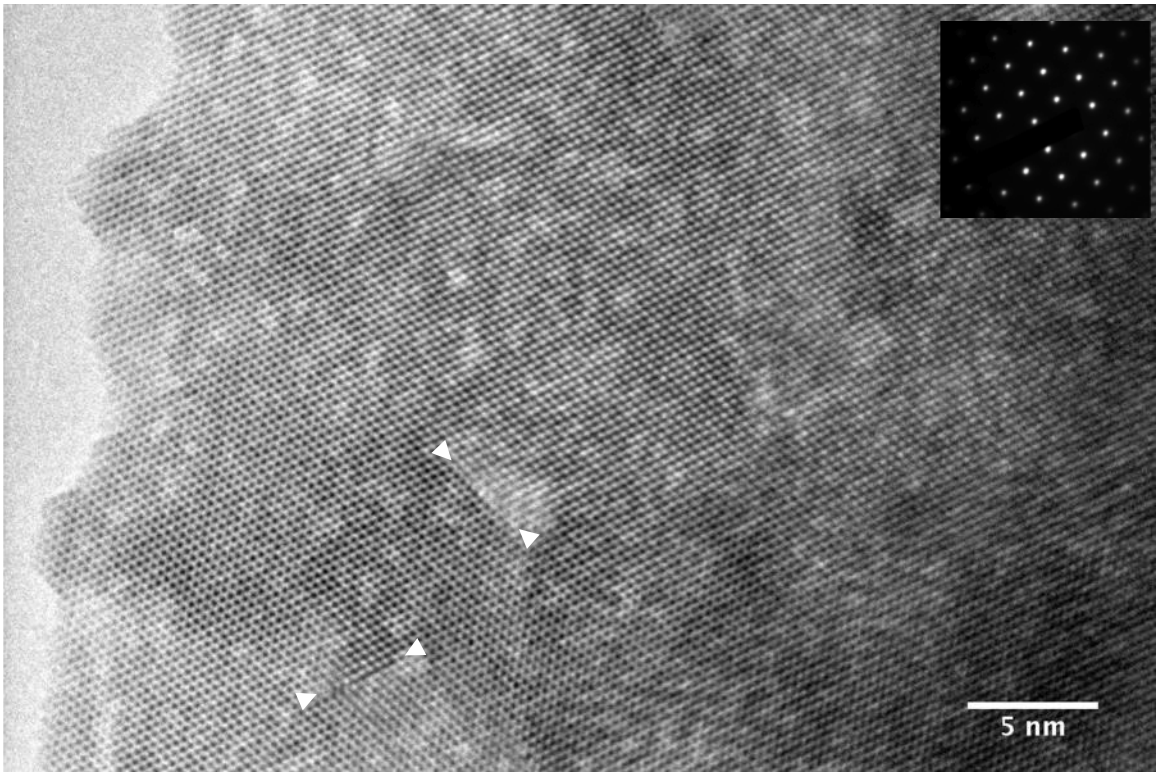

Figure A.2 Cross-section HRTEM image of CeO_2 before irradiation. There are two dislocations (indicated by pairs of arrows) in this area, caused by thin film growth or sample preparation. Electron beam is along [011] direction.

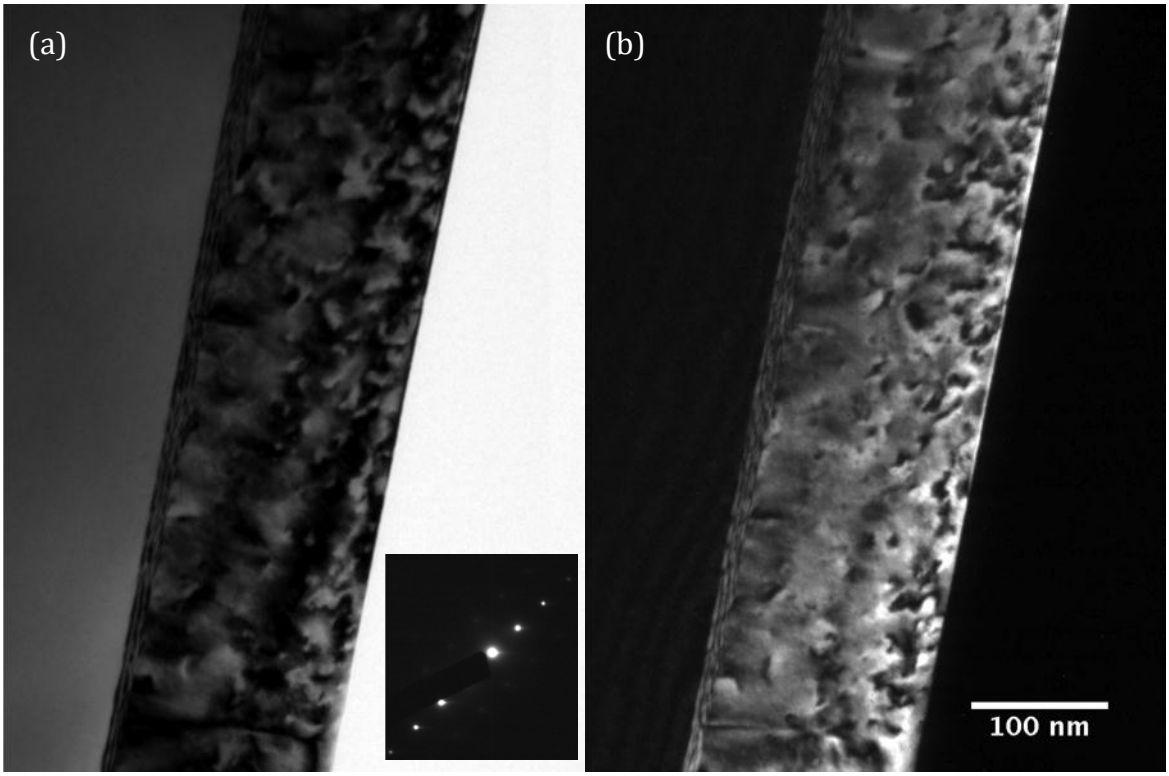

Figure A.3 Cross-section (a) bright-field and (b) dark-field images of CeO_2 thin film on STO substrate before irradiation.

The thickness of thin film is ~160 nm. Preexisted defects/defect clusters can be easily found, which were generated during thin film growth.

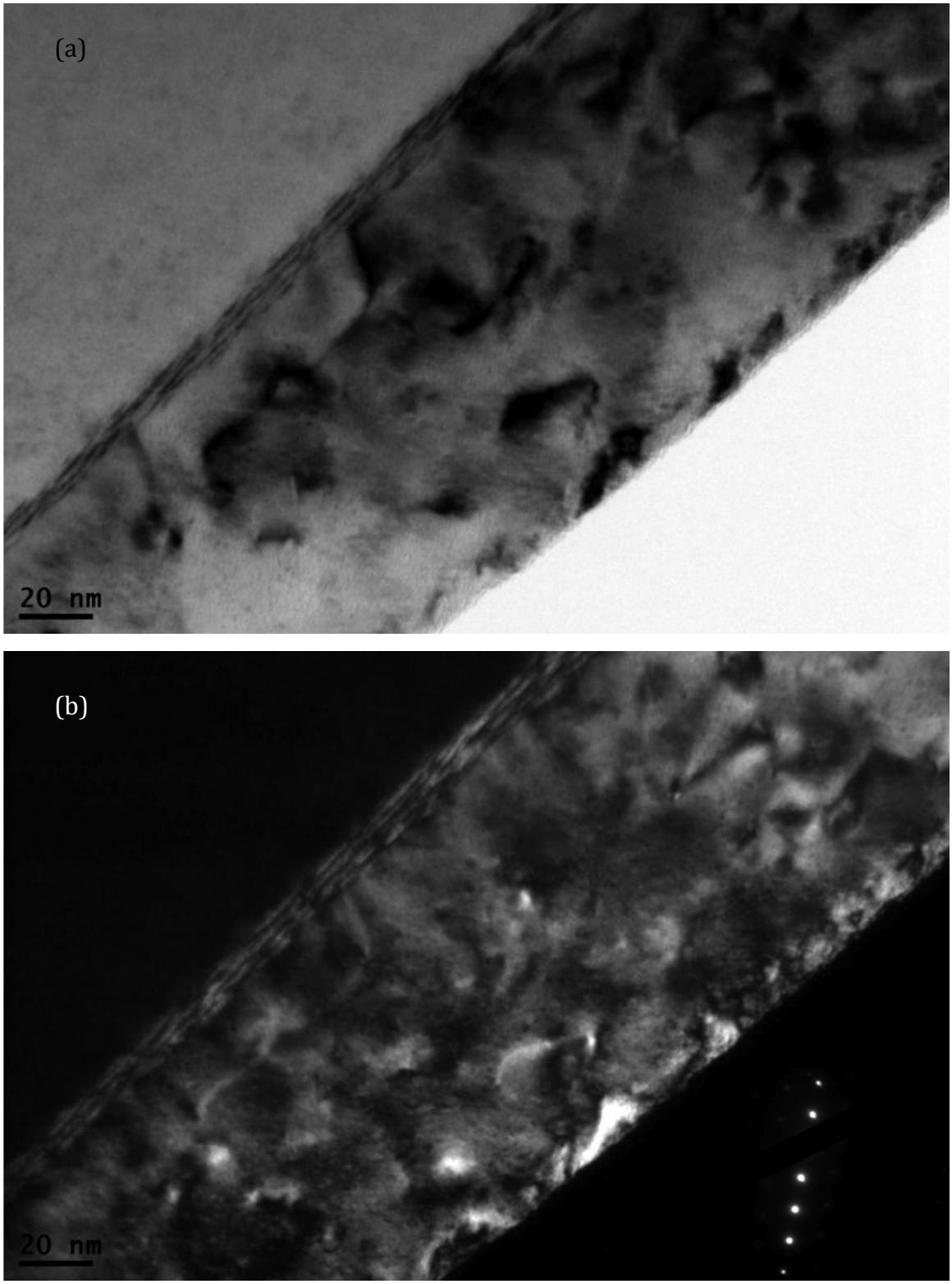

Figure A.4 Cross-section (a) bright-field and (b) dark-field images of CeO_2 thin film on STO substrate before irradiation. These images are taken along the electron beam direction of [011], and the diffraction vector g = [1-11].

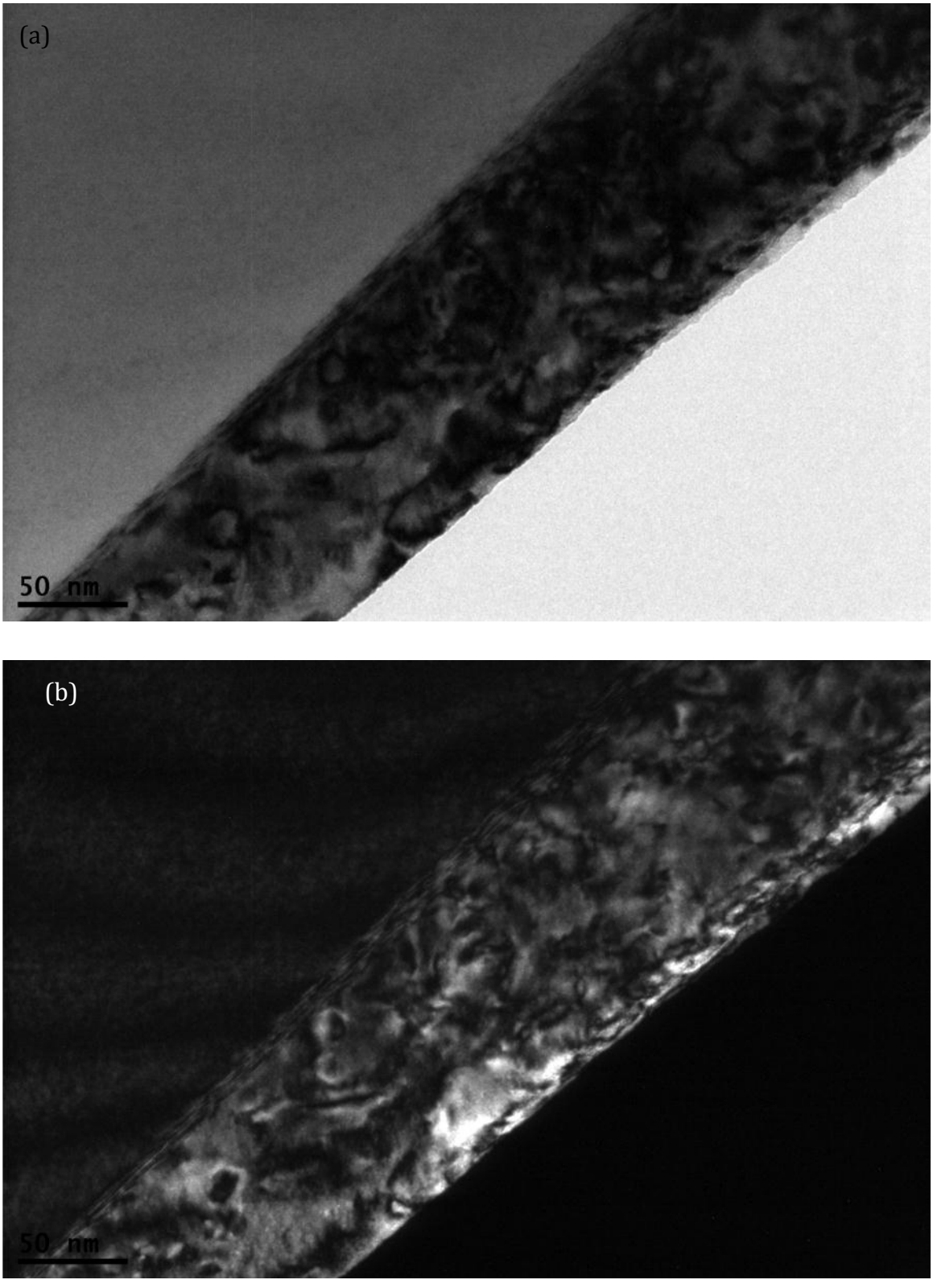

Figure A.5 Cross-section (a) bright-field and (b) dark-field images of CeO_2 thin film on STO substrate before irradiation. These images are taken along the electron beam direction of [011], and the diffraction vector g = [-200]

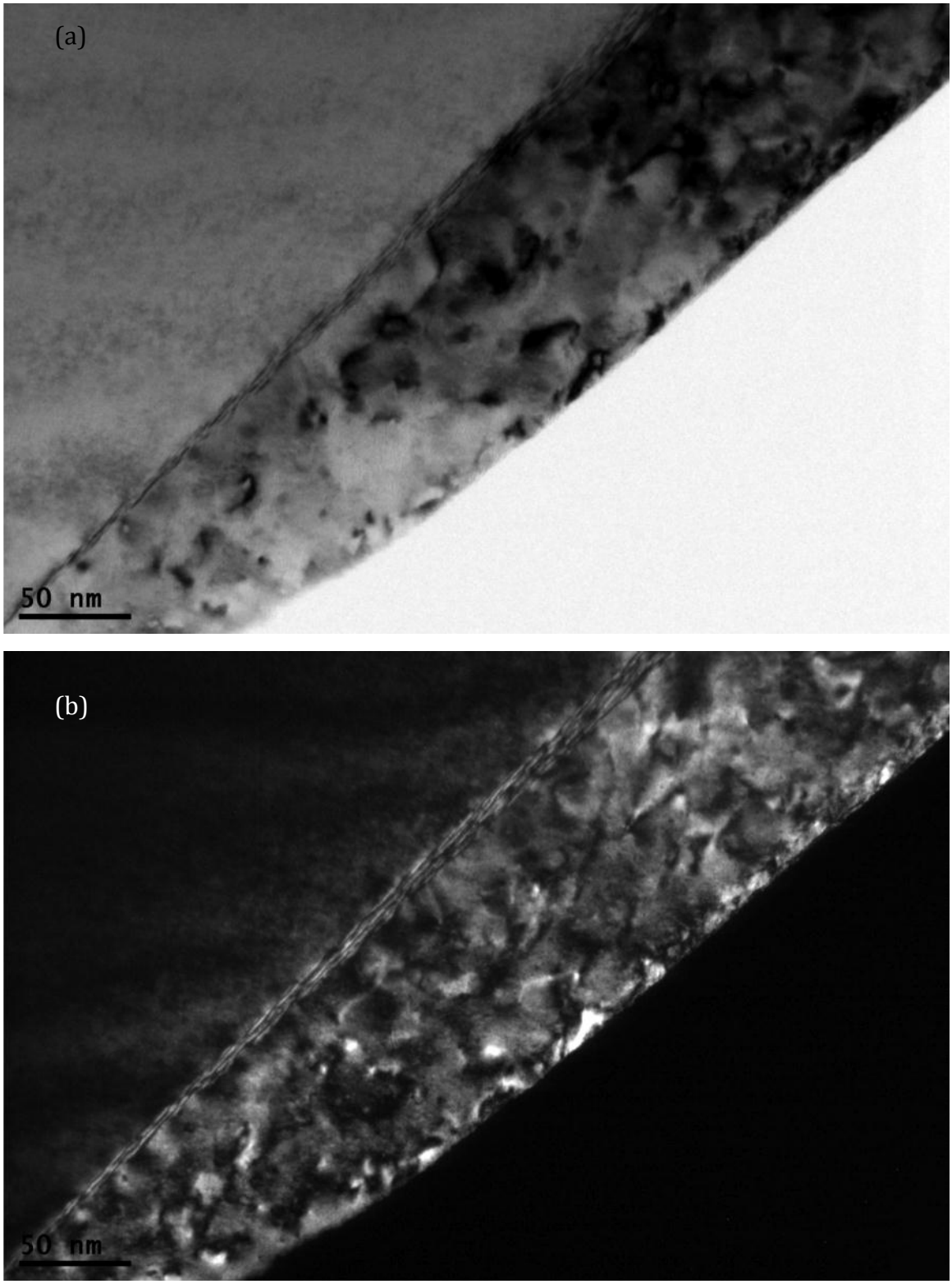

Figure A.6 Cross-section (a) bright-field and (b) dark-field images of CeO_2 thin film on STO substrate before irradiation. These images are taken along the electron beam direction of [011], and the diffraction vector g = [1-11].

A.3 Microstructure of CeO_2 irradiated with 700 keV Xe^+ at 600°C

A.3.1 Irradiation dose is $2x10^{16}$ ions/cm^2

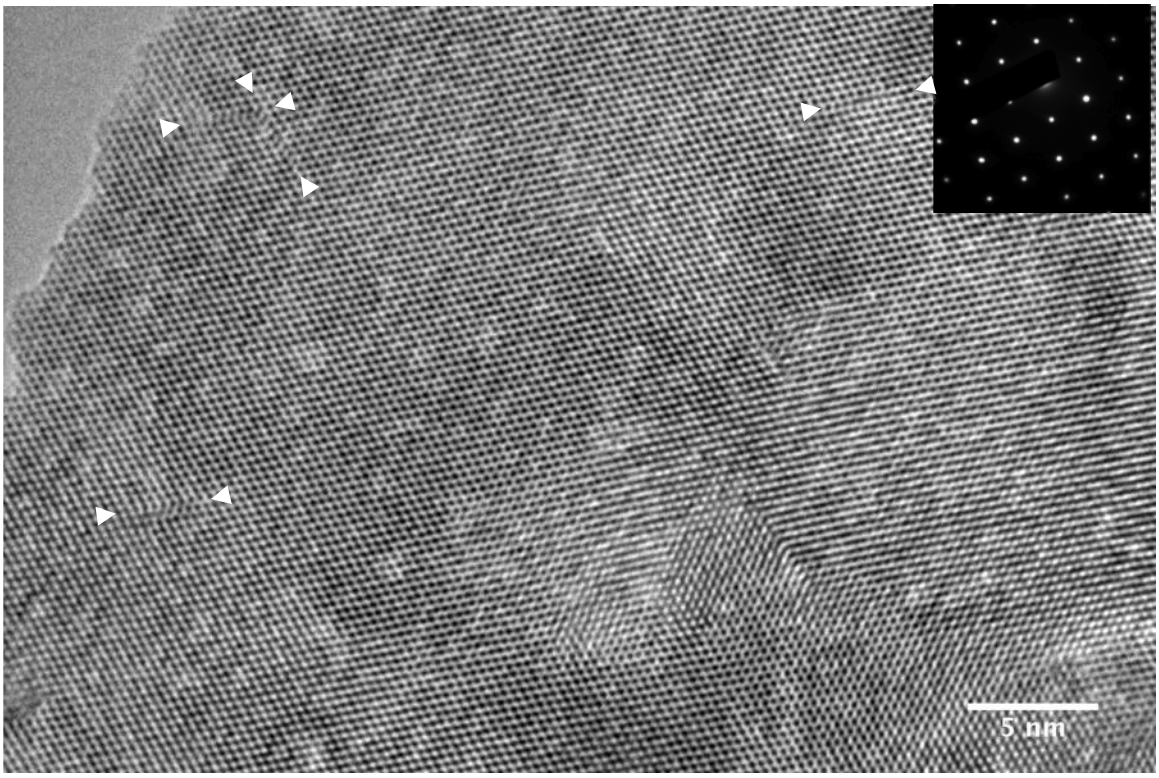

Figure A.7 Cross-section HRTEM image of CeO_2 irradiated at 600°C with 700 keV Xe^+ to the dose of $2x10^{16}$ ions/cm^2. Edge dislocations and dislocation loops are indicated by pairs of arrows.

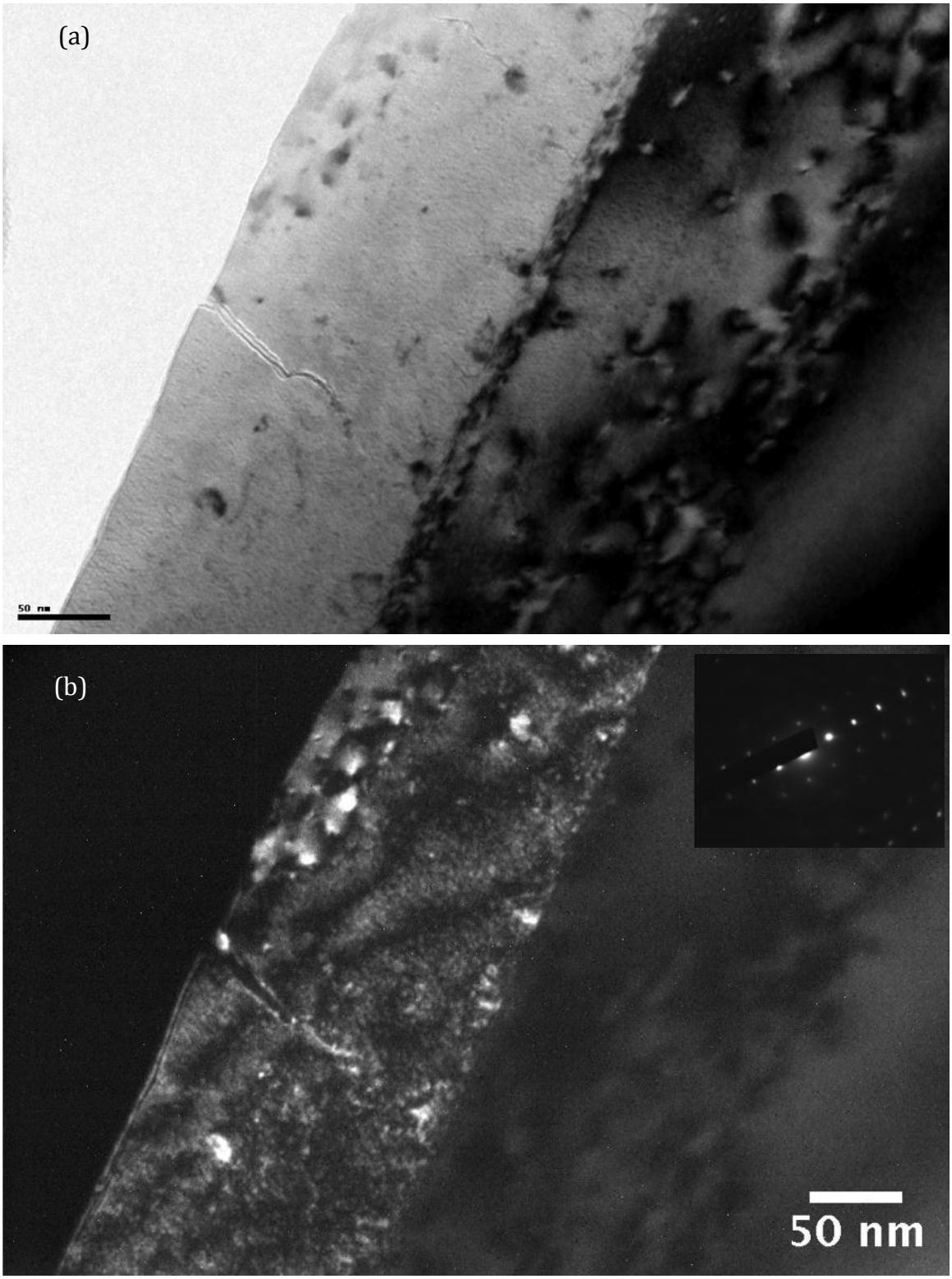

Figure A.8 Cross-section (a) bright-field and (b) dark-field TEM images of CeO_2 irradiated with 700 keV Xe^+ at 600°C to a dose of $2x10^{16}$ ions/cm^2.

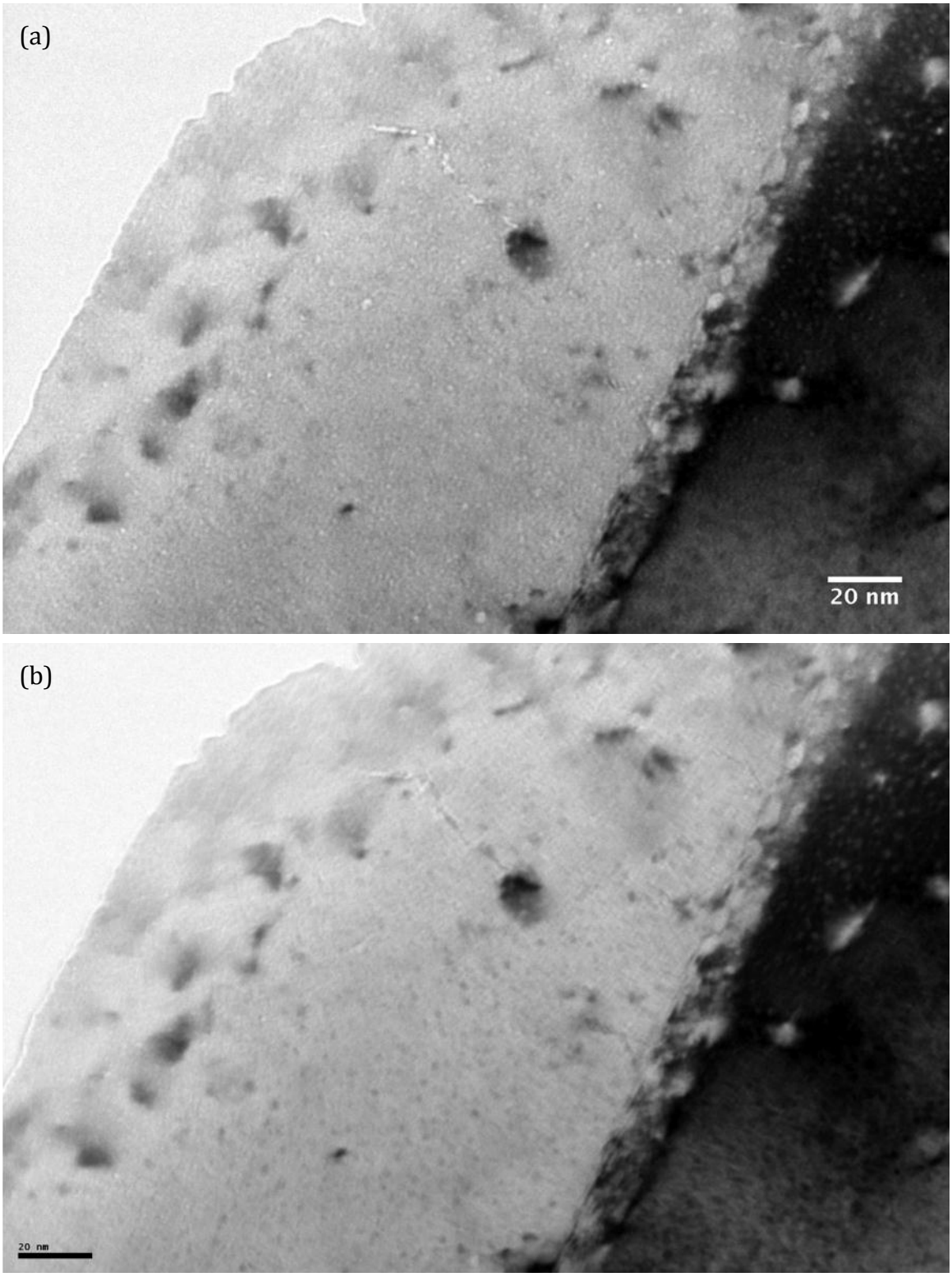

Figure A.9 Cross-section bright-field images of CeO_2 irradiated with 700 keV Xe^+ at 600°C to a dose of $2x10^{16}$ ions/cm^2, registered by (a) under-focusing and (b) over-focusing the objective lens.

Electron diffraction patterns show that CeO_2 thin film and bombarded STO substrate remains crystalline. There are no distorted diffraction spots observed. The stopping range of Kr ions is ~165 nm. The thin film thickness after irradiation is ~ 155 nm, 5 nm less than the original specimen. Gas bubbles are displayed as white dots surrounded by black edges in Fig. 2.3(a) and black dots in Fig. 2.3(b). Most of bubbles are in a size of ~1 nm in diameter, while the big ones can reach a size of ~3 nm in diameter. At this irradiation condition, bubbles are able to move and merge. Some bubbles gather together and form a line. This line will develop into a crack when it reaches the surface, so that gas will be released from the crystal.

A.3.2 Irradiation dose is $5x10^{16}$ ions/cm^2

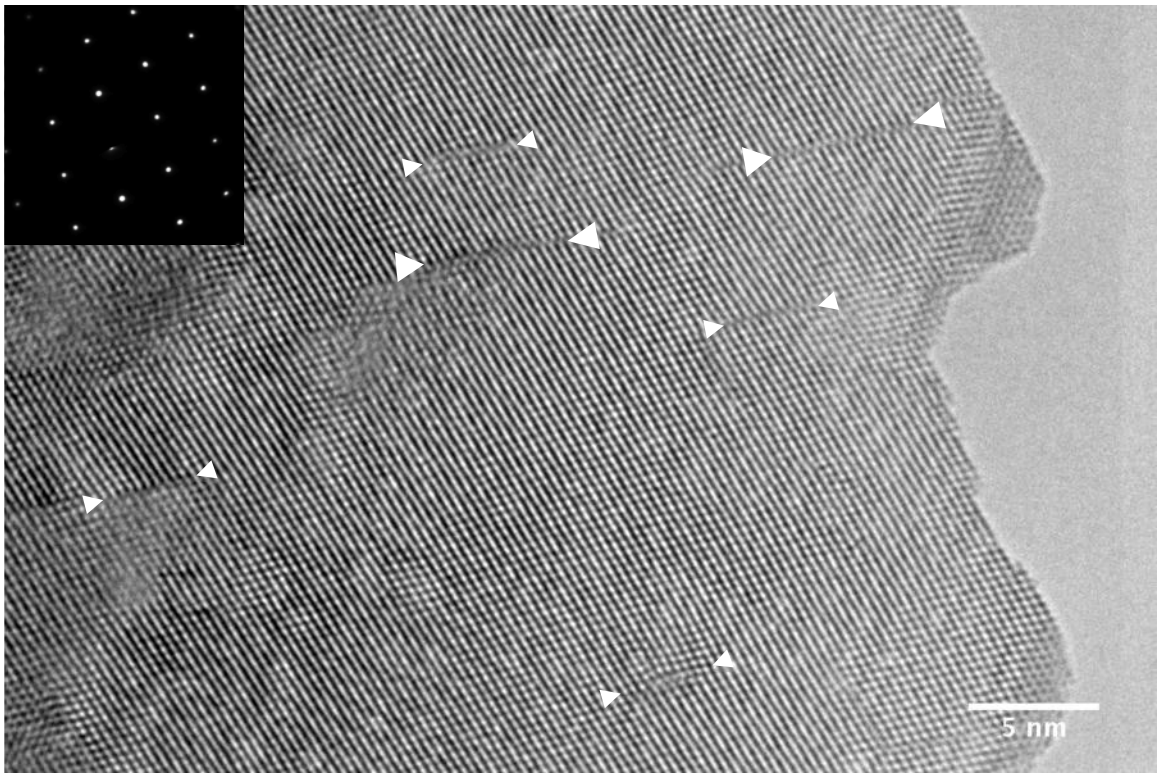

Figure A.10 Cross-section HRTEM image of CeO_2 irradiated at 600°C with 700 keV Xe^+ to the dose of $5x10^{16}$ ions/cm^2. Edge dislocations and dislocation loops are indicated by pairs of arrows.

Density and size of dislocations increase compared to the specimen irradiated to the dose of $2x10^{16}$ ions/cm^2. These dislocations are Ce interstitial dislocations whose direction is [111].

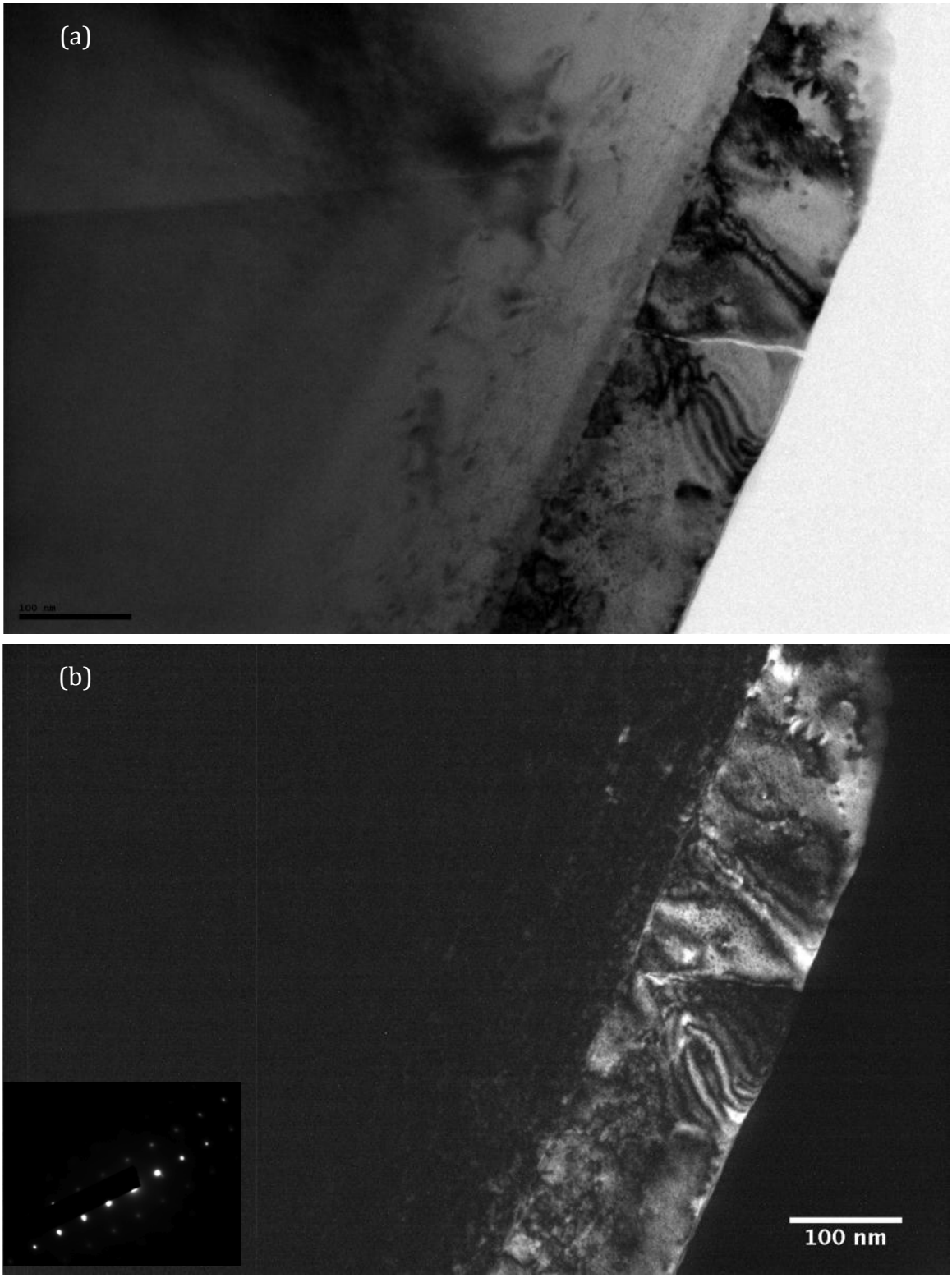

Figure A.11 Cross-section (a) bright-field and (b) dark-field TEM images of CeO_2 irradiated with 700 keV Xe^+ at 600°C to a dose of $5x10^{16}$ ions/cm^2.

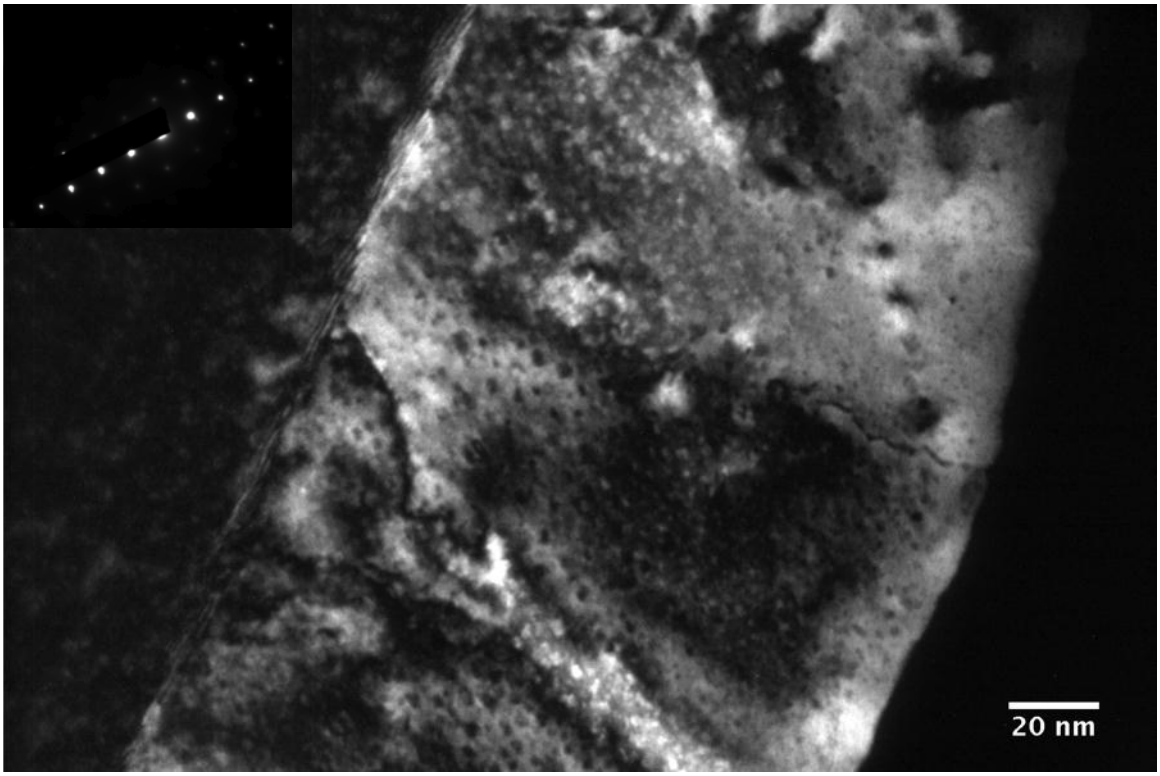

Figure A.12 Dark-field TEM image of CeO_2 irradiated with 700 keV Xe^+ at 600°C to a dose of $5x10^{16}$ ions/cm^2.

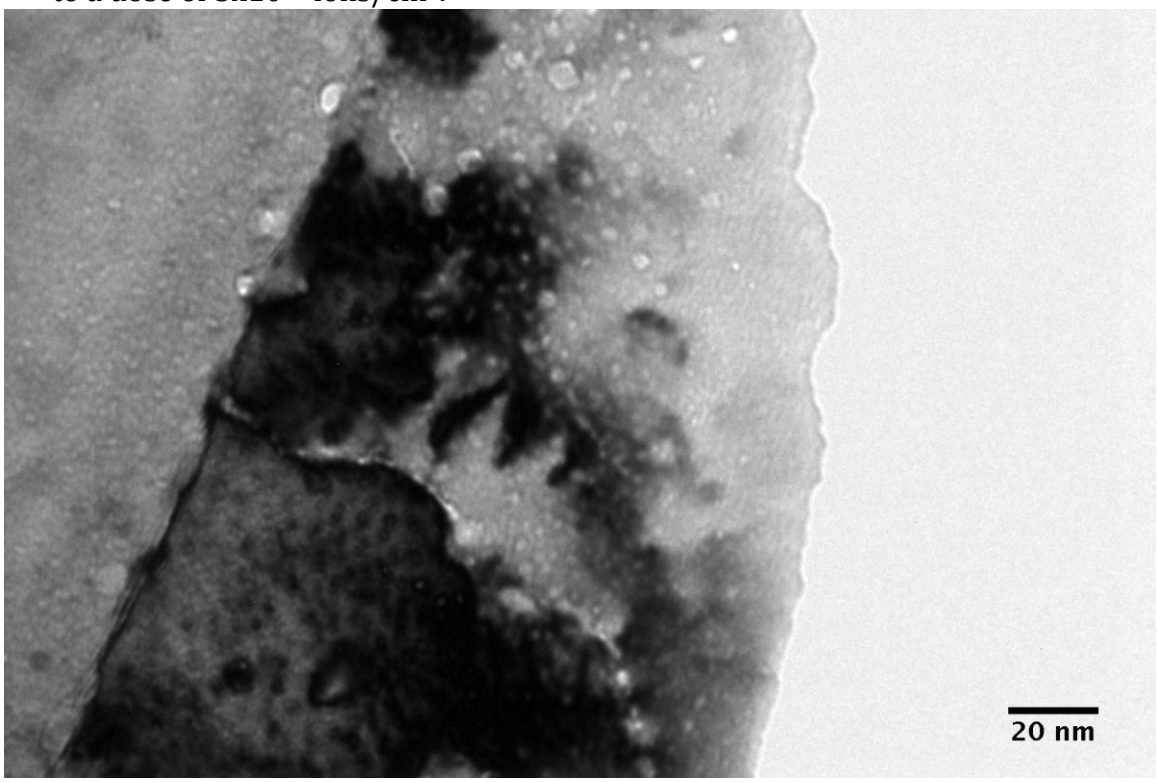

Figure A.13 Bright-field TEM image of CeO_2 irradiated with 700 keV Xe^+ at 600°C to a dose of $5x10^{16}$ ions/cm^2.

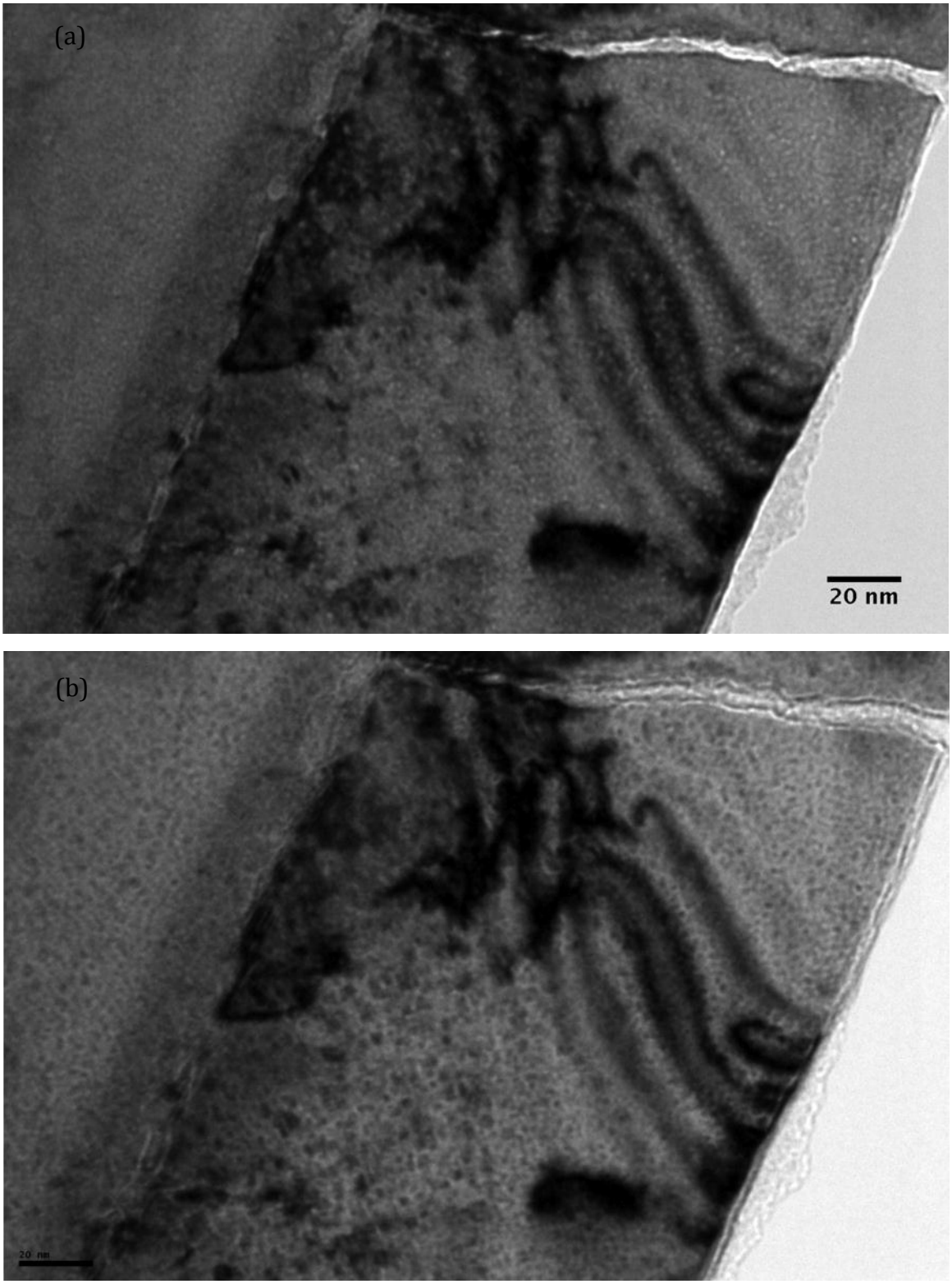

Figure A.14 Cross-section bright-field images of CeO_2 irradiated with 700 keV Xe^+ at 600°C to a dose of $5x10^{16}$ ions/cm^2, registered by (a) under-focusing and (b) over-focusing the objective lens.

Dislocation loops in dark hemispherical shape can be seen on figure A.12 and A.13. The size of these loops is in a range of 3 – 5 nm. There are two types of features on figure A.12: dark hemispherical dislocations and dot-like dislocation. The nature of these features will be confirmed further. Another guess for the hemispherical feature is precipitate of Xe or another phase of cerium oxide. Gas bubbles are displayed with reversed contrast in figure A.14 (a) and (b). Bubbles in this area have a size of ~1 nm in diameter. In thinner area, the bubble size can reach 6 nm in diameter as shown in figure A.13. The variance of bubble size in different area might be caused by Argon ion milling. The CeO_2 thin film thickness measured in figure A.14 is ~150 nm. Compared to the original specimen, CeO_2 thin film is reduced by 10 nm at this irradiation dose.

A.3.3 Irradiation dose is $1x10^{17}$ ions/cm^2

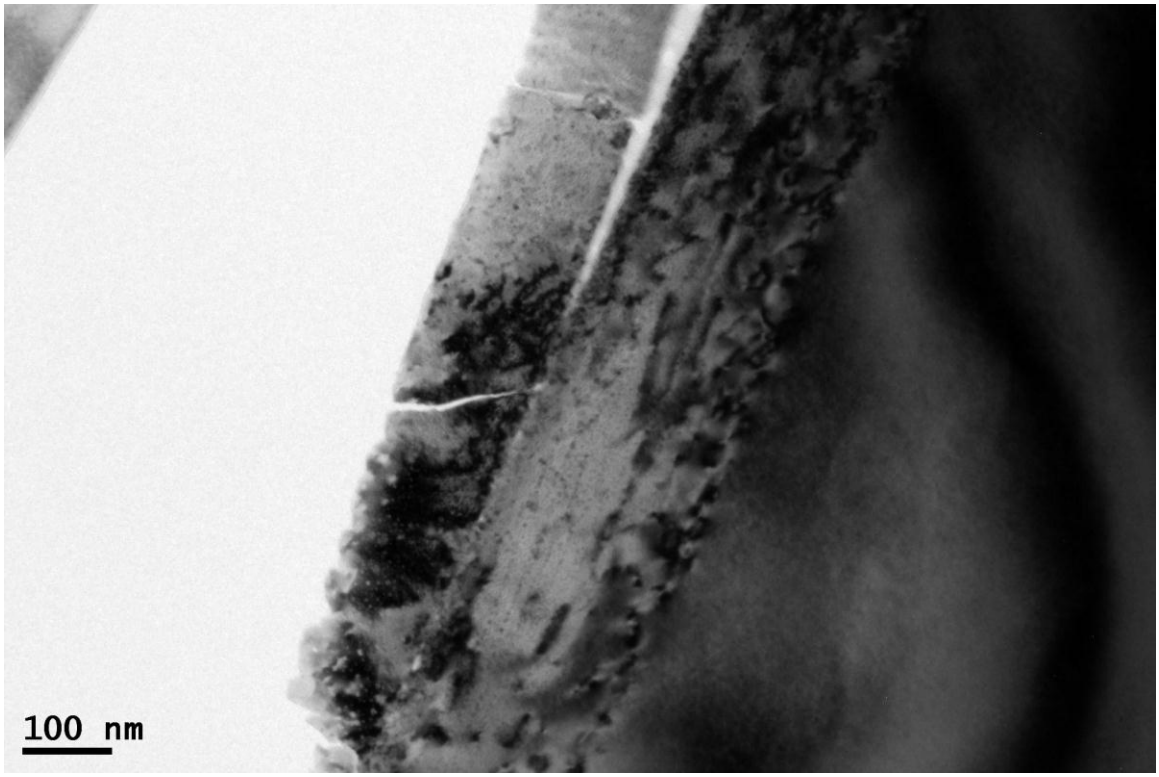

Figure A.15 Cross-section bright-field image of CeO_2 irradiated with 700 keV Xe^+ at 600°C to a dose of $1x10^{17}$ ions/cm^2.

The measured thickness of CeO_2 thin film is ~145 nm, which is 15 nm thinner than unirradiated thin film. This is due to the sputtering process during irradiation. Xe stopping range in substrate is 220 nm.

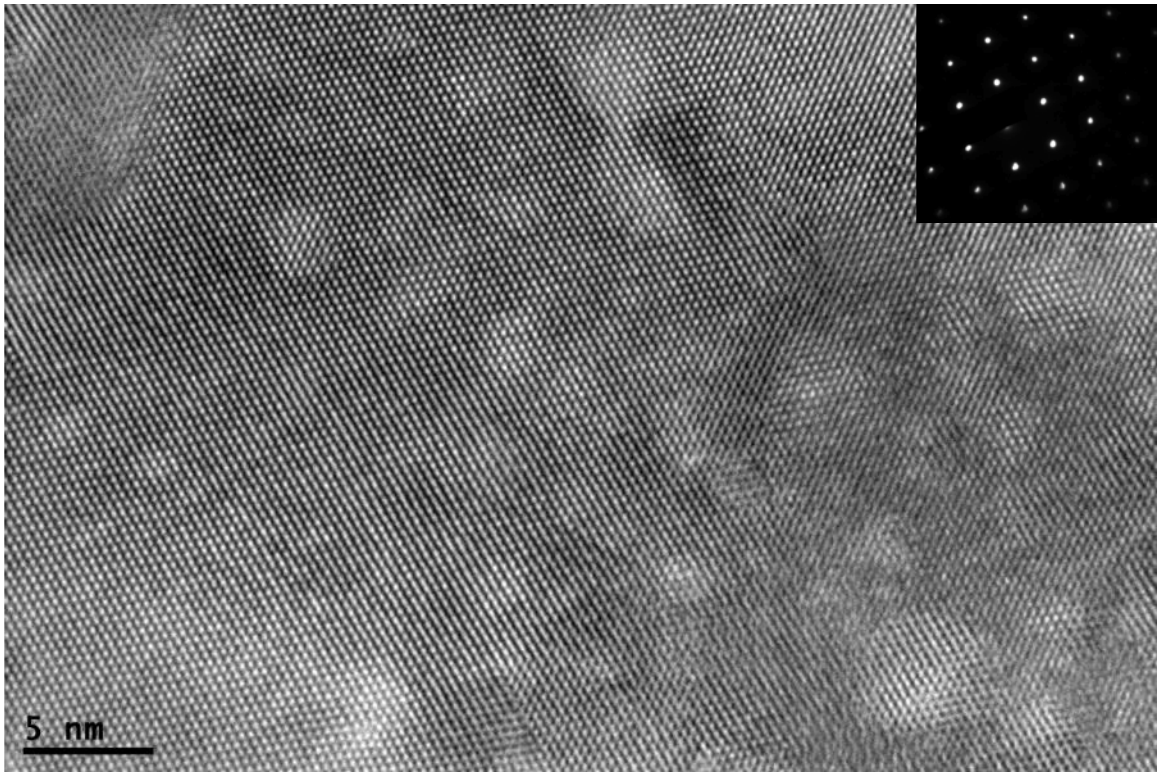

Figure A.16 Cross-section HRTEM image of CeO_2 irradiated with 700 keV Xe^+ at 600°C to a dose of $1x10^{17}$ ions/cm^2.

It is difficult to find dislocations when electron beam are right on the zone axis, because few missing/extra atom layers can not be reflected on lattice image. There are only few dislocations appear on this image. The inset diffraction pattern also show the specimen remains single crystalline. There are no distorted spots observed.

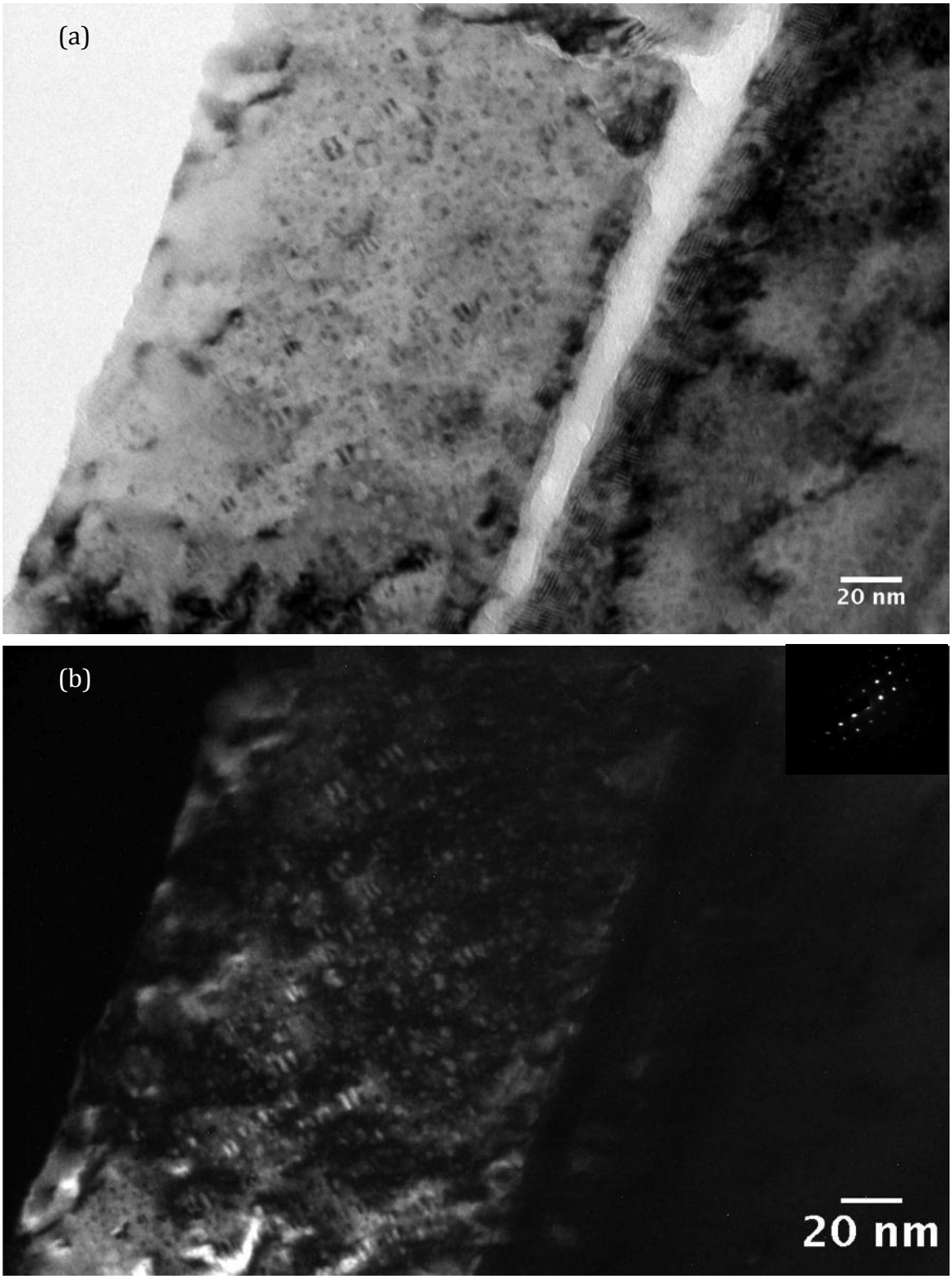

Figure A.17 Cross-section (a) bright-field and (b) dark-field TEM images of CeO_2 irradiated with 700 keV Xe^+ at 600°C to a dose of $1x10^{17}$ ions/cm^2. These micrographs are taken along the [011] direction with g = 11-1.

In these images, dislocation loops show elliptical strain contrast. The sizes of dislocation loops are in a range of 3 − 7 nm. The density of dislocation loops is more than 3 times higher than that shown in figure A.12 and A.14.

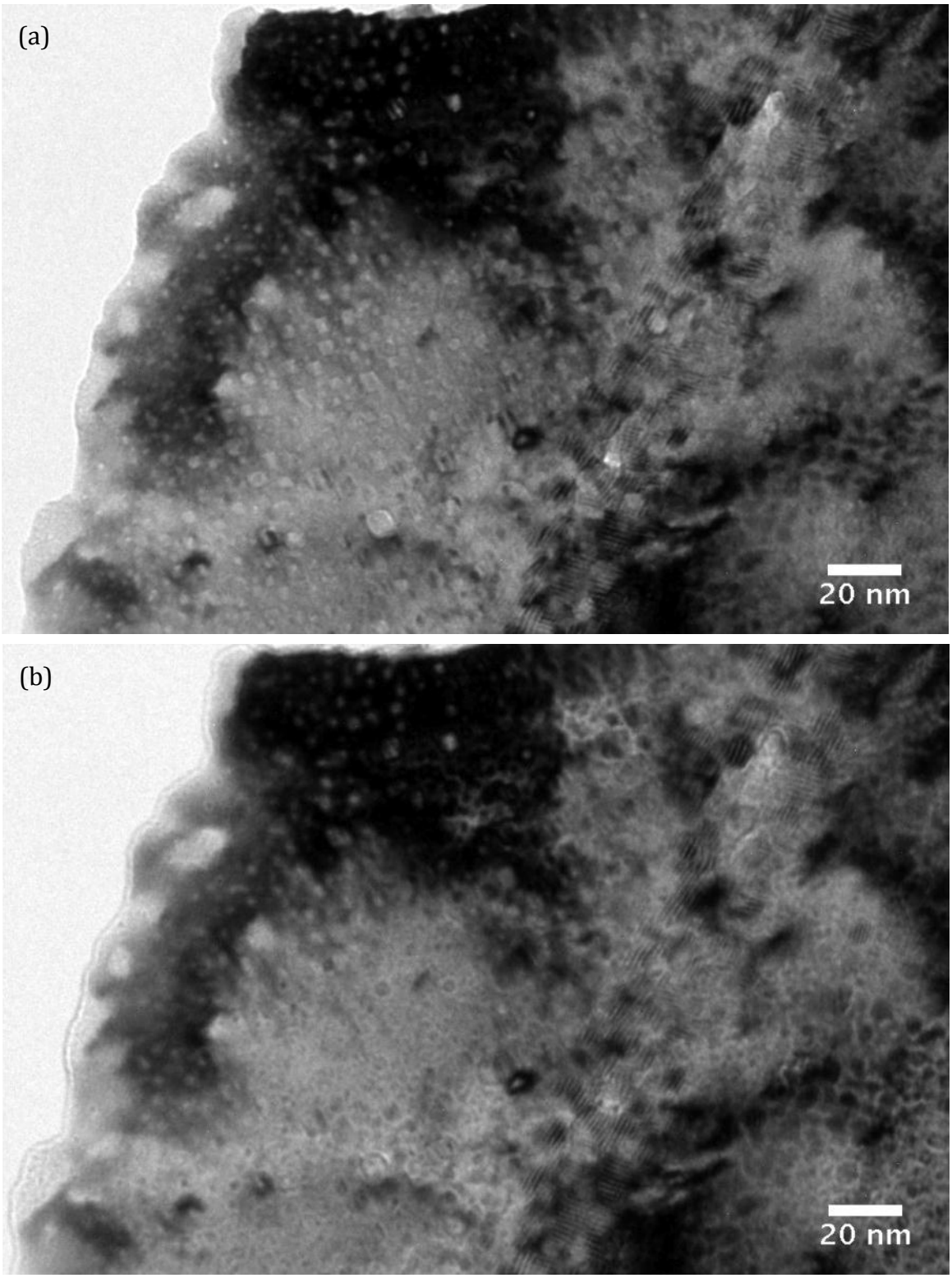

Figure A.18 Cross-section bright-field images of CeO_2 irradiated with 700 keV Xe^+ at 600°C to a dose of $1x10^{17}$ ions/cm^2, registered by (a) under-focusing and (b) over-focusing the objective lens.

A.3.4 Comparison of microstructures of CeO_2 irradiated to different doses

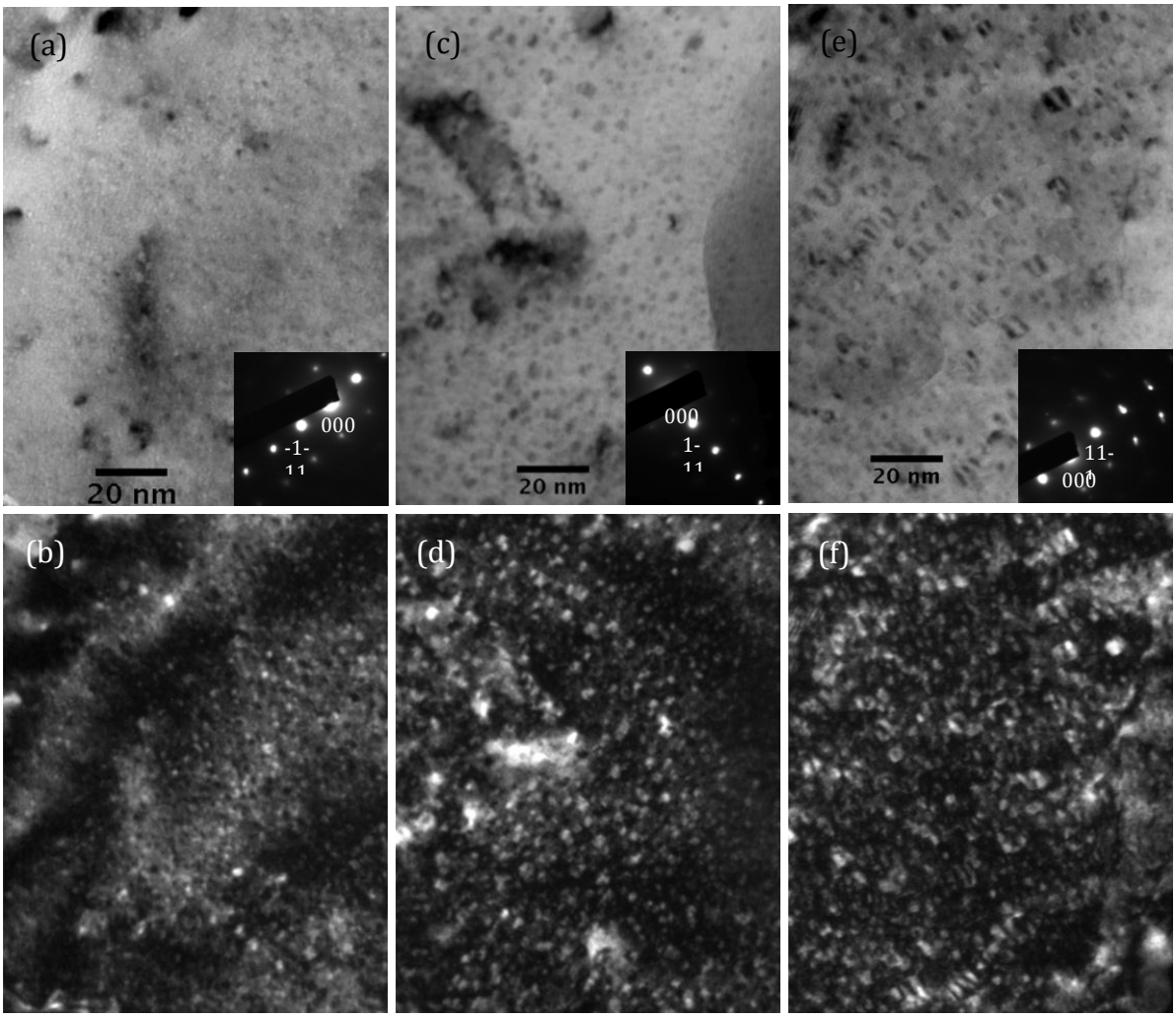

Figure A.19 Bright-field and dark-field electron micrographs of CeO_2 irradiated at 600°C with 700 keV Xe ions. (a) and (b) $2x10^{16}$ ions/cm^2; (c) and (d) $5x10^{16}$ ions/cm^2; (e) and (f) $1x10^{17}$ ions/cm^2.

Figure A.19 show the growth of dislocation loops with the increase of dose during irradiations of 700 keV Xe ions at 600°C. In figure A.19(a), defect clusters/dislocation loops have a mean size of 1.7 nm in diameter, and the maximum size is ~ 2 nm. In the specimens irradiated to higher doses, some of the defect clusters grow into bigger dislocation loops of 4-7 nm appear. The mean diameters are 2.7 nm for the specimen shown in figure A.19(b), and 4.6 nm for the specimen shown in figure A.19(c). When increasing the irradiation dose, size of dislocation loops increases while the density (~ 0.085 nm^{-2}) almost stays unvaried.

The diffraction patterns in insets indicate the crystalline structure of CeO_2 even at the highest dose of $1x10^{17}$ ions/cm^2 (peak dpa is 14.64). The crystal is in [011] direction, and

the dislocation loops lying on the {111} plane. The nature of these dislocation loops is still not clear, which will be investigated further.

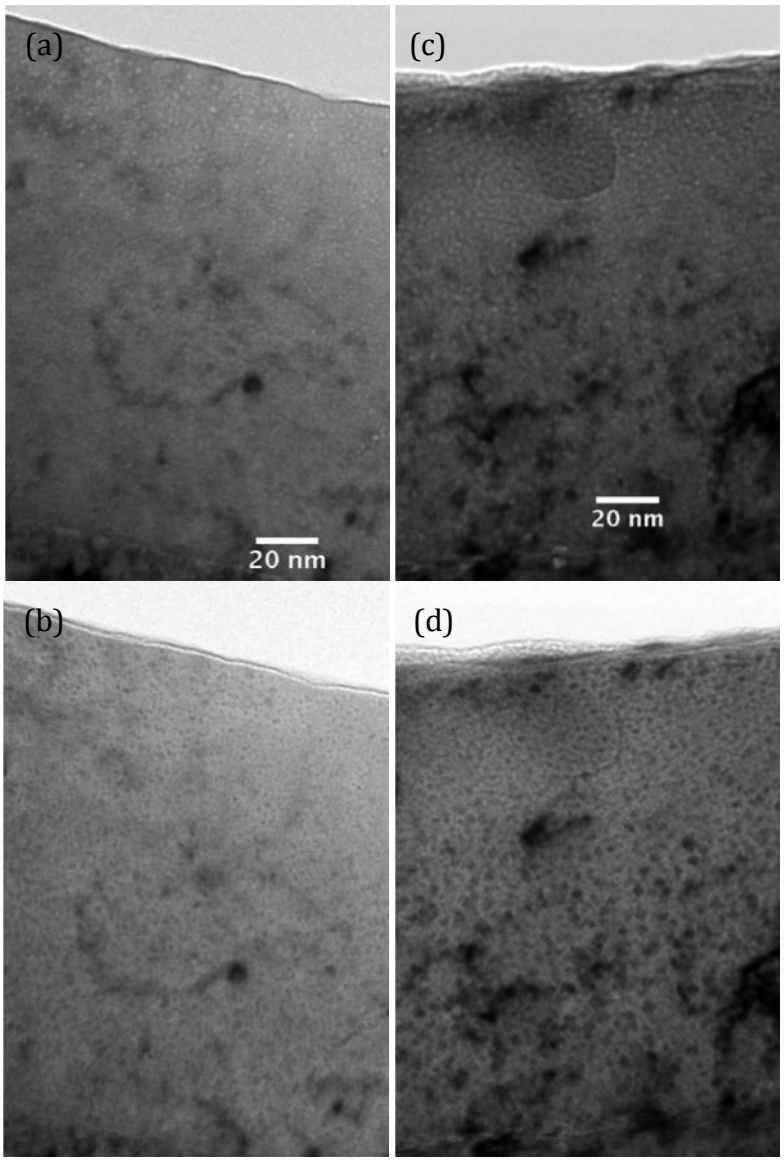

Figure A.20 Bright-field micrographs of CeO_2 irradiated at 600°C with 700 keV Xe ions, registered by (a)(c) underfocusing and (b)(d) overfocusing the objective lens. (a) and (b) $2x10^{16}$ ions/cm^2; (c) and (d) $5x10^{16}$ ions/cm^2.

A.4 Microstructure of CeO_2 irradiated with 1 MeV Kr^+ at 600°C

A.4.1 Irradiation dose is $2x10^{16}$ ions/cm^2

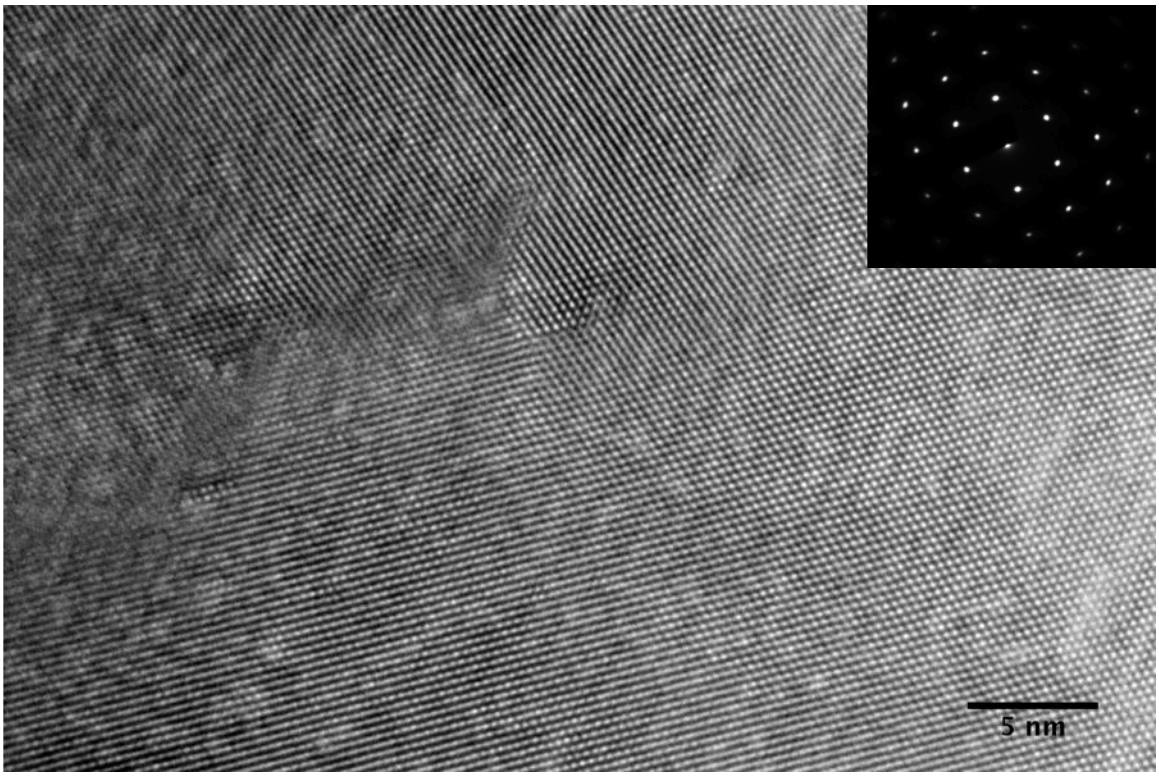

Figure A.21 Cross-section (a) bright-field and (b) dark-field TEM images of CeO_2 irradiated with 1 MeV Kr^+ at 600°C to a dose of $2x10^{16}$ ions/cm^2. These micrographs are taken along the [011] direction with g = 11-1.

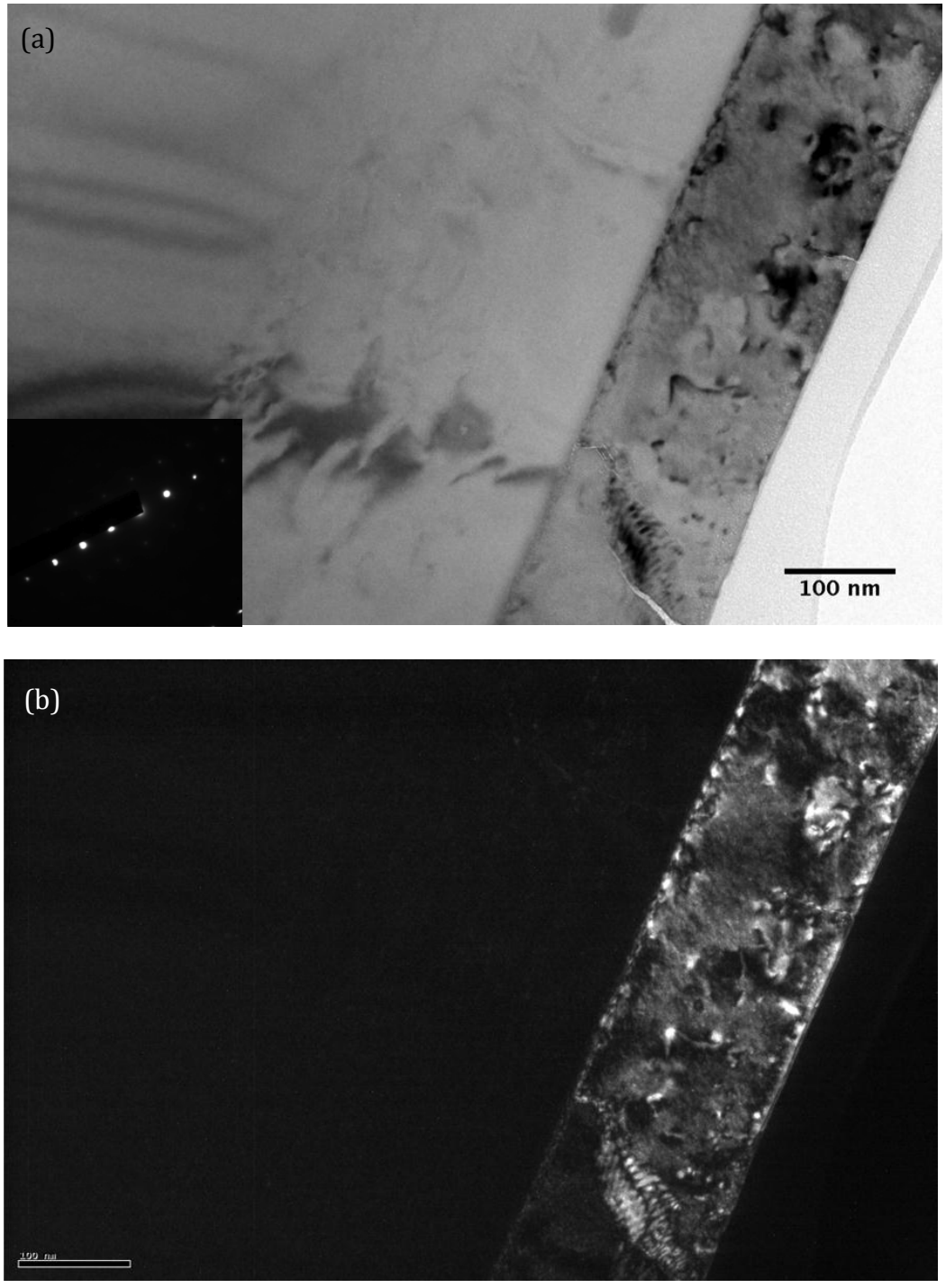

Figure A.22 Cross-section HRTEM image of CeO_2 irradiated with 1 MeV Kr^+ at 600°C to a dose of $2x10^{16}$ ions/cm^2.

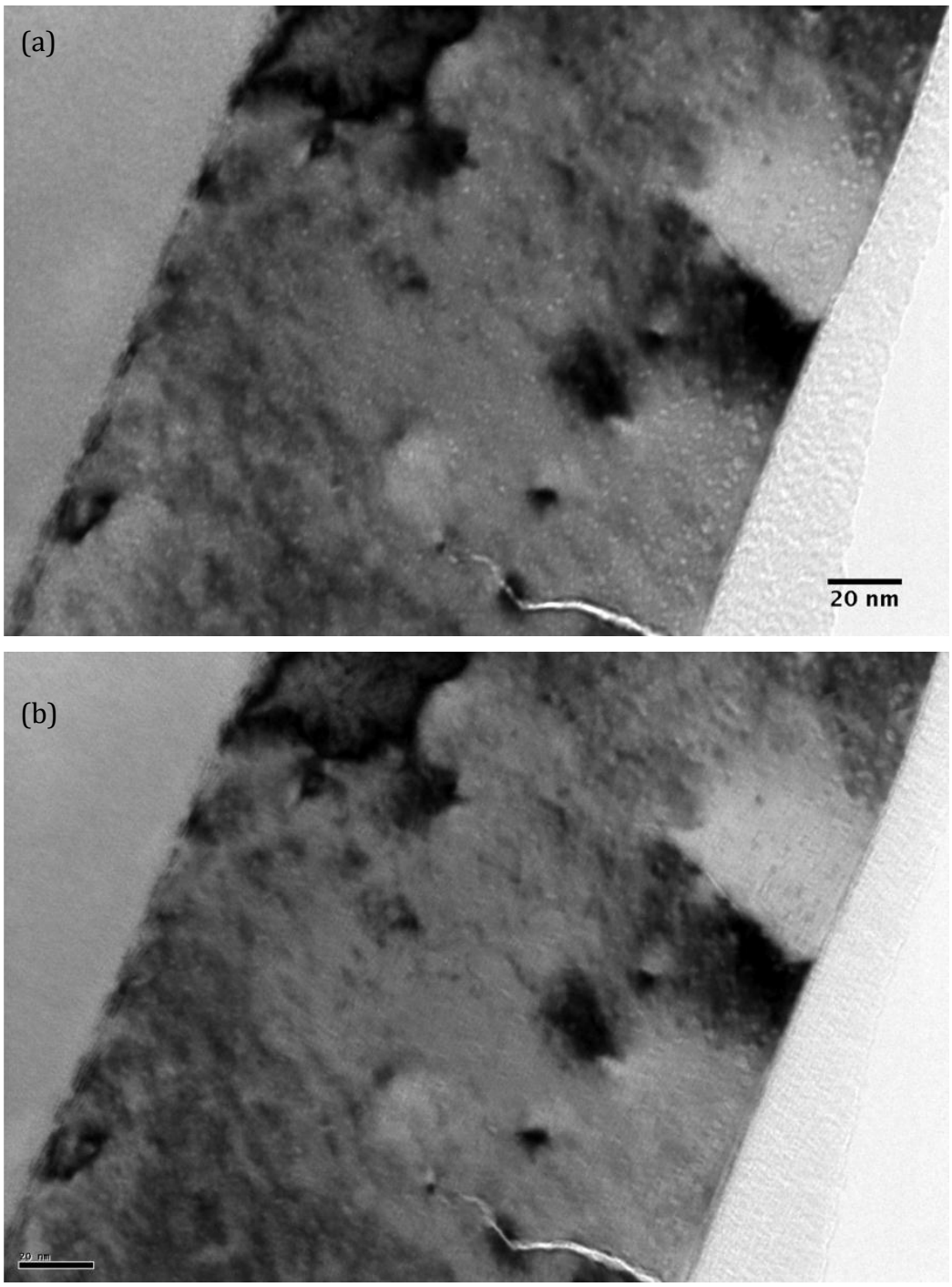

Figure A.23 Cross-section bright-field images of CeO_2 irradiated with 1 MeV Kr^+ at 600°C to a dose of $2x10^{16}$ ions/cm^2, registered by (a) under-focusing and (b) over-focusing the objective lens.

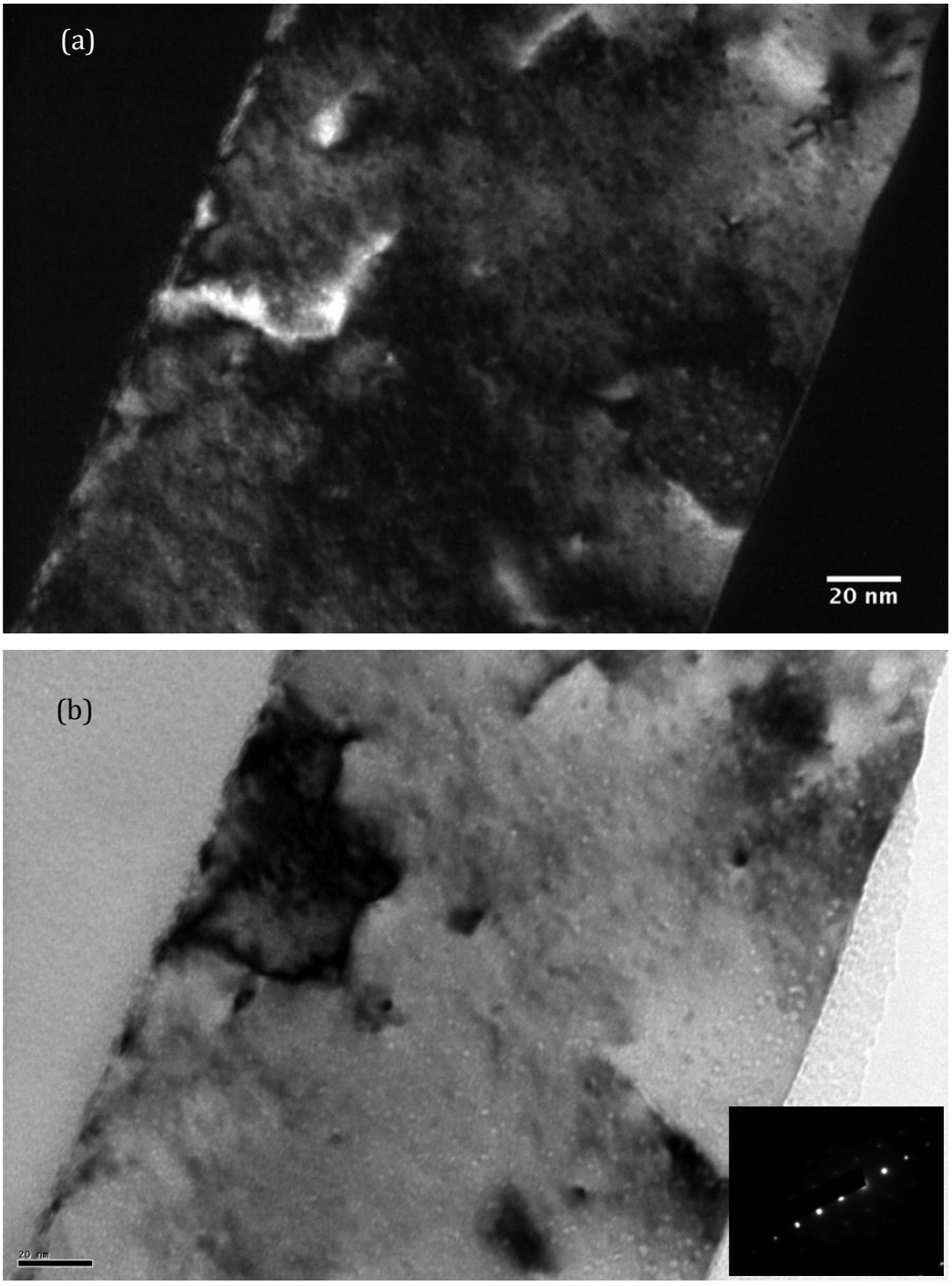

Figure A.24 Cross-section (a) bright-field and (b) dark-field TEM images of CeO_2 irradiated with 1 MeV Kr^+ at 600°C to a dose of $2x10^{16}$ ions/cm^2. These micrographs are taken along the [011] direction with g = 11-1.

A.4.2 Irradiation dose is $5x10^{16}$ ions/cm^2

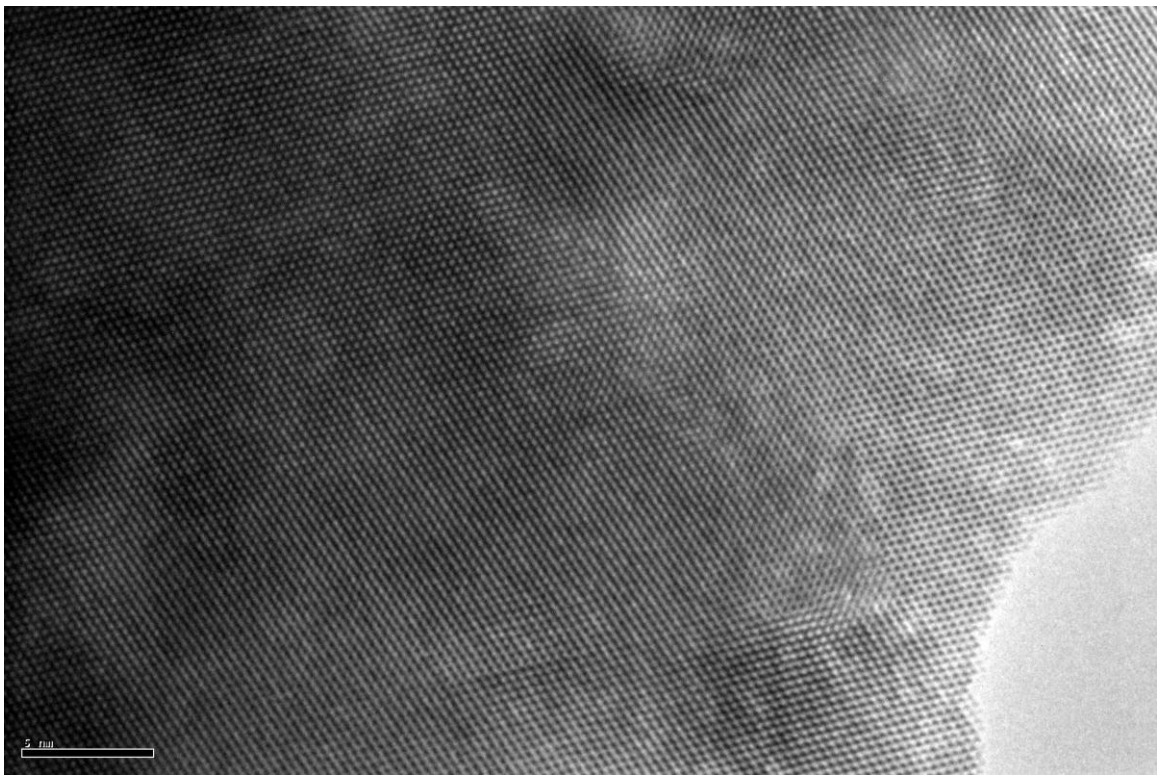

Figure A.25 Cross-section HRTEM image of CeO_2 irradiated with 1 MeV Kr^+ at 600°C to a dose of $5x10^{16}$ ions/cm^2.

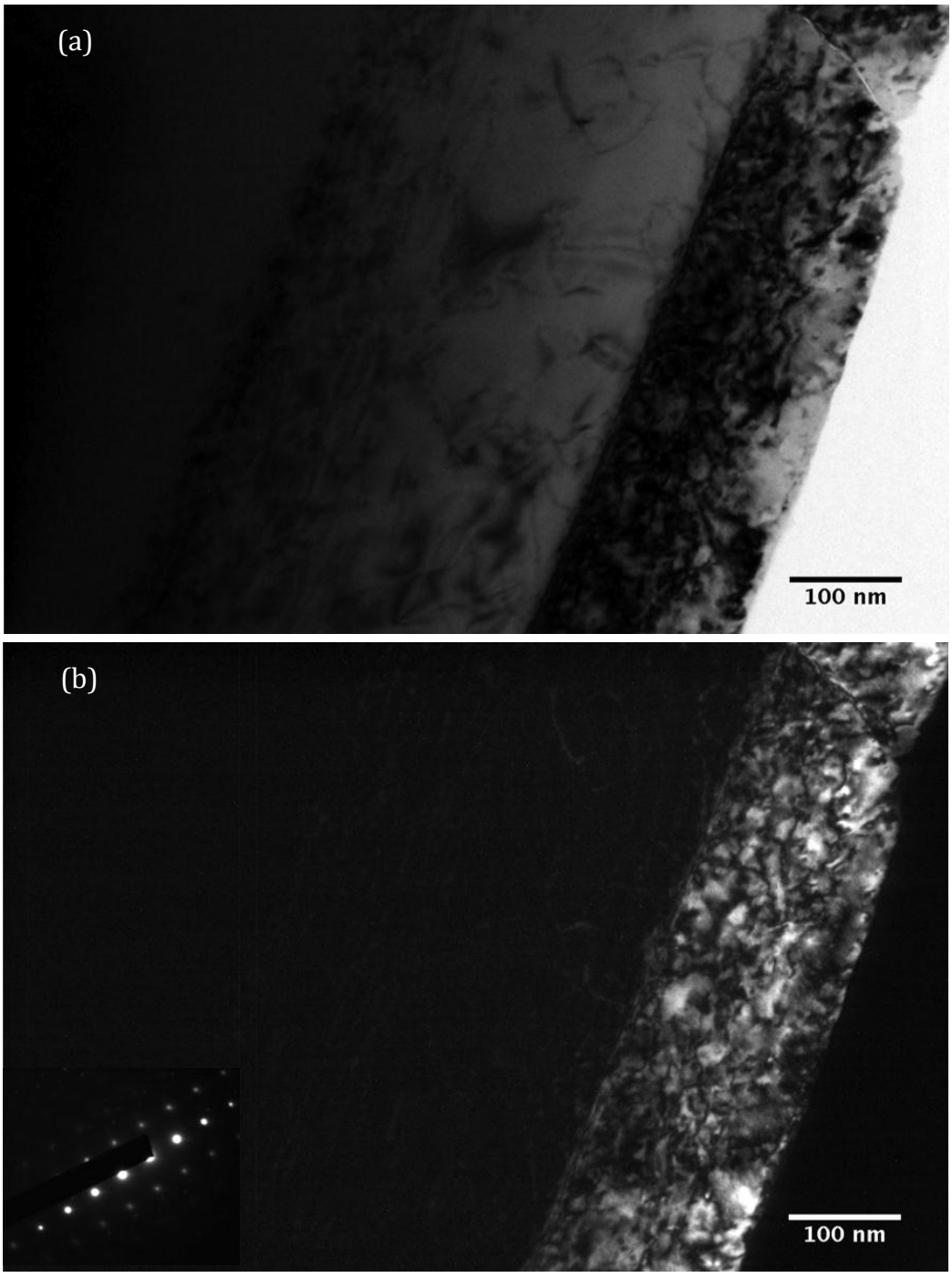

Figure A.26 Cross-section (a) bright-field and (b) dark-field TEM images of CeO_2 irradiated with 1 MeV Kr^+ at 600°C to a dose of $5x10^{16}$ ions/cm^2. These micrographs are taken along the [011] direction with g = 11-1.

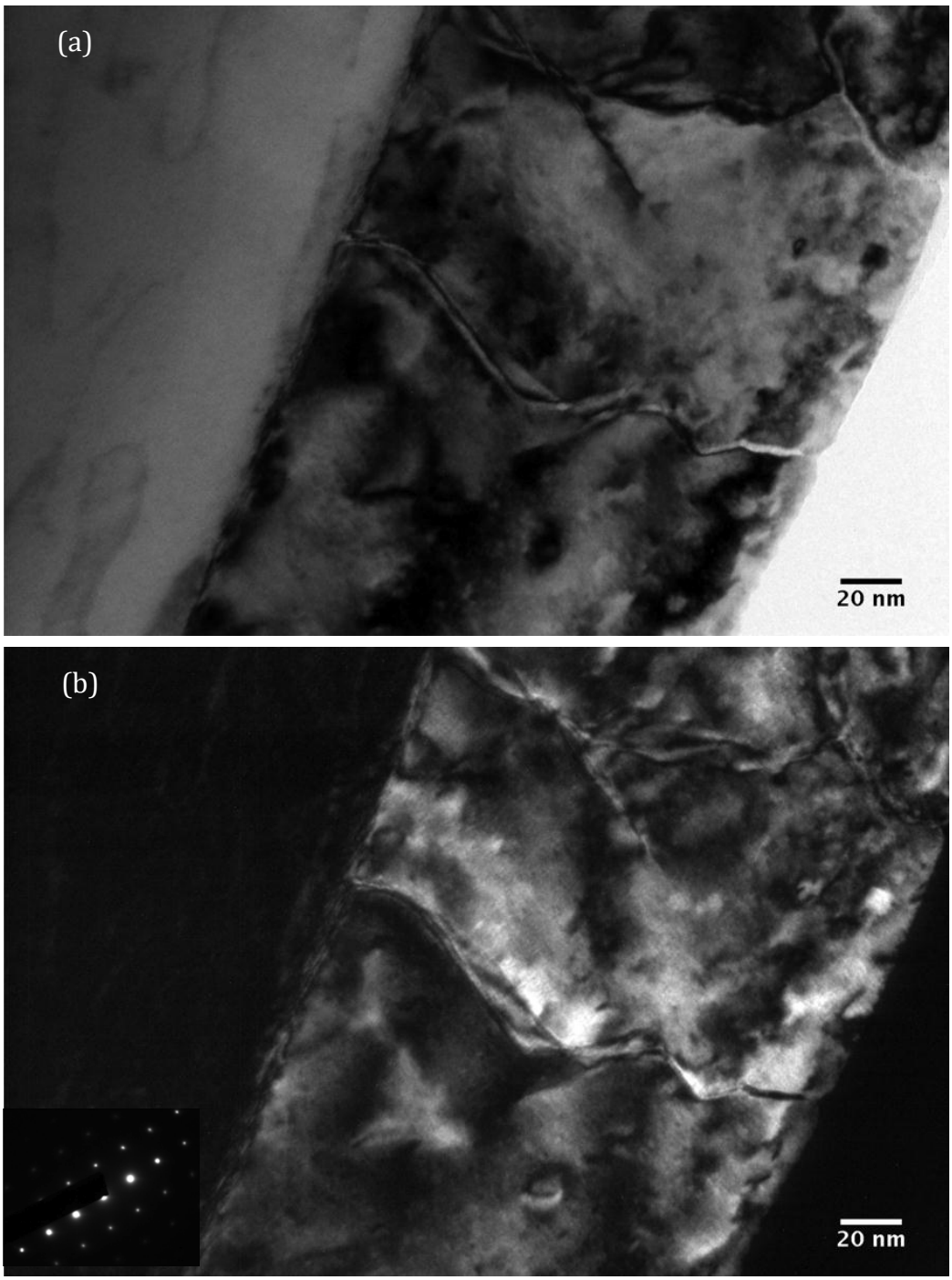

Figure A.27 Cross-section (a) bright-field and (b) dark-field TEM images of CeO_2 irradiated with 1 MeV Kr^+ at 600°C to a dose of $5x10^{16}$ ions/cm^2. These micrographs are taken along the [011] direction with g = 11-1.

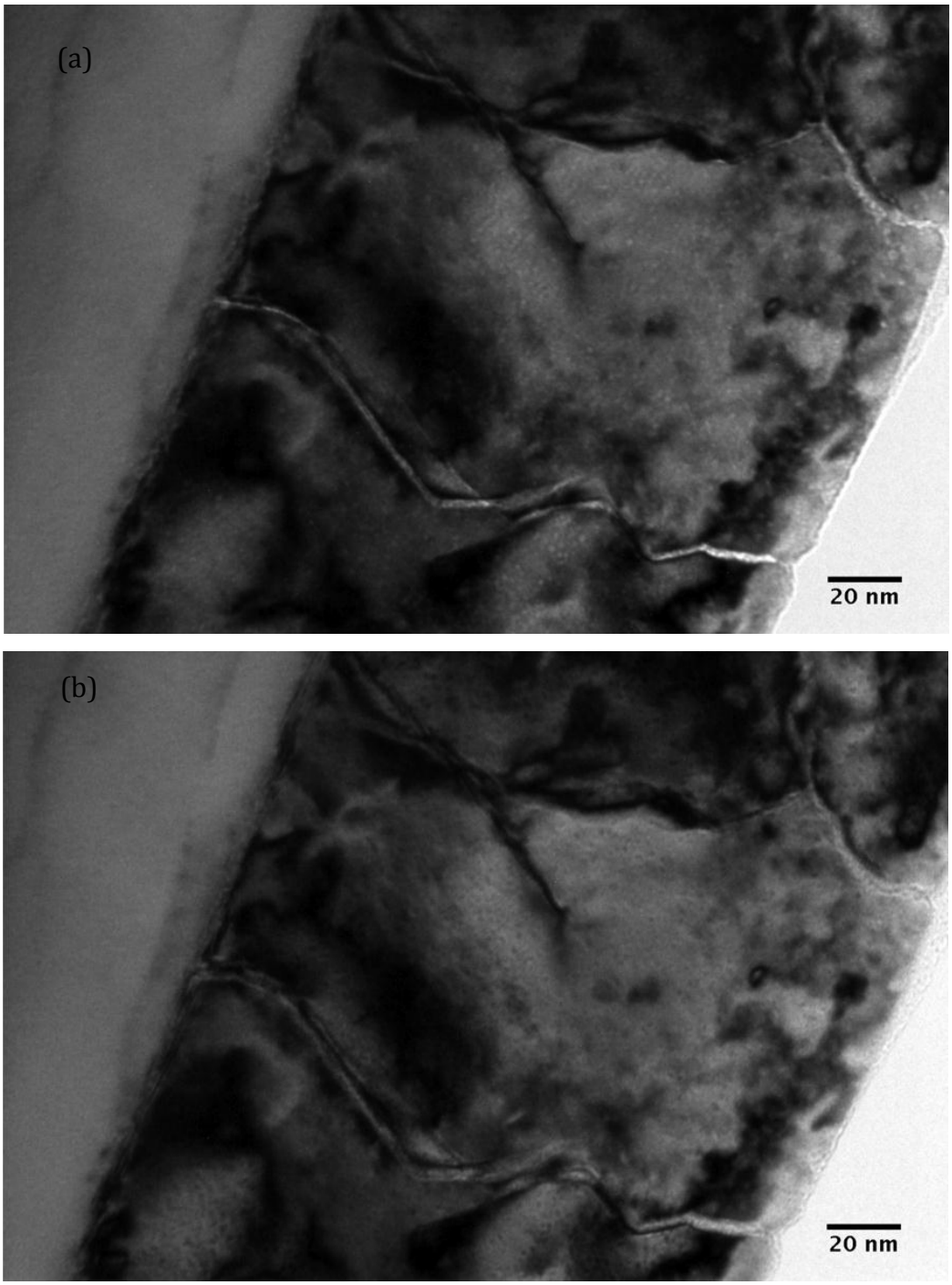

Figure A.28 Cross-section bright-field images of CeO_2 irradiated with 1 MeV Kr^+ at 600°C to a dose of $5x10^{16}$ ions/cm^2, registered by (a) under-focusing and (b) over-focusing the objective lens.

A.4.3 Irradiation dose is $1x10^{17}$ ions/cm^2

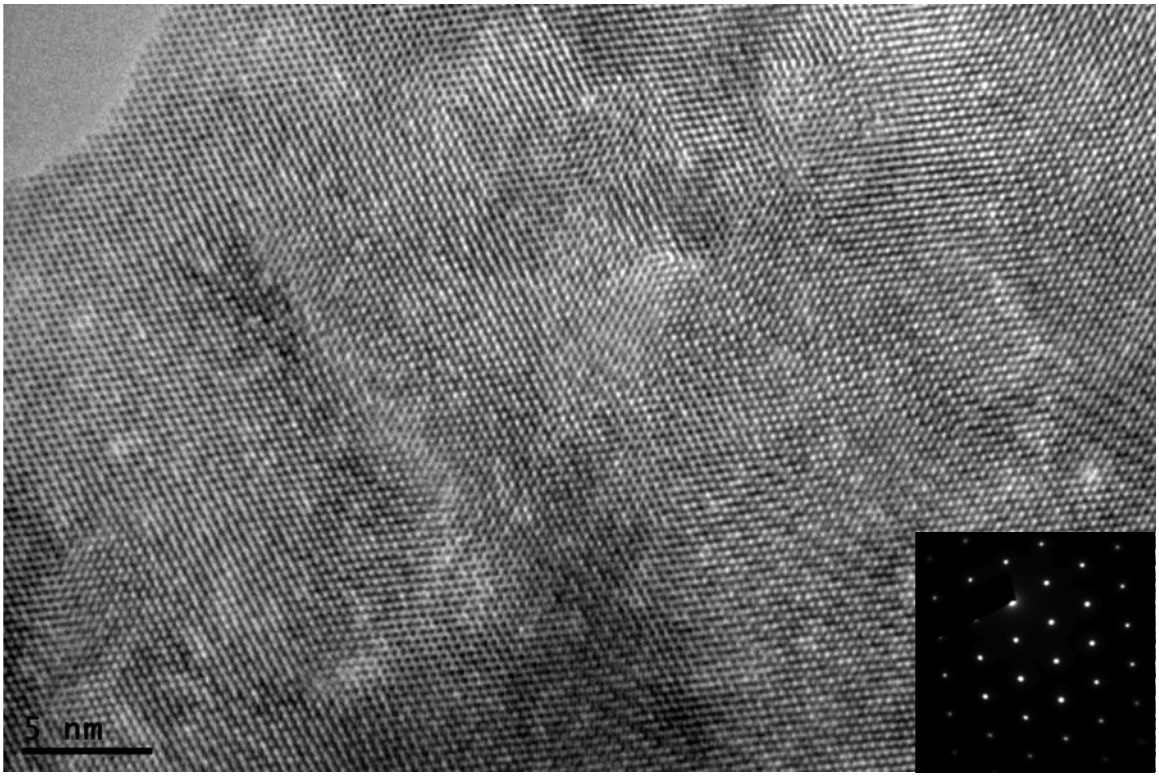

Figure A.29 Cross-section HRTEM image of CeO_2 irradiated with 1 MeV Kr^+ at 600°C to a dose of $1x10^{17}$ ions/cm^2.

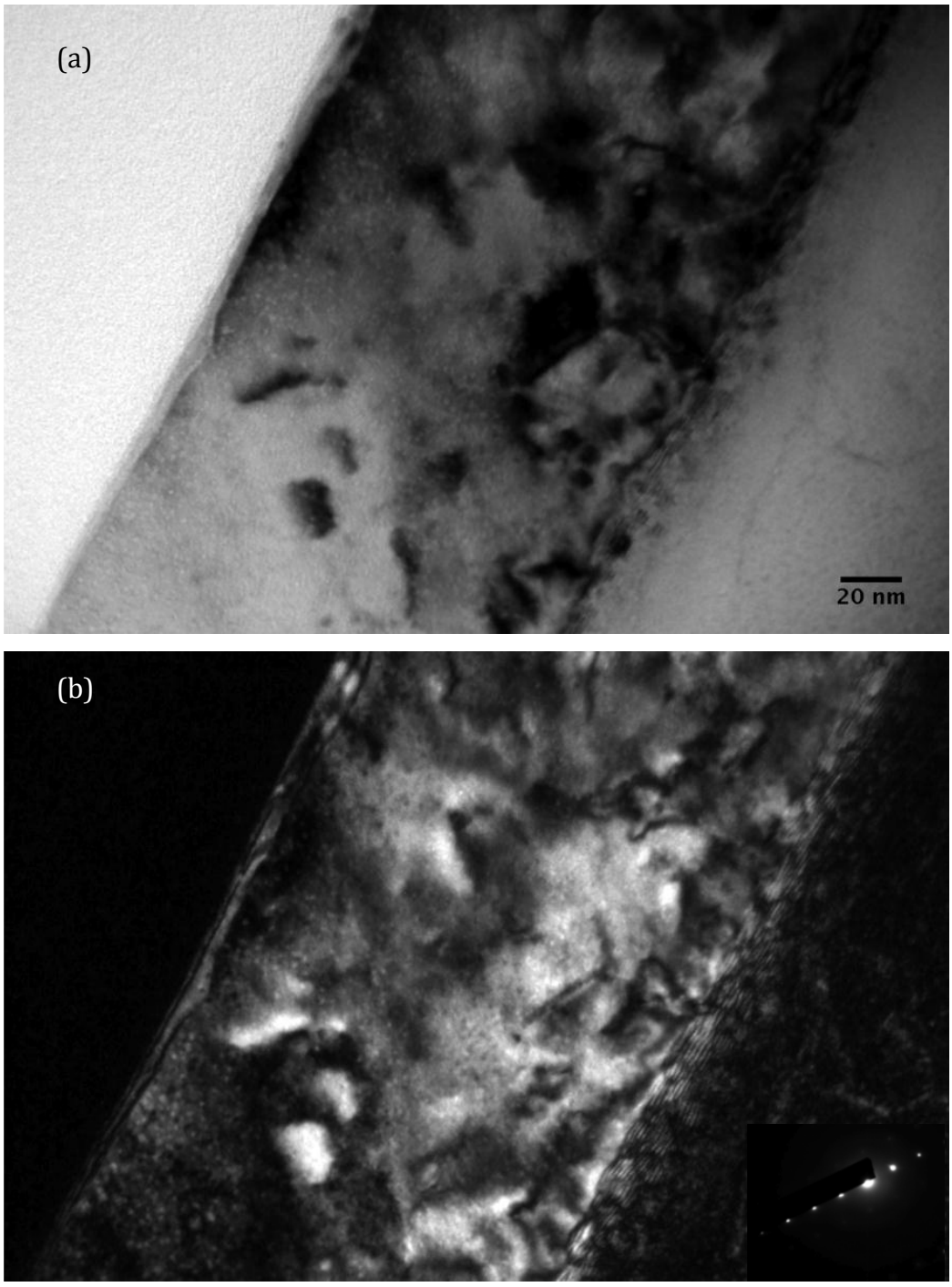

Figure A.30 Cross-section (a) bright-field and (b) dark-field TEM images of CeO_2 irradiated with 1 MeV Kr^+ at 600°C to a dose of $1x10^{17}$ ions/cm^2. These micrographs are taken along the [011] direction with g = 11-1.

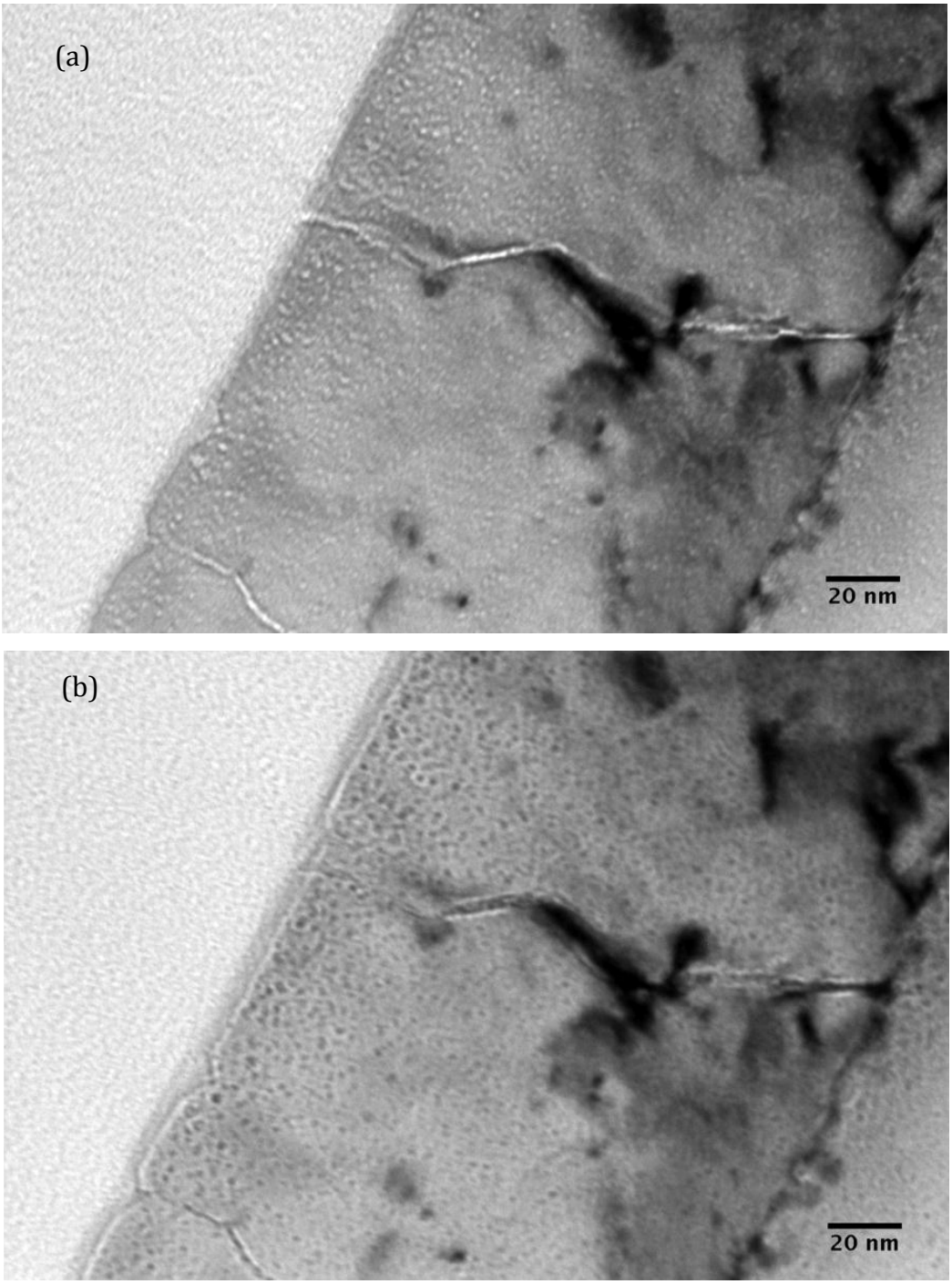

Figure A.31 Cross-section bright-field images of CeO_2 irradiated with 1 MeV Kr^+ at 600°C to a dose of $1x10^{17}$ ions/cm^2, registered by (a) under-focusing and (b) over-focusing the objective lens.

A.5 Microstructure of CeO_2 irradiated with 700 keV Xe^+ at room temperature

A.5.1 Irradiation dose is $2x10^{16}$ ions/cm^2

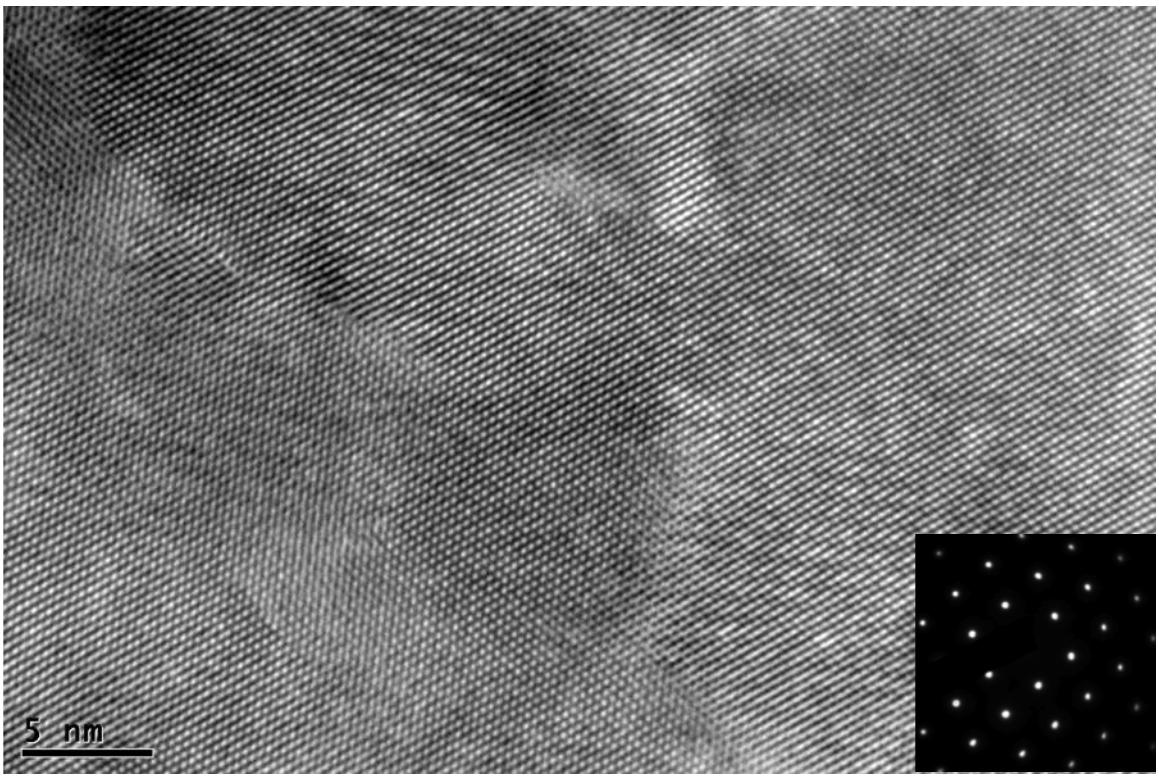

Figure A.32 HRTEM image of CeO_2 irradiated with 700 keV Xe^+ at room temperature to a dose of $2x10^{16}$ ions/cm^2.

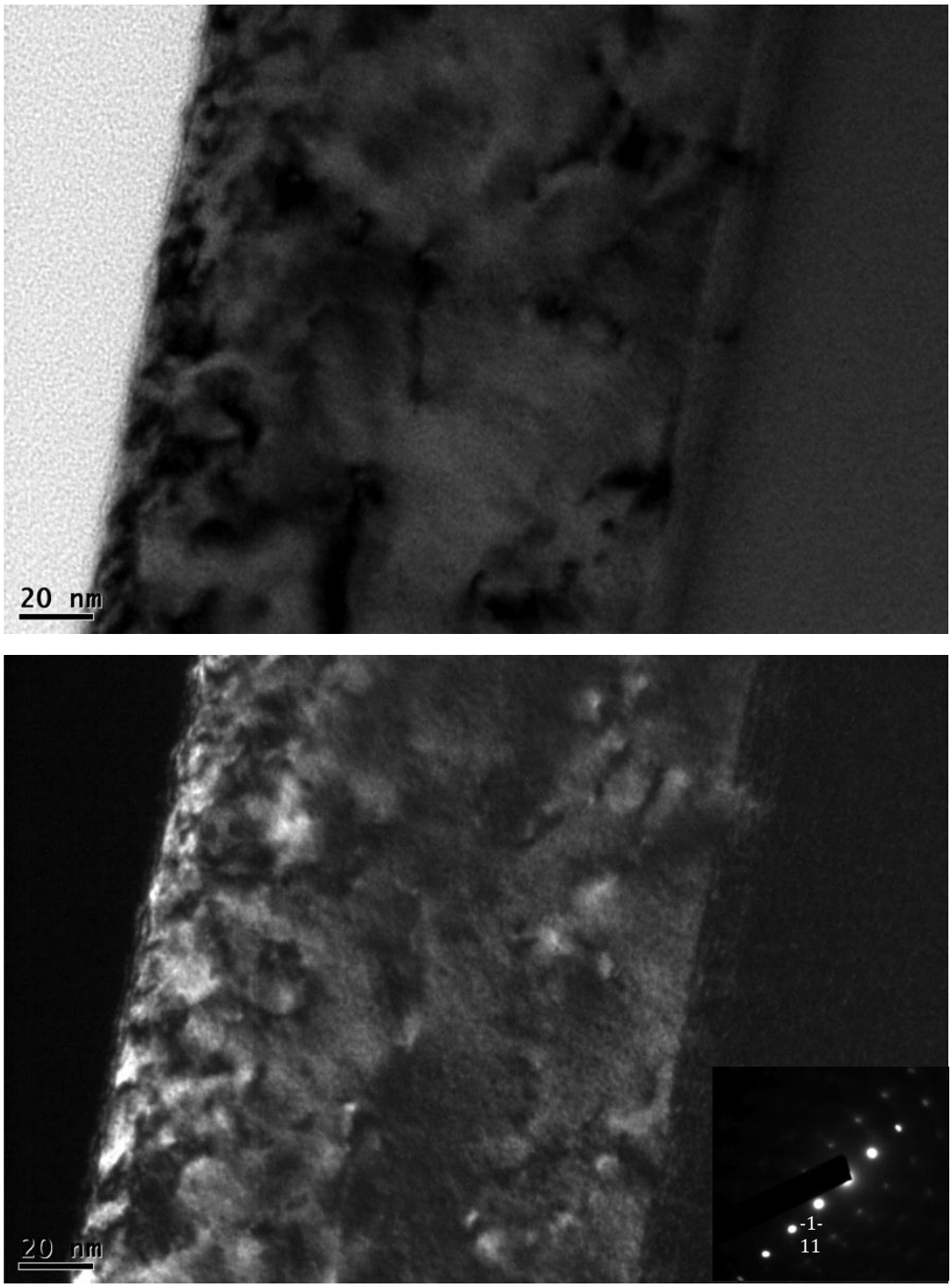

Figure A.33 Bright-field and dark-field images of CeO_2 irradiated with 700 keV Xe^+ at room temperature to a dose of $2x10^{16}$ ions/cm^2. The images are taken along [011] direction with g = -1-11.

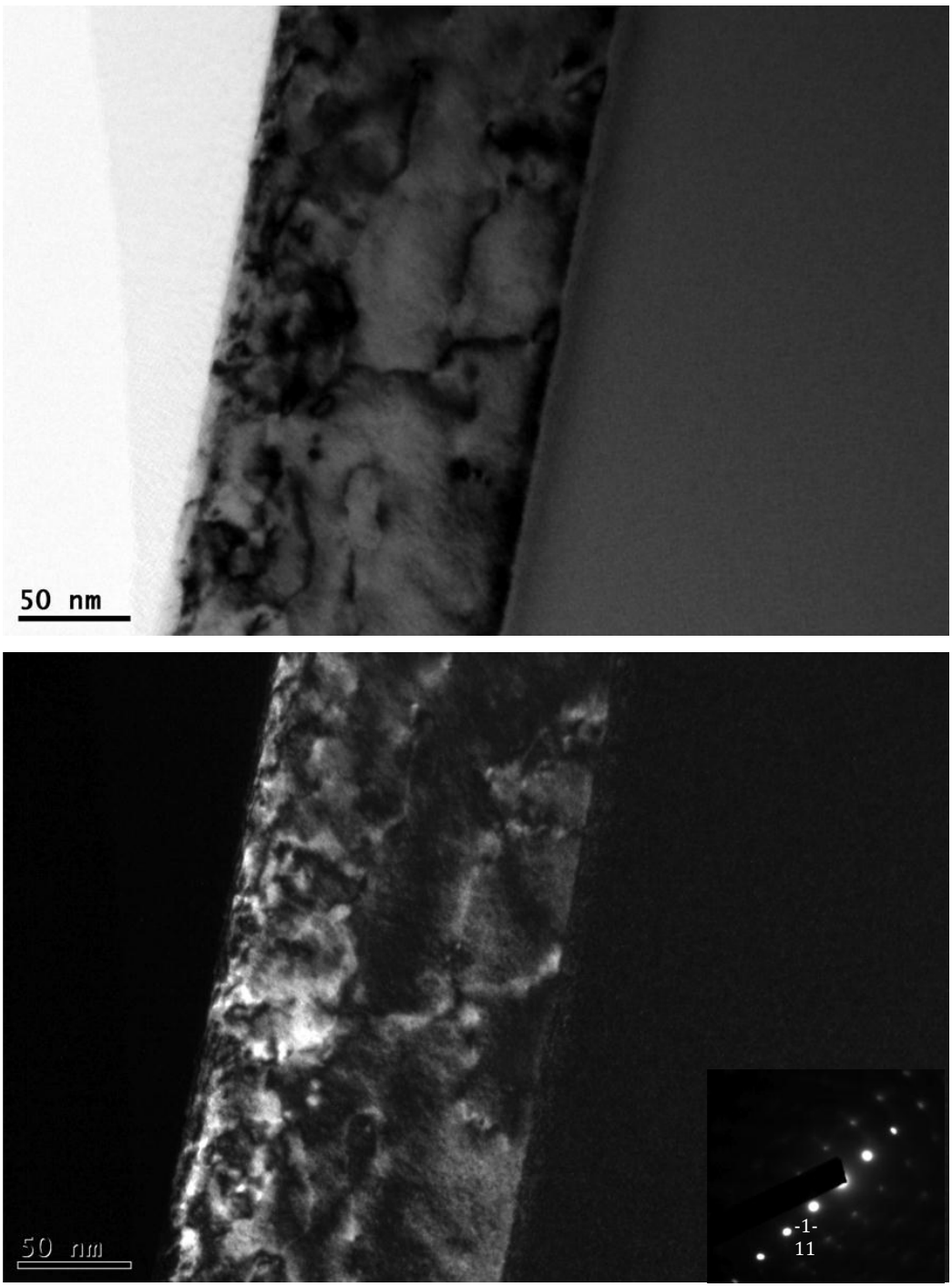

Figure A.34 Bright-field and dark-field images of CeO_2 irradiated with 700 keV Xe^+ at room temperature to a dose of $2x10^{16}$ ions/cm^2. The images are taken along [011] direction with g = -1-11.

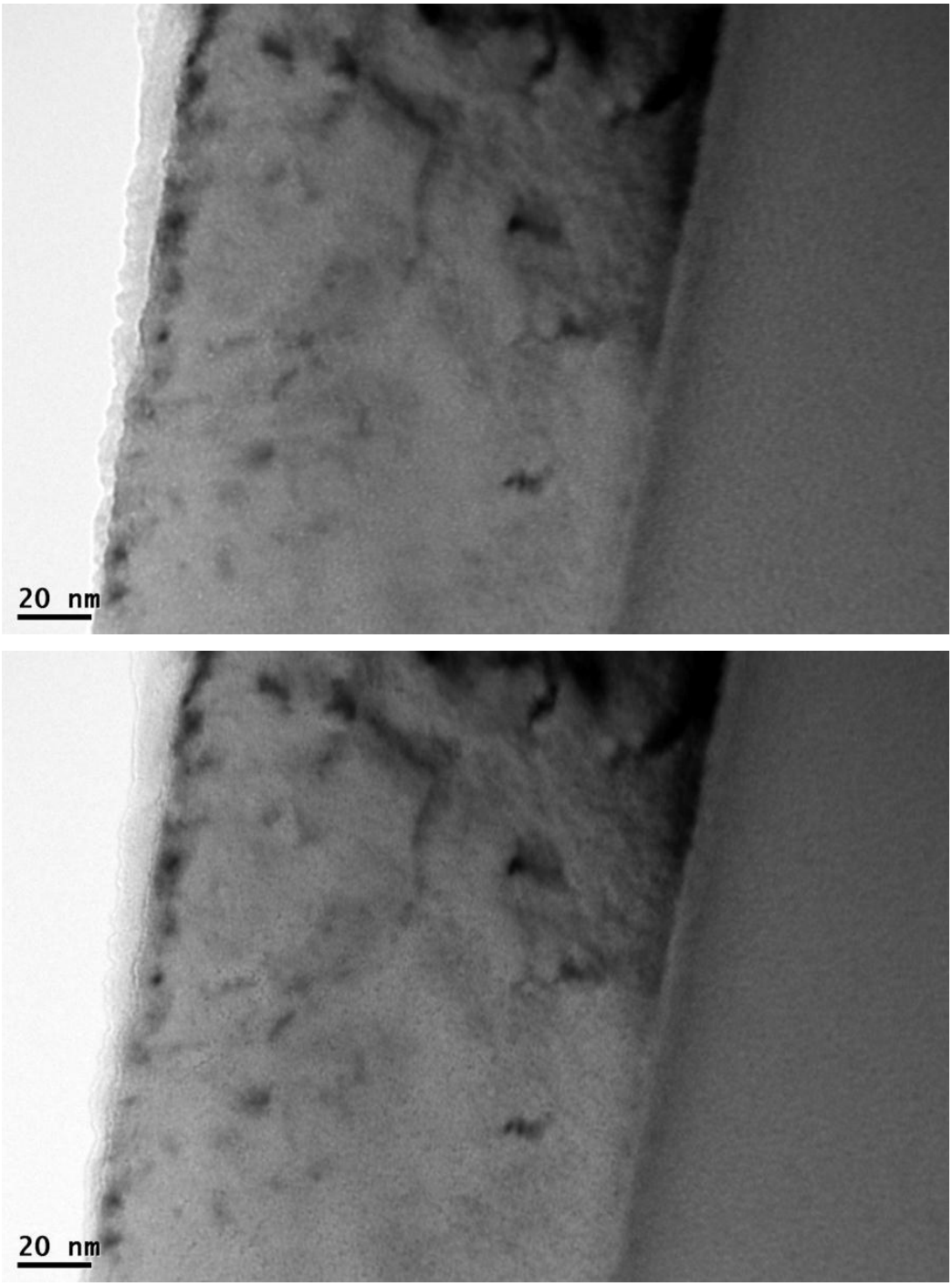

Figure A.35 Bright-field images of CeO_2 irradiated with 700 keV Xe^+ at room temperature to a dose of $2x10^{16}$ ions/cm^2, registered by underfocusing and overfocusing the objective lens . The images are taken along [011] direction with g = -1-11.

A.5.2 Irradiation dose is $5x10^{16}$ ions/cm^2

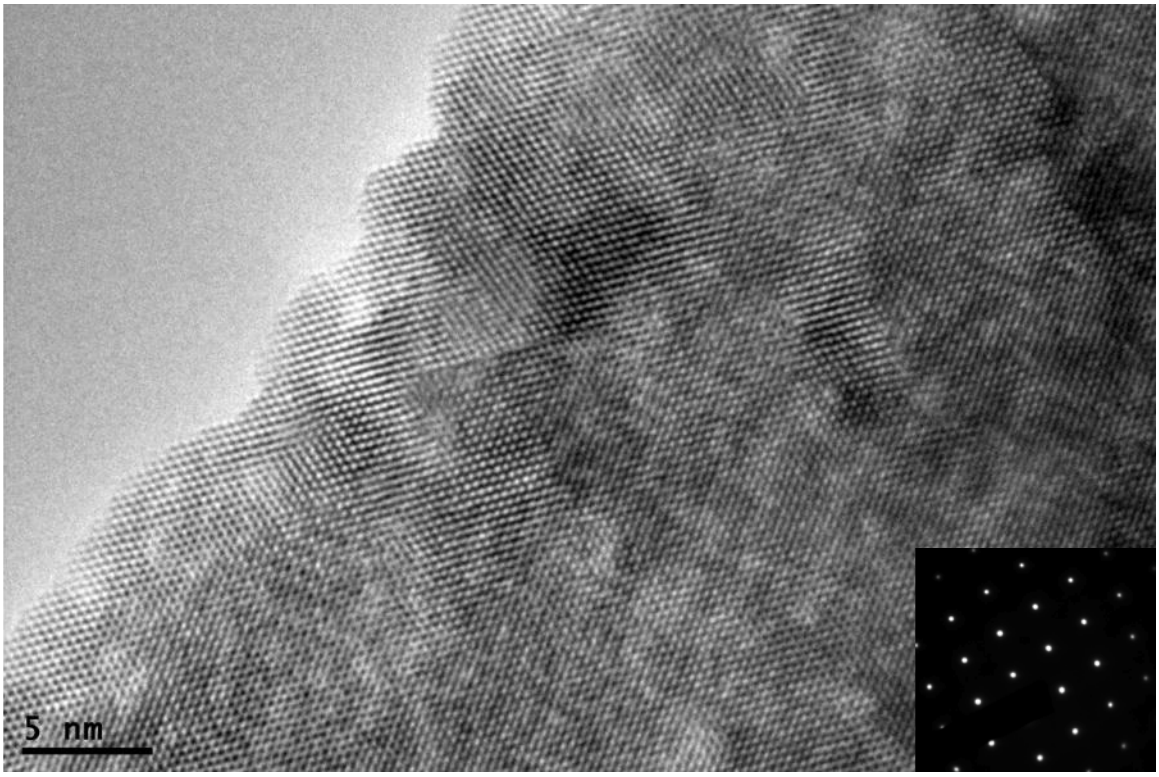

Figure A.36 HRTEM image of CeO_2 irradiated with 700 keV Xe^+ at room temperature to a dose of $5x10^{16}$ ions/cm^2.

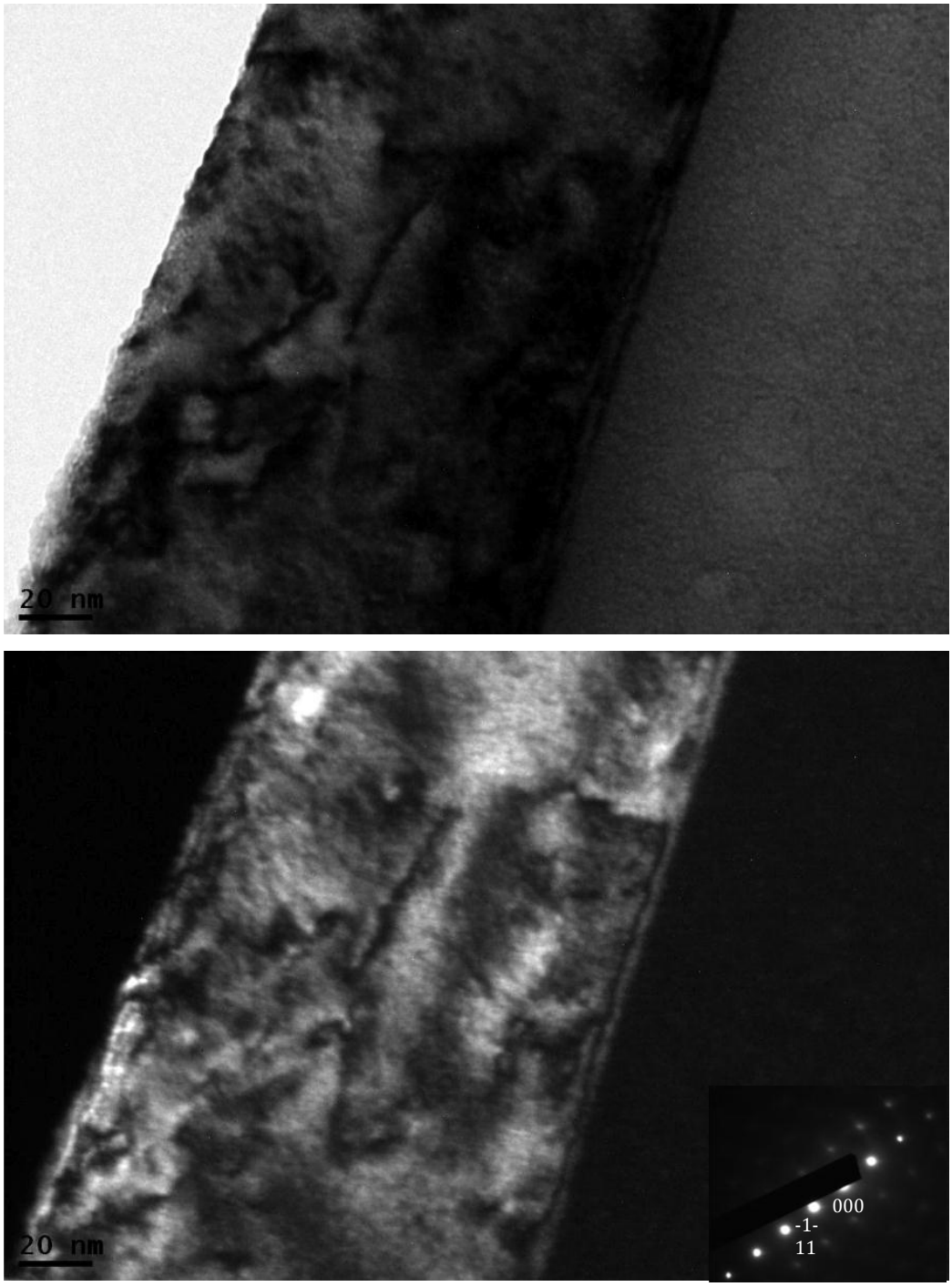

Figure A.37 Bright-field and dark-field images of CeO_2 irradiated with 700 keV Xe^+ at room temperature to a dose of $5x10^{16}$ ions/cm^2. The images are taken along [011] direction with g = -1-11.

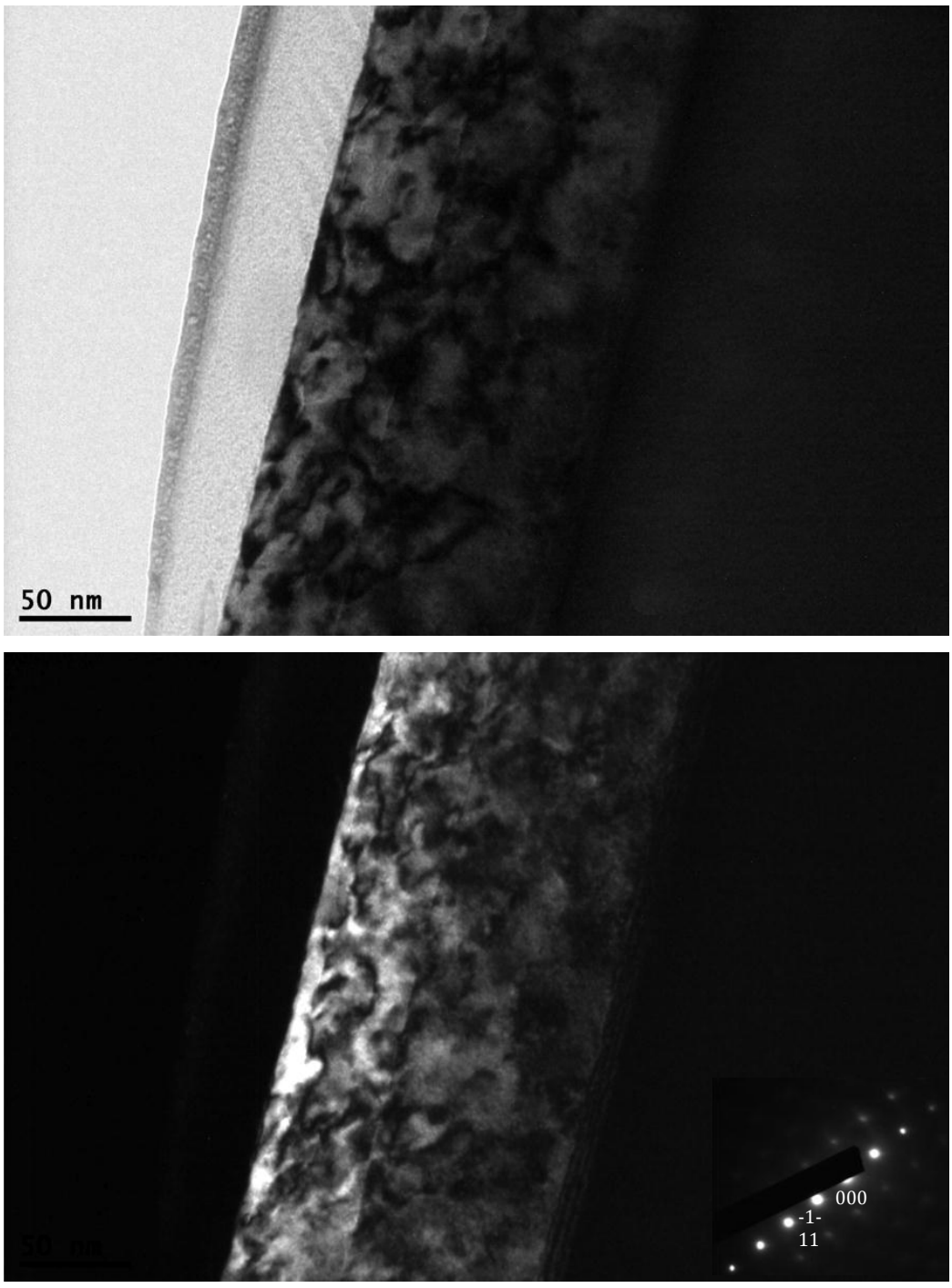

Figure A.38 Bright-field and dark-field images of CeO_2 irradiated with 700 keV Xe^+ at room temperature to a dose of $5x10^{16}$ ions/cm^2. The images are taken along [011] direction with g = -1-11.

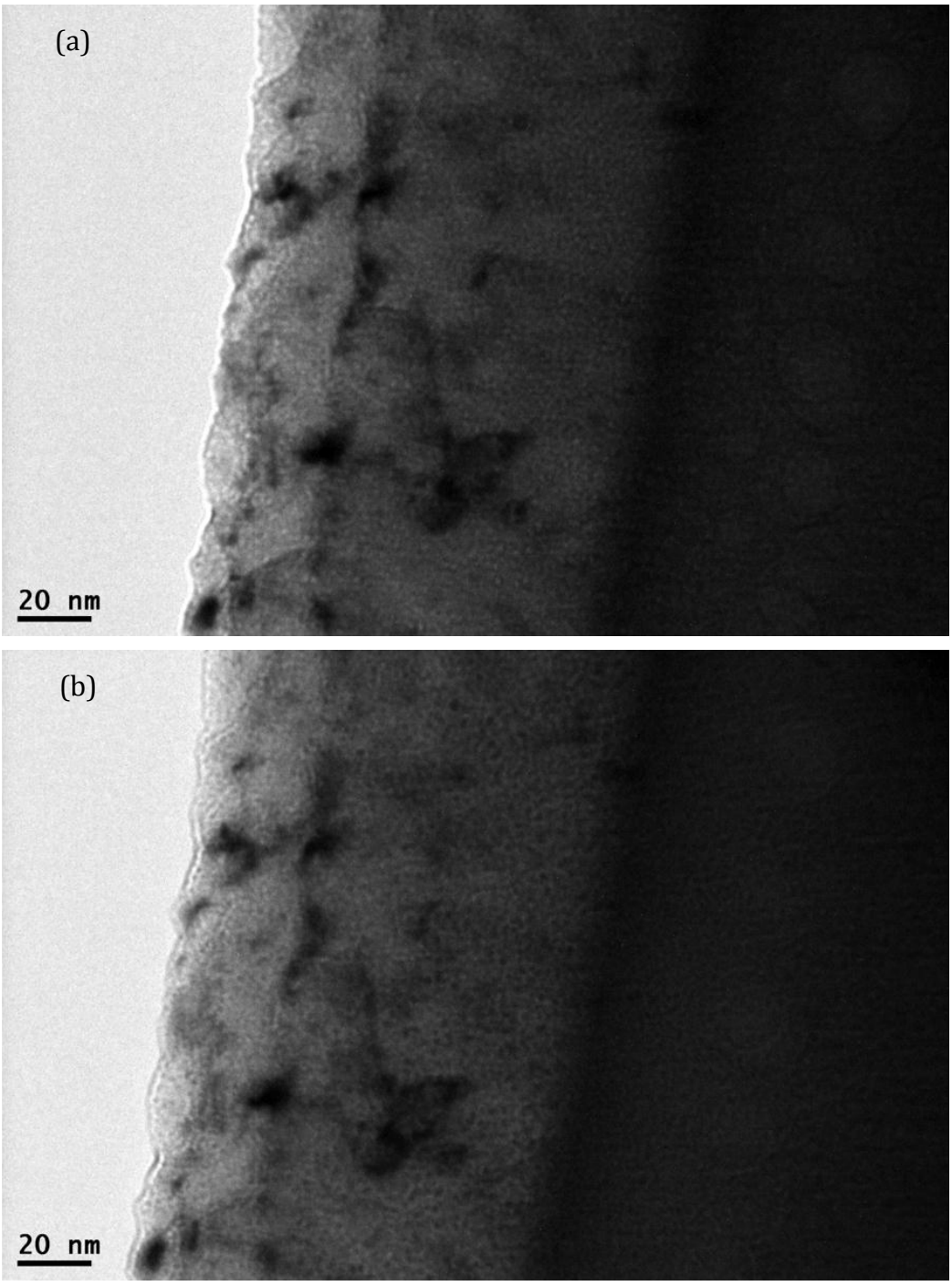

Figure A.39 Bright-field images of CeO_2 irradiated with 700 keV Xe^+ at room temperature to a dose of $2x10^{16}$ ions/cm^2, registered by (a) underfocusing and (b) overfocusing the objective lens . The images are taken along [011] direction with g = 1-11

A.6 Microstructure of as-prepared CeO_2 annealed at 600°C

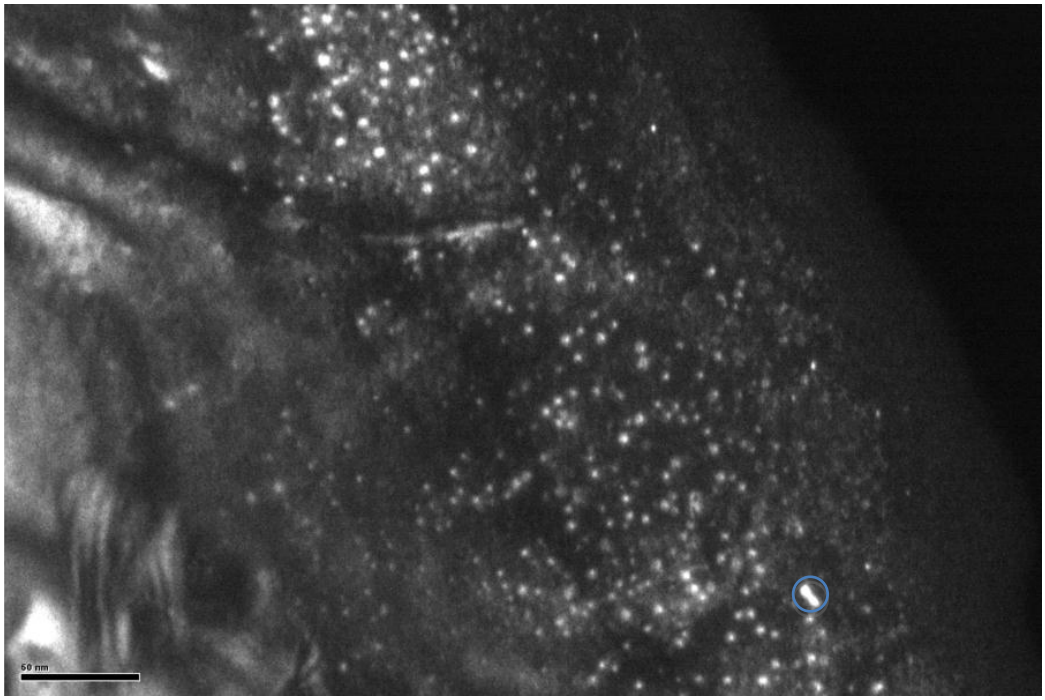

Figure A.40 Weak-beam dark-field micrograph of as-prepared CeO_2 annealed at 600°C, taken alone the direction of [001] with g = -2-20.

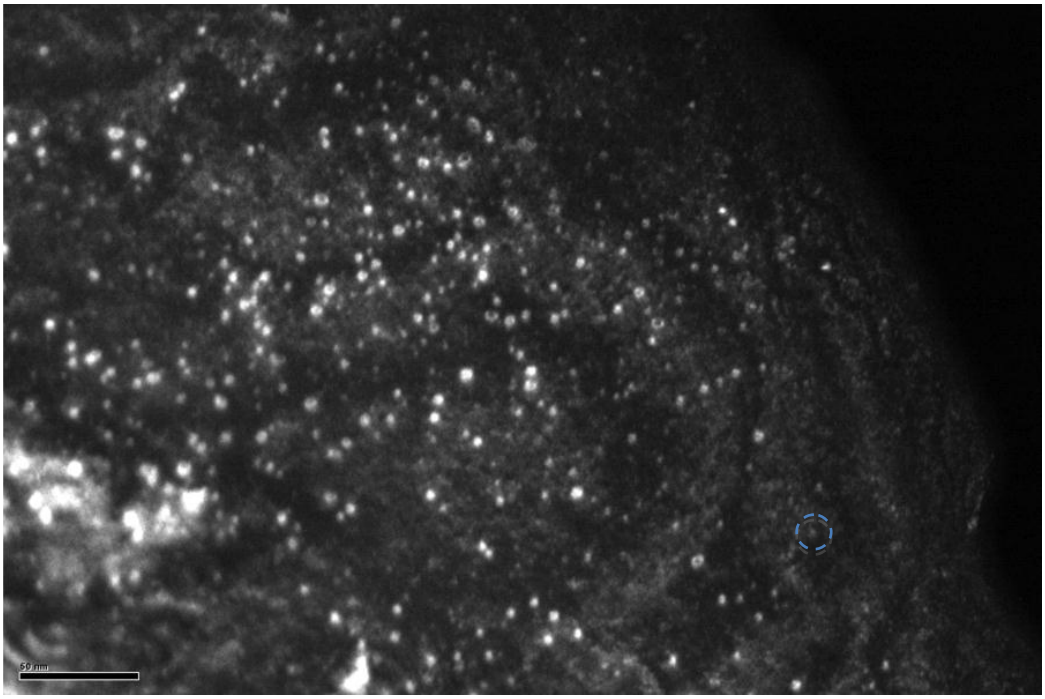

Figure A.41 Weak-beam dark-field micrograph of as-prepared CeO_2 annealed at 600°C, taken alone the direction of [001] with g = -220.

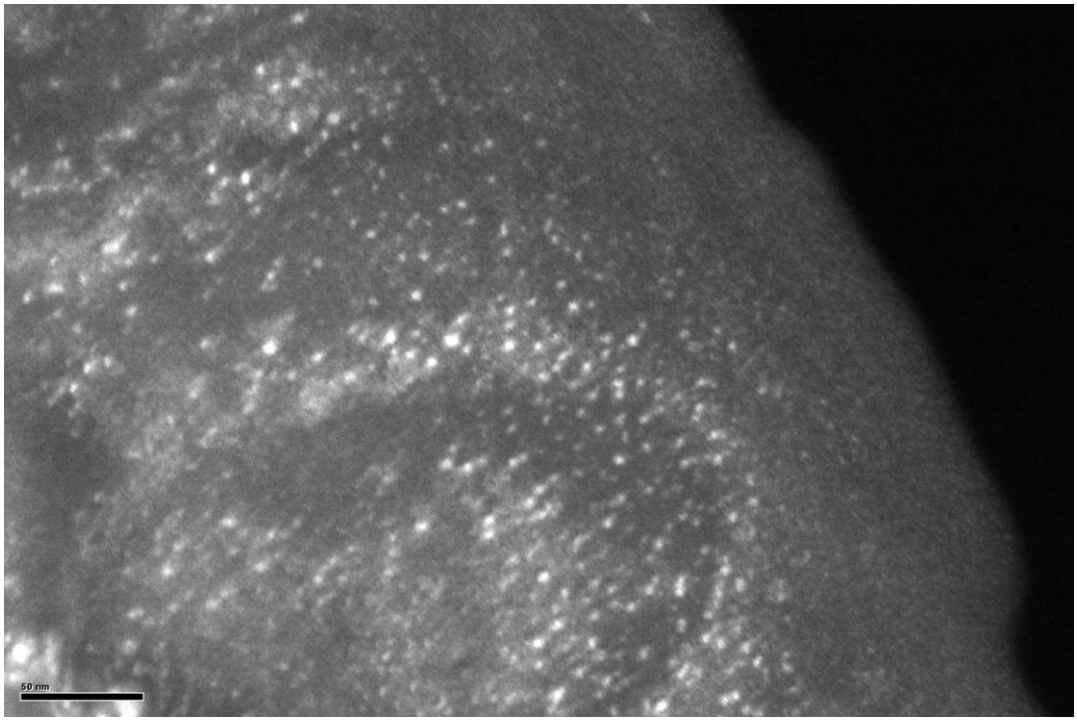

Figure A.42 Weak-beam dark-field micrograph of as-prepared CeO_2 annealed at 600°C, taken alone the direction of [001] with g = 020.

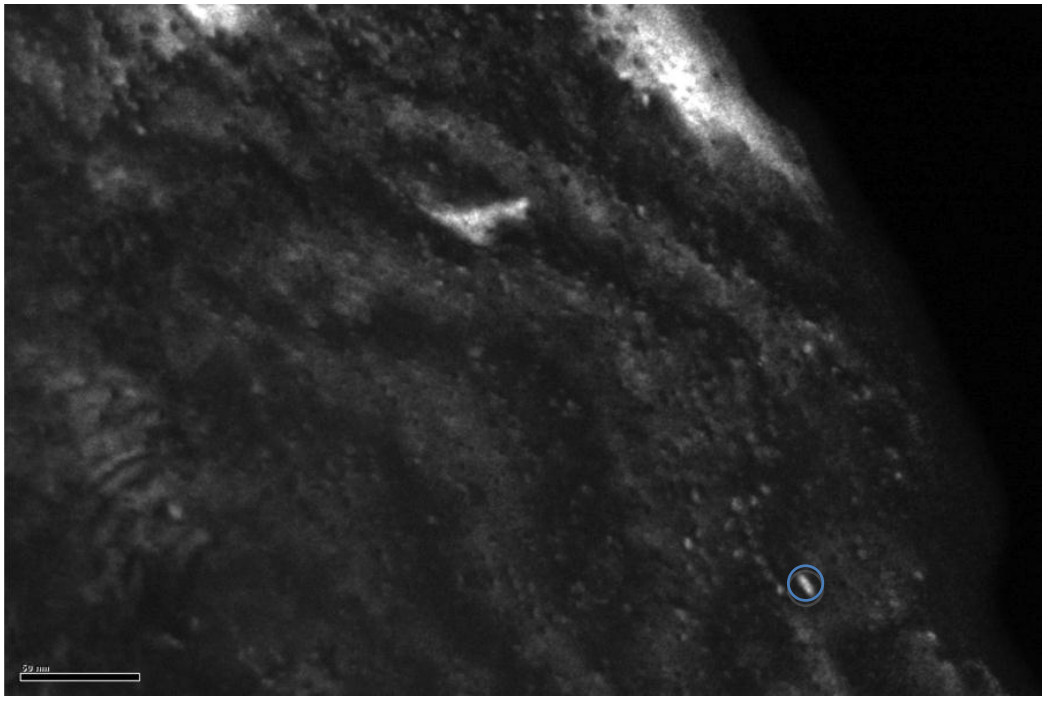

Figure A.43 Weak-beam dark-field micrograph of as-prepared CeO_2 annealed at 600°C, taken alone the direction of [001] with g = -200.

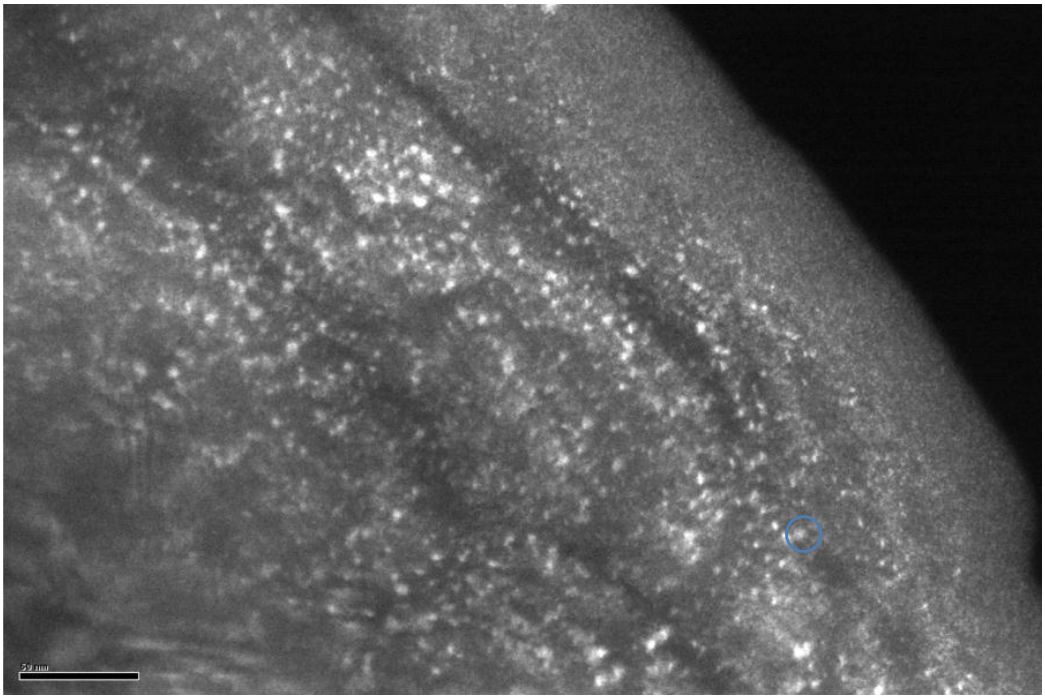

Figure A.44 Weak-beam dark-field micrograph of as-prepared CeO_2 annealed at 600°C, taken alone the direction of [011] with g = 1-11.

The determination of burger vector is carried out by comparing visibility of same dislocation loops observed at different diffraction vectors. The dislocation loop marked by circles on different images shows an example. It is visible when g = -2-20, -200, 1-11, and disappears when g = -220. According to the criteria of g•b = 0, the burger vector is parallel to the direction of [-1-11].

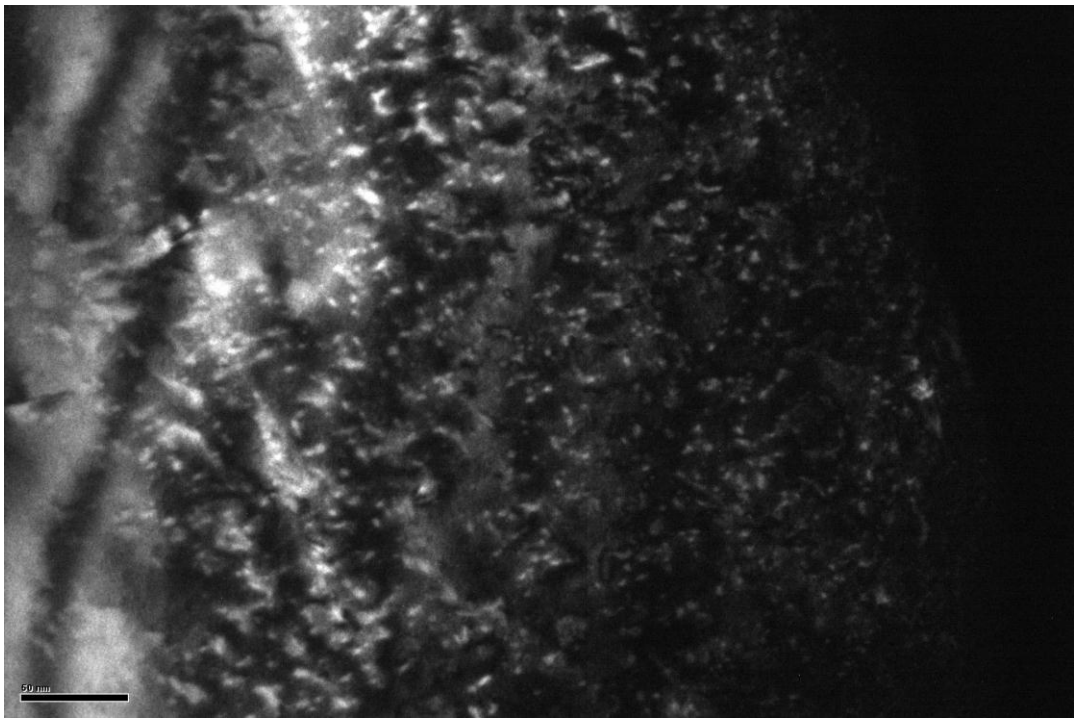

Figure A.45 Weak-beam dark-field micrograph of as-prepared CeO_2 before annealing, taken alone the direction of [001] with g = -2-20.

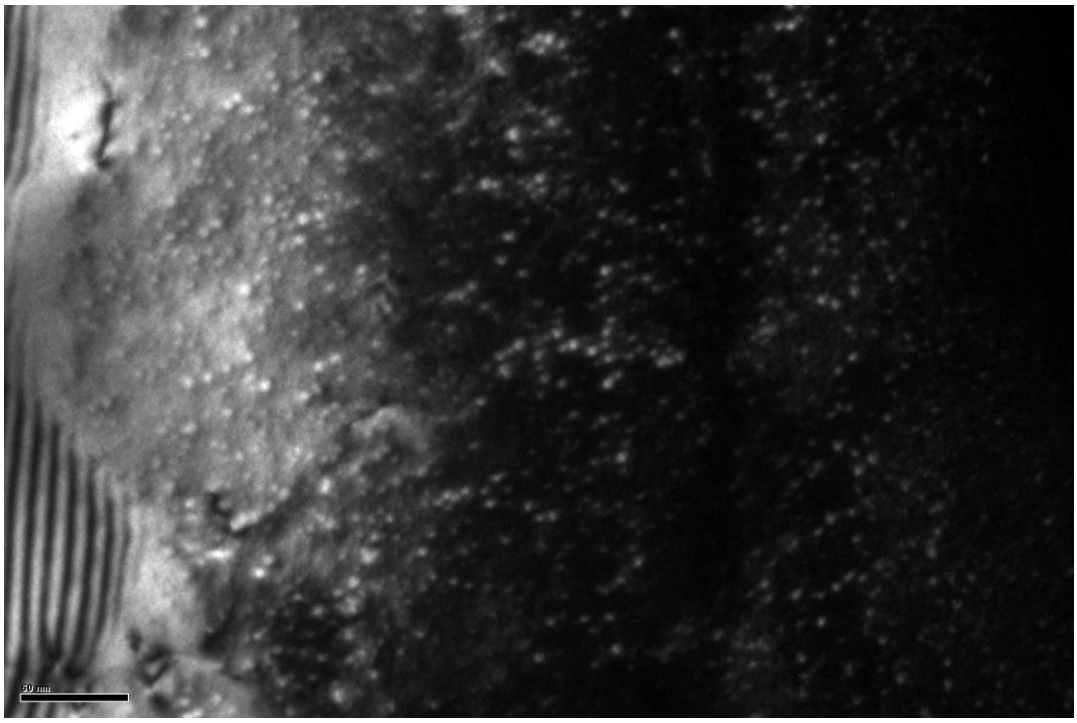

Figure A.46 Weak-beam dark-field micrograph of as-prepared CeO_2 during annealing at 600°C, taken alone the direction of [001] with g = -2-20.

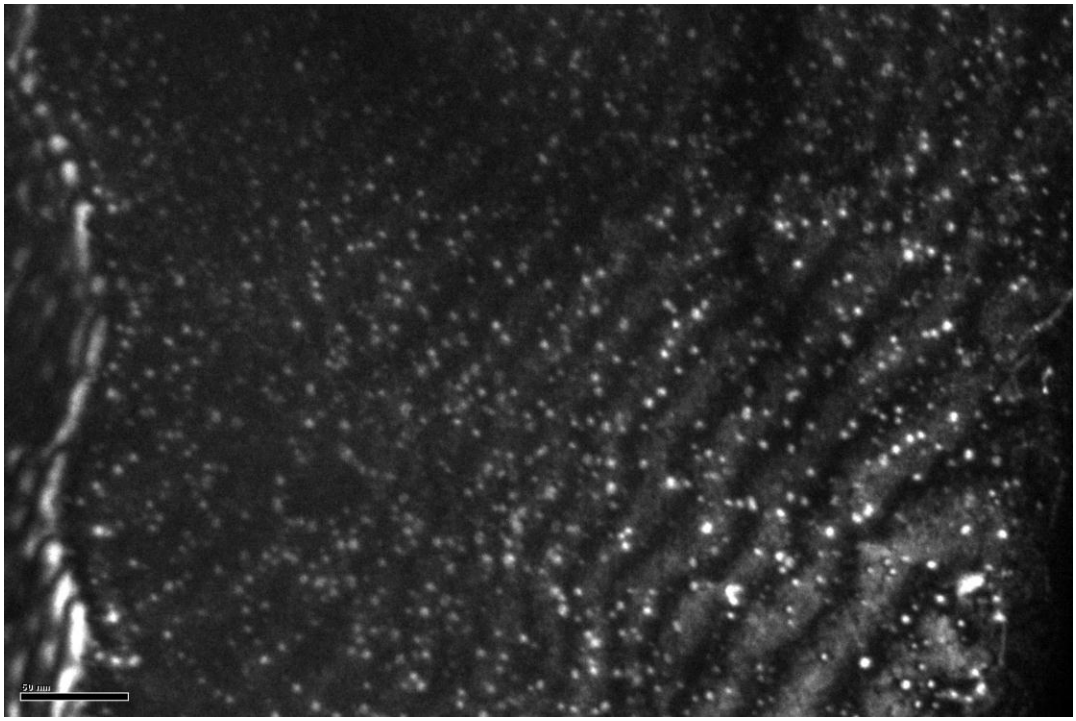

Figure A.47 Weak-beam dark-field micrograph of as-prepared CeO_2 after annealing at 600°C for 3 hours, taken alone the direction of [001] with g = -2-20.

Before annealing, dislocations on CeO_2 show irregular shape (figure A.45), whereas the dislocations form round loops after annealing (figure A.46 and A.47).

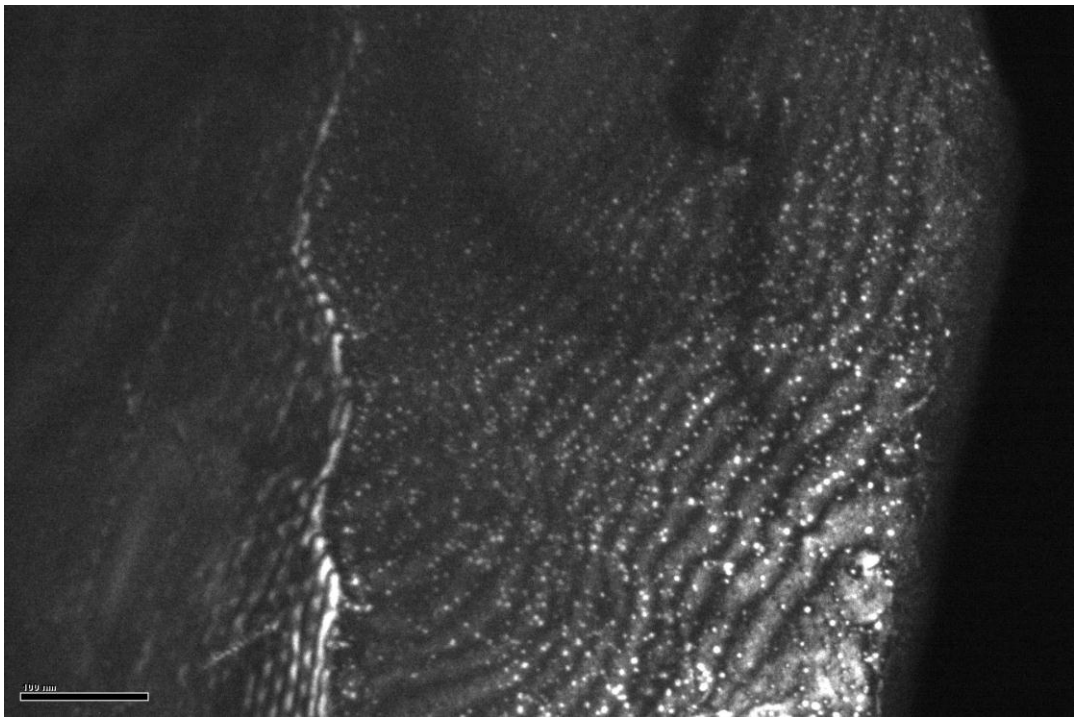

Figure A.48 Weak-beam dark-field micrograph of as-prepared CeO_2 after annealing at 600°C for 3 hours, taken alone the direction of [001] with g = -2-20.

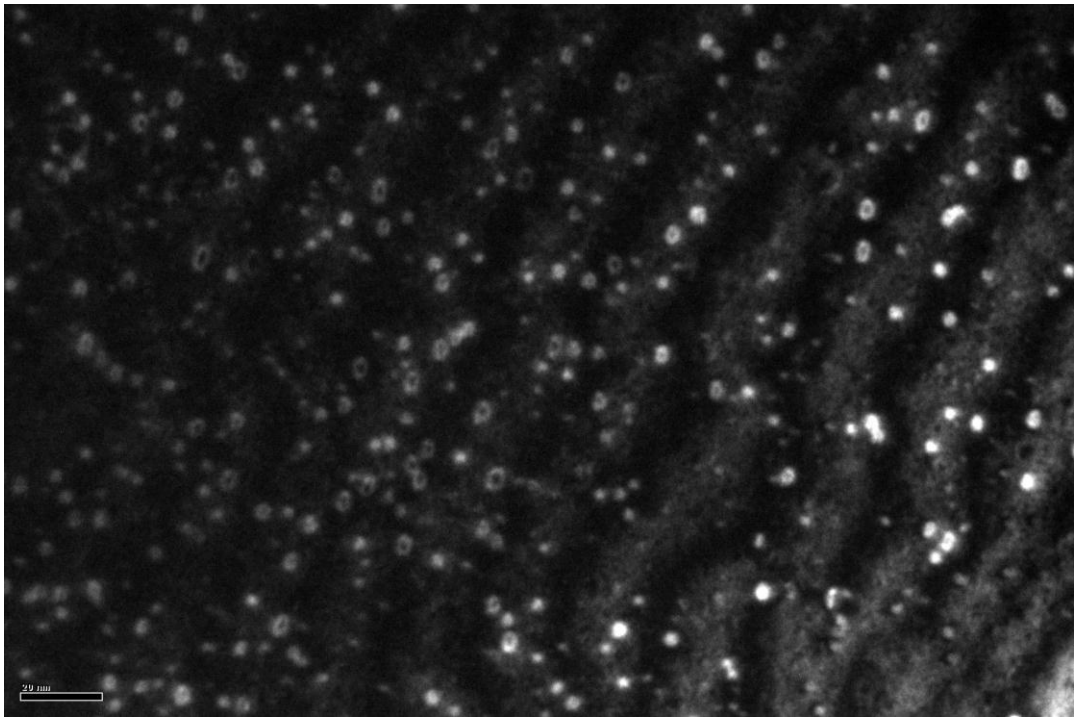

Figure A.49 Weak-beam dark-field micrograph of as-prepared CeO_2 after annealing at 600°C for 3 hours, taken alone the direction of [001] with g = -2-20.

The dislocation loops are likely to be caused by Argon ions during ion-milling process, since the density of dislocation loops changes dramatically from the pure CeO_2 area (the right side of figure A.48) to the area covered with $SrTiO_3$ substrate (the left side of figure A.48). If the defects are generated from film growth, it is expected to observe relatively even distribution of the defects on all area. The detailed structure of dislocation loops displayed in figure A.49.

A.7 Microstructure of CeO_2 irradiated with 1MeV Kr at room temperature

A.7.1 Irradiation dose is $2x10^{16}$ ions/cm^2

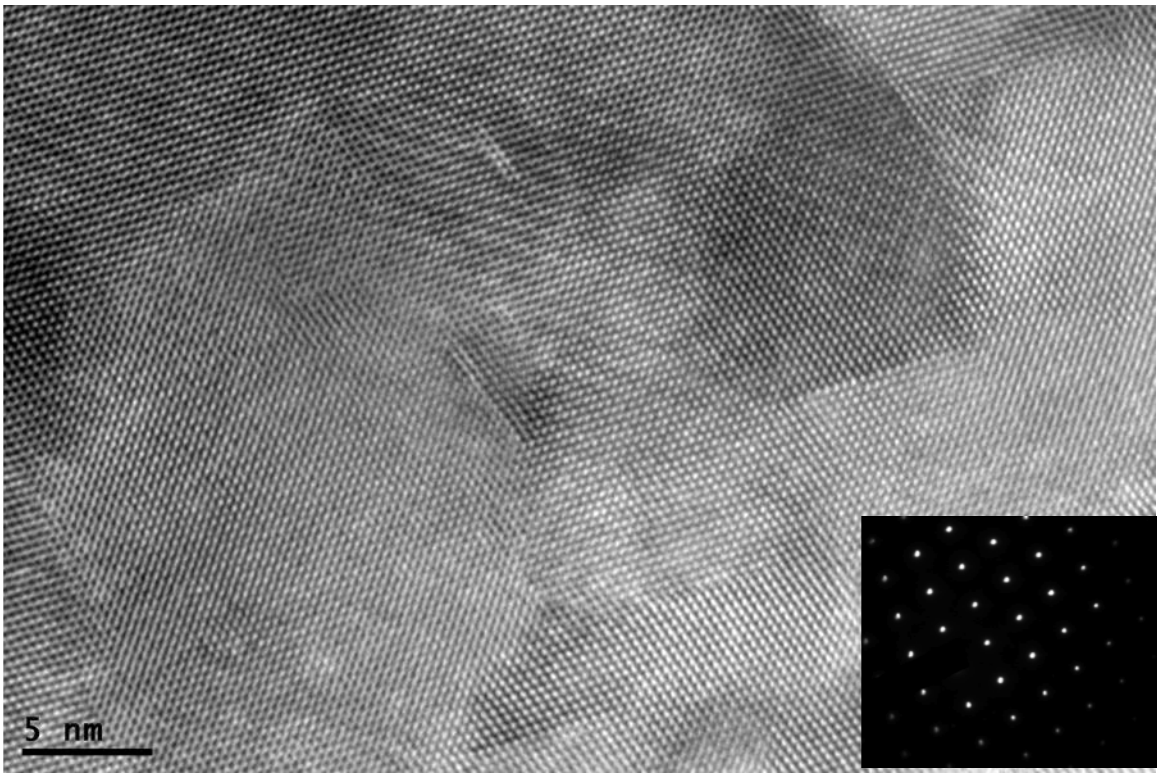

Figure A.50 Cross-section HRTEM image of CeO_2 irradiated with 1 MeV Kr^+ at room temperature to a dose of $2x10^{16}$ ions/cm^2.

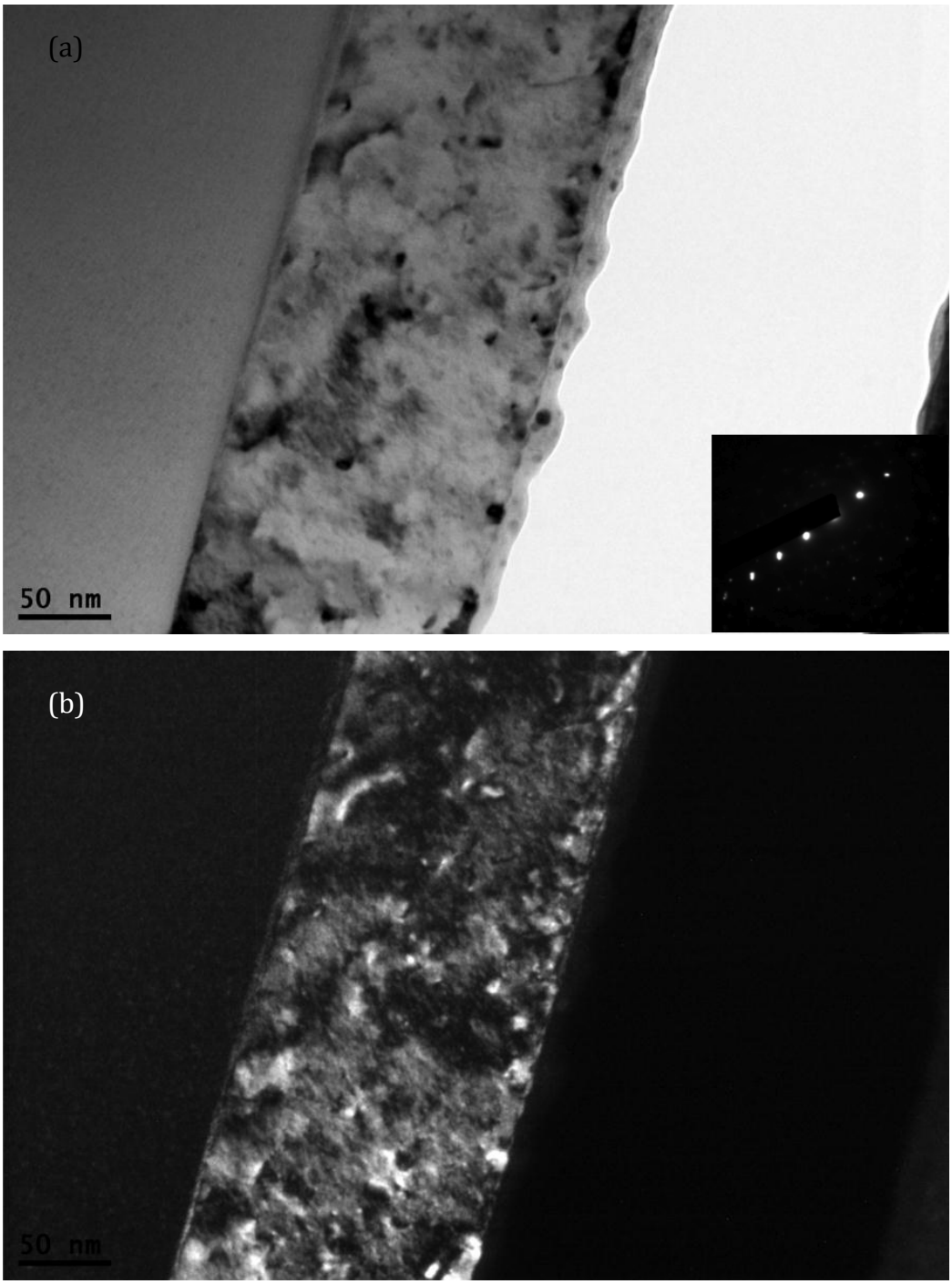

Figure A.51 (a) Bright-field and (b) dark-field images of CeO_2 irradiated with 1 MeV Kr^+ at room temperature to a dose of $2x10^{16}$ ions/cm^2. The images are taken along [011] direction with g = -1-11

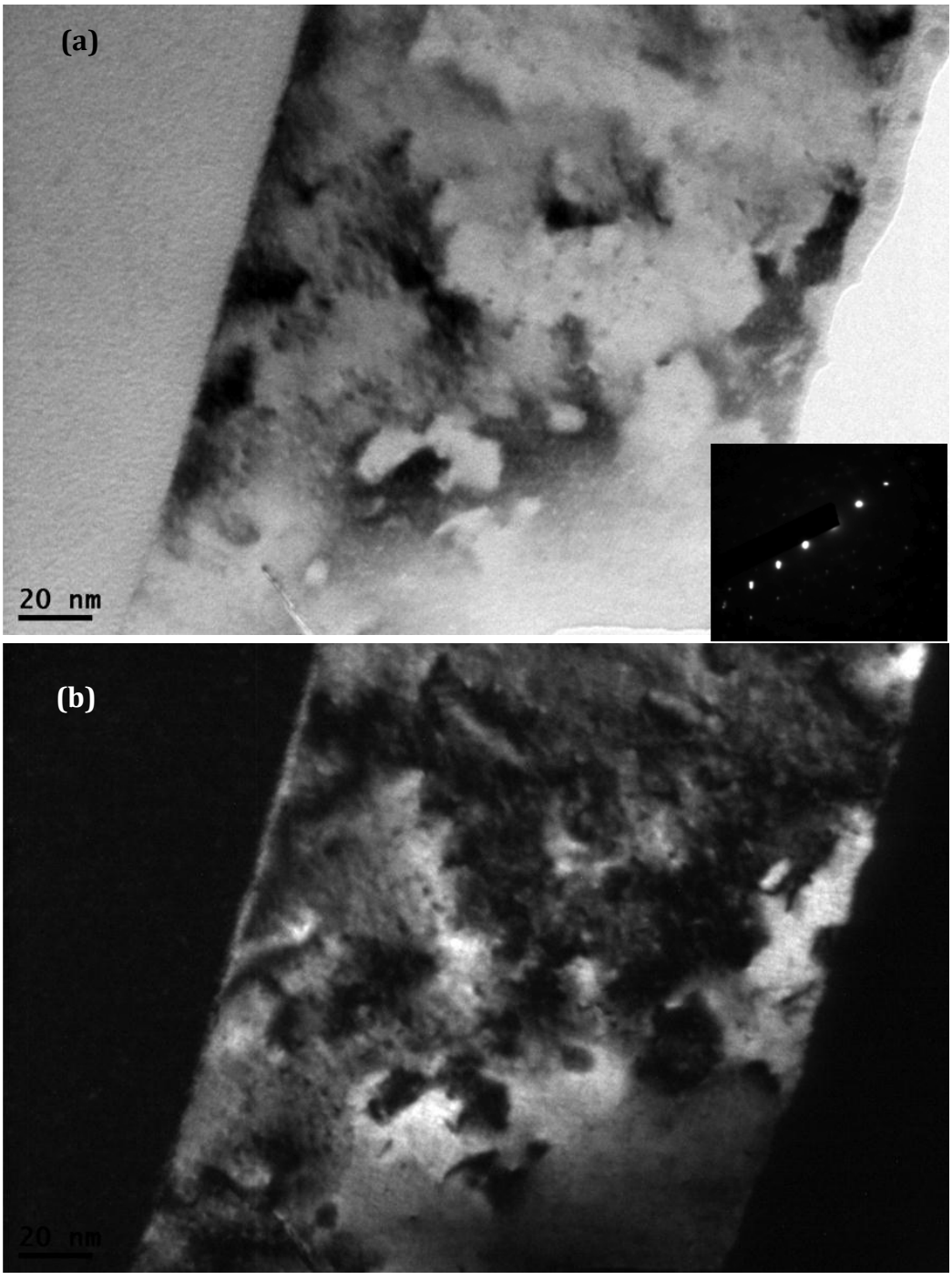

Figure A.52 (a) Bright-field and (b) dark-field images of CeO_2 irradiated with 1 MeV Kr^+ at room temperature to a dose of $2x10^{16}$ ions/cm^2. The images are taken along [011] direction with g = -1-11.

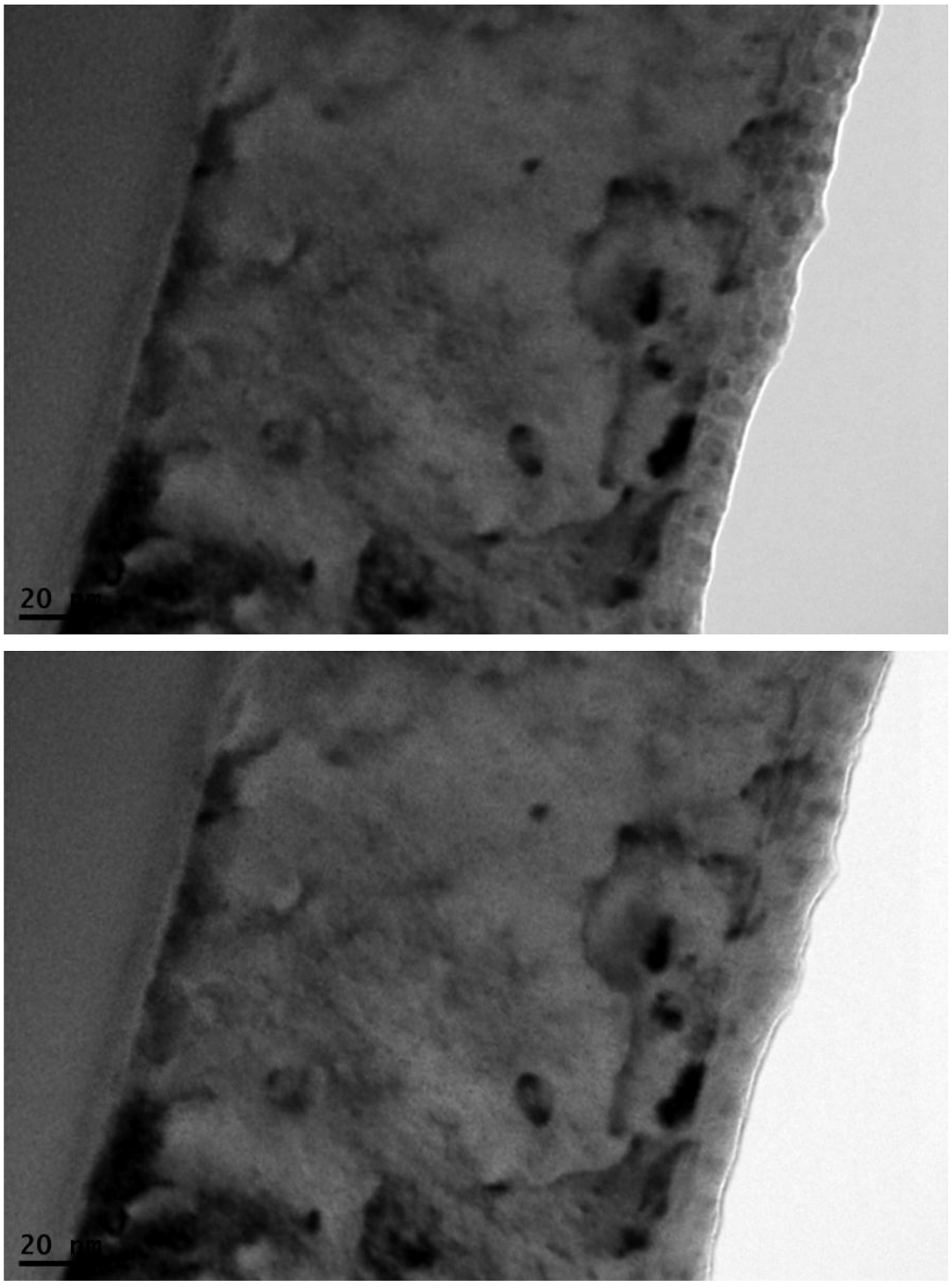

Figure A.53 Bright-field images of CeO_2 irradiated with 1 MeV Kr^+ at room temperature to a dose of $2x10^{16}$ ions/cm^2, registered by underfocusing and overfocusing the objective lens . The images are taken along [011] direction with g = -1-11.

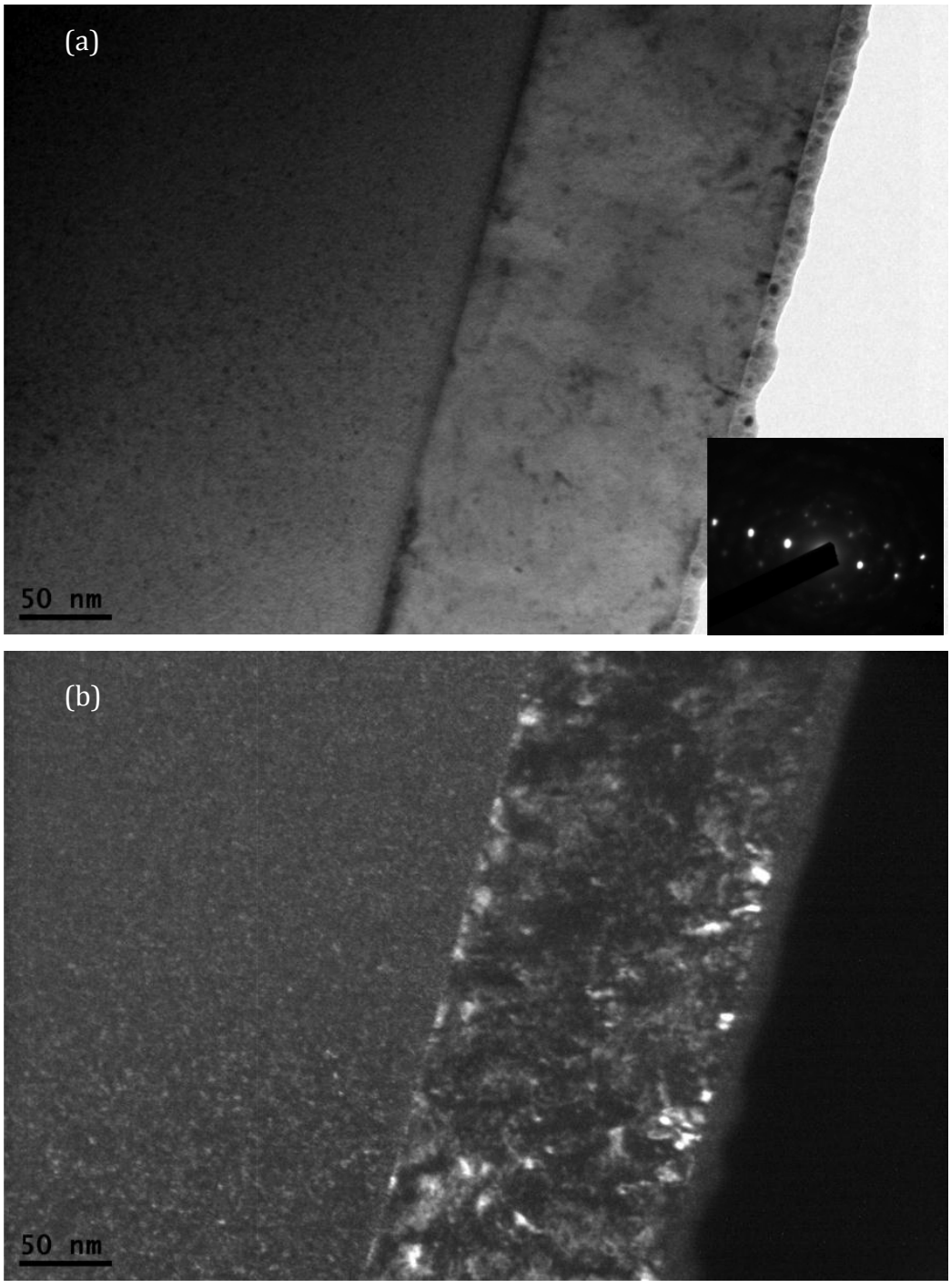

Figure A.54 (a) Bright-field and (b) dark-field images of CeO_2 irradiated with 1 MeV Kr^+ at room temperature to a dose of $2x10^{16}$ ions/cm^2. The images are taken along [011] direction with g = -200.

A.7.2 Irradiation dose is $5x10^{16}$ ions/cm^2

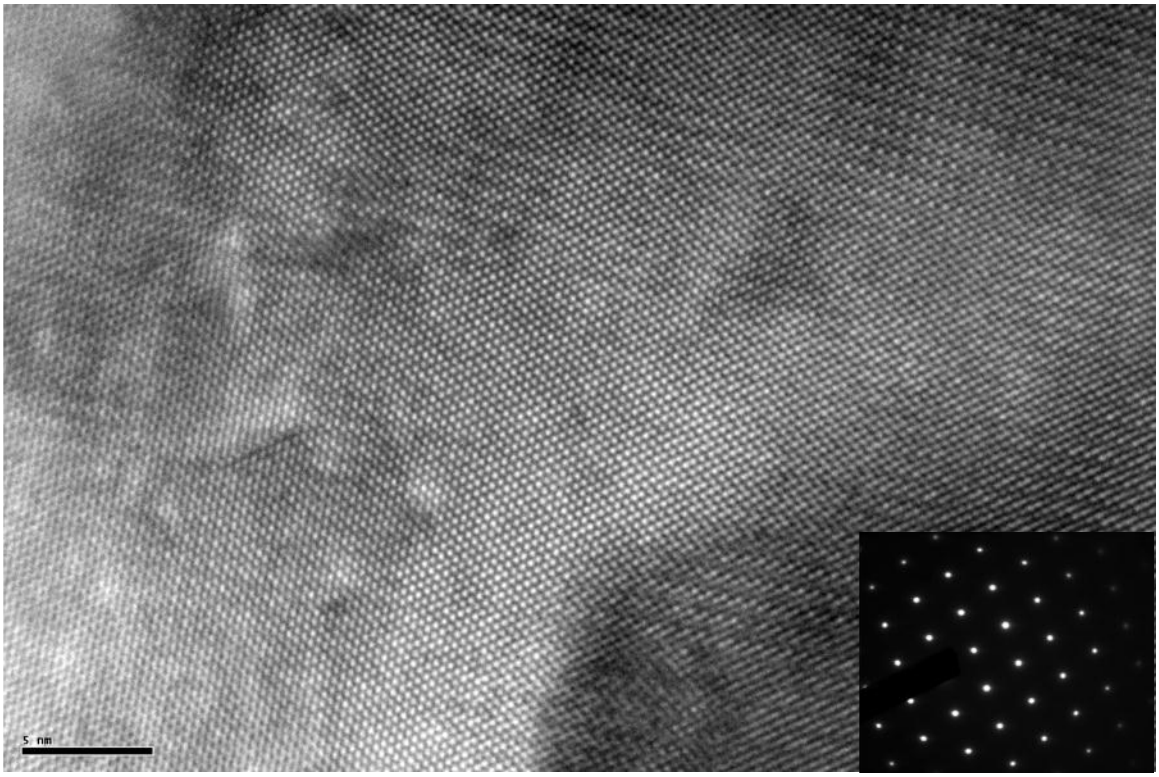

Figure A.55 Cross-section HRTEM image of CeO_2 irradiated with 1 MeV Kr^+ at room temperature to a dose of $5x10^{16}$ ions/cm^2.

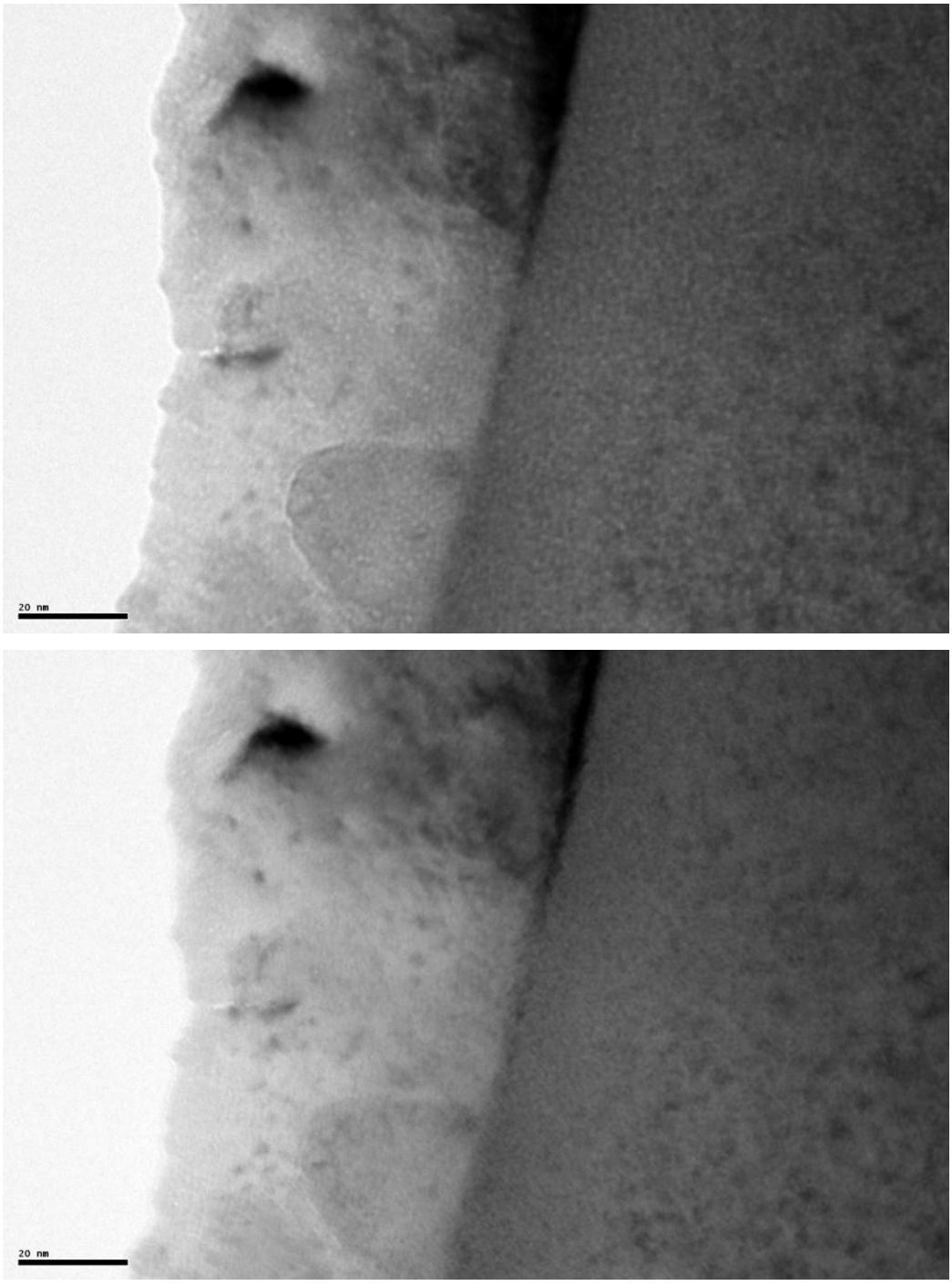

Figure A.56 Bright-field images of CeO_2 irradiated with 1 MeV Kr^+ at room temperature to a dose of $5x10^{16}$ ions/cm^2, registered by underfocusing and overfocusing the objective lens. The images are taken along [011] direction with g = -1-11.

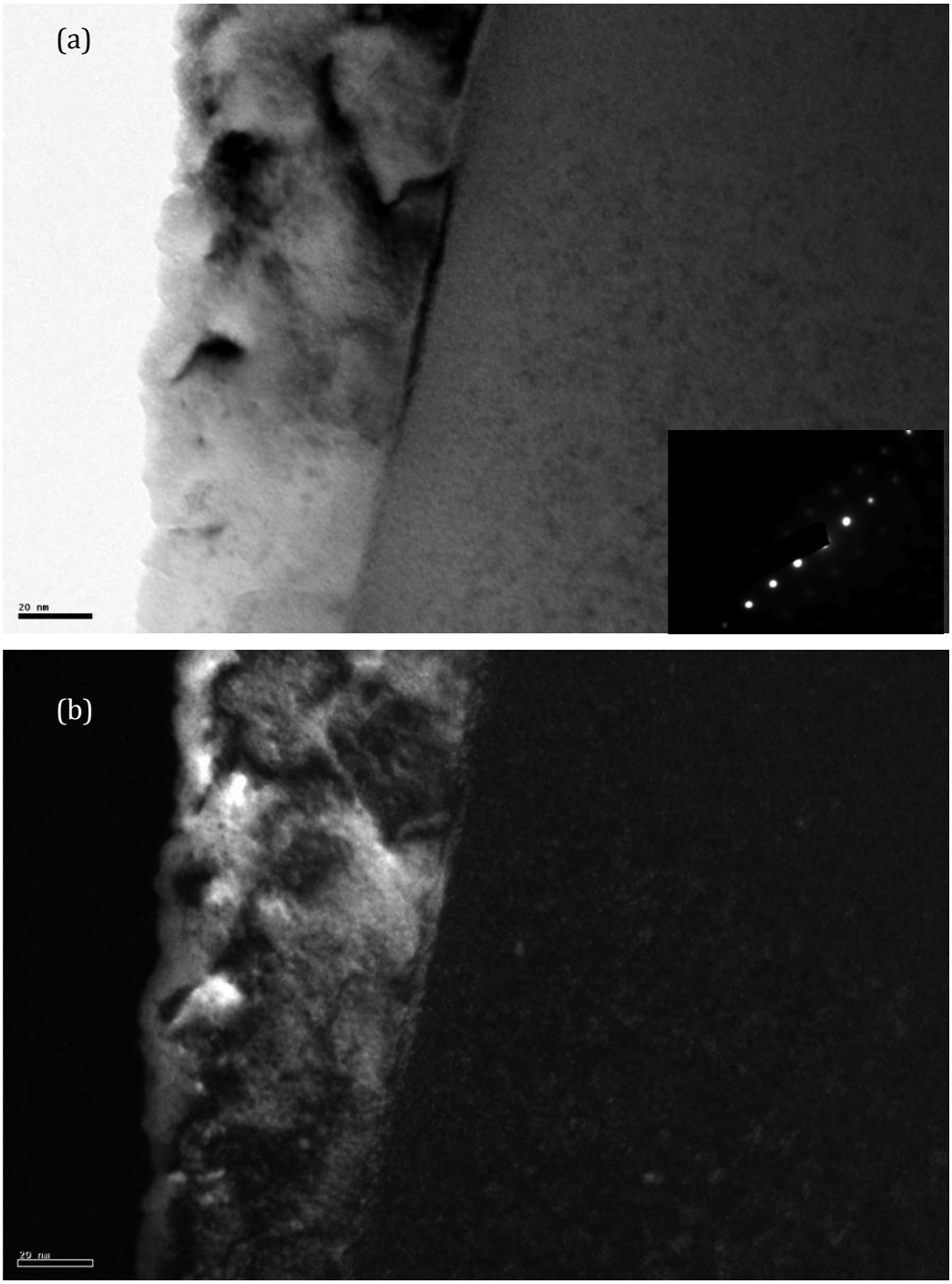

Figure A.57 (a) Bright-field and (b) dark-field images of CeO_2 irradiated with 1 MeV Kr^+ at room temperature to a dose of $5x10^{16}$ ions/cm^2. The images are taken along [011] direction with g = -1-11.

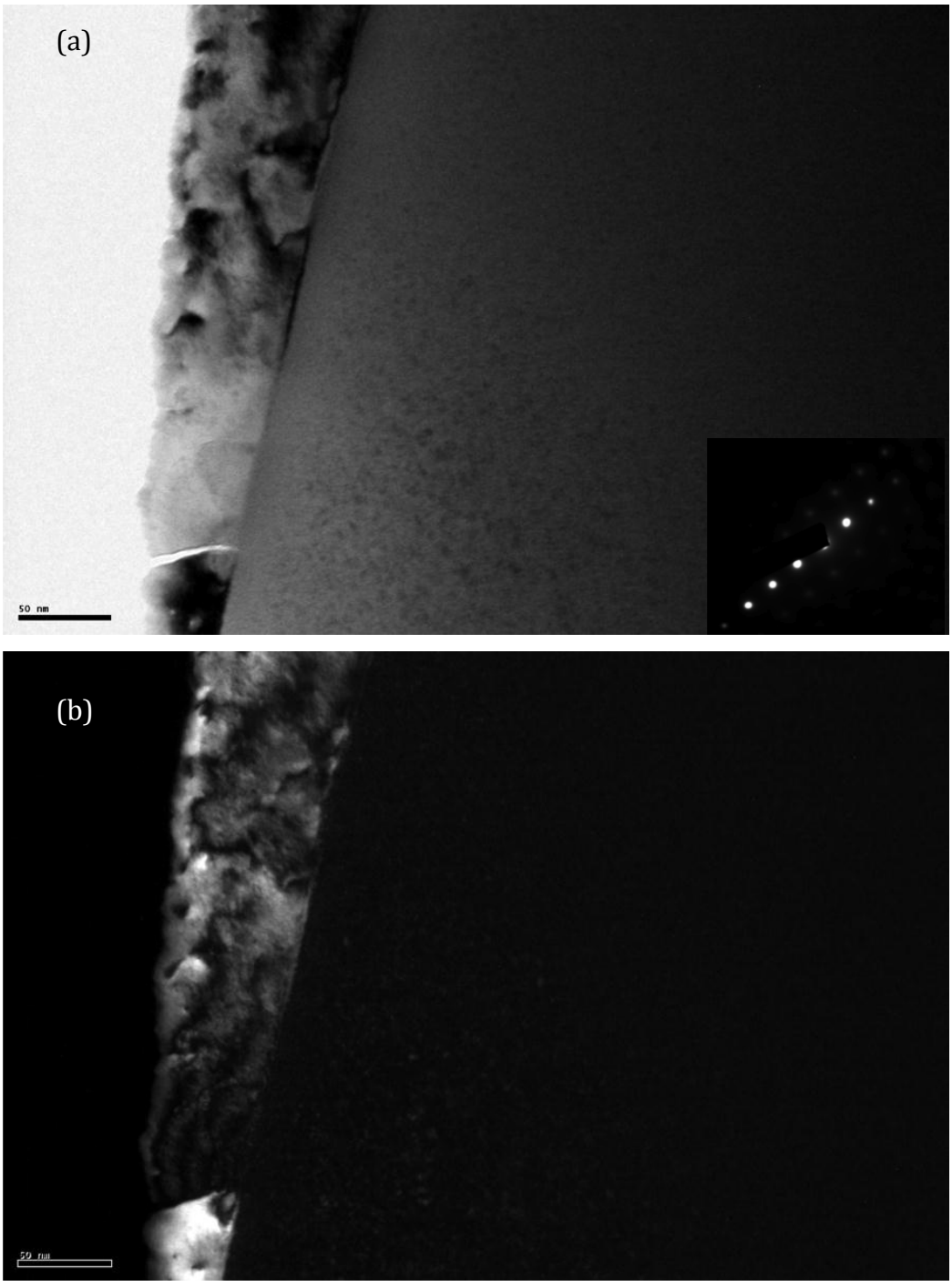

Figure A.58 (a) Bright-field and (b) dark-field images of CeO_2 irradiated with 1 MeV Kr^+ at room temperature to a dose of $5x10^{16}$ ions/cm^2. The images are taken along [011] direction with g = -1-11.

A.7.3 Irradiation dose is $1x10^{17}$ ions/cm^2

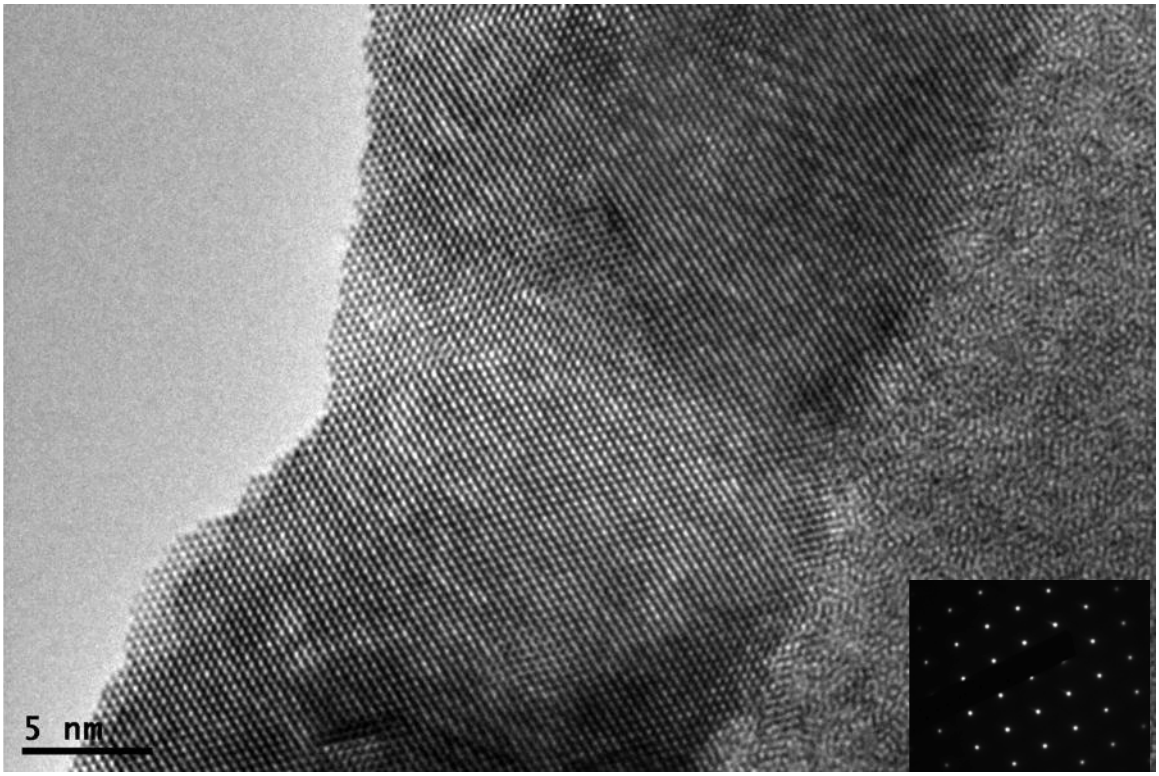

Figure A.59 Cross-section HRTEM image of CeO_2 irradiated with 1 MeV Kr^+ at room temperature to a dose of $1x10^{17}$ ions/cm^2.

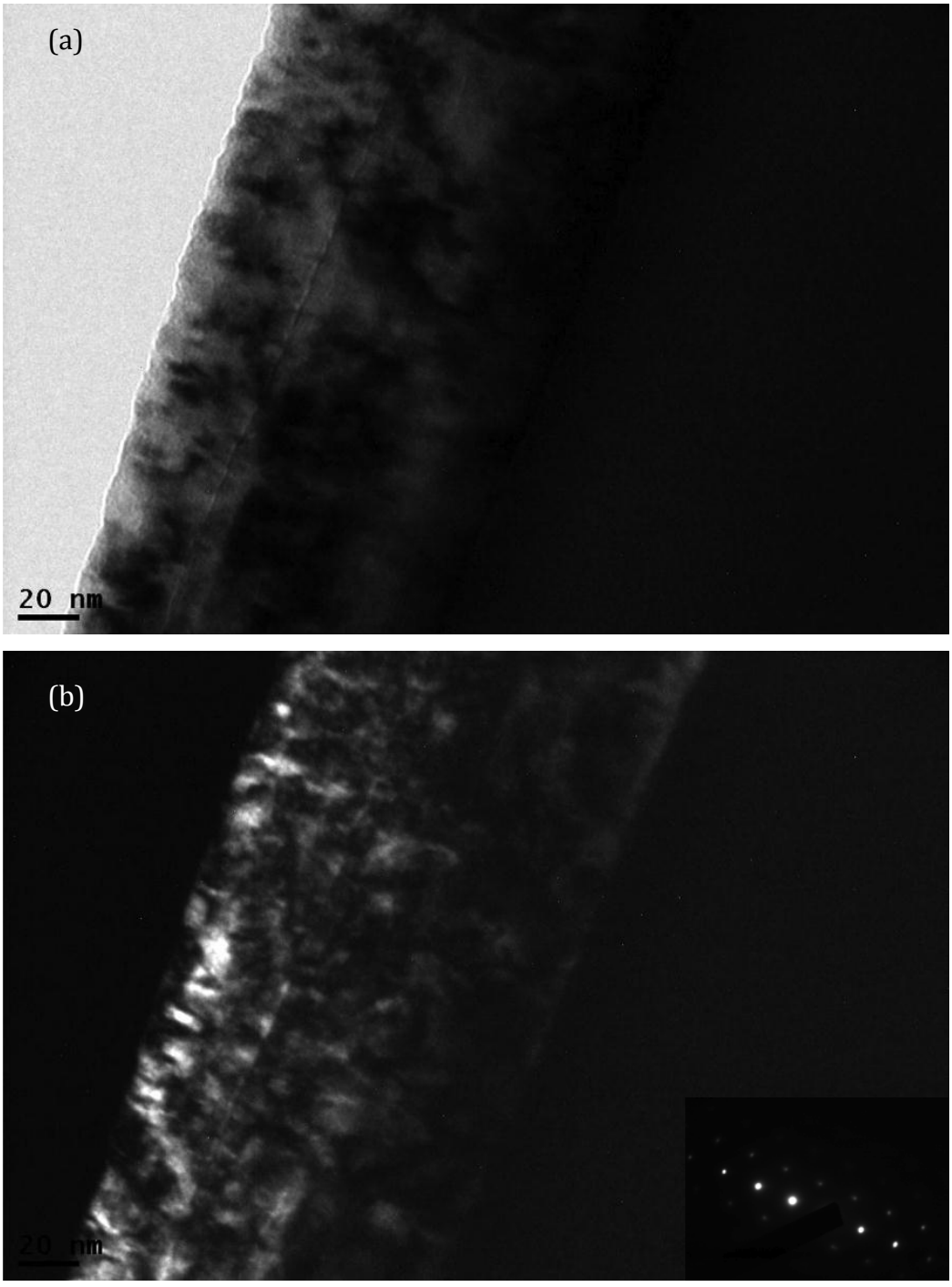

Figure A.60 (a) Bright-field and (b) dark-field images of CeO_2 irradiated with 1 MeV Kr^+ at room temperature to a dose of $1x10^{17}$ ions/cm^2. The images are taken along [011] direction with g = -1-11.

Appendix B. Rate Theory Program for Dislocation Loop Calculation

```
PROGRAM distribution
c
c#############################################################
####################
c
c     Program
c
c     Jerome Jonnet
c
c     Last modified version: 09/11/2006
c
c#############################################################
####################
c
      IMPLICIT NONE
c
      external foncresol, fonc, fonccoal
c     , jac
      integer i, j, m, neq, iout, jac, TL
      integer ITOL, ITASK, ISTATE, IOPT, LRW, LIW,
     & MF, IPAR
      double precision tmin, tmax, dtout, timp
      double precision tmUO2, den, molw, avn, nav, conv1, a, bv, vol,
     & vol23, zvrho, zirho, zvcav, zicav, nuv, nui, evmUO2,
     & evm, evfUO2, evf, eimUO2, eim, d0G, emG, sig, fden, nu,
```

```
     & xi, fn, rg, volg, tk, tm, bolzev, bolzcal, rgas, rtk, ktk,
     & ktkcal, wov, woi, dvt, di, alpha, fdot0, K, G, dgieKb, ddo,
     & Pi, dv, c1, dgieMz, dgtG, dg2G, K1, Kdi,
     & SumSqrtN, SumN, N,
     & ccell, cv0
      parameter (neq=6000)
      parameter (TL=360)
      parameter (LIW=30+neq)
c     parameter (LIW=30)
      parameter (LRW = 22 +  9*neq + 2*neq**2)
c     parameter (LRW = 20 + 16*neq)
      double precision y(neq), ydot(neq), Rha(neq-1), Lha(neq-1)
      double precision T, TOUT, RTOL, T_dummy
      double precision :: ATOL(neq), RWORK(LRW), RPAR(2*neq+2)
      double precision AverSqrtN(TL), Sumy(TL), AverN(TL)
      integer IWORK(LIW)
c
      write(6,*)
      write(6,*)" ********************************************** "
      write(6,*)" Calcul de distribution de boucles de dislocations "
      write(6,*)" ********************************************** "
c
c         Importation de la derniere distribution calculee
c         open(unit=77,file='result_11_volbis_restart2')
c         read(77,10) timp
c 10      format(e18.8)
c         do m=1,1499
c                   read(77,*) y(m)
c         enddo
c         do m=1500,neq-1
c                   y(m)=y(1499)
```

```
c         enddo
c         read(77,*,end=11) y(neq)
c
c 11   close(77)
c
      timp = 0.0D0
c         interstitials
      y(1)=0.0D0
c         di-interstitials
      y(2)=0.0D0
      do m=3,neq-2
        y(m)=0.0D0
      enddo
c         derniere equation
      y(neq-1)=0.0D0
c         vacancies
      y(neq)=0.0D0
c
      open(unit=99,file='result_new_2_8_impl')
      open(unit=88,file='param_2_8_impl')
c
      Pi = 4.*datan(1.0D0)
c
      tmUO2 = 2923.0D0
      den = 7.3D0
      molw = 172.0D0
      avn = 6.023D23
      nav = (den/molw)*avn
c
      conv1 = 6.7D22
      a = 5.41D-8
```

```
      bv = dsqrt(2.0D0)*a/2.
c
      vol = 3.96D-23
      vol23 = vol**(2./3.)
c
      zvrho = 1.0D0
      zirho = 1.0005D0
      zvcav = 1.0D0
      zicav = 1.0D0
c
      nuv = 5.0D13
      nui = 5.0D12
      evmUO2 = 2.4D0
      evm = evmUO2
      evfUO2 = 2.747D0
      evf = evfUO2
c     ######################################## Eim
      eimUO2 = 0.6D0
      eim = eimUO2
c
      d0G = 2.1D-4
      emG = 3.95D0
      sig = 0.*1500.*68947.
      fden = 1.0D0
c
      nu = 0.31D0
c     ######################################## xi
      xi = 0.5D0
      fn = 1.0D0
      rg = 2.16D-8
      volg = (4./3.)*Pi*(rg**3)
```

```
c
      tk = 523.0D0
      tm = tmUO2
c
      bolzev = 8.625D-5
      bolzcal = 1.98D0
      rgas = 1.38D-16
      rtk = rgas*tk
      ktk = bolzev*tk
      ktkcal = bolzcal*tk
c
      cv0 = 2.*dexp(-evf/ktk)
c
      wov = nuv*dexp(-evm/ktk)
      woi = nui*dexp(-eim/ktk)
      dvt = xi*(a**2)*wov
c          ######################################## Di
      di = (2.*xi*(a**2)*woi/3.)
c     di=1.0D-17
c
      alpha = 12.*(wov+woi)
      K = 0.00033
      fdot0 = conv1*K
      G = 3.82D11
c
      dgieKb = (fdot0/15.)*((1.8D-10)/(tm-tk)**2.4)**(5./3.)
      dv = dvt+0.*dgieKb
      c1 = 1.2D-29
      dgieMz = c1*fdot0
      dgtG = d0G*dexp(-emG/ktk)
      dg2G = dgtG+dgieMz
```

```
c
      ddo = 2.*bv
c
      ccell= 4.599D-8
c
      K1 = 12.*(wov+woi)
      Kdi = dsqrt(2.0D0)*di/(vol23)
      Rha(1)=0.0D0
      Lha(1)=0.0D0
      do m=2,neq-1
        Rha(m)=(2.*Pi/vol)*zirho*di*dsqrt(m*(ccell**2)/Pi)
        Lha(m)=(2.*Pi/vol)*zvrho*dv*dsqrt(m*(ccell**2)/Pi)
c                   write(88,*) Rha(m), Lha(m)
      enddo
c
      tmin = timp
      tmax = 2.2D10
c         ###################### deltat
      dtout = 10.0D0
c
      write(88,*) eim, xi, di, dv, alpha, neq, dtout
      close(88)
c
C RPAR,IPAR = user-defined real and integer arrays passed to F and JAC.
C Note that the main program must declare arrays Y, RWORK, IWORK,
C and possibly ATOL, RPAR, and IPAR.
c
      RPAR(1) = K
      RPAR(2) = K1
      RPAR(3) = Kdi
      do i=1, neq-1
```

```
      RPAR(3+i) = Rha(i)
    enddo
    do i=1, neq-1
      RPAR(3+neq-1+i) = Lha(i)
    enddo
    RPAR(2*neq+2) = di
c
c
    T = 0.0D0
    TOUT = 1.0D1
    ITOL = 1
    RTOL = 1.0D-6
    do j=1, neq
      ATOL(j) = 1.0D-13
    enddo
    ITASK = 1
    ISTATE = 1
    IOPT = 0
    MF = 22
    jac = 1
c
c
    write (6,120)
 120  format(//' time          ci          c2i          c(n-1)i          cni
          cv'//)
    do iout=1,TL
      call dvode (fonccoal, neq, y, T, TOUT, ITOL, RTOL, ATOL,
    &   ITASK, ISTATE, IOPT, RWORK, LRW, IWORK, LIW, JAC, MF,
    &   RPAR, IPAR)
c     WRITE(6,20) T, y(1), y(2), y(neq-2), y(neq-1), y(neq)
c 20   FORMAT(' At t =',D12.4,'   y =',5D14.6)
```

```
cc      call foncresol(neq, y, ydot, K, K1, Kdi, Rha, Lha, di)
cc      do i=1,neq
cc        y(i)=y(i)+ydot(i)*dtout
cc      enddo
      SumSqrtN = 0.0D0
      SumN = 0.0D0
      Sumy(iout) = 0.0D0
      N = 2.0D0
      do j=2,neq-1
        SumSqrtN=SumSqrtN+sqrt(N)*y(j)
        SumN=SumN+N*y(j)
        Sumy(iout)=Sumy(iout)+y(j)
        N=N+1
      enddo
      AverSqrtN(iout)=SumSqrtN/Sumy(iout)
      AverN(iout)=SumN/Sumy(iout)
      if (MOD(tout, 1.0D1).eq.0.) then
        write(6,140) TOUT , y(1), y(2), y(neq-2), y(neq-1), y(neq),
     $               di
140     format(d14.5,d14.5,d14.5,d14.5,d14.5,d14.5,d14.5)
        write(99,141) TOUT
141     format(d18.8)
        do j=1,neq
          write(99,*) y(j)
        enddo
        do j=2,neq-2
          write(99,*) j, y(j)/Sumy(iout)
        enddo
      endif
    tout = tout + 10
    enddo
```

```
      write(99,*) "Average sqrtN="
      do iout=1,TL
        write(99,*) iout, 0.2595*AverSqrtN(iout)
      enddo
      write(99,*) "Sum y="
      do iout=1,TL
        write(99,*) iout, Sumy(iout)
      enddo
c     do j=1,neq
c       write(99,*) y(j)
c     enddo
      close(99)
c
      write(6,*)
      write(6,*)" ********** "
      write(6,*)" Calcul OK ! "
      write(6,*)" ********** "
      END
c
c
c//////////////////////////////////////////////////////////////
c                     SUBROUTINES
c
c        **********************
c        Sous-routine standard
c        **********************
c
      subroutine fonc(neq, T_dummy, y, ydot, RPAR, IPAR)
      implicit none
      integer neq, m, i, j, IPAR(*)
      double precision K, K1, Kdi, sumR, sumL,
```

```
     & Pi, ccell, vol, Dvol, a, di, T_dummy
      double precision :: y(neq), ydot(neq), Rha(neq-1), Lha(neq-1),
     & RPAR(*)
c
      Pi = 4.*atan(1.0D0)
c
      K = RPAR(1)
      K1 = RPAR(2)
      Kdi = RPAR(3)
      do i=1, neq-1
        Rha(i) = RPAR(3+i)
      enddo
      do i=1, neq-1
        Lha(i) = RPAR(3+neq-1+i)
      enddo
      di = RPAR(2*neq+2)
c
      a = 5.47D-8
      vol = 4.2D-23
      ccell = 4.599D-8
c         ################################# Dvol
      Dvol = di
c
      sumL=0.1D0
      do m=2,neq-1
        sumL = sumL + Lha(m)*y(m)
      enddo
      sumL = sumL*y(neq)
c
      sumR=0.1D0
      do m=2,neq-2
```

```
      sumR = sumR + Rha(m)*y(m)
    enddo
    sumR = sumR*y(1)
c       ci
    ydot(1) = K - K1*y(neq)*y(1) - Kdi*y(1)*y(1) - sumR
   &    + Lha(2)*y(2)*y(neq)
c       c2i
    ydot(2) = (1./2.)*Kdi*y(1)*y(1) + Lha(3)*y(3)*y(neq)
   &    - Lha(2)*y(2)*y(neq) - Rha(2)*y(2)*y(1)
c
    do m=3,neq-2
      ydot(m) = Rha(m-1)*y(m-1)*y(1) + Lha(m+1)*y(m+1)*y(neq)
   &      - Rha(m)*y(m)*y(1) - Lha(m)*y(m)*y(neq)
    enddo
c       derniere equation
    ydot(neq-1) = Rha(neq-2)*y(neq-2)*y(1)
c        - Rha(neq-1)*y(neq-1)*y(1)
   &    - Lha(neq-1)*y(neq-1)*y(neq)
c       vacancies
    ydot(neq) = K - K1*y(neq)*y(1) - sumL
c
    return
    end
c
c       ****************************************
c       Sous-routine pour la remise en solution
c       ****************************************
c
    subroutine foncresol(neq, T_dummy, y, ydot, RPAR, IPAR)
    implicit none
    integer neq, m, i, j, IPAR(*), imp
```

```
      double precision K, K1, Kdi, sumR, sumL,
     & Pi, ccell, vol, Dvol, a, di, T_dummy, ra, mua, F, K3
      double precision :: y(neq), ydot(neq), Rha(neq-1), Lha(neq-1),
     & RPAR(*)
c
      Pi = 4.*atan(1.0D0)
c
      K = RPAR(1)
      K1 = RPAR(2)
      Kdi = RPAR(3)
      do i=1, neq-1
        Rha(i) = RPAR(3+i)
      enddo
      do i=1, neq-1
        Lha(i) = RPAR(3+neq-1+i)
      enddo
      di = RPAR(2*neq+2)
c
      a = 5.47D-8
      F = 3.82D11
      ccell= 4.599D-8
c         ############################## mua
      mua = 1.0D-7
c
      ra = dsqrt(4.0135D-20/(Pi*mua))
      imp = floor(Pi*ra**2/ccell**2)+1
c
      sumL=0.0D0
      do m=2,neq-1
        sumL = sumL + Lha(m)*y(m)
      enddo
```

```
      sumL = sumL*y(neq)
c
      sumR=0.0D0
      do m=2,neq-2
        sumR = sumR + Rha(m)*y(m)
      enddo
      sumR = sumR*y(1)
c
c         Nombre d'interstitiels remis en solution
      K3=0.0D0
      do i=2,neq-1
        K3 = K3 + y(i)*(dble(i))*dble(min(i,imp))
      enddo
      K3 = K3*F*mua*(ccell**2)
c
c         ci
      ydot(1) = K - K1*y(neq)*y(1) - Kdi*y(1)*y(1) - sumR
     &     + Lha(2)*y(2)*y(neq) + K3
c         c2i
      ydot(2) = (1./2.)*Kdi*y(1)*y(1) + Lha(3)*y(3)*y(neq)
     &     - Lha(2)*y(2)*y(neq) - Rha(2)*y(2)*y(1)
     &     + y(2+imp)*F*mua*(dble(2+imp))*(ccell**2)
     &     - y(2)*F*mua*(dble(2))*(ccell**2)
c
      do m=3,neq-2
        if (m.lt.(neq-1-imp)) then
          ydot(m) = Rha(m-1)*y(m-1)*y(1) + Lha(m+1)*y(m+1)*y(neq)
     &                      - Rha(m)*y(m)*y(1) - Lha(m)*y(m)*y(neq)
     &                      + y(m+imp)*F*mua*(dble(m+imp))*(ccell**2)
     &                      - y(m)*F*mua*(dble(m))*(ccell**2)
        else
```

```
        ydot(m) = Rha(m-1)*y(m-1)*y(1) + Lha(m+1)*y(m+1)*y(neq)
     &                    - Rha(m)*y(m)*y(1) - Lha(m)*y(m)*y(neq)
     &                    - y(m)*F*mua*(dble(m))*(ccell**2)
       endif
     enddo
c        derniere equation
     ydot(neq-1) = Rha(neq-2)*y(neq-2)*y(1)
c         - Rha(neq-1)*y(neq-1)*y(1)
     &    - Lha(neq-1)*y(neq-1)*y(neq)
     &    - y(neq-1)*F*mua*(dble(neq-1))*(ccell**2)
c        vacancies
     ydot(neq) = K - K1*y(neq)*y(1) - sumL
c
     return
     end
c
c
c    subroutine jac(neq, T, y, ydot, RPAR, IPAR)
c    implicit none
c    integer neq, IPAR
c    double precision T
c    double precision :: y(neq), ydot(neq), RPAR(*)
c
c    return
c    end
c
c
c
c        ****************************************
c        subroutine for coalescence mechanism
c        ****************************************
```

```
c
      subroutine fonccoal(neq, T_dummy, y, ydot, RPAR, IPAR)
      implicit none
      integer neq, m, i, j, IPAR(*), imp
      double precision K, K1, Kdi, sumR, sumL,
     & Pi, ccell, vol, Dvol, a, di, T_dummy, ra, mua, F, K3
      double precision :: y(neq), ydot(neq), Rha(neq-1), Lha(neq-1),
     & RPAR(*), coall_plus(neq-1), coall_minus(neq-1)
c
      Pi = 4.*atan(1.0D0)
c
      K = RPAR(1)
      K1 = RPAR(2)
      Kdi = RPAR(3)
      do i=1, neq-1
        Rha(i) = RPAR(3+i)
      enddo
      do i=1, neq-1
        Lha(i) = RPAR(3+neq-1+i)
      enddo
      di = RPAR(2*neq+2)
c
      a = 5.41D-8
      vol = 3.96D-23
      F = 3.82D11
      ccell= 4.599D-8
      Dvol=di
c         ############################## mua
      mua = 30.0D-17
c
      ra = dsqrt(4.0135D-20/(Pi*mua))
```

```
      imp = floor(Pi*ra**2/ccell**2)+1
c
      sumL=0.0D0
      do m=2,neq-1
        sumL = sumL + Lha(m)*y(m)
      enddo
      sumL = sumL*y(neq)
c
      sumR=0.0D0
      do m=2,neq-2
        sumR = sumR + Rha(m)*y(m)
      enddo
      sumR = sumR*y(1)
c
c         Nombre d'interstitiels remis en solution
c     K3=0.0D0
c     do i=2,neq-1
c       K3 = K3 + y(i)*(dble(i))*dble(min(i,imp))
c     enddo
c     K3 = K3*F*mua*(ccell**2)
c
c         ci
c     ydot(1) = K - K1*y(neq)*y(1) - Kdi*y(1)*y(1) - sumR
c    &     + Lha(2)*y(2)*y(neq) + K3
c         c2i
c     ydot(2) = (1./2.)*Kdi*y(1)*y(1) + Lha(3)*y(3)*y(neq)
c    &     - Lha(2)*y(2)*y(neq) - Rha(2)*y(2)*y(1)
c    &     + y(2+imp)*F*mua*(dble(2+imp))*(ccell**2)
c    &     - y(2)*F*mua*(dble(2))*(ccell**2)
c
c     do m=3,neq-2
```

```
c       if (m.lt.(neq-1-imp)) then
c         ydot(m) = Rha(m-1)*y(m-1)*y(1) + Lha(m+1)*y(m+1)*y(neq)
c    &                    - Rha(m)*y(m)*y(1) - Lha(m)*y(m)*y(neq)
c    &                    + y(m+imp)*F*mua*(dble(m+imp))*(ccell**2)
c    &                    - y(m)*F*mua*(dble(m))*(ccell**2)
c       else
c         ydot(m) = Rha(m-1)*y(m-1)*y(1) + Lha(m+1)*y(m+1)*y(neq)
c    &                    - Rha(m)*y(m)*y(1) - Lha(m)*y(m)*y(neq)
c    &                    - y(m)*F*mua*(dble(m))*(ccell**2)
c       endif
c     enddo
      do i=2,neq-1
         coall_plus(i)=0.0D0
         do j=2,i
            if ((i-j).gt.0) then
               coall_plus(i) = coall_plus(i)
     &              + (dsqrt(dble(j)) + dsqrt(dble(i-j)))
     &       *(1./dsqrt(dble(j))+1./dsqrt(dble(i-j)))*y(j)*y(i-j)
            endif
         enddo
         coall_plus(i)=(8.*a*Dvol)/(vol*Pi)*coall_plus(i)
         coall_minus(i)=0.0D0
         do j=2,neq-1
            coall_minus(i)=coall_minus(i)
     &              +(dsqrt(dble(i))+dsqrt(dble(j)))
     &           *(1./dsqrt(dble(i))+1./dsqrt(dble(j)))*y(i)*y(j)
         enddo
         coall_minus(i)=(8.*a*Dvol)/(vol*Pi)*coall_minus(i)
      enddo
c
c     ci
```

```
      ydot(1)=K-K1*y(neq)*y(1)-Kdi*y(1)*y(1)-sumR
     &        + Lha(2)*y(2)*y(neq)
c     c2i
      ydot(2)=(1./2.)*Kdi*y(1)*y(1)+Lha(3)*y(3)*y(neq)
     &      -Lha(2)*y(2)*y(neq)-Rha(2)*y(2)*y(1)
     &      +coall_plus(2)-coall_minus(2)
c
      do m=3,neq-2
         ydot(m)=Rha(m-1)*y(m-1)*y(1)+Lha(m+1)*y(m+1)*y(neq)
     &       -Rha(m)*y(m)*y(1)-Lha(m)*y(m)*y(neq)
     &       +coall_plus(m)-coall_minus(m)
      enddo
c         derniere equation
      ydot(neq-1) = Rha(neq-2)*y(neq-2)*y(1)
c          - Rha(neq-1)*y(neq-1)*y(1)
     &    - Lha(neq-1)*y(neq-1)*y(neq)
     &    +coall_plus(neq-1)-coall_minus(neq-1)
c         vacancies
      ydot(neq) = K - K1*y(neq)*y(1) - sumL
c
      return
      end
c
c
c     subroutine jac(neq, T, y, ydot, RPAR, IPAR)
c     implicit none
c     integer neq, IPAR
c     double precision T
c     double precision :: y(neq), ydot(neq), RPAR(*)
c
c     return
```

```
c     end
```

Biography

Bei Ye received her B.S. in Nuclear Engineering and Technology from Tsinghua University, China in July 2000. After that, she worked as an engineer in Shanghai Nuclear Engineering Research and Design Institute (SNERDI). The four years of work experience and the earlier college education inspired her to pursue higher education in the USA. She became a graduate student of the Department of Nuclear, Plasma and Radiology Engineering at University of Illinois at Urbana-Champaign in August 2004, and earned her M.S. in Nuclear Engineering in 2007. Her master's thesis was titled: *Effects of Thermal-hydraulic Feedback on Burnup Modeling of the Deep Burn Modular High Temperature Reactor (DB-MHR)*. After the M.S. degree, she continued her Ph.D. study in nuclear material area under the advisorship of Prof. James F. Stubbins. Following the completion of her doctoral degree, she will continue working in the field of nuclear engineering.